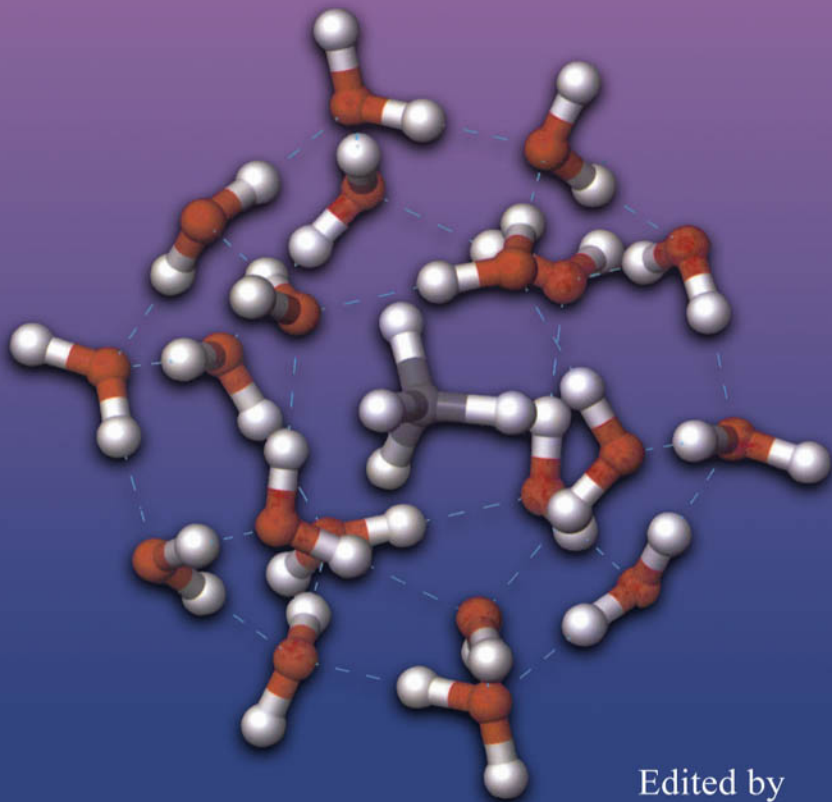


*Advances in the*  
**STUDY OF GAS  
HYDRATES**



Edited by  
**CHARLES E. TAYLOR AND  
JONATHAN T. KWAN**

# Advances in the Study of Gas Hydrates

*This page intentionally left blank*

# Advances in the Study of Gas Hydrates

Edited by

Charles E. Taylor

*U.S. DOE/NETL*

*Pittsburgh, Pennsylvania*

and

Jonathan T. Kwan

*Mewbourne School of Petroleum and Geological Engineering*

*The University of Oklahoma*

*Norman, Oklahoma*

**KLUWER ACADEMIC PUBLISHERS**

NEW YORK, BOSTON, DORDRECHT, LONDON, MOSCOW



eBook ISBN: 0-306-48645-8  
Print ISBN: 0-306-48481-1

©2004 Springer Science + Business Media, Inc.

Print ©2004 Kluwer Academic/Plenum Publishers  
New York

All rights reserved

No part of this eBook may be reproduced or transmitted in any form or by any means, electronic, mechanical, recording, or otherwise, without written consent from the Publisher

Created in the United States of America

Visit Springer's eBookstore at:  
and the Springer Global Website Online at:

<http://www.ebooks.kluweronline.com>  
<http://www.springeronline.com>

# Preface

This book had its genesis in a symposium on gas hydrates presented at the 2003 Spring National Meeting of the American Institute of Chemical Engineers. The symposium consisted of twenty papers presented in four sessions over two days. Additional guest authors were invited to provide continuity and cover topics not addressed during the symposium.

Gas hydrates are a unique class of chemical compounds where molecules of one compound (the guest material) are enclosed, without bonding chemically, within an open solid lattice composed of another compound (the host material). These types of configurations are known as clathrates. The guest molecules, usually gases, are of an appropriate size such that they fit within the cage formed by the host material. Common examples of gas hydrates are carbon dioxide/water and methane/water clathrates. At standard pressure and temperature, methane hydrate contains by volume 180 times as much methane as hydrate. The United States Geological Survey (USGS) has estimated that there is more organic carbon contained as methane hydrate than all other forms of fossil fuels combined. In fact, methane hydrates could provide a clean source of energy for several centuries.

Clathrate compounds were first discovered in the early 1800s when Humphrey Davy and Michael Faraday were experimenting with chlorine-water mixtures. Working during the winter, the scientists noticed that as the mixtures cooled during the night, a solid material formed at temperatures above the normal freezing point of water. Throughout the remainder of the century, many other scientists studied these strange materials, and generally worked out the process by which typically unstable open frameworks of water molecules (and other substances as well) were stabilized by the inclusion, without bonding, of smaller guest molecules into cavities within the structure. Much work was done cataloging the various molecules that could co-exist as hosts (lattice-formers) and guests, and the various conditions at which each molecule was stable. However, because natural occurrences were not known, the subject remained largely an academic curiosity.

Hydrate research entered its next phase in the 1930s, when E.G. Hammer-schmidt determined that methane hydrate was responsible for plugging natural gas pipelines, particularly those located in cold environments. For the next 40 years, a small body of researchers investigated the physics of various clathrates, including

the construction of the first predictive models of their formation. A prime focus of this work was (and continues to be) the development of chemical additives and other methods to inhibit hydrate formation.

In the late 1960s, the global view of clathrate science began to change dramatically when “solid natural gas” or methane hydrate was observed as a naturally-occurring constituent of subsurface sediments in the giant gas fields of the Western Siberia basin. Shortly thereafter, hydrate was also found in shallow, sub-permafrost sediments on the North Slope of Alaska. Soon, scientists, particularly those in the former Soviet Union, began to speculate that the low temperature/high pressure conditions necessary for hydrate formation should exist extensively around the globe, not only in permafrost regions, but also under deep oceans. The global hunt for methane hydrate was on.

Because methane hydrate quickly dissociates (similar to melting) when removed from its natural environment, no one actually saw marine methane hydrate until 1974 when Soviet scientists recovered large hydrate nodules from the floor of the Black Sea. Then, in the early 1980s, the research vessel *Glomar Challenger* traveled the globe collecting cores of ocean bottom sediments as part of a renewed round of Deep Sea Drilling Project tests. Many of the samples found chemical evidence for hydrate. One core taken off the coast of Guatemala included a one-meter long core composed almost entirely of methane hydrate.

The recent flurry in hydrate research was ignited in the mid-90s when Japan and India, two countries with large energy needs but limited domestic energy resources, began aggressive well-funded hydrate programs in preparation for commercial production of methane. At the same time, continued environmental concerns rapidly escalated the demand for natural gas. In 1998 and 1999, international efforts resulted in the drilling of the first two wells designed specifically to investigate methane hydrate-bearing strata. The first well (the Mallik 3L-18C) was drilled into hydrate-bearing strata below permafrost on the McKenzie River delta in the Northwest Territories of Canada. The second well was drilled by a consortium of Japanese government agencies and commercial interests in 3,100 feet of water off the southeastern Japanese coast adjacent to a deep ocean trench known as the Nankai Trough. Both wells have shown the presence of large volumes of methane hydrate.

For many years, the Ocean Drilling Program at Texas A&M has explored the ocean sediments around the globe. Their efforts in the last few voyages to recover and analyze the hydrates in deep water have moved the understanding of hydrate deposition and its science to a higher level. In 2003, projects in Alaska and deep water Gulf of Mexico sponsored by US DOE and under the direction of NETL began. The results of all these projects—both domestic and international—should shorten the time required to make hydrates a commercially viable product. This can be expected in the next ten to fifteen years.

The book is organized in five parts. The discussions cover topics from the basic research of hydrate chemical and physical properties to the understanding of their formation and decomposition; from the mathematical modeling to the practical applications of hydrates. The authors share their diverse and timely research as well as their expert insights.

As presented in this book, research in gas hydrates has advanced to cover several areas such as improved detection technologies, computer modeling of hydrate physical properties, and laboratory investigations on both naturally occurring and laboratory synthesized hydrates.

Charles E. Taylor  
Jonathan T. Kwan

*This page intentionally left blank*

# Contents

## SECTION I: MODELING OF HYDRATES

<b>1. TOWARDS A FULL DYNAMIC MODEL OF CO<sub>2</sub> HYDRATE FORMATION IN AQUEOUS SOLUTIONS: Phase Field Theory of Nucleation and Growth</b> .....	3
L. Gránásy, T. Pusztai, G. Tegze, T. Kuznetsova, and B. Kvamme	
<b>2. STATISTICAL THERMODYNAMIC MODEL OF CLATHRATE HYDRATES WITH MULTIPLE FILLING OF CAGES</b> .....	19
A. A. Pomeransky and V. R. Belosludov	
<b>3. PHENOMENOLOGICAL MODELING OF HYDRATE FORMATION AND DISSOCIATION</b> .....	27
M. C. Gonzalez Chacin, Richard G. Hughes, Faruk Civan, and Charles E. Taylor	
<b>4. EFFECT OF CONDUCTIVE AND CONVECTIVE HEAT FLOW ON GAS PRODUCTION FROM NATURAL HYDRATES BY DEPRESSURIZATION</b> .....	43
Mehran Pooladi-Darvish and Huifang Hong	
<b>5. AN APPLICATION USED FOR CORRECTING THERMAL GRADIENTS BELOW PERMAFROST USING AN EMPIRICAL DIFFUSION MODEL: Anadarko's Hot Ice #1 Gas Hydrates Case Study</b> .....	67
K. E. Newsham, R. Sigal, and J. T. Kwan	
<b>6. GAS PRODUCTION FROM CLASS 1 HYDRATE ACCUMULATIONS</b> .....	83
George J. Moridis and Timothy S. Collett	

## SECTION II: DETECTION OF HYDRATES

7. **A PROJECT UPDATE OF METHANE HYDRATE  
PRODUCTION FROM ALASKAN PERMAFROST .....** 101  
Keith Millheim, Jonathan Kwan, Williams Maurer,  
William MacDonald, Tom Williams, Ali Kadaster,  
Tommy Thompson, Richard Sigal, David Copeland,  
Donn McGuire, Steve Runyon, Bill Liddell, Carl Sondergeld, and  
Chandra Rai
8. **SEISMIC DETECTION AND QUANTIFICATION OF GAS  
HYDRATES USING ROCK PHYSICS AND INVERSION .....** 117  
Haibin Xu, Jianchun Dai, Fred Snyder, and Nader Dutta
9. **EXPERIMENT AND MODELING OF HYDRATE  
EQUILIBRIUM LINE IN GAS, GAS CONDENSATE,  
BLACK OIL, AND DRILLING COMPLETION FLUIDS .....** 141  
Keshawa Shukla, Aftab Khokhar, and Bayram Kalpakci

## SECTION III: LABORATORY STUDIES OF HYDRATES

10. **SOLUBILITY MEASUREMENTS FOR CO<sub>2</sub> AND METHANE  
MIXTURE IN WATER AND AQUEOUS ELECTROLYTE  
SOLUTIONS NEAR HYDRATE CONDITIONS .....** 157  
Ying Irene Zhang, Pallav Jain, Roger Chen, Douglas Elliot,  
Kyoo Song, Walter Chapman, Riki Kobayashi, and Heng-Joo Ng
11. **NUCLEATION MECHANISMS OF CLATHRATE HYDRATES ...** 173  
A. A. Pomeransky, V. R. Belosludov, and T. M. Inerbaev
12. **THE MSU MICELLAR-SOLUTION GAS HYDRATE STORAGE  
PROCESS FOR NATURAL GAS .....** 185  
Rudy E. Rogers, Yu Zhong, John A. Etheridge, and  
Larry E. Pearson
13. **ENHANCEMENT IN THE STORAGE OF METHANE IN  
HYDRATES .....** 199  
Charles E. Taylor, Dirk D. Link, Heather A. Elsen, and  
Edward P. Ladner

**14. STRENGTH AND ACOUSTIC PROPERTIES OF OTTAWA SAND CONTAINING LABORATORY-FORMED METHANE GAS HYDRATE.....** 213  
William J. Winters, William F. Waite, and David H. Mason

**15. INVESTIGATING METHANE HYDRATE IN SEDIMENTS USING X-RAY COMPUTED TOMOGRAPHY.....** 227  
Barry M. Freifeld and Timothy J. Kneafsey

**16. METHANE HYDRATE STUDIES: Delineating Properties of Host Sediments to Establish Reproducible Decomposition Kinetics.....** 239  
Devinder Mahajan, Phillip Servio, Keith W. Jones, Huan Feng, and William J. Winters

**AUTHOR INDEX.....** 251

**KEYWORD INDEX.....** 253



*This page intentionally left blank*

Section I

Modeling of Hydrates

*This page intentionally left blank*

# Towards a Full Dynamic Model of CO<sub>2</sub> Hydrate Formation in Aqueous Solutions: Phase Field Theory of Nucleation and Growth

L. Gránásy,\* T. Pusztai, G. Tegze, T. Kuznetsova, and B. Kvamme\*

## 1. INTRODUCTION

The amount of carbon bound in natural gas hydrates is conservatively estimated to be twice the amount of carbon to be found in all known fossil fuels on Earth [1]. Assuming that the lattice is filled to the maximum capacity, 1 m<sup>3</sup> gas hydrate may release about 164 m<sup>3</sup> methane under standard temperature and pressure (STP) condition [2]. CO<sub>2</sub> hydrate is significantly more stable thermodynamically than methane hydrate. Storage of CO<sub>2</sub> in hydrate reservoirs through replacement of natural gas is therefore considered as an interesting option for safe long terms

---

L. GRÁNÁSY • Research Institute for Solid State Physics and Optics, H-1525 Budapest, POB 49, Hungary

T. PUSZTAI • Research Institute for Solid State Physics and Optics, H-1525 Budapest, POB 49, Hungary

G. TEGZE • Research Institute for Solid State Physics and Optics, H-1525 Budapest, POB 49, Hungary

T. KUZNETSOVA • Department of Physics, University of Bergen, Allégaten 55, N-5007 Bergen, Norway

B. KVAMME • Department of Physics, University of Bergen, Allégaten 55, N-5007 Bergen, Norway

\* grana@szfki.hu & bjorn.kvamme@fi.uib.no

storage of  $\text{CO}_2$ , which can be economically feasible due to the produced natural gas. The efficiency of any exploitation strategy based on  $\text{CO}_2$  depends on the composite dynamics of the system, where knowledge of the kinetics of hydrate reformation is crucial. Storage of  $\text{CO}_2$  in aquifers is another option for reducing  $\text{CO}_2$  emissions to the atmosphere. This option is already in use outside the coast of Norway, where  $\text{CO}_2$  from the Sleipner field is being injected into the Utsira formation. Similar storage option may be used outside the northern part of Norway. In these regions the seabed temperature may reach as low as  $-1^\circ\text{C}$  and there may be regions of the reservoirs beneath that are inside the hydrate stability zones. Therefore, hydrate may form homogeneously from dissolved  $\text{CO}_2$  or at the interface between free  $\text{CO}_2$  and water.

Development of the related technologies requires a detailed understanding of all processes involved a knowledge that can be gained by combined experimenting and modeling. An essential ingredient of such an approach is the development of appropriate theoretical tools that can describe all stages of the processes involved. One of the little understood steps of hydrate formation is nucleation, in which nanometer sized hydrate crystallites form via thermal fluctuations.

In this paper, we apply the phase field theory for describing the nucleation and growth of  $\text{CO}_2$  hydrate under conditions specific to underwater reservoirs. The phase field theory (PFT) is one of the most potent methods developed recently to model solidification in binary, ternary and multi-component melts. Over the past decade the ability of the PFT to describe complex solidification morphologies has been demonstrated [3]. This includes the thermal and solutal dendrites [4–6], the eutectic/peritectic fronts [8–10], and crystal nucleation in alloys [11,12]. It has been shown that for systems (Lennard-Jones, ice-water and hard sphere) where the input parameters of the PFT are known with satisfactory accuracy, it predicts the nucleation rate with a far better accuracy than the sharp interface droplet model of the classical theory that, in turn, fails by several orders of magnitude. Herein we show that using reasonable input data, similar differences occur in the case of hydrate formation. We also calculate the growth rate of hydrate particles and, on a model system; we address problems associated with freezing in the presence of walls including solidification in a porous medium and channels.

## 2. MODELS FOR NUCLEATION AND GROWTH

The freezing of homogeneous undercooled liquids starts with the formation of heterophase fluctuations whose central part shows crystal-like atomic arrangement. Those heterophase fluctuations that exceed a critical size (determined by the interplay of the interfacial and volumetric contributions to the cluster free energy) have a good chance to reach macroscopic dimensions, while the smaller ones decay with a high probability. (Heterophase fluctuations of the critical size are called *nuclei*.) The description of the near-critical fluctuations is problematic even in

single component systems. The main difficulty is that the typical size of the critical fluctuations, forming on the human time scale, is about 1 nm, comparable to the thickness of the crystal-liquid interface, which in turn extends to several molecular layers [13]. Therefore, the droplet model of the classical nucleation theory, which relies on a sharp interface and bulk crystal properties, is inappropriate for such fluctuations. Field theoretic models, that predict a diffuse interface, offer a natural way to handle such a situation [14]. For example, in recent works, the phase field theory has been shown to describe such fluctuations quantitatively [11,12,15].

## 2.1. Phase field theory of nuclei

Our starting point is the standard phase field theory of binary alloys as developed by several authors [6,16]. In the present approach, the local state of the matter is characterized by two fields; a structural order parameter,  $\phi$ , called the *phase field*, that describes the transition between the disordered liquid and ordered crystalline structures, and a conserved field, the coarse-grained solute concentration,  $c$ .

The structural order parameter can be viewed as the Fourier amplitude of the dominant density wave of the time averaged singlet density in the solid. As pointed out by Shen and Oxtoby [17] if the density peaks in the solid can be well approximated by Gaussians placed to the atomic sites, all Fourier amplitudes can be expressed uniquely in terms of the amplitude of the dominant wave, thus a single structural order parameter suffices. Here we take  $m = 0$  in the solid and  $m = 1$  in the liquid. We assume mass conservation, which implies that the integral of the conservative fields over volume is a constant.

The free energy of the system is a functional of these fields:

$$F = \int d^3r \left\{ \frac{1}{2} \varepsilon^2 T (\nabla m)^2 + f(m, c) \right\}, \quad (1)$$

where  $\varepsilon$  is a constant,  $T$  is the temperature, and  $f(m, c)$  is the local free energy density. The first term on the right hand side is responsible for the appearance of the diffuse interface. The local free energy density has the form  $f(m, c) = w T g(m) + [1 - p(m)] f_S(c) + p(m) f_L(c)$ , where the “double well” and “interpolation” functions have the forms  $g(m) = \frac{1}{4} m^2 (1 - m)^2$  and  $p(m) = m^3 (10 - 15m + 6m^2)$ , respectively, that emerge from the thermodynamically consistent formulation of the PFT [18],  $w$  is the free energy scale, while the free energy densities of the homogeneous solid and liquid,  $f_S$  and  $f_L$ , depend on the local value of  $c$ . These relationships result in a free energy surface that has two minima, whose relative depth depends on the deviation from equilibrium.

Being in unstable equilibrium, the critical fluctuation (the nucleus) can be found as an extremum of this free energy functional [11,12,14,15,19], subject to the solute conservation constraint discussed above. To impose this constraint one adds the volume integral over the conserved field times a Lagrange multiplier,  $\lambda$ , to

the free energy:  $\lambda \int d^3r c(\mathbf{r})$ . The field distributions, that extremize the free energy, have to obey the appropriate Euler-Lagrange (EL) equations, which in the case of such local functional take the form

$$\begin{aligned}\frac{\delta F}{\delta m} &= \frac{\partial \psi}{\partial m} - \nabla \frac{\partial \psi}{\partial \nabla m} = 0 \\ \frac{\delta F}{\delta c} &= \frac{\partial \psi}{\partial c} - \nabla \frac{\partial \psi}{\partial \nabla c} = 0\end{aligned}\tag{2}$$

where  $\delta F/\delta m$  and  $\delta F/\delta c$  stands for the first functional derivative of the free energy with respect to the fields  $m$  and  $c$ , respectively while  $\psi$  is the total free energy density. The EL equations have to be solved assuming that unperturbed liquid exists in the far field, while, for symmetry reasons zero field gradients exist at the center of the fluctuations. Under such conditions, the Lagrange multiplier can be identified as  $\lambda = -(\partial \psi / \partial c)_{r \rightarrow \infty}$ .

Assuming spherical symmetry that is reasonable considering the low anisotropy of the crystal-liquid interface at small undercoolings, the EL equations take the following form:

$$\varepsilon^2 T \left\{ \frac{d^2 m}{dr^2} + \frac{2}{r} \frac{dm}{dr} \right\} = w T g'(m) + p'(m) \{f_L - f_S\} \tag{3a}$$

and

$$0 = w T g(m) + [1 - p(m)] \frac{\partial f_S}{\partial c} + p(m) \frac{\partial f_L}{\partial c} - \frac{\partial f_L}{\partial c} \Big|_{r \rightarrow \infty} \tag{3b}$$

Here' stands for differentiation with respect to the argument of the function. The last term in eqn. (3b) originates from the Lagrange multiplier. Since the right hand side of eqn. (3b) is a function of fields  $c$  and  $m$ , it provides the implicit relationship  $c = c(m)$ . Accordingly, eqn. (3a) is an ordinary differential equation for  $m(r)$ . This equation has been solved here numerically using a fourth order Runge-Kutta method. Since  $m$  and  $dm/dr$  are fixed at different locations, the central value of  $m$  that satisfies  $m \rightarrow m_\infty = 1$  for  $r \rightarrow \infty$ , has been determined iteratively. Having determined the solutions  $m(r)$  and  $c(r)$ , the work of formation of the nucleus  $W^*$  can be obtained by inserting the solution into the free energy functional. Provided that the bulk free energy densities,  $f_S(c)$  and  $f_L(c)$ , are known, the only model parameters, we need to fix to evaluate  $W^*$ , are  $w$  and  $\varepsilon$ . These model parameters are related to the interface thickness and the interfacial free energy [6,19], thus these quantities can be used to determine  $w$  and  $\varepsilon$ , and calculate  $W^*$  *without adjustable parameters*.

The steady state nucleation rate (number of nuclei formed in unit volume and time),  $J_{SS}$ , can be calculated as

$$J_{SS} = J_0 \exp\{-W^*/kT\}, \quad (4)$$

using the classical nucleation prefactor [20],  $J_0$ , verified experimentally on oxide glasses [21].

## 2.2. Classical droplet model (CDM) of nuclei

For comparison with the phase field theory, we calculate the height of the nucleation barrier using the sharp interface droplet model of the classical nucleation theory. In this approach, the free energy of heterophase fluctuations of radius  $R$  is given as  $W_{\text{CDM}} = -(4\pi/3)R^3\Delta g + 4\pi R^2\Gamma_\infty$ , where  $\Delta g = \rho(\mu_L - \mu_S)$  is the volumetric Gibbs free energy difference between the bulk liquid and solid,  $\mu_L$  and  $\mu_S$  are the chemical potential of the liquid and the solid, and  $\Gamma_\infty$  is the free energy of the equilibrium planar interface. Then, the free energy of the critical fluctuation of radius  $R_{\text{CDM}}^* = 2\Gamma_\infty/\Delta g$  is  $W_{\text{CDM}}^* = (16\pi/3)\Gamma_\infty^3/\Delta g^2$ . These results are expected to be accurate when the interface is thin relative to the radius of the critical fluctuation,  $d \lesssim R$ .

## 2.3. Phase field theory of polycrystalline growth

To address hydrate crystallization and polycrystalline growth, we rely on an extension of the phase field theory developed recently [11,12,22], which relies on the orientation field,  $\theta$ , first introduced by Kobayashi, Warren and Carter [23]. This field specifies the local orientation of the crystal planes in the laboratory system, and allows the description of polycrystalline solidification and grain boundary evolution. It is normalized so that it varies between 0 and 1, while the orientation angle covers 0 and  $2\pi/n$ , where  $n$  is the symmetry index (e.g.,  $n = 6$  applies for six-fold symmetry). In order to handle nucleation of crystallites with different crystallographic orientations, we assume that  $\theta$  fluctuates in space and time. This extension of the orientation field to the liquid phase captures the short-range order existing in the liquid. The orientation field is strongly coupled to the phase field so that structural and orientational changes take place simultaneously at the crystal-liquid interface. This coupling is realized by adding an orientational contribution to the free energy functional.

$$F = \int d^3r \left\{ \frac{1}{2}\varepsilon^2 T (\nabla m)^2 + f(m, c) + f_{\text{ori}}(m, \nabla\theta) \right\}, \quad (5)$$



where  $f_{ori}(\mathbf{m}, \nabla\theta) = [1 - p(\mathbf{m})]HT|\nabla\theta|$  is the driving force for orientational ordering, and  $H$  is a constant.

The equations of motion for the three fields are

$$\begin{aligned}\dot{\phi} &= -M_m \frac{\delta F}{\delta m} = M_m \left\{ \nabla \left( \frac{\partial f}{\partial \nabla m} \right) - \frac{\partial f}{\partial m} \right\} + \zeta_m \\ \dot{c} &= \nabla M_c \nabla \frac{\delta F}{\delta c} = \nabla \left\{ Dc(1 - c) \nabla \left[ \left( \frac{\partial f}{\partial c} \right) - \nabla \left( \frac{\partial f}{\partial \nabla c} \right) \right] \right\} + \zeta_j, \\ \dot{\theta} &= -M_\theta \frac{\delta F}{\delta \theta} = M_\theta \left\{ \nabla \left( \frac{\partial f}{\partial \nabla \theta} \right) - \frac{\partial f}{\partial \theta} \right\} + \zeta_\theta\end{aligned}\quad (6)$$

Here  $\xi_i (i = m, j, \theta)$  are Langevin noise terms for the two non-conserved fields  $m$  and  $\theta$ , and for the concentration flux  $j$ , that model the thermal fluctuations in the system. Introducing the time scale  $\tau = \xi^2/D_l$ , where  $\xi$  is a length scale and  $D_l$  the diffusion coefficient of the liquid, the following dimensionless forms emerge for the deterministic part of the equations of motion:

$$\begin{aligned}\tilde{m} &= \frac{M_m \varepsilon^2 T}{D_l} \left[ \tilde{\nabla} (s^2 \tilde{\nabla} m) - \frac{\partial}{\partial \tilde{x}} \left\{ s \frac{\partial s}{\partial \tilde{\theta}} \frac{\partial m}{\partial \tilde{y}} \right\} + \frac{\partial}{\partial \tilde{y}} \left\{ s \frac{\partial s}{\partial \tilde{\theta}} \frac{\partial m}{\partial \tilde{x}} \right\} \right. \\ &\quad \left. - \xi^2 \frac{w(c)Tg'(m) + p'(m)\{f_L(c, T) - f_S(c, T) - HT|\tilde{\nabla}\theta|/\xi\}}{\varepsilon^2 T} \right] \\ \tilde{c} &= \tilde{\nabla} \left\{ \frac{v_m}{RT} \lambda c(1 - c) \tilde{\nabla} \left[ (w_B - w_A)Tg(m) + [1 - p(m)] \frac{\partial f_S}{\partial c}(c, T) \right] \right. \\ &\quad \left. + p(m) \frac{\partial f_L}{\partial c}(c, T) \right\} \\ \tilde{\theta} &= \chi \left[ \tilde{\nabla} \left\{ [1 - p(m)] \frac{\tilde{\nabla}\theta}{|\tilde{\nabla}\theta|} \right\} - \frac{\varepsilon^2}{H\xi} s \frac{\partial s}{\partial \theta} |\tilde{\nabla}\phi|^2 \right]\end{aligned}$$

where tilde denotes differentiation with respect to dimensionless quantities. Here  $M_c = (v_m/RT)Dc(1 - c)$  is the mobility of the concentration field,  $v_m$  the average molar volume,  $D = Ds + (D_l - D_s)p(m)$  is the diffusion coefficient, and  $\lambda = D/D_l$  is the reduced diffusion coefficient, while  $\chi = M_\theta \xi HT/D_l$  is the dimensionless orientational mobility. Note a second term on the RHS of the equation for the orientation field included recently [24].

In this work, these equations were solved numerically using an explicit scheme and MPI protocol on a PC cluster consisting of 56 nodes, built up in the Research Institute for Solid State Physics and Optics, Budapest. A periodic boundary condition is applied at the borders of the simulation window, unless stated otherwise.

To study solidification in a confined space, we introduce “walls”, where the normal component of  $\nabla m$  and  $\nabla c$  are set zero (“no flux” boundary condition). The former ensures a 90 degrees contact angle, while the latter realizes a chemically inert wall.

## 2.4. Material properties

The molar Gibbs free energy of the aqueous CO<sub>2</sub> solution has been calculated as  $G_L = (1 - c)G_{L,w} + cG_{L,CO_2}$ , where  $c$  is the mole fraction of CO<sub>2</sub>. The partial molar Gibbs free energy of water in solution has been obtained as  $G_{L,w} = G_{L,w}^0 + RT \ln[(1 - c)\gamma_{L,w}(c)]$ , where the free energy of pure water has been calculated as

$$G_{L,w}^0 = \sum_{i=0}^3 \frac{k_i}{T^i} \quad (7)$$

with coefficients  $k_i$  taken from Ref. 25. Here  $R$  is the gas constant and  $\gamma_{L,w}$  is the activity coefficient of water in solution. The partial molar free energy of CO<sub>2</sub> in solution is  $G_{L,CO_2} = G_{L,CO_2}^\infty + RT \ln[c\gamma_{L,CO_2}(c)]$ , where the molar free energy of CO<sub>2</sub> at infinite dilution,  $G_{L,CO_2}^\infty = -19.67$  kJ/mol, has been taken from molecular dynamics simulations [26]. The temperature and pressure dependent activity coefficient of CO<sub>2</sub> in aqueous solution deduced from CO<sub>2</sub> solubility experiments of Stewart and Munjal [27] have been fitted using the form

$$\ln \gamma_{L,CO_2} = \sum_{i=0}^5 a_i(T) [\ln x]^i, \quad (8)$$

with  $a_i(T)$  given by third order polynomials. The activity coefficient of water,  $\gamma_{L,w}$  in aqueous solution has been obtained from eqn. (6) via the Gibbs-Duhem relationship.

The Gibbs free energy of the hydrate is given by  $G_S = (1 - c)G_{S,w} + cG_{S,CO_2}$ . Owing to the lack of experimental information, the partial molar quantities have been calculated using the model described in Ref. 25. For water and CO<sub>2</sub> we use the relationships  $G_{S,w} = G_{S,w}^0 + RT(3/23) \ln(1 - \theta)$ , and  $G_{S,CO_2} = G_{S,CO}^{\text{inc}} + RT \ln[\theta/(1 - \theta)]$ , respectively, where the hole occupancy is  $\theta = c/(3/23)$ . Here, the partial molar Gibbs free energies of the empty clathrate,  $G_{S,w}^0$ , and that of guest inclusion,  $G_{S,CO}^{\text{inc}}$ , are given by eqn. (6), with the appropriate  $k_i$  taken from Ref. 25.

Following other authors [28], we approximate the free energy of the hydrate-solution interface by that of the ice-water interface, taken from the work of Hardy,  $29.1 \pm 0.8$  mJ/m<sup>2</sup> [29]. This is in good agreement with recent experimental data for the CO<sub>2</sub> hydrate system ( $\sim 30$  mJ/m<sup>2</sup>), we became aware recently [30]. Owing to a lack of information on the CO<sub>2</sub> hydrate/aqueous solution interface, we use the 10%–90% interface thickness,  $d$ , (the distance on which the phase field changes between 0.1 and 0.9) as an adjustable parameter in the calculations. Molecular dynamics simulations on other clathrate hydrates indicate that the full interface thickness is about 2–3 nm [31], that corresponds to roughly  $d \approx 1 - 1.5$  nm. Assuming that similar values apply for the CO<sub>2</sub> hydrate, we vary  $d$  in the 0.125 – 1.5 nm

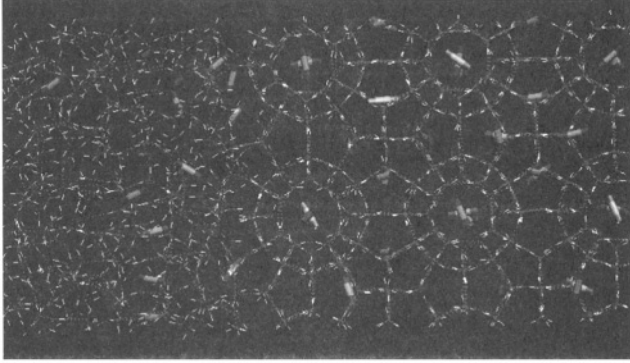


**Figure 1.** Snapshot of a molecular dynamics simulation on the melting of  $\text{CO}_2$  hydrate in the presence of water. The simulation consists of 920 water and 108  $\text{CO}_2$  molecules (represented by SPC and EP M2 potentials, respectively), and has been performed at 276.15 K and 200 Bar. Note the regular clathrate cages inside the solid (on the right) and the distorted cages at the interface (on the left). The diameter of the  $\text{H}_2\text{O}$  cages of circular projection (tetrakaidecahedra) is 0.866 nm. The rods at the center of the cages denote the  $\text{CO}_2$  molecules. [This picture have been made using the Visual Molecular Dynamics package (Humphrey, W.; Dalke, A.; Schulten, K. J. Molec. Graphics, 1996, 14, 33).]

range. Indeed MD simulations of the melting of  $\text{CO}_2$  hydrate, performed at the University of Bergen, indicate  $d$  in the same range, although a dynamic broadening of the interface cannot be excluded (Figure 1).

The computations are performed under conditions typical for the seabed reservoirs, i.e.  $T = 274$  K,  $p = 15$  MPa ( $\sim 1500$  m depth), furthermore, we assume that water has been saturated by  $\text{CO}_2$  ( $c = 0.033$ , obtained by extrapolating the relevant data by Teng and Yamasaki [32]). These experimental data are for synthetic average seawater. The salinity of groundwater in reservoirs may vary from close to zero up to seawater salinity in regions where the penetration of seawater dominates the salinity.

In the 2D phase field simulations for  $\text{CO}_2$  hydrate we used  $\varepsilon^2 = 1.3944 \times 10^{-15}$  J/cm K,  $w = 3.6372$  J/cm<sup>3</sup> K,  $D_l = 10^{-5}$  cm<sup>2</sup>/s,  $D_s = 0$ ,  $\xi = 10^{-8}$  cm,  $m_m = M_m \varepsilon^2 T / D_l = 4.4308$ , and  $\chi = 0.8381$ , while the time and spatial steps were  $\Delta t = 0.04 \tau$  and  $\Delta x = \xi$ , respectively. Simulations for confined space were done for Ni-Cu, using the properties given in previous works of us [11, 12].

### 3. RESULTS

#### 3.1. Hydrate nucleation

The free energy surface, corresponding to  $\varepsilon$  and  $w$  that reproduce the ice-water interface free energy and a 10%–90% thickness of 1 nm at  $T = 274$  K, is shown in

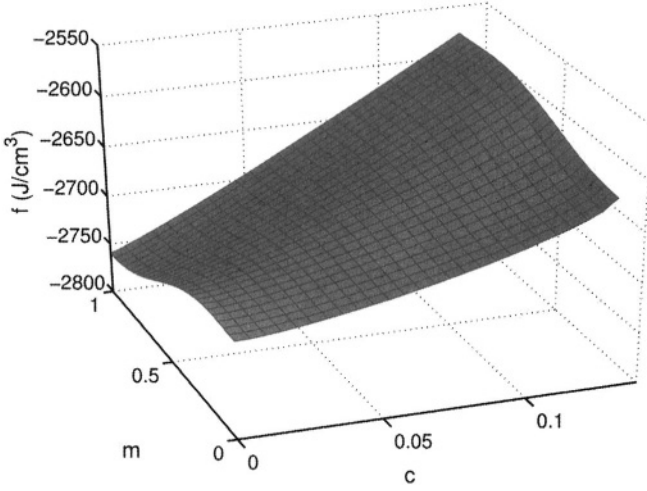


**Figure 2.** Free energy density surface for the  $\text{CO}_2$  hydrate system at 274 K, evaluated with free energy scale  $w$  corresponding  $d = 1$  nm and  $\Gamma\infty = 29.1 \pm 0.8$  mJ/m<sup>2</sup>. (m—phase field, c—mol fraction of  $\text{CO}_2$ .)

Figure 2 The radial structural order parameter and concentration profiles of the critical fluctuations forming in saturated aqueous  $\text{CO}_2$  solution ( $c = 0.033$ ) at the same temperature are shown in Figure 3 as a function of the interface thickness,  $d$ .

Remarkably, at the realistic interface thickness ( $d = 1.0$  to  $1.5$  nm) the bulk crystalline structure is not yet established even at the center of the nucleus, indicating that the nucleus is softer (the molecules have larger amplitude of oscillations around the crystal sites) than the bulk crystal. Despite these, we have almost full hole-occupancy in the central part,  $c = 0.1235$  or  $\theta = 0.946$ . Furthermore, the interface thickness for the concentration field is far sharper than for structure. It extends to only a few Å, which is consistent with the picture that the nucleus is a small piece of hydrate crystal embedded into the solution, however, built of somewhat distorted  $\text{H}_2\text{O}$  cages seen at the interface in MD simulations with realistic potentials (Figure 1) [33]. It is remarkable, that the interface for the solute falls close to the classical radius  $R_{\text{CDM}}^* = 1.76$  nm.

In agreement with previous studies on other systems [11,12,15], a substantial difference can be seen between predictions made for the height of the nucleation barrier by the phase field theory and the classical droplet model (Table 1). This difference emerges from the fact that the interface thickness is comparable to the size of the critical fluctuation. As one should expect, for decreasing interface thickness, the PFT prediction for the height of the nucleation barrier converges to that by the sharp interface CDM ( $W_{\text{PFT}}^* \rightarrow W_{\text{CDM}}^*$  for  $d \rightarrow 0$ ; see Figure 4), indicating the coherency of our results. These findings imply that, similarly to many other systems, in hydrate forming systems the classical droplet

**Table 1.** Free energy of critical fluctuations ( $W^*$ ) vs. the interface thickness in the CO<sub>2</sub> hydrate system, as predicted by the phase field theory (PFT) and the classical droplet model (CDM) at 274 K and  $c = 0.033$ .

$d$ (nm)	$W_{\text{PFT}}^*(10^{-19} \text{ J})$	$W_{\text{CDM}}^*(10^{-19} \text{ J})$
0.125	3.61	
0.25	3.46	
0.5	3.18	
1.0	2.66	3.76
1.5	2.23	

model of crystal nuclei is rather inaccurate and should be replaced by more advanced approaches such as the phase field theory.

The temperature and composition dependencies of the free energy of nuclei are shown for both cluster models in Figure 5 (in the case of PFT  $d = 1$  nm is assumed). With decreasing temperature and increasing mole fraction of CO<sub>2</sub> dissolved in water, the height of the nucleation barrier decreases, leading to enhanced nucleation rate.

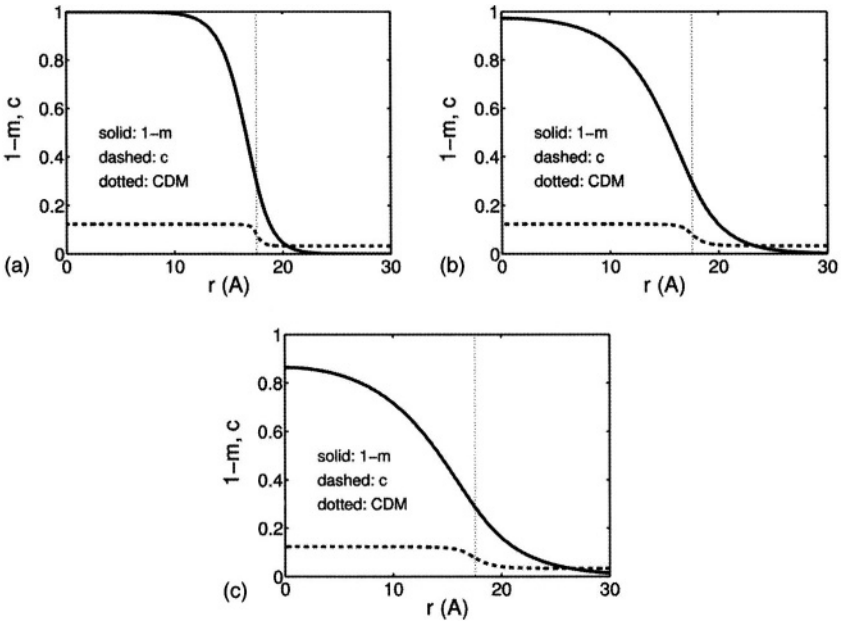


**Figure 3.** Radial  $1 - m$  profiles (solid lines) and CO<sub>2</sub> concentration profiles (dashed lines) for critical fluctuations calculated at  $T = 274$  K, for 10%–90% interface thickness  $d =$  (a) 0.5, (b) 1.0 and (c) 1.5 nm. For comparison the critical radius from the CDM is also shown (dotted lines). Note that with increasing interface thickness the difference between the PFT and CDM predictions for the height of the nucleation barrier increases (see Table 1).

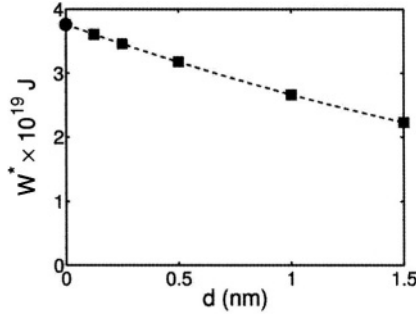


**Figure 4.** Height of the nucleation barrier for CO<sub>2</sub> hydrate formation as a function of interface thickness in the phase field theory (squares). For comparison, the prediction of the classical droplet model that assumes a sharp interface ( $d = 0$ ) is also presented (circle). Note that for  $d \rightarrow 0$  the PFT results converge to the value predicted by the CDM (dashed line—2<sup>nd</sup> order polynomial fitted to the PFT results).

We note finally, that the predicted  $W^*$  is rather sensitive to the values of  $\Gamma_\infty$  and  $d$  used to fix the model parameters  $\varepsilon$  and  $w$ . Thus, accurate results may only be expected if these input properties are known with a high accuracy. Unfortunately, none of them is available for the CO<sub>2</sub> hydrate/solution interface (the values used here and in other work [28] are only rough estimates). Therefore, further effort is needed to establish accurate nucleation rates. For example, careful experiments using the grain boundary groove method [29] could provide a reasonably accurate value for the interfacial free energy. Another possible way to determine the interfacial properties is via MD simulations [13,34] with realistic interaction potentials. Work is underway in these directions.

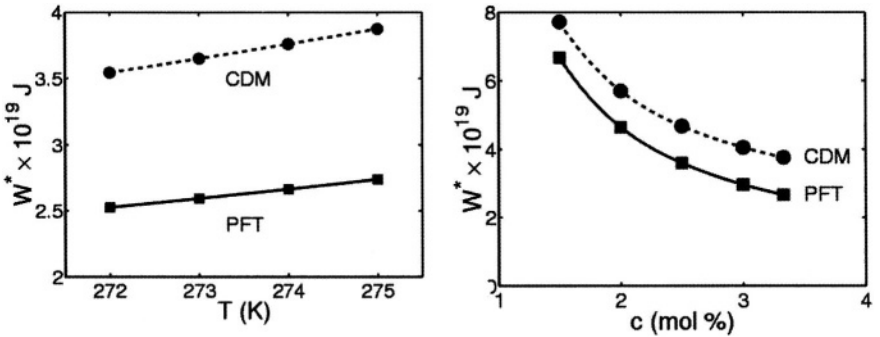


**Figure 5.** Left: Height of the nucleation barrier for CO<sub>2</sub> hydrate formation as a function of temperature in the phase field theory (squares) and the classical droplet model (circles). Right: Height of the nucleation barrier for CO<sub>2</sub> hydrate formation as a function of the initial composition of the water solution in the phase field theory (squares) and the classical droplet model (circles).

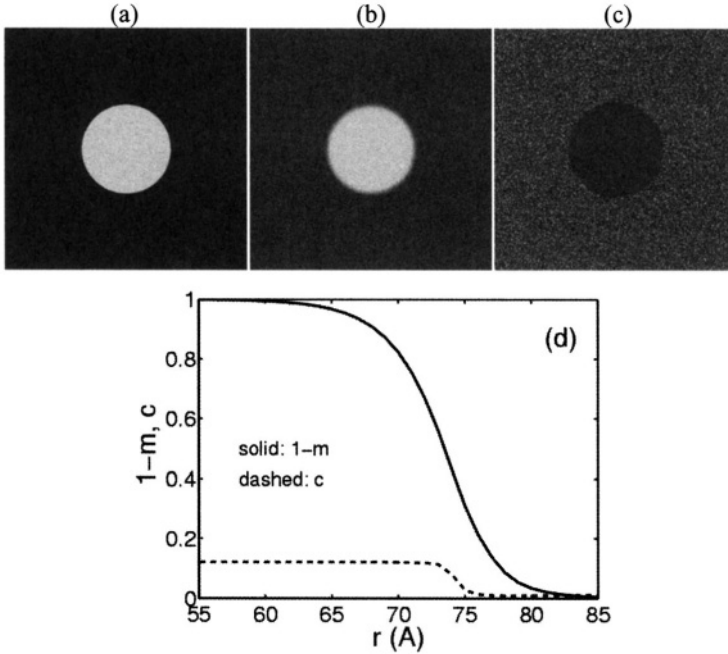


**Figure 6.** Growth of a supercritical  $[R(t = 0) = 2.5 \text{ nm}]$   $\text{CO}_2$  hydrate particle in saturated aqueous solution at 274 K and 15 MPa in the phase field theory ( $d = 1.0 \text{ nm}$ , isotropic case). (a) Composition map (aqueous solution—blue, hydrate—yellow); (b) phase field map (solid—yellow, liquid—red); (c) orientation field (different colors denote different orientations). (d) Radial phase field and composition field profiles. The growth shapes are shown after 94 ns. The computations refer to a  $40 \times 40 \text{ nm}$  area.

### 3.2. Growth of $\text{CO}_2$ hydrate particles

The growth of a supercritical  $\text{CO}_2$  hydrate particle is shown in Figure 6. Maps of the three fields and the radial phase field and concentration profiles are presented. Note a  $\text{CO}_2$  depletion zone ahead of the solidification front (Figure 6a), which is responsible for the diffusion governed slowing down of growth. The radius of the particle (defined by the position where  $m = 0.5$ ) is presented as a function of time in Figure 7. The time-dependence indicates that, as expected, growth is governed here by  $\text{CO}_2$  diffusion in the liquid.

### 3.3. Crystal growth in the presence of walls

A recent experimental work addresses hydrate formation in aqueous solution in porous media and rectangular channels [30]. To study solidification in such confined spaces, we introduced walls into the PFT simulations. In our model, the

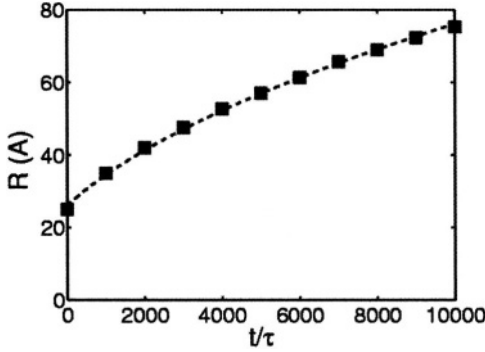


**Figure 7.** Radius of the CO<sub>2</sub> particle as a function of reduced time during the early growth stage in 2D. (Here  $\tau = 10^{-11}$  s.) Dashed line denotes an  $R = [A(t - t_0)]^{1/2}$  function fitted to the  $R(t)$  relationship [ $A = (0.51 \pm 0.01) \times 10^{-5} \text{ cm}^2/\text{s}$  and  $t_0 = (-1328 \pm 58) \times 10^{-11} \text{ s}$ ]. The average growth rate for the period shown is  $\sim 5.3 \text{ cm/s}$ . Growth rate, however, slows down as  $v = (1/2)[A/(t - t_0)]^{1/2}$ , yielding  $\sim 11 \text{ } \mu\text{m/s}$  after 1 s, unless interaction with other particles or the morphological instability intervenes.

“no-flux” boundary condition is used to realize a rectangular contact angle and a chemically inert wall. In the simulations, the orientation field can be either random [no preferred orientation (glassy wall)] or one may chose preferred orientation(s). The introduction of such walls allows the study of heterogeneous crystal nucleation on particles, rough surfaces, and crystallization in porous matter or in channels. Preliminary results obtained with ideal solution thermodynamics (Ni-Cu system) are shown in Figures 8 and 9. The observed morphologies resemble closely to those seen during hydrate formation in porous matter and in rectangular channels [30]. A similar approach will be used in the future for a quantitative modeling of hydrate formation in confined geometries.

#### 4. CONCLUSIONS

The nucleation and growth of CO<sub>2</sub> hydrate in aqueous solution is addressed using a phase field theory we developed recently. It has been demonstrated under typical conditions, that the thickness of the hydrate-solution interface is comparable with the size of nuclei, implying that the classical droplet model is rather inaccurate. Indeed, as found for many other systems [11,15], the nucleation barriers predicted by the phase field theory and the classical droplet model differ considerably. Apparently, advanced models are needed to evaluate the rate of hydrate nucleation accurately. The phase field theory is used to predict the growth rate of CO<sub>2</sub> hydrate in aqueous solution. The growth is governed by CO<sub>2</sub> diffusion in the liquid. We have introduced walls into the phase field simulations and demonstrated



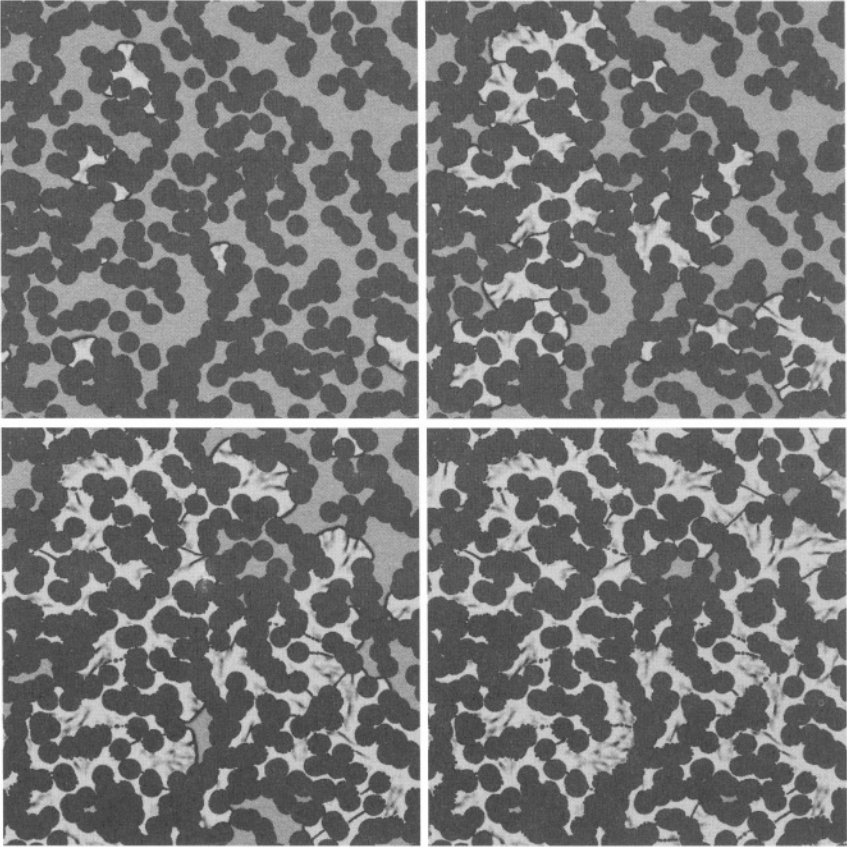


**Figure 8.** Solidification in porous matter. Blue—particles of porous matter, dark yellow—liquid, bright yellow—solid.

the possibility for modeling solidification in confined space (channels/porous media).

## ACKNOWLEDGMENTS

This work has been supported by the Hungarian Academy of Sciences under contract No. OTKA-T-037323 and by the Norwegian Research Council under project Nos. 153213/432 and 151400/210. T. P. acknowledges support by the Bolyai János Scholarship of the Hungarian Academy of Sciences.

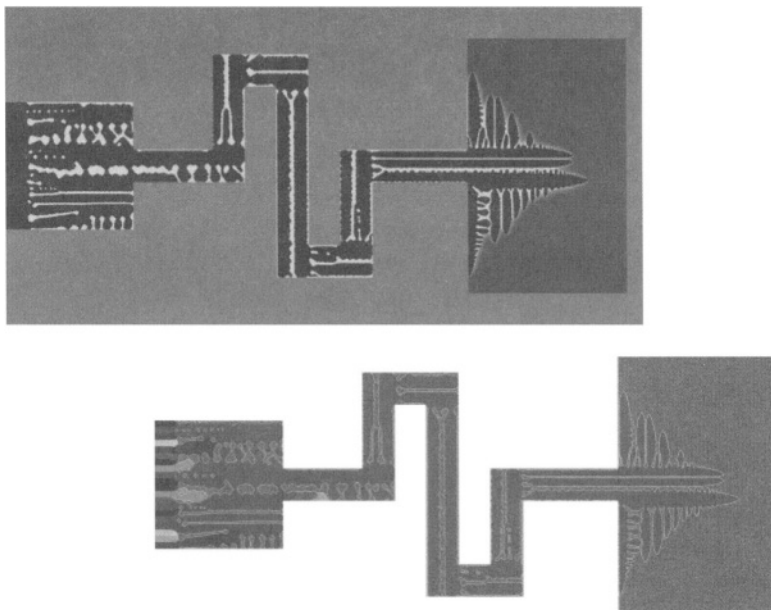


**Figure 9.** Dendritic solidification in rectangular channel. Upper panel: composition map (blue—solidus, yellow—liquidus). Lower panel: orientation map (different colors stand for different crystal orientation). Note that a single orientation has been selected.

## REFERENCES

1. Milich, L. Global Environmental Change-Human and Policy Dimensions, 1999, 9, 179.
2. Mienert, J.; Andreassen, K.; Posewang, J.; Lukas, D. Ann. N. Y. Acad. Sci., 2000, 912, 200.
3. Boettinger, W. J.; Warren, J. A.; Beckermann, C.; Karma, A. Ann. Rev. Mater. Res., 2002, 32, 163.
4. Kobayashi, R. Physica D, 1993, 63, 410.
5. Karma, A.; Rappel, W.-J. Phys. Rev. E, 1998, 57, 4323.
6. Warren, J. A.; Boettinger, W. J. Acta Metall. Mater., 1995, 43, 689.
7. Karma, A. Phys. Rev. E, 1994, 49, 2245.
8. Drolet, F.; Elder, K. R.; Grant, M.; Kosterlitz, J. M. Phys. Rev. E, 2000, 61, 6705.
9. Nestler, B.; Wheeler, A. A. Physica D, 2000, 138, 114.
10. Lo, T. S.; Karma, A.; Plapp, M. Phys. Rev. E, 2001, 63, 031504.
11. Gránásy, L.; Börzsönyi, T.; Pusztai, T. Phys. Rev. Lett., 2002, 88, 206105.
12. Gránásy, L.; Börzsönyi, T.; Pusztai, T. J. Cryst. Growth., 2002, 237–239, 1813.
13. Davidchack, R. L.; Laird, B. B. J. Chem. Phys., 1998, 108, 9452.
14. Oxtoby, D. W. Annu. Rev. Mater. Res., 2002, 32, 39.
15. Gránásy, L.; Pusztai, T.; Tóth, G.; Jurek, Z.; Conti, M.; Kvamme, B. J. Chem. Phys. 2003, 119, 10376.
16. Caginalp, G.; Jones, J. Ann. Phys. (N.Y.), 1995, 237, 66.
17. Shen, Y. C.; Oxtoby, D. W. J. Chem. Phys., 1996, 105, 6517.

18. Wang, S. L.; Sekerka, R. F.; Wheeler, A. A.; Murray, B. T.; Coriell, S. R.; Braun, R. J.; McFadden, G. B. *Physica D*, 1993, 69, 189.
19. Cahn, J. W.; Hilliard, J. E. *J. Chem. Phys.*, 1958, 28, 258; 1959, 31, 688.
20. Kelton, K. F. *Solid State Phys.*, 1991, 45, 75.
21. Kelton, K. F.; Greer, A. L. *Phys. Rev. B*, 1988, 38, 10089.
22. Gránáry, L.; Pusztai, T.; Warren, J. A.; Douglas, J. F.; Börzsönyi, T.; Ferreira, V. *Nature Mater.*, 2003, 2, 92.
23. Kobayashi, R.; Warren, J. A.; Carter, W. C. *Physica D*, 1998, 119, 415.
24. Warren, J. A.; Gránásy, L.; Pusztai, T.; Börzsönyi, T.; Tegze, G.; Douglas, J. F. *Proc. TMS Ann. Meeting*, San Francisco, 2004, accepted for publication.
25. Kvamme, B.; Tanaka, H. *J. Phys. Chem.*, 1995, 99, 7114.
26. Kvamme, B. unpublished.
27. Stewart, P. B.; Munjal, P. J. *Chem. Eng. Data*, 1970, 15, 67.
28. Kashchiev, D.; Firoozabadi, A. *J. Cryst. Growth*, 2002, 243, 476.
29. Hardy, S. C. *Philos. Mag.*, 1977, 35, 471.
30. Tohidi, B. presented at "Workshop on Reservoir Storage of  $\text{CO}_2$ ", November 6 and 7, 2003, University of Bergen, Norway.
31. Pratt, R. M.; Mei, D.-H.; Guo, T.-M.; Sloan, E. D. *J. Chem. Phys.*, 1997, 106, 4187.
32. Teng, H.; Yamasaki, A. *J. Chem. Eng. Data*, 1998, 43, 2.
33. Harris, J. G.; Yung, K. H. *J. Phys. Chem.*, 1995, 99, 12021.
34. Hoyt, J. J.; Asta, M.; Karma, A. *Phys. Rev. Lett.*, 2001, 86, 5530.

# Statistical Thermodynamic Model of Clathrate Hydrates with Multiple Filling of Cages

A. A. Pomeransky\* and V. R. Belosludov

## 1. INTRODUCTION

Until recently only clathrate gas hydrates with single occupancy of cages, which could contain only one guest molecule in a cage of water host framework, have been considered. Recent experimental studies [1] had demonstrated, that hydrates formed by very small molecules (Ar, Kr, N<sub>2</sub>, O<sub>2</sub>), can contain two guest molecules in a large cage. These results significantly supplement investigations, started after discovery of unexpected formation of the structure II hydrates by these very small molecules, instead of the S-I structure, which would be expected in the case of ordinary single filling. In very recent work [2] structure-II hydrates of molecular hydrogen, containing four hydrogen molecules in large cages and two molecules in small cages, have been obtained under pressure. Existing explanations of apparent violation of the established correspondence between size of the guest molecule and the formed clathrate structure usually refer to more favorable for very small molecules small-to-large cages ratio in the structure II in comparison with the structure I. But there are theoretical reasons to think that multiple cage filling may be significant in this case.

In the suggested model of clathrate nucleation [12] the Stackelberg rule, connecting guest molecule size and the structure formed, is strictly valid. For such

---

A. A. POMERANSKY • Institute of Inorganic Chemistry SB RAS 3, Lavrentiev Ave.,  
Novosibirsk, 630090 Russia

V. R. BELOSLUDOV • Institute of Inorganic Chemistry SB RAS 3, Lavrentiev Ave.,  
Novosibirsk, 630090 Russia

\*pom@casper.che.nsk.su

small molecules initially there can form only nuclei of the structure I hydrates. But big cavities are unstable with single filling by these very small molecules. Then the growth of the structure I nuclei must change to growth of the structure II hydrate. This effect of initial nucleation of structure I with subsequent transition to growth of the structure II hydrate was really observed by Kuhs et al. [1]. Our model suggests that it is just double filling of large cages (here we do not consider hydrogen) explains the mechanism of structure transformation. Really, growth of clathrate nuclei is performed by successive completion of small and large cavities. Completion of large cages of the structure I with single filling gives unstable cavities. Around two guest molecules a part of large structure-I cavity can be completed to a large cavity of the structure II which is more stable. When this occurs for some two “next-neighbor” large cavities (without common faces, such large cages are connected by a small cage) of the structure I nucleus, there forms a diner nucleus of the structure II able to grow further.

There is another important not completely solved problem related to multiple filling of cages. It is, also unexpected, formation of the structure II hydrates by a mixture of two guests each of which separately forms the structure I hydrate. This effect was observed and investigated by Sloan and coworkers (see the review [3]). The explanation of this effect at present also is connected with different small-to-large cages ratio in the two hydrate structures. The pairs of hydrate-formers giving such effect include one most small and one of the most large guest molecules among the structure I formers. Our model of hydrate nucleation suggests that in this case also there initially can form only nuclei of the structure I hydrates around each type of guest molecules or containing mixed guests. The ‘pure’ hydrates of these so different guests have different lattice constants: one is more stretched relative to other. Therefore if, in a structure-I nucleus with big guest, completion of large cages occurs around single small guest molecules, these large cavities will be unstable. But stable structure-II large cavity can be built around two small guest molecules. We see that the explanation of this effect is the same as in previous case of structure II formation by extremely small molecules, and similar mechanism of structure I – structure II transformation of nuclei works. Thus, the role of multiple filling of cages in kinetic mechanisms of hydrate formation is decisive. It is interesting to investigate also the role of multiple filling in thermodynamic properties of hydrates. Though in absolute values its contributions in thermodynamic functions can be small in comparison with those of single-filled cavities, these contributions probably are significant near structural phase transitions.

Generally accepted now and most frequently used the van der Waals-Platteeuw (vdW-P) model of clathrate hydrates [4–7], formulated in the framework of statistical thermodynamics (STD), is valid only for hydrates with single filling of cages. In this paper we present a generalization of the STD vdW-P theory for arbitrary filling. The generalized model is formulated straightforwardly for the grand canonical ensemble of the guest subsystem, as in the theory of adsorption [8].

Though it was known starting from the first papers by van der Waals, that hydrates are described by the mixed statistical ensemble, canonical for water host subsystem and grand canonical for the guest subsystem, most later formulations started from the canonical ensemble for guests, with subsequent summation in order to obtain the grand canonical partition function. Our approach simplifies significantly derivation of the vdW-P theory even in the ordinary case of single filling, and permits to write easily basic expressions of the theory in the general case of multiple cage filling. The results obtained for equilibrium distribution of cage occupancies (Langmuir isotherms) in the framework of STD model are compared with those obtained from simple kinetic model of chemical equilibrium, their coincidence is shown and the microscopic expressions are obtained for phenomenological parameters of the kinetic model (Langmuir's constants). Thus, the microscopic STD theory, in comparison with the kinetic model, allows, in principle, to calculate any thermodynamic functions (chemical potentials, heat capacities, ...) for multiple filling of cages directly from the molecular parameters, in the same way as in the ordinary vdW-P theory. General relationships for main thermodynamic quantities are obtained (chemical potentials of water molecules in the host crystalline lattice and guest molecules, internal energy) generalizing corresponding results of the vdW-P theory.

The first version of this paper was presented as a poster at the workshop [9]. Recently a generalization of the vdW-P model for multiple filling of cages, starting from the canonical ensemble for guests, and results of extensive calculations were presented [10].

## 2. SIMPLE CHEMICAL KINETIC MODEL

As a starting point for subsequent comparison with the STD model we derive simple chemical kinetic model of cage filling analogous to models of localized adsorption. Considering filling of a cage by  $m$  guest molecules as a  $m$ -stage chemical reaction one can write equations of chemical equilibrium as

$$y_k/y_{k-1} = A_k, \quad \sum_{k=0}^m y_k = 1 \quad (1)$$

where  $y_k = N_k/N$  is the fraction of cages containing  $k$  guest molecules ( $k = 0, 1, \dots, m$ ),  $A_k = C_k p$ ,  $p$ —gas pressure of the guest,  $C_k$ —the equilibrium (Langmuir's) constants for the reaction of inclusion of one guest molecule into the cage containing  $k-1$  guest molecules.

The solution of the system of equations (1) is

$$y_0 = 1/S, \quad y_k = (A_1 A_2 \dots A_k)/S, \quad k \geq 1,$$

where

$$S = 1 + A_1 + A_1 A_2 + \cdots + A_1 A_2 \dots A_m.$$

It is convenient to introduce the variables  $A'_k = A_1 \dots A_k = C'_k p^k$ , where  $C'_k = C_1 C_2 \dots C_k$ . Then

$$y_0 = \frac{1}{1 + C'_1 p + C'_2 p^2 + \cdots + C'_m p^m}, \quad y_k = \frac{C'_k p^k}{1 + C'_1 p + C'_2 p^2 + \cdots + C'_m p^m} \quad (2)$$

This is the form similar to Langmuir's isotherms for multilayer localized adsorption. For  $m = 2$  they were written (in terms of  $C_k$ ) in [11] and used in recent experimental studies for fitting measured data. The modified constants  $C'_k$  introduced here have the meaning of Langmuir's constants for reaction of inclusion of the group of  $k$  guest molecules into the empty cage.

### 3. STATISTICAL THERMODYNAMIC MODEL (GENERALIZED vdW-P MODEL)

Hydrate crystal in equilibrium with the guest gas is described by the mixed statistical ensemble ( $V, T, \mu_g, N_W$ ) where  $V$  is volume,  $T$ —temperature,  $\mu_g$  is the chemical potential of guest molecules,  $N_W$  is the number of water molecules in the crystal. This ensemble is canonical for water host subsystem (with partition function  $Z_W$ ) and grand canonical for guest subsystem. The partition function of the crystal

$$\Xi = Z_W \Xi_g^N, \quad (3)$$

$N$  is the number of cages (here we restrict to the case of one type of cages, generalization to arbitrary number of different cages is straightforward).  $\Xi_g$  is the partition function of indefinite ( $\leq m$ ) number of guest molecules inside one cage

$$\Xi_g = 1 + \lambda_g z_1 + \lambda_g^2 z_2 + \cdots + \lambda_g^m z_m, \quad (4)$$

$\lambda_g = \exp(\beta\mu_g)$  is the absolute activity ( $\beta = 1/kT$ ), and  $z_k$  the canonical partition function of  $k$  guest molecules inside cage

$$z_k = \frac{1}{k!h^{3k}} \int d\Gamma_k e^{-\beta[K_k(q)+U(r)]}. \quad (5)$$

Here  $K_k(q) = 1/2m(\Sigma q^2)$  is the kinetic energy and  $U_k(r)$  is the potential energy of  $k$  guest molecules in the cage,  $d\Gamma$  is phase-space volume element ( $h$  is the Planck constant).

By the definition of the grand canonical ensemble the probability to find  $k$  particles in one cage is equal to

$$y_k = \frac{\lambda_g^k z_k}{\Xi_g}. \quad (6)$$

Representing  $z_k$  as products of kinetic and configuration partition functions  $z_k^{kin} z_k'$  we have  $z_k^{kin} = (z_1^{kin})^k$ ,  $z_1^{kin} = z_1^{gas}$ . Then, equating as usual, activities of the guest in the clathrate and gas phase, when  $\lambda_g z_1^{gas} = \beta p$  ( $p$  is the guest gas pressure), we obtain

$$y_k = \frac{(\beta p)^k z_k'}{\Xi_g} \quad \Xi_g = \sum_{k=0}^m (\beta p)^k z_k', \quad (7)$$

where  $z_k'$  are the configuration integrals

$$z_k' = \frac{1}{k!} \int d\mathbf{r}_1 \dots d\mathbf{r}_k e^{-\beta U_k(r_1, \dots, r_k)} \quad (8)$$

Comparing (7) with (2) we obtain the microscopic statistical expression for Langmuir's constants

$$C_k' = \beta^k z_k'. \quad (9)$$

for general case of arbitrary cage filling. Equally easily one obtains from the partition functions general expressions for chemical potential of water molecules

$$\begin{aligned} \mu_w &= -kT[\partial(\ln \Xi)/\partial N_w]_{T, N, \lambda_g} = \mu_w^0 - kT(N/N_w) \ln \Xi_g \\ &= \mu_w^0 + kT(N/N_w) \ln y_0 \end{aligned} \quad (10)$$



and internal energy of hydrate crystal

$$\begin{aligned}
 E &= kT^2[\partial(\ln \Xi)/\partial T]_{V, N_w, \lambda_g} = E^0 + \frac{kT^2 N}{\Xi_g} \sum_{k=1}^m \lambda_g^k \frac{\partial z'_k}{\partial T} \\
 &= E^0 + kT^2 N \sum_{k=1}^m y_k \frac{\partial \ln z'_k}{\partial T}.
 \end{aligned}
 \tag{11}$$

Equations (7), (9), (10), (11) and similarly derived expressions for other thermodynamic variables constitute the basis of the STD theory for clathrate gas hydrates and permit to calculate arbitrary thermodynamic parameters of these compounds.

## 4. CONCLUSIONS

The important role of multiple cage filling in kinetic mechanisms of hydrate formation is described. Possible mechanisms of the structure II hydrates formation by the most small molecules (Ar, Kr, N<sub>2</sub>, O<sub>2</sub>) and by mixtures of the structure-I formers are suggested on the base of new model of clathrate crystal nucleation. A generalization of the van der Waals-Platteeuw (vdW-P) statistical thermodynamic model of clathrate hydrates, applicable for arbitrary multiple filling, is formulated. The formulation in terms of grand canonical ensemble for the guest subsystem simplifies derivation of the results even in the ordinary case of single filling. Comparison with simple chemical kinetic model of multiple filling gives microscopic expressions for Langmuir's constants.

## ACKNOWLEDGMENTS

This investigation was supported by Siberian Branch of Russian Academy of Sciences (Grant No. 147).

## REFERENCES

1. Kuhs, W. F.; Chazallon, B.; Radaelli, P. G.; and Pauer, F. J. Incl. Phenom. Mol. Recogn. Chem., 1997, 29, 65.
2. Mao, W. L.; Mao, H.; et al. Science, 2002, 297, 2247.
3. Sloan, E. D. Jr. Nature, 2003, 426, 353, and references therein.
4. van der Waals, J. H.; and-Platteeuw, J. C. Adv. Chem. Phys., 1959, 2, pp. 1–57.

5. Davidson, D. W. In *Water: A Comprehensive Treatise*; Franks, F., Ed.; Plenum: New York, 1973, Vol. 2, p. 115.
6. Sloan, E. D. Jr. *Clathrate Hydrates of Natural Gases*; Marcel Dekker: New York, 1998.
7. Dyadin, Yu. A.; and Belosludov, V. R. In *Comprehensive Supramolecular Chemistry*; MacNicol, D. D.; Toda, F.; and Bishop, R., Eds.; Pergamon: Oxford, 1996, Vol. 6, Ch. 24, pp. 789–824.
8. Kittel, C. *Thermal Physics*; Wiley: New York, 1969).
9. Pomeransky, A. A.; and Belosludov, V. R. In *Architecture of Supramolecular Systems: Trends and Developments*, Russian-French Workshop, Program and abstracts; Inst. of Inorg. Chem.: Novosibirsk, 2001, pp. 30–31.
10. Klauda, J. B.; and Sandler, S. I. *Chem. Eng. Sci.*, 2003, 58, 27.
11. van Hinsberg, M. G. E. PhD Thesis; Univ. of Amsterdam, 1994.
12. Pomeransky, A. A.; Belosludov, V. R.; and Inerbaev, T. M. This book, p. 130.

*This page intentionally left blank*

# Phenomenological Modeling of Hydrate Formation and Dissociation

**Maria Carolina Gonzalez Chacin,  
Richard G. Hughes,\* Faruk Civan,  
and Charles E. Taylor**

## 1. INTRODUCTION

Since the pioneering work of Hammerschmidt [1], the hydrate formation and dissociation phenomena have been the subject of numerous studies (Sloan, [2], and Makogan, [4]). Englezos, et al. [5,6]) proposed a model for hydrate formation based on experimental data they collected on the formation of hydrates of methane, ethane, and their mixtures at constant pressure or temperature. The turbidity time was identified visually as a transition from a clear to translucent solution. An induction period was defined, beginning with the initiation of the experiment until the attainment of the turbidity point. The dominant process during the induction time was assumed to be physical absorption of the gas in the liquid. A growth period was then noted which started at the turbidity point and continued until the

---

MARIA CAROLINA GONZALEZ CHACIN • Mewbourne School of Petroleum and Geological Engineering, University of Oklahoma, T 301 Sarkeys Energy Center, 100 East Boyd St., Norman, OK 73019, U.S.A.

RICHARD G. HUGHES • Mewbourne School of Petroleum and Geological Engineering, University of Oklahoma, T 301 Sarkeys Energy Center, 100 East Boyd St., Norman, OK 73019, U.S.A.

FARUK CIVAN • Mewbourne School of Petroleum and Geological Engineering, University of Oklahoma, T 301 Sarkeys Energy Center, 100 East Boyd St., Norman, OK 73019, U.S.A.

CHARLES E. TAYLOR • U.S. Department of Energy, National Energy Technology Laboratory, P.O. Box 10940, Pittsburgh, PA 15236-0940

\* Telephone (405) 325-6778, Fax: (405) 325-7477, E-mail: [rg Hughes@ou.edu](mailto:rg Hughes@ou.edu).

experiment concluded. The experimental data collected during this period was also considered in modeling. The overall driving force for the crystallization process was assumed to be the difference between the dissolved gas fugacity and the three-phase equilibrium fugacity at the experimental conditions.

Carrying out a parametric analysis with the Englezos *et al.* model [5,6] and experimental data, Skovborg and Rasmussen [7] concluded that the agreement between some of the experimental data and the model was questionable. They observed that the model performed well on the early-time data, but that there were discrepancies with the late-time data. The model indicated increasing rate of reaction with time, while the experimental data did not reflect such behavior. Examining the other available experimental information (Bishnoi *et al.*, [7,8]), Skovborg and Rasmussen [7] noticed that the reaction rate was constant or, in some cases had a declining tendency. The transfer of gas from the gas phase to or through the liquid phase was considered to be the determining step.

The discrepancies between experimental data and the Englezos, *et al.* model is because the total reaction rate was assumed proportional to the second moment of the particle size distribution, which in effect determines the total surface area of the particles. This area increases as the particles grow and therefore the reaction rate increases with time. Also, Englezos, *et al.* neglected the interactions between hydrate particles in the population mass balance, assuming that the particles would always be small in comparison to the medium containing them. However, the number of particles and their size will grow and eventually the particles will interact with each other. These interactions may turn into a coagulation process when the container space restricts their growth. Thus, at longer times, hydrate particles will be a part of a continuous medium forming a hydrate bulk phase. Hence, the total surface area per volume of the particles will decrease and consequently the probability of interactions between the reactants will also decline. The low gas permeability of the hydrate and the low diffusion coefficient of methane in water are the key factors limiting the mass transfer and the hydrate reaction.

Natarajan *et al.* [8] presented some induction data measurements for formation of methane, ethane, and carbon dioxide hydrates. These measurements were obtained in the same equipment using the same experimental procedure as in Englezos, *et al.* [5]. A meta-stable region for hydrate nucleation was considered. They used the crystallization theory to formulate a model for the hydrate induction time required for formation of stable hydrate nuclei. Makogon [9] and Englezos, *et al.* [5,6] pointed out the similarities between the crystallization and hydrate formation processes. Thus, the hydrate formation process was divided into two periods: “nucleation” and “growth”. During the nucleation phase, hydrate nuclei are generated from a super-saturated aqueous solution. The nucleation process ends by the appearance of critical-sized stable hydrate nuclei.

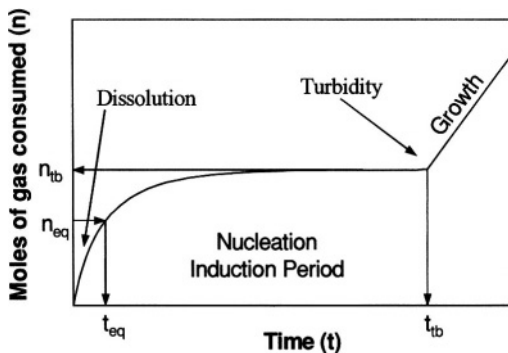


**Figure 1.** Typical hydrate nucleation and growth trends (after Natarajan et al., [8]).

Natarajan et al. [8] measured the moles of gas consumed with time during a typical hydrate formation experiment. They observed trends schematically described in Figure 1. The growth period was assumed to start after the “turbidity time”. A slight dip in the reactor pressure occurred at the turbidity point due to the sudden loss of super-saturation in the liquid. A sharp discontinuity was also observed in the curve of moles of gas consumed vs. time, with a slight rise in the solution temperature at the turbidity point, due to the heat release during the stable nuclei formation. Natarajan et al. [8] obtained their experimental data at isothermal and isobaric conditions only during the induction time. The measured induction times for methane showed an exponential tendency with the fugacity-based driving force.

An examination of the various experimental data including the NETL-generated data processed in this study reveal three basic insights about the hydrate formation process:

The hydrate formation process occurs in a three-step sequence:

1. Transport of gas from the gas phase to the aqueous liquid phase.
2. Diffusion of gas from the aqueous phase and through the liquid film to the hydrate-liquid interface.
3. Reaction of gas with the aqueous phase to form hydrates at the interface.

There is a critical radius of the hydrate nuclei. Nuclei having a radius greater than the critical radius are stable and continue to grow, while the nuclei with radius smaller than the critical radius re-dissolve in the liquid medium.

The rate of the phase transformation is directly related to the three-phase equilibrium pressure. The deviations from the three-phase equilibrium will generate conditions necessary for formation and thus the reaction takes place.

Here, a simple model for analysis of experimental data is developed in view of these insights. Both equilibrium and non-equilibrium models are presented and the data of Makogan and Holditch [9,10] and the present in-house experimental data are analyzed using these models. Our studies indicate that hydrate formation is best described using the non-equilibrium model while the equilibrium model best describes the hydrate dissociation process. The present model is not intended to be predictive; rather it provides a means of analyzing experimental data in order to gain insights into the mechanism of the hydrate formation and dissociation processes.

## 2. PROCESS DESCRIPTION

The proposed model considers a closed reactor, where methane and water are brought in contact at low temperature and high pressure, to form a hydrate. The formation process is divided into three time periods (See Figure 1): dissolution, induction, and growth periods. During the first and second periods, the gas and liquid phases are present in the chamber. During the dissolution period, the governing process is the mass transfer from the gas to the liquid. This period ends when the gas saturates the liquid. Hence, the concentration of the gas in the water increases, and super-saturated regions appear, leading to a clustering of water molecules around gas molecules. The induction period ends when clusters attain a critical size. Natarajan et al. [8] modeled the induction and dissolution periods with the same approach although the dominant processes involved during the dissolution and induction periods are different. The third time period is defined as the growth period. A three- phase system, consisting of the liquid, gas, and hydrate, is present. It is assumed that an excess amount of gas is available in the chamber during the whole process, and the gas volume reduction is negligible, given that the change of volume of water at different pressures is negligible and the volume occupied by the solution reacted and the hydrate formed are similar. Figure 2 shows a schematic of the processes involved during this period.

Although the liquid can achieve uniform super-saturation before the appearance of the hydrate nuclei (Englezos et al., [5]), experimental evidence indicates that the nucleation and growth occur predominantly at the gas-liquid interface, where the super-saturation is higher than anywhere else in the liquid. The appearance of a hydrate layer between the gas and liquid phases depends on the mixing conditions of the system and the amount of un-reacted water present in the system.

### 2.1. Equilibrium Model

The Clapeyron equation describes the equilibrium vapor pressure dependence on temperature. It can be applied to any kind of phase equilibrium including

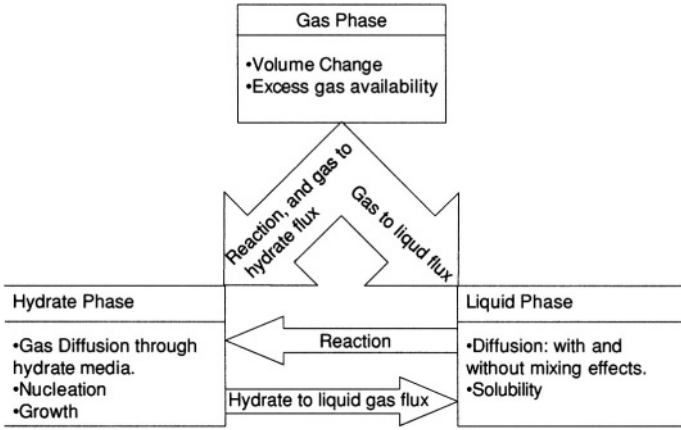


**Figure 2.** Mass transfer phenomenon during growth period at constant temperature and pressure.

solid-vapor (Elliot and Lira, [11]) as long as the system is univariant, as is the case for simple hydrates (van der Waals and Platteuw, [12]). This relationship can be expressed as:

$$\ln P = - \left( \frac{\Delta H}{Z \mathfrak{R}} \right) \frac{1}{T} \quad (1)$$

where  $P$  and  $T$  are the prevailing pressure and temperature,  $\Delta H$  is the heat of formation/dissociation,  $Z$  is the gas deviation factor and  $\mathfrak{R}$  is the universal gas constant. Thus, plotting  $\ln P$  vs.  $1/T$  will generate a straight line. Sloan [2]) stated that such linear plots might either indicate a constant  $\Delta H$  of hydrate formation when the compressibility factor, and the stoichiometric ratio of water and the guest molecule can be considered constants, or the non-linear behaviors of these factors cancel each other. The slope for the formation and dissociation should be the same for equilibrium processes. The statistical thermodynamic software package Hydooff (Sloan, [3]) was used to predict the equilibrium hydrate pressure for a given temperature, and these results were compared with the experimental pressures. This program assumes equilibrium between the three phases, and has a stated error of 5% when compared to experimental data.

## 2.2. Non-equilibrium Model

The in-house data calculations (see results for equilibrium approach calculations) indicated that the hydrate formation process did not follow an equilibrium path. Also Sloan [2] pointed out that the Clapeyron equation presents



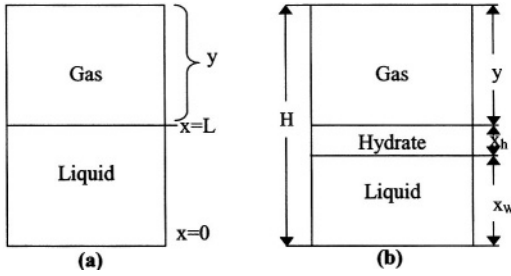


**Figure 3.** System Configuration for: (a) Dissolution and Induction Periods and (b) Hydrate Growth Period.

discrepancies with the experimental values because hydrate formation is non-stoichiometric. Such discrepancies are not important at equilibrium conditions because the non-stoichiometry remains approximately constant over small temperature ranges. The temperature ranges involved in the experimental data analyzed here are large. Therefore, a different approach is necessary to analyze such data.

We propose a non-equilibrium approach to analyze the data that is based on the process description presented earlier. The conceptual system configurations during the dissolution and induction periods, and the hydrate growth period are shown in Figure 3. The gas and liquid phases initially occupy certain prescribed regions of the reactor (Figure 3a). For the induction and growth periods, all hydrate particles are assumed to migrate to the gas-liquid interface rapidly and grow there (Figure 3b).

### 2.2.1. Gas Phase Equations

Neglecting the water vapor pressure, the cumulative gas consumption can be expressed as the difference between the initial and instantaneous moles of methane in the gas phase:

$$Q(t) = \frac{V_o}{RT} \left[ \left( \frac{P}{Z} \right)_0 - \left( \frac{P}{Z} \right)_t \right] \quad (2)$$

During the dissolution time period, this gas consumption is assumed to be going into the liquid phase. The discussion below will present equations defining how the consumption is handled for other time periods.

### 2.2.2. Induction Period

The mass conservation equation for this period is expressed as:

$$R + \frac{\partial Q}{\partial t} = 0 \quad (3)$$

The rate of reaction  $R$  is assumed to have the same driving force that Natarajan, et al. (1994) proposed:

$$R = k_{induction} \left( \frac{f_g^L}{f_e} - 1 \right)^{n_{induction}} \quad (4)$$

where  $f_e$  is the fugacity of the gas at the three-phase equilibrium condition,  $n_{induction}$  is the nucleation index, and  $k_{induction}$  is a constant. The reaction index,  $n_{induction}$ , is not assumed to be equal to one. Rather, its value is determined by means of the experimental data. The departure from equilibrium can be expressed by either  $f_g^L/f_e$  or  $f_g^V/f_e$ . These ratios will be equal to unity when equilibrium is attained. The ratio  $f_g^V/f_e$  can be estimated using an equation of state for the gas phase. The water vapor pressure can be neglected and the gas phase is assumed pure methane. Further,  $f_g^L/f_e$ , can be estimated using an equation of state for the liquid system, but the mole fraction of the gas in the liquid cannot be determined at non-equilibrium conditions. The concentration of the gas in the liquid will vary with the distance from the interface and this variation will be related to the mixing rate, among other factors. Therefore, there are many factors that can interfere with the  $f_g^L/f_e$  calculation adding errors to the expression of the driving force and the reaction rate. Therefore, the driving force used in the non-equilibrium model calculations is taken as  $(f_g^V/f_e - 1)$ .

### 2.2.3. Growth Period

The start of this period was identified by an abrupt change in the slope of the cumulative gas consumption curve. This coincides with the turbidity point observations of Natarajan et al. [8]. Thus, the growth period definition for this model is similar to that proposed by Natarajan et al. Similar to the induction period, it is assumed that the gas consumed from the gas phase is totally converted into hydrate during the growth period. The gas consumed from the liquid by the reaction will be replaced, and the saturation of the liquid will hold during this period. Because we assume that all hydrate being formed migrates rapidly to the gas-liquid interface and grow

as a “layer” there, we can compute the “thickness” of this “layer” using

$$x_H = \frac{\int_0^t R dt}{A \rho_{gas} \left[ \frac{\text{volume}_{gas}}{\text{volume}_{hydrate}} \right]} \quad (5)$$

where  $R$  is the rate of reaction, and  $\rho_{gas}$  is the molar gas density. The kinetics of this reaction will be assumed to follow a power-law form as:

$$R = k_{growth} \left( \frac{f_g^v}{f_e} - 1 \right)^{n_{growth}} \quad (6)$$

The fugacity of the gas is a function of the temperature and pressure at the reaction condition. The reaction is assumed to occur below the hydrate layer as soon as the gas permeating through the hydrate layer reaches the water below. The pressure below the hydrate layer is assumed to be equal to the fugacity of the gas and is calculated using Darcy’s law for gas flow through porous media (Collins, [13]):

$$q(t) = -\frac{K_H A}{P_1 \mu_g} \left( 1 + \frac{2b}{P_1 + P_2} \right) \left( \frac{P_2^2 - P_1^2}{2x_h} \right) \quad (7)$$

where  $b$  is the Klinkenberg constant. Because pressures in the experiments are typically fairly high, the term involving the Klinkenberg constant is neglected. As for the remaining terms,  $P_1$  is the pressure at the gas-hydrate interface,  $P_2$  is the pressure at the liquid-hydrate interface,  $K_H$  is the effective permeability of the hydrate patches, and  $\mu_g$  is the gas viscosity. The pressure at the liquid-hydrate interface,  $P_2$  is assumed to be equal to the fugacity of the gas.

Note that the assumption of a Darcy flux is only for convenience. Any closed form equation that would allow the calculation of the pressure below the hydrate “layer” could be used.

### 3. EXPERIMENTAL STUDIES

A number of publications present data on hydrate formation and/or dissociation. Experimental equipment and procedures differ slightly but are essentially similar. As this paper analyzes the in-house data from experiments at NETL, these experiments will be described in detail.

Experiments were conducted in a high-pressure view cell (Figure 4). The cell is constructed of 316-stainless steel with 6.35 cm (2.5 inches) OD and is 27.4 cm

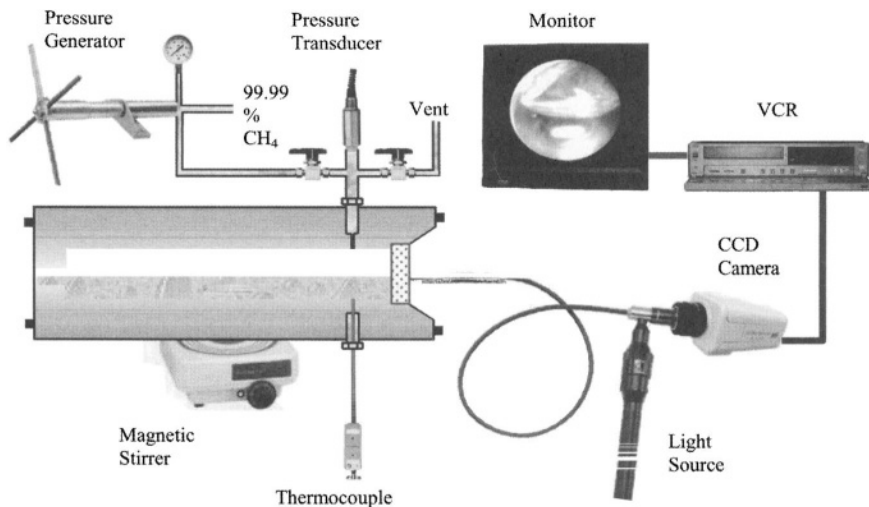


**Figure 4.** Schematic of Hydrate View Cell.

(11 inches) in length. The internal volume of the cell is approximately 40 ml. The cell is fitted with two machined end-caps, one of which contains a sapphire window to allow for observation of the contents of the cell using a CCD camera. The cell is fitted with ports to accommodate the fill gas inlet and reaction product outlet, a pressure transducer to monitor the internal pressure of the gas inside the cell, and a thermocouple that terminates inside the cavity of the cell to monitor the temperature of the liquid/hydrate mixture.

While the working pressure of the cell is rated at 220 MPa (32,000 psia), all experiments were conducted at 13.8 MPa (2,000 psig) or less. The temperature of the cell is controlled by the flow of a glycol/water solution from an external circulating temperature bath through a coil of 0.64 cm ( $\frac{1}{4}$  inch) copper tubing that is wrapped around the outside of the cell. Several layers of insulating material are wrapped around the cell to help maintain constant temperature.

A typical experiment involves filling the cell with approximately 20 ml ( $\pm 0.1$  ml) of double-distilled water. A Teflon<sup>®</sup>-coated stir bar is also placed inside the cell. The end caps are placed on the cell and tightened to specifications. An external magnetic stirrer is used to obtain a high degree of vortex mixing inside the cell. The cell is connected to a gas manifold and purged several times with methane. Following the purge procedure, the cell is charged with methane at pressures of 8.3–10.3 MPa (1,200–1,500 psig). Using the external circulating temperature bath, the temperature of the water in the cell is gradually lowered until formation of the methane hydrate is observed. Then, the temperature of the cell is lowered to approximately  $-10^{\circ}\text{C}$  and held constant as the unabsorbed methane is released from

Table 1. Average Deviation of Experimental Data from HydoFF Calculation

	Dissociation Slope	Formation Slope	HydoFF Dissociation Slope	HydoFF Formation Slope
Run 1	-9,865	-400	-7,605	-8,554
Run 2	-7,657	-413	-8,577	-8,009
Run 3	-8,494	-420	-8,025	-8,129
Run 4	-8,494	-3,500	-7,426	-7,958
Run 5	-8,304	-3,603	-7,631	-7,900
Run 6	-6,362	-22,899	-7,539	-8,567

the cell. The cell is finally allowed to warm slowly to a temperature between 10° C and room temperature, which causes the hydrate to release its absorbed methane gas.

3.1. Application of the Equilibrium Approach

An example plot of the formation and dissociation results is shown in Figure 5 and the slope values for all of the runs are shown in Table 1. The slope differences between the formation and dissociation data are pronounced, while the slopes of the dissociation data and the predicted values are similar. The predicted values were calculated assuming that the hydrate formation occurs at equilibrium condition. Thus, we can deduce that the dissociation occurs at equilibrium conditions while the formation does not.

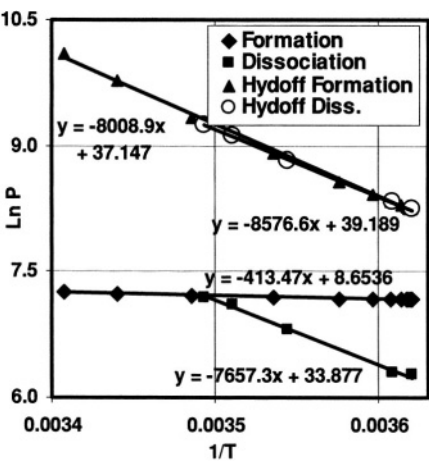


Figure 5. Experimental and Software Formation and Dissociation Trend Lines for Run 2.

### 3.2. Application of the Non-equilibrium Approach

The model for hydrate formation was applied to three experimental data sets, namely the in-house data of NETL runs 2 and 3, and the published data of Makogon and Holditch [9]. All of them formed methane hydrate with pure water. The NETL runs 2 and 3 have in common the same experimental set up, but run 2 was conducted under dynamic conditions and run 3 under static conditions. The Makogon and Holditch data was obtained at dynamic conditions with a similar set up but different equipment. The parameters  $k$  and  $n$  for induction and growth periods were calculated from NETL run 2 at isothermal and non-isothermal conditions, and from NETL run 3 and the Makogon data at non isothermal conditions. The data set and calculus election was done to achieve elements for comparison of the effect of temperature changes, mixing conditions and equipment on the hydrate formation process. The equilibrium pressure at each temperature was calculated using the CMTD three-phase equilibrium subroutine (Sloan, [2]). The effective permeability of the hydrate patches was approximated to be equal to  $4.3 \times 10^{-4} \text{ m}^2$  and the gas volume was assumed constant during the reaction for all the cases studied.

In general, the initial temperature changes affect the pressure in the chamber. The temperature decreases and therefore the pressure falls. The isothermal gas mass balance translates the pressure declines to gas consumption. Thus, the amount of gas reacted in the hydrate formation according to isothermal calculations is higher than in the non-isothermal calculations. The non-isothermal calculations follow closer the experimental ( $dQ/dt$  and  $Q$ ) behavior, and present better results in terms of our assumption of equality between the amount of gas consumed during induction and growth periods and the amount of gas reacted. The differences between the isothermal and non-isothermal models confirm that the temperature changes during the hydrate formation have a significant effect on the model calculations of the amount of gas consumed from the gas phase, the amount of gas reacted, and the rate of reaction. The isothermal model assuming an average temperature of 276 K did not yield reasonable matches to the data and will not be shown.

The NETL run 2 and run 3 non-isothermal gas consumption curves are similar in some aspects as the existence of an initial moderated increase in the gas consumption, then a plateau and an abrupt gas consumption, and at last decline. But if we observe closely the numbers at the time axis, we can notice that the dissolution and induction periods last longer in the run 3 than the run 2. The dissolution and induction periods last  $1.4 \times 10^4$  seconds and  $7.1 \times 10^4$  seconds for run 2 and run 3, respectively. Therefore, it can be inferred that the mixing conditions do not affect the existence of dissolution, induction, and growth periods, but do effect the time that the system takes to achieve the conditions necessary to pass from one period to other. Extending this to a general case, it indicated that the low mixing speeds lead to the periods longer than for high mixing speeds.

Table 2. Optimum parameters *k* and *n*.

Data Set	Condition	Period	<i>N</i>	<i>k</i>	$R^2 \text{ } Q_i-Q_{i-1}$
NETL Run 2 (Dynamic)	<i>Isothermal</i>	Induction	0.611	4.02E-08	0.62
		Growth	0.998	2.59E-06	0.03
	<i>Non Isothermal</i>	Induction	−2.306	3.05E-08	0.89
		Growth	2.007	1.62E-05	0.40
NETL Run 3 (Static)	<i>Non Isothermal</i>	Induction	−2.746	1.511E-08	0.54
		Growth	2.634	9.05E-06	0.50
Makogon (Dynamic)	<i>Non Isothermal</i>	Induction	0.927	1.11E-06	0.97
		Growth	3.29	4.65E-05	0.84

3.2.1. Case 1: NETL Run 2: Dynamic conditions

The amount of gas in the cell at the initial conditions was 0.0795 moles and the total amount of gas consumed during the hydrate formation was calculated from a gas mass balance as 0.0494. The latter accounts for the gas dissolved in the water and the gas converted into hydrate. The total amount of gas reacted in the hydrate formation was calculated as 0.0378 moles from the integration of the rate of reaction (R) using the optimum parameters for each period. The best estimate parameter values and the coefficient of regression are presented in Table 2. Figure 6 shows a reasonable comparison of the amounts of gas consumed from the gas phase during the hydrate formation period and the results of the integration of R for each time for the non-isothermal calculations.

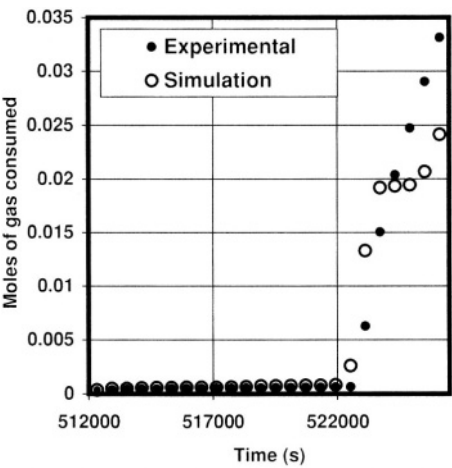
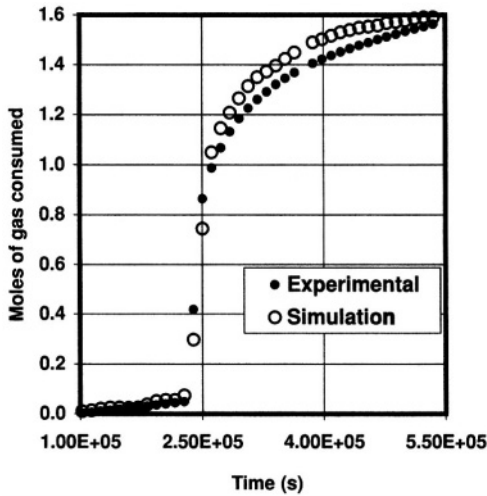


Figure 6. Comparison of experimental and simulation results—NETL run 2.



**Figure 7.** Comparison of experimental and simulation results—Makogon and Hoditch data [9].

### 3.2.2. Case 2: NETL Run 3: Static Conditions

The non-isothermal calculations of the rate of reaction were performed using NETL run 3 data. The total gas consumed was calculated from gas phase mass balance and is equal to 0.0468 moles. The total amount of gas consumed along with this calculation was 0.0468 moles. This number represents approximately 60% of the initial gas in the reactor. The total amount of gas reacted in the hydrate formation was calculated as 0.0370 moles from the integration of the rate of reaction (R) using the optimum parameters for each period. The best estimate parameter values and the coefficient of regression are presented in Table 2. The result obtained from the gas mass balance is 0.0432 moles. The comparison of the cumulative gas consumed from the gas phase and the cumulative gas reacted in the hydrate formation with time is similar to that of Figure 7.

We can notice that, similarly to NETL run 2 non-isothermal case, the assumption of the amount of gas consumed during the induction and growth periods equaling to the gas reacted on the hydrate formation is not accomplished. Also, notice that the total amount of gas consumed during NETL run 2 (0.0494 moles) is higher than the total amount of gas consumed during NETL run 3 (0.0468 moles), but the amount of gas converted into hydrate are practically equal (0.0378 moles for run 2 vs. 0.0370 for run 3). The differences in the total amount of gas consumed are caused by the different mixing speeds. In the case of the static conditions the concentration of gas in the liquid is not homogenous and the highest concentration will be located at the gas-liquid interface reducing the mass transfer driving force, and lowering the gas to liquid mass-transfer rate. Therefore, the



static system takes longer to achieve the gas concentration in the water necessary for hydrate formation. Also, the localization of the hydrate clusters is more likely to be primarily at the interface while liquid regions have not reached the saturation conditions. In terms of the modeling, the difference between calculated gases reacted and calculated gas consumed during the hydrate formation may be in part due to the gas being dissolved into the non-saturated liquids of the system.

### 3.2.3. Case 3: Makogan and Holditch Data

The data of Makogan and Holditch [9] is based on a different experimental apparatus, however similar to our's. The data was digitized and thereafter used to calculate the rate of formation as the NETL data runs. The initial gas in the reactor was 3.742 moles, and the cumulative gas consumed at the end of the reactions was 1.728 moles. This represents 47% of initial amount of gas. The integration of the rate of reaction reveals that the total amount of gas converted into hydrate according to the model was 1.570 moles, and it is almost the same as the gas reacted according to the mass balance, which indicated that the amount of gas converted in hydrate is equal to 1.590 moles. Figure 7 shows a reasonably good agreement between the cumulative gas consumed during the reaction process (Induction and growth periods) and the gas consumed in the reaction (integration of rate of reaction) with time. The best estimate parameter values and the coefficient of regression are presented in Table 2.

## 4. CONCLUSIONS

The proposed hydrate formation and dissociation models describe fairly well the behavior of the experimental data for different experimental conditions and apparatus, while providing important insights into the mechanism of the hydrate formation and dissociation processes.

## REFERENCES

1. Hammerschmidt, E. G.: "Preventing and Removing Gas Hydrate Formation in Natural Gas Pipelines," Oil&Gas Journal, Vol. 37, No. 52, pp. 66, 69,71–72, 1939.
2. Sloan, E. D.: *Clathrate Hydrates of Natural Gases*, Second Edition, Marcel Dekker, Inc. New York. 1998.
3. Sloan, E. D.: *Hydrate Engineering*, Monograph Volume 21, First Edition, SPE Henry L. Doherty Series, 2000.
4. Makogan, Y. F.: *Hydrates of Hydrocarbons*, PennWell Books, Tulsa, Oklahoma, 1997.

5. Englezos, P., Kalogerakis, N., Dholabhai, P. D., and Bishnoi, P. R.: "Kinetics of Formation of Methane and Ethane Gas Hydrates", Chem. Engng. Sci., vol 42, No. 11, pp. 2647–2658, 1987.
6. Englezos, P., Kalogerakis, N., Dholabhai, P. D., and Bishnoi, P. R.: "Kinetics of Gas Hydrates Formation from Mixtures of Methane and Ethane", Chem. Engng. Sci., vol 42, No. 11, pp. 2669–2666, 1987.
7. Skovborg, P. and Rasmussen, P.: "A Mass Transport Limited Model for the Growth of Methane and Ethane Gas Hydrates", Chem. Eng. Sci., 49, pp. 1131. 1994.
8. Natarajen, V., Bishnoi, P. R., and Kalogerakis, N.: "Induction Phenomena in Gas Hydrate Nucleation", Chem. Eng. Sci., 49, pp. 2075–2084, 1994.
9. Makogon, Y. and Holditch, S.: "Gas Hydrates- Conclusion: Experiments Illustrate Hydrate Morphology, Kinetics", OGJ, February 12, 2001.
10. Makogon, Y. and Holditch, S.: "Gas Hydrates as a Resource and a Mechanism for Transmission", Proceedings of the SPE annual technical conference and exhibition held in San Antonio, Texas, 29 September-2 October, 2002.
11. Elliot, R. and Lira, C.: *Chemical Engineering Thermodynamics*, Prentice-Hall International, 1999.
12. Van der Waals, J. H., Platteeuw, J. C.: "Clathrate Solutions", advanced Chemistry Physics, Vol. 2 (1959).
13. Collins, R. E.: *Flow of Fluids Through Porous Materials*, First Edition, Penn Well Books, Tulsa OK. 1961.

*This page intentionally left blank*

# Effect of Conductive and Convective Heat Flow on Gas Production from Natural Hydrates by Depressurization

Mehran Pooladi-Darvish\* and Huifang Hong

## 1. INTRODUCTION

Formation of gas hydrates requires the presence of hydrate-forming gases and water under appropriate pressures and temperatures. In natural environments, these conditions could occur offshore in shallow depths below the ocean floor and on-shore beneath the permafrost. The geothermal gradient of the earth increases the pressure requirement for the stability of the hydrate at a much greater rate than that provided by the available increased pressure due to the hydrostatic gradient. Therefore, there is a depth interval where hydrates may be stable. Figure 1 demonstrates a case of hydrate stability with depth in a permafrost environment [1]. In the permafrost regions [2], where surface temperatures are well below zero, gas hydrates can be present at depths between 150 and 2000 m. Under offshore conditions, the hydrate stability depth is usually between 100 and 500 m below the ocean floor [3], although hydrates at the ocean floor have also been reported.

Several groups have attempted estimating the amount of natural gas contained in the form of hydrates. The estimates of the amount of methane in hydrates among different studies differ by a factor of at least ten, and demonstrate our limited knowledge for accurately characterizing hydrate-bearing formations [4]. Despite

---

MEHRAN POOLADI-DARVISH • University of Calgary, 2500 University Drive N.W. Calgary, Alberta T2N 1N4

HUIFANG HONG • University of Calgary, 2500 University Drive N.W. Calgary, Alberta T2N 1N4

Telephone: (403) 220-8779, E-mail: pooladi@ucalgary.ca

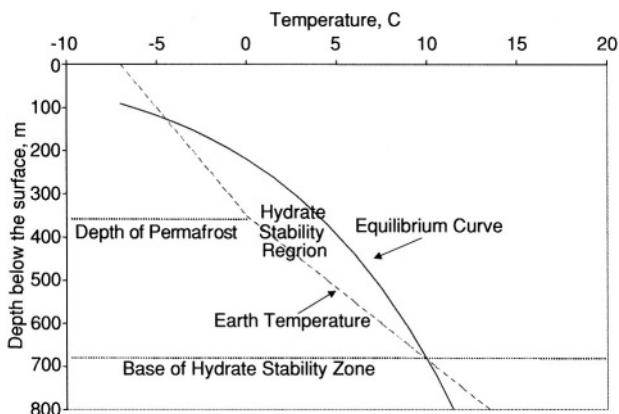


**Figure 1.** An example of hydrate stability zone for a permafrost reservoir (Geothermal gradient =  $0.03\text{ }^{\circ}\text{C/m}$ , pore-pressure gradient =  $10\text{ kPa/m}$ , depth of permafrost =  $350\text{ m}$ , temperature at the permafrost surface =  $-7.5\text{ }^{\circ}\text{C}$ ), modified from Holder et al.<sup>[1]</sup>

the uncertainties, pertaining to the areal and vertical extent of the hydrate-bearing formation and the concentration of the hydrate within the pore space, a summary of 10 studies estimates the carbon mass in hydrates at about 10 tetratonnes. This is roughly twice the total amount of carbon in all other recoverable and non-recoverable fossil fuels: coal, oil and natural gas. Stated otherwise, the trapped methane represents 20,000 trillion ( $20 \times 10^{15}$ ) cubic meters of methane, two orders of magnitude greater than the amount of conventional recoverable methane, which is estimated to be 250 trillion cubic meters [3]. The enormous amount of methane trapped in natural hydrates has motivated governments and industry to test various hydrate production techniques; among them are the efforts at the Mallik field in Northwest Territories, Canada [5].

One of the key requirements of any production technique is to provide the heat necessary for the endothermic reaction of hydrate decomposition. The least energy intensive method suggested is the depressurization technique, where the heat of decomposition is provided by the surrounding formation. Because of the small natural heat flux, it is anticipated that this technique could be attractive only when there is large surface area for decomposition and heat transfer [6]. This can be materialized in reservoirs where the base of hydrate stability zone depicted in Figure 1 divides the reservoir into two parts of a hydrate zone at top and a free-gas/water zone at the bottom. Figure 2 is a schematic of such a reservoir.

The most common form of the depressurization technique envisions drilling through the hydrate layer, and completing the well in the free-gas zone. Gas production from this layer leads to pressure reduction and decomposition of the overlying hydrate. Heat flows towards the cooled region from the surrounding formation. The only field case of gas production from a hydrate reservoir in the Messoyakha field

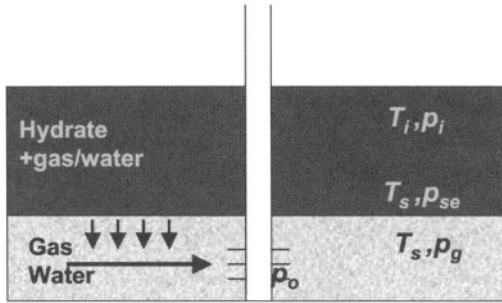


**Figure 2.** Schematic representation of production from a hydrate reservoir with underlying free gas.

was primarily based on the depressurization technique [7]. It is foreseen by many that the next commercial project for gas production from hydrate reservoirs will use this technique [8], partially because this is estimated to be by far more economic than the other two methods of thermal stimulation and inhibitor injection [9].

In this paper, we will examine the role of heat transfer in a reservoir producing by the depressurization method. In particular, we will study the importance of convective heat transfer as compared with conductive heat transfer, examine the importance of heat supplied from the base- and cap-rock and the sensible heat within the hydrate zone.

## 2. BACKGROUND

Gas production from natural hydrates is meaningful only if the thermal energy of the produced methane is more than the heat required for the endothermic reaction of hydrate decomposition. Burning hydrate samples vividly demonstrate that gas production from hydrates will lead to energy production. Holder et al. [10] have shown that the energy value of the produced gas is about 10 times more than the energy required for the dissociation of the hydrate within typical reservoirs. This additional energy is the potential prize that all recovery techniques are after. In addition to heat flow, at least two other mechanisms are involved in the depressurization technique: the flow of the produced fluids and the intrinsic kinetics of hydrate decomposition [6, 11]. None of the analytical models and the earlier numerical models includes all the three mechanisms. In the following, we briefly review some of the assumptions with respect to heat flow in the models developed for the depressurization technique.

Most models developed for studying the depressurization technique have included some sort of heat transfer formulation. While some have ignored convection in comparison with conduction [6, 12], others have ignored conduction in comparison with convection [13,14]. Yet others have ignored both forms of heat flow [15–17]. Most of the above models ignore heat flow from the non-hydrate-bearing

formation, *i.e.* the base- and cap-rock, to the decomposition zone. Another prevalent assumption is the presence of a sharp interface between the hydrate zone and the decomposed zone, which limits the surface area of hydrate decomposition. It will be shown in this work that this assumption is not valid for the depressurization technique when presence of a mobile phase allows pressure reduction and hydrate decomposition deep within the hydrate zone.

More recently, comprehensive numerical models have been developed which relaxes most of the above assumptions [18–20]. These models include the equations of convective and conductive heat transfer from within and outside the reservoir, equations of multi-phase flow and a kinetic-reaction equation for the decomposition of the hydrate. Therefore, these models are most suitable for examining the above assumptions and for finding whether in the depressurization technique the rate of natural heat transfer is sufficient to sustain a reasonably high rate of hydrate decomposition and gas generation. In this paper, we will use one of these models [20, 21] and through hypothetical case studies investigate the rate of gas generation and production in the depressurization technique. Furthermore, we will examine how the different forms of heat affect the depressurization technique. With the exception of the results of the base case [20], other cases are presented for the first time.

### 3. PHYSICAL MECHANISMS AND MATHEMATICAL MODEL

In decomposition by the depressurization method three mechanisms of fluid flow, heat transfer and intrinsic decomposition of hydrates are involved. The interplay of these mechanisms is schematically shown in Figures 2 and 3, which depict the pressure and temperatures at different locations, along with the important driving forces.

Let us consider two modes of production, constant rate and constant pressure. In constant rate production, bottomhole pressure reduces with time until it eventually falls below the equilibrium pressure of the hydrate at  $T_i$ . In constant pressure production, the bottomhole pressure needs to be below the equilibrium pressure of the hydrate at  $T_i$  for hydrate to decompose. This pressure is denoted by  $p_o$  in Figures 2 and 3. The reduction in pressure from  $p_i$  to  $p_o$  at the wellbore is transferred to the hydrate-fluid interface, resulting in pressure  $p_g$  there. The difference between  $p_g$  and  $p_o$  is the driving force for the gas flow. Kim et al. [22] suggested that the intrinsic rate of hydrate decomposition at a constant temperature is proportional to a driving force required for the breakage of the hydrate cage. In their model, the driving force for the intrinsic decomposition of the hydrate is the difference between the fugacity of the hydrocarbon gas in the fluid surrounding the hydrate particle, and that on the surface of the solid hydrate. We have used fugacity in our model. For demonstration purposes in Figures 2 and 3 however,

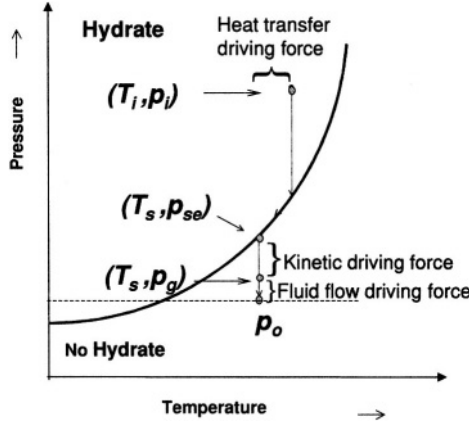


**Figure 3.** Schematic diagram demonstrating the pressure and temperature regime for the decomposition of hydrates in the depressurization technique.

the fugacity is replaced with pressure, as is the case for an ideal gas. For a hydrate interface that is at a temperature  $T_s$ , the equilibrium decomposition pressure is determined from Figure 3 and is called  $p_{se}$ . The difference between  $p_g$  and  $p_{se}$  is the driving force for intrinsic kinetics of hydrate decomposition. The initial hydrate temperature in this hypothetical example was assumed to be  $T_i$ . The reason for the difference between  $T_i$  and  $T_s$  is the cooling that occurs due to endothermic hydrate decomposition. Under a driving force of  $T_i - T_s$ , conductive heat flows from the surrounding formation to the cooled region. Additional heat exchange occurs by convective heat transfer.

The decomposition process as described above is a combination of multi-phase fluid flow, conductive and convective heat transfer, and kinetic decomposition at the hydrate interface. The equation of conservation of energy is given by [20, 21],

$$\begin{aligned} & \nabla \cdot (k_c \nabla T) - \nabla \cdot (\rho_g \vec{u}_g D h_g + \rho_w \vec{u}_w D h_w) + \dot{q}_{mw} h_w + \dot{q}_{mg} h_g + \dot{Q}_H + \dot{Q}_{in} \\ & = \frac{\partial}{\partial t} [(1 - \phi) \rho_R U_R + \phi (S_H \rho_H U_H + S_w \rho_w U_w + S_g \rho_g U_g)] \quad (D=r, z) \end{aligned} \quad (1)$$

In Equation (1), the first and second terms represent conductive and convective heat flow respectively, while the third and fourth terms account for heat removed/added by the producing/injecting fluids. The rate of heat taken by hydrate decomposition is represented by  $\dot{Q}_H$ , and  $\dot{Q}_{in}$  is the direct heat input such as heat conducted from the cap- and base-rock. The term on the right-hand side is the accumulation term, given as the rate of change of internal energy of the formation.



In the next section, we manipulate the different terms of Equation (1) to study the effect of different mechanisms of heat flow on hydrate decomposition.

#### 4. SCOPE OF THE STUDY

A numerical simulator based on Equation (1) along with fluid flow and kinetics equation's has been developed and extensively validated [20, 21]. This model is used to study effect of heat flow on gas production from a hypothetical hydrate reservoir in the permafrost region. The hydrate-bearing layer overlies a free gas zone similar to that of the Messoyakha field in Siberia [7]. Figure 1 shows a schematic diagram of hydrate stability zone in the reservoir of our interest, where the interface separating the hydrate layer from the free-gas zone is at equilibrium. By moving downward, hydrate disappears due to natural temperature increase, assumed to be 0.03 K/m. The reservoir of this study is assumed to cover 10m above and 10 m below the hydrate-free-gas interface. At the interface, the initial pressure is 6913 kPa and temperature is 283.15 K. These initial conditions represent a typical case where the depth of methane-hydrate occurrence is about 680 m below ground surface in a permafrost region. The original free gas in place is  $23.2 \times 10^6 \text{ sm}^3$  and that in the form of hydrate is  $38.4 \times 10^6 \text{ sm}^3$ . Figure 4 shows the initial condition in the reservoir. A well is located in the center of the reservoir that has a radius of 200 m, and is producing gas at a constant bottomhole pressure (BHP) of 4000 kPa from the free gas zone. The permeability of the rock is 20 md, and the relative permeability and capillary pressure functions are depicted in Figure 5 and 6, respectively. The saturation of the phases in the reservoir and the other

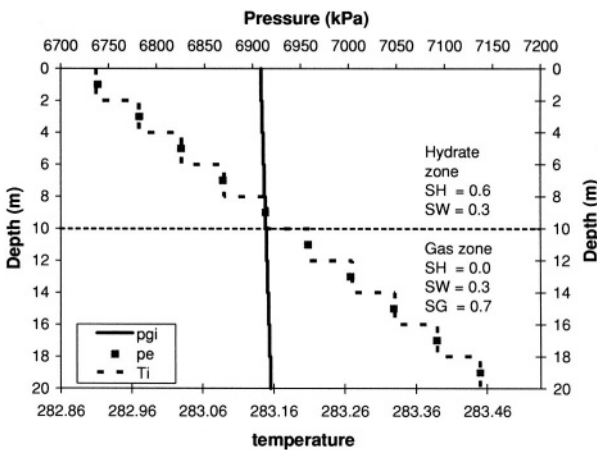
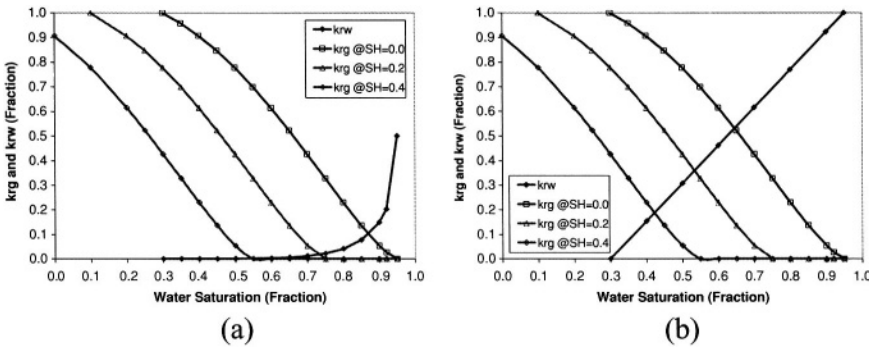


Figure 4. Initial pressure, temperature and saturation in the reservoir.



**Figure 5.** Relative permeability for water and gas in the presence of hydrate (a) for the Base Case, (b) for Cases 2 and 3.

parameters used in the studies are listed in Tables 1 and 2 and are similar to those given elsewhere [20, 21].

For the base case (CASE 1), the rock-thermal conductivity is 1.5 W/m-K, and any possible heat flow from the base- and cap-rock into the reservoirs is computed by a semi-analytical integral method suggested by Vinsome and Westerveld [23]. This method has been extensively used in thermal reservoir simulators that require accurate estimation of heat exchange between the reservoir and the base- and cap-rock. The velocities in the convective term of Equation (1) are calculated using the multi-phase flow equations along with the relative permeability function of Figure 5a.

To study the effect of heat transfer on hydrate decomposition, we manipulate different terms of Equation (1). To examine the importance of the convective heat

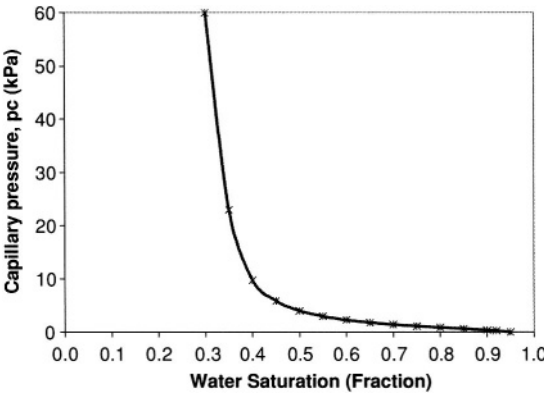


**Figure 6.** The water-gas capillary pressure function.

Table 1. Reservoir geometry and properties

Initial free gas in place (std m <sup>3</sup> )	$2.325 \times 10^7$
Initial gas in hydrate (std m <sup>3</sup> )	$3.842 \times 10^7$
Reservoir Radius (m)	200
Hydrate zone (m)	10
Gas zone (m)	10
Porosity	0.28
Permeability (md)	20
$S_{wi}$	0.3
$S_{Hi}$ (hydrate zone)	0.6
$S_{gi}$ (hydrate zone)	0.1
$S_{Hi}$ (gas zone)	0.0
$S_{gi}$ (gas zone)	0.7
Initial pressure at bottom of hydrate zone (kPa)	6913
Initial Temperature at bottom of hydrate zone (K)	283.15

flow in CASE 2, we allow for larger water flow by modifying the water relative permeability to that of Figure 5b, and in Case 3 we remove the effect of convective heat transfer by setting the velocities in the convective term of Equation (1) to zero.

The thermal conductivity,  $k_c$  used in Equation (1) is that of the formation and is calculated using Equation (2) as a volume average of the thermal conductivity of the rock,  $k_{c,rock}$ , and other constituents.

$$k_c = k_{c,rock} (1 - \phi) + \phi (k_{c,H} S_H + k_{c,w} S_w + k_{c,g} S_g) \quad (2)$$

Table 2. Values of other parameters <sup>[20,21]</sup>

Density (kg/m <sup>3</sup> )	
Rock	2650
Hydrate	919.7
Heat capacity (J/kg K)	
Rock	800
Hydrate	1600
Thermal conductivity (W/mK)	
Rock	1.5, 8.0
Hydrate	0.393
Water	0.6
Kinetic parameters	
$k_d^o$ (kmolCH <sub>4</sub> /m <sup>2</sup> kPa·s)	$1.24 \times 10^3$
AHS (m <sup>-1</sup> )	$3.00 \times 10^5$
$E/R$ (K)	9400
Heat of decomposition (J/mol)	51,858

Table 3. List of the case studies and their objectives—A void value means the base case values

Objective of study	Case #	Rock thermal conductivity	Relative permeability to water	Velocity in heat flow equation	Heat exchange with cap-/base-rock	Porosity
BASE CASE	1	1.5	Low	Included	Included	0.28
Convective heat flow	2		High			
	3		High	Excluded		
Conductive heat flow inside the reservoir	4				Insulated	
	5	8.0			Insulated	
Conductive heat flow from outside and inside	6	8.0				
Porosity/Sensible Heat	7					0.1

To examine the importance of heat conduction,  $k_{c,rock}$  will be varied between 1.5 and 8.0 W/mK. These values are close to that of thermal conductivity of vitrous Silica and Quartz, respectively [24]. Furthermore, to study the importance of heat flow from outside the reservoir,  $\dot{Q}_{in}$  is set to zero. Finally, formation porosity is varied to investigate the effect of sensible heat.

Table 3 gives the list of case studies and the parameters used. The cases are further explained when each case is discussed.

5. RESULTS

We have used two types of plots to study the results. The first type is a performance plot, which depicts gas generation and production as a function of time. The term generation is used for the gas resulted from decomposition of hydrate, and production is used for the total gas produced from the wellbore. The second type is a distribution plot, which shows pressure and saturation as a function of radial distance or depth. The radial pressure and saturation distributions in these figures are for the grid-blocks closest to the interface between the hydrate and gas zones and the vertical ones are for the grid-blocks closest to the wellbore.

The results for the base-case (CASE 1) are shown in Figures 7a to 7d. Figure 7a shows that about half of the produced gas for the first 300 days of production is from hydrate decomposition. The hydrate recovery, defined as the percentage of the original hydrate that has decomposed, is 22%. The solid line in Figure 7b shows the gas production rate for CASE 1, while the solid squares show the gas production rate if there was no hydrate decomposition. The results indicate that

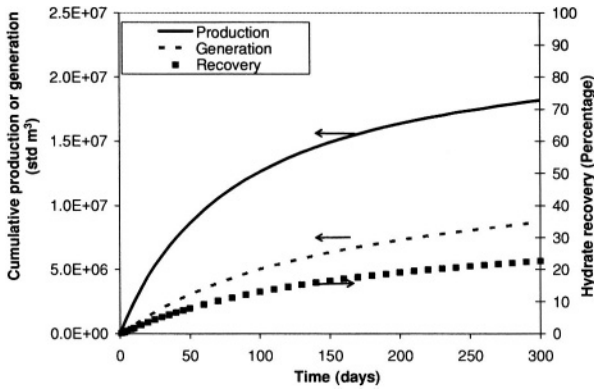


Figure 7a. Cumulative gas production, generation and hydrate recovery vs. time of CASE 1.

the decline in gas production rate is much smaller for the hydrate reservoir. The difference between the two curves is due to hydrate decomposition, shown using the open triangles. As seen in Figure 7b, rate of gas generation initially increases as pressure reduced within the formation, and then declines as rate of hydrate decomposition is restricted by the rate of heat flow. Figure 7b shows that after 300 days of production, rate of gas generation is nearly equal to the total rate of gas production. Results shown in Figure 7b indicate that the economic life of a gas reservoir may be significantly increased when there is a hydrate layer at top.

Figure 7c indicates a sharp pressure gradient close to the wellbore because of the radial flow. The low pressure values there have resulted in more hydrate decomposition close to the wellbore, as is shown by the lower hydrate saturation values in this figure. Figure 7d shows the vertical profile of hydrate saturation and temperature profiles near the wellbore. The step change is because of the constant

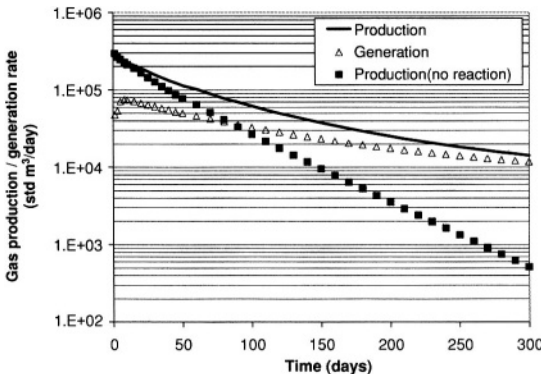
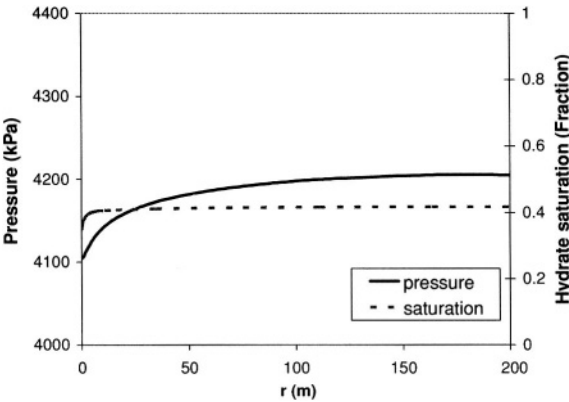
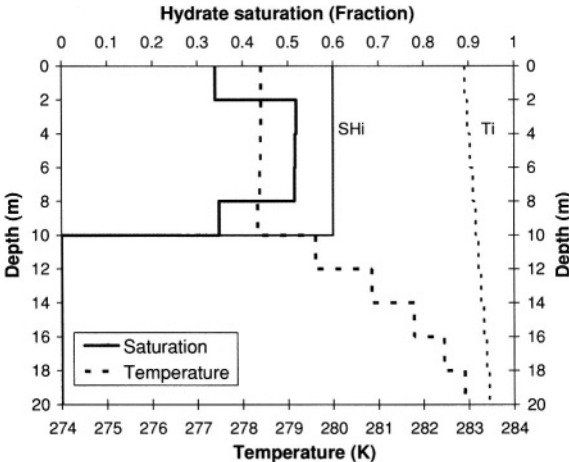


Figure 7b. Gas production and generation rates vs. time of CASE 1.



**Figure 7c.** Radial pressure and hydrate saturation profiles @300 days of CASE 1.

values in each grid block. In this graph and all other ones, no attempt is made to smooth the results. Figure 7d indicates that hydrate decomposition occurred within the whole thickness of the hydrate zone. The assumption of a sharp decomposition front made in most analytical solutions was not found to be valid. The reason is that the pressure reduction from the free-gas zone propagated into the hydrate zone through the mobile phase(s), resulting in hydrate decomposition deep within the hydrate zone. The hydrate-saturation profile in Figure 7d indicates that more hydrate decomposed at the bottom and top of the hydrate zone. This is because the rate of heat flow is the highest there, drawing heat from the underlying free gas zone and the cap rock, respectively. The hydrates in between are insulated by



**Figure 7d.** Vertical hydrate saturation and temperature profiles @ 300 days of CASE 1.

hydrates at the bottom and top, as seen by the flat temperature profile in the hydrate zone in Figure 7d denoting a small conductive-heat flux.

For continuous hydrate decomposition, heat needs to be provided continuously. In general, one may be able to name a number of heat sources. First in the decomposing zone, the internal energy of the constituents surrounding the hydrate particles (i.e. water, rock and gas), can provide for part of the heat of decomposition. Then heat can flow within the reservoir by mechanisms of convection and conduction. Finally, heat can flow into the reservoir by conduction from the base- and cap-rock. The effect of these sources of energy is examined separately, starting with convection inside the reservoir.

### 5.1. Convective Heat Transfer

Convective heat is the heat transferred by the flowing fluids. The results of the base-case indicated no water production. This is partly due to the shape of the relative permeability curve chosen that results in little water mobility for water saturations as high as 0.65 (See Figure 5a). In CASE 2, the role of convective heat transfer is increased by changing the relative permeability function to that of Figure 5b. This will lead to more heat transfer by convection, caused by more flow of water that has the highest specific heat among the constituents of the formation. In CASE 3, the effect of convective heat transfer was totally removed, by setting the velocity terms of Equation (1) equal to zero. The results are shown in Figure 8a and 8b.

While, Figure 8a shows that for CASEs 2 and 3 water production is significantly larger than that of CASE 1, Figure 8b shows that there is little difference between gas generation and production for all cases. A careful comparison of the results indicates that as heat transfer by convection decreased, rate of gas

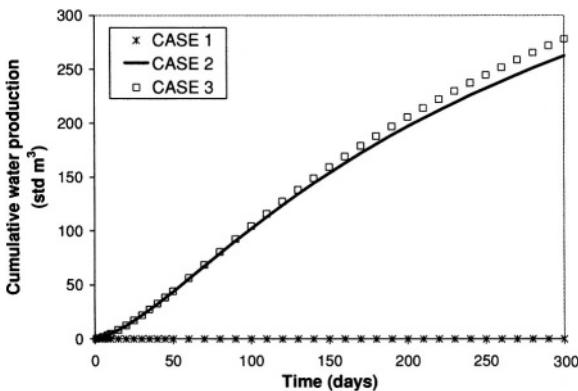
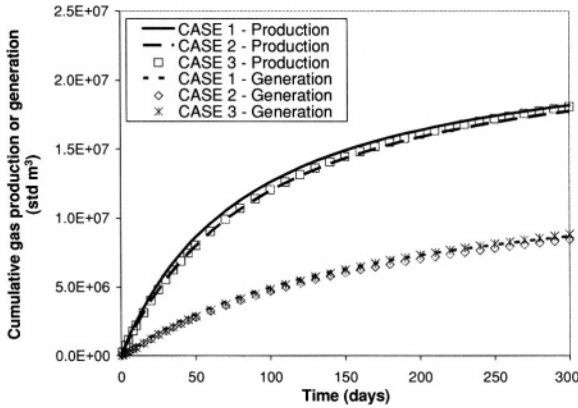


Figure 8a. Cumulative water production for CASEs 1 to 3.



**Figure 8b.** Cumulative gas production and generation for CASEs 1 to 3—effect of convection.

generation increased. CASE 2 that has the highest heat transfer by convection, has the lowest gas generation, while CASE 3 that has the least convective heat transfer has the highest rate of gas generation. This could be partly because flow of water from the decomposing region leads to replacement of the water with gas, which has a much smaller specific heat capacity. There will be therefore less heat capacity in the decomposing zone to provide for the heat of decomposition. A study of temperatures in the hydrate zone indicates that in the presence of convection in CASE 2, temperature is slightly (0.03 K) smaller than that in CASE 3.

The results of CASEs 1 to 3 suggest that for the reservoir and flow conditions considered here, heat transfer by convection plays a small role. If the water flow is more, the convective heat transfer could have a larger effect on the process due to the large heat capacity of the water. In this study, the effect of convective heat flow was found to be slightly negative for hydrate decomposition. However, this is not a general conclusion as different geometries and flow patterns change the direction of convective heat flow.

## 5.2. Conductive Heat Flow Inside the Reservoir

To study the importance of heat conduction inside the reservoir, we first remove the effect of heat conduction from the base- and cap-rock in CASE 4, and then increase the thermal conductivity of the rock in CASE 5 to a value of 8.0 W/(m.K). Using Equation (2) along with values of 1.5 and 8.0 for the rock thermal conductivity, one obtains an initial thermal conductivity of 1.2 and 6.2 W/(m.K) in the hydrate zone for CASEs 1 and 5, respectively. Comparing these values with thermal conductivity of measured hydrate samples in recent studies suggests that the above values cap the lower and higher ends of the measured values [25, 26].



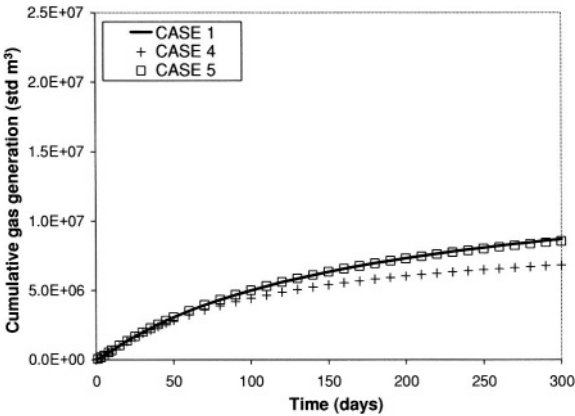


Figure 9a. Cumulative gas generation vs. time for CASEs 1, 4 and 5—effect of conduction.

The results for CASEs 1, 4 and 5 are presented in Figures 9a to 9c. Figure 9a shows the cumulative gas generated by hydrate decomposition for CASE 4 [insulated,  $k_{c,rock} = 1.5 \text{ W/m}\cdot\text{K}$ ] is significantly less than that of CASE 1 [external heat flow,  $k_{c,rock} = 1.5 \text{ W/m}\cdot\text{K}$ ]. Figure 9b, shows similar results and suggests that the rate of gas production at 300 days for CASE 4, is about 60% of CASE 1. In CASE 5 however, [insulated,  $k_{c,rock} = 8.0 \text{ W/m}\cdot\text{K}$ ], the cumulative gas generated and rate of gas production over the 300 days of simulation are about the same as those of CASE 1. In CASE 5, the additional heat flow within the formation has compensated for the lack of heat input from the base- and cap-rock. It is expected however that gas production from CASE 4 (and even CASE 5) would decline below that of

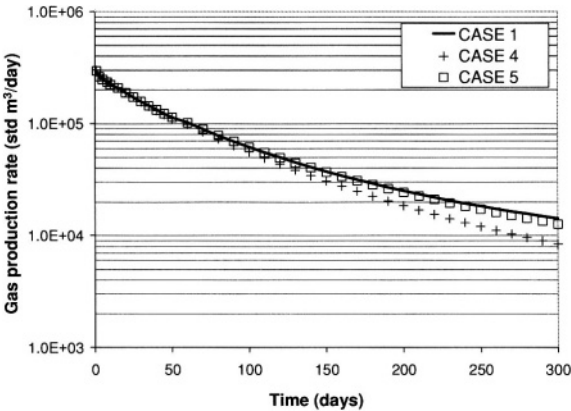
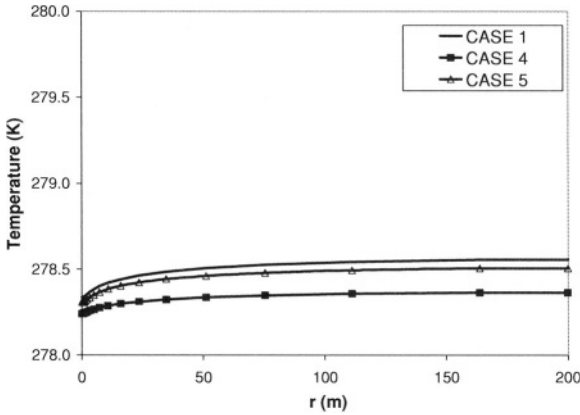


Figure 9b. Gas production rate vs. time for CASEs 1, 4 and 5—effect of conduction.



**Figure 9c.** Radial temperature profile at 300 days for CASES 1, 4 and 5—effect of conduction.

CASE 1 as production time increases. This is because the hydrate decomposition in CASEs 4 and 5 would cease when the reservoir temperature drops to 278.1 K, which is the equilibrium temperature at the production pressure of 4000 kPa. A rough estimation shows that a maximum of 30.4% of the original hydrate could decompose, before the process becomes self-limiting. This estimation applies to both CASEs 4 and 5, while in CASE 1, continuous heat flow from the base- and cap-rock would allow complete decomposition of the hydrate.

Figure 9c shows the radial temperature profile in the reservoir and shows that CASE 4 [insulated,  $k_{c,rock} = 1.5 \text{ W/m}\cdot\text{K}$ ] has the lowest temperature.

### 5.3. Conductive Heat Flow from Inside and Outside the Reservoir

In CASE 5, it was seen that an increase in thermal conductivity of the reservoir rock, increased the rate of heat flow to the decomposing hydrate to a point that it compensated for the lack of heat flow from the base- and cap-rock. CASE 6 examines the effect of increased thermal conductivity in the reservoir as well as the base- and cap-rock. Figures 10a to 10e show the results. Figure 10a shows that a higher thermal conductivity leads to a significant increase in gas generation and production as compared to CASE 1. Hydrate recoveries at 300 days for CASEs 1 and 6 are 22% and 33%, respectively. Figure 10b shows that at 300 days, rate of gas production for CASE 6 is about 80% more than rate of gas production for CASE 1. Figure 10c shows that for CASE 6 more of the hydrate has decomposed and therefore the gas pressure is higher as seen in Figure 10d. Figure 10e shows the temperature profile with depth and indicates that for CASE 6 the hydrate temperature is slightly more, while the temperature of the underlying zone is slightly less, indicating that the heat flow to the decomposing zone occurs at the

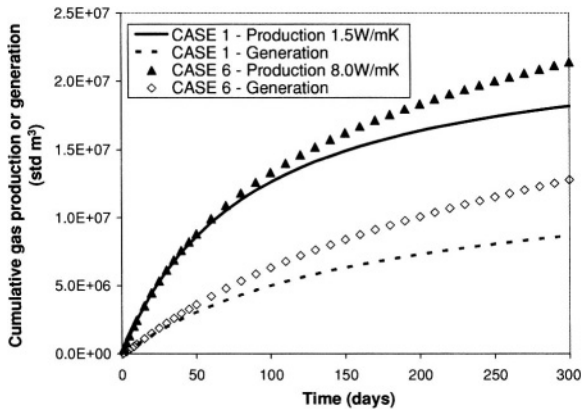


**Figure 10a.** Cumulative gas production and generation vs. time—effect of thermal conductivity of rock.

smaller temperature gradient. Figure 10e further shows that the majority of the extra decomposition in CASE 6, as compared to CASE 1 is at the top and bottom of the hydrate zone. The conducted heat is consumed there and barely penetrates into the hydrate in between.

5.4. Sensible Heat

The above studies considered that part of heat of decomposition supplied from the adjacent formation, while another part of the heat is supplied from the heat content

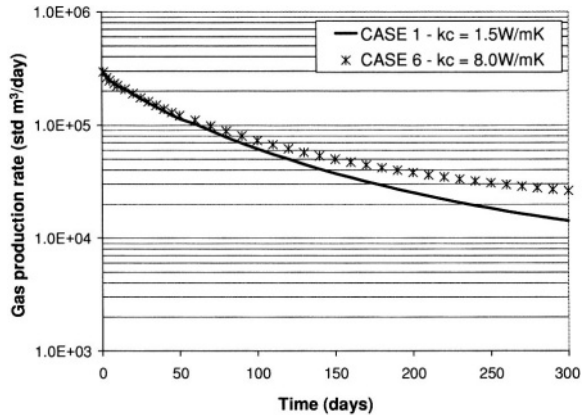


**Figure 10b.** Gas production rate vs. time-effect of thermal conductivity of rock.

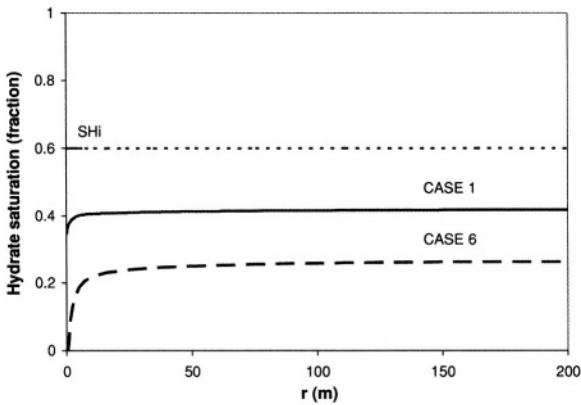


Figure 10c. Radial hydrate saturation profile at 300 days—effect of thermal conductivity of rock.

of the rock and fluids surrounding the hydrate particles within the decomposing zone. Previous analytical solutions[6] have shown that rate of hydrate decomposition is strongly affected by a dimensionless group called Stefan Number. Stefan Number is defined as the ratio of the sensible heat of the formation to heat of decomposition,  $Ste = \frac{c_p(T_i - T_{oe})}{\phi \Delta H} \frac{\rho}{\rho_H}$ , where  $c_p$  and  $\rho$  are the heat capacity and density of the formation composed on rock, hydrate and fluids, respectively. Other terms are given in the Nomenclature. One can see that  $Ste$  increases as porosity reduces. The results of analytical studies have shown that recovery rate of hydrate decomposition increases as  $Ste$  increases. As porosity decreases and  $Ste$  increases, the amount of hydrate in porous media decreases. It is clear that as porosity approaches zero, there is no hydrate in porous media to decompose. Therefore, the appropriate interpretation of the effect of  $Ste$  on rate of hydrate decomposition is that as  $Ste$

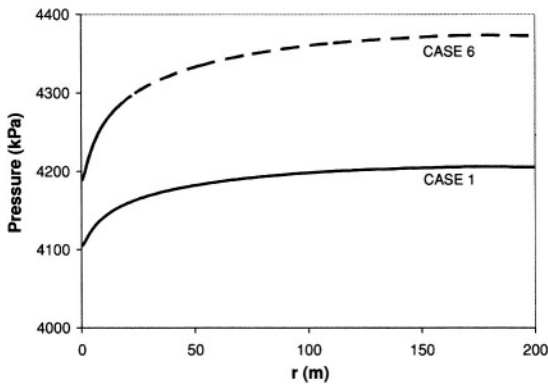
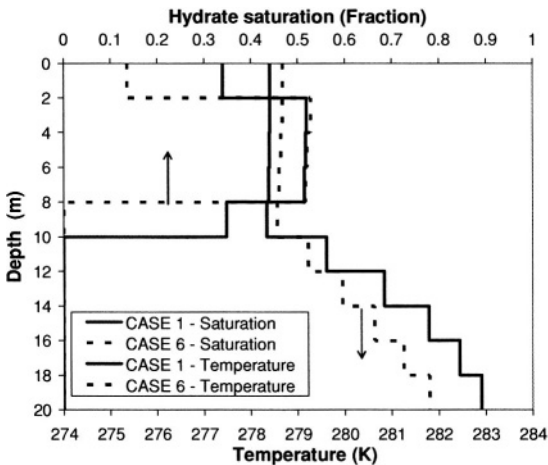


Figure 10d. Radial hydrate pressure profile at 300 days—effect of thermal conductivity of rock.



**Figure 10e.** Vertical hydrate saturation and temperature profiles at 300 days—effect of thermal conductivity of rock.

increases the rate of recovery of hydrate, as measured as the decomposed percent of the original hydrate, increases. This is further explained below.

To study the effect of porosity on rate of hydrate decomposition, porosity in CASE 7 was reduced to 0.10. The original free gas and that in hydrates of CASE 7 is roughly 1/3 of that of CASE 1. Results are shown in Figures 11a to 11c. Figure 11a indicates that the higher sensible heat in CASE 7 has resulted in more gas generation. However, the total produced gas is less, because of a smaller amount of free gas in CASE 7. Hydrate recovery at 300 days for CASE 7 is 66% as opposed

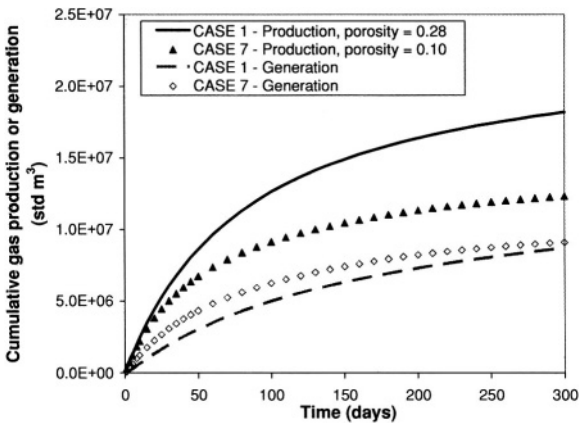


**Figure 11a.** Cumulative gas production and generation vs. time—effect of porosity.

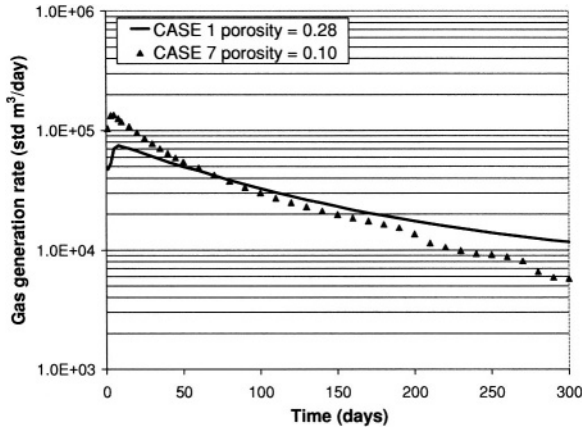


**Figure 11b.** Gas generation rate vs. time for CASE 1 and CASE 7—effect of porosity.

to 22% for CASE 1. Figure 11b shows that the rate of gas generation in CASE 7 is initially larger than that in CASE 1, but falls below that of CASE 1 at later times. The reasons can be explained by the interplay of pressure and temperature effects in CASE 7. A smaller amount of free gas in CASE 7 leads to faster pressure drop, and a larger driving force for hydrate decomposition. Furthermore, a larger *Ste* in CASE 7 results in faster decomposition of the available hydrate. Both of these lead to high initial rate of hydrate decomposition, which leads to fast depletion of the

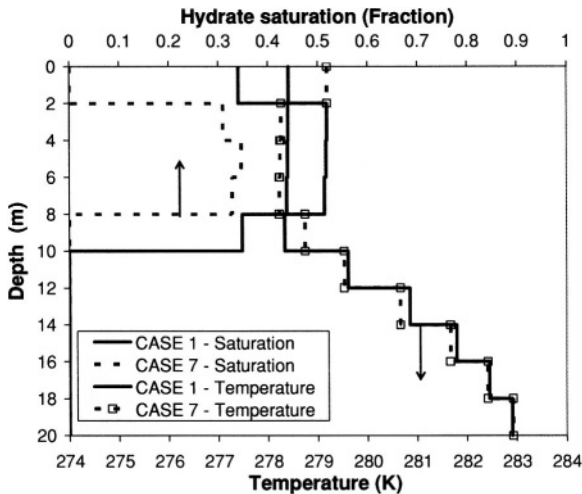


**Figure 11c.** Vertical temperature and hydrate saturation profiles at 300 days for CASE 1 and CASE 7—effect of porosity.

hydrate in CASE 7. Figure 11c shows that at 300 days, the hydrate in the top and bottom layers have been totally decomposed and therefore there is less hydrate available for decomposition leading to low generation rates at late times.

## 6. DISCUSSION

Hydrate decomposition by the depressurization technique is governed by three mechanism of heat transfer, fluid flow and kinetics of hydrate decomposition. In this study we conducted sensitivity studies to investigate effect of different heat transfer mechanism on hydrate decomposition. Changing heat flow however does not happen in isolation. For example when an increased rate of heat flow leads to a larger rate of hydrate decomposition, the additional generated gas changes the pressure field and thereby affects the fluid flow.

Although the trends observed in the case studies of this paper are believed to remain true for other cases, the relative importance of each component of heat flow is case-dependent. For example, it was observed that the heat flow from the base- and cap-rock provides a large component of the heat of hydrate decomposition. However, for a reservoir and hydrate zone much thicker than that studied here, one would expect that the importance of the heat from outside the reservoir as compared to the sensible heat inside the reservoir would be much smaller than that observed in this study.

## 7. CONCLUSIONS

1. For the cases studied, the depressurization method led to decomposition of a considerable portion of the hydrate (20–60%) during the 300 days of the study. This leads to significant increase of production life of a gas reservoir that has a hydrate cap.
2. Convective heat transfer was found to play a very small role, while heat flow by conduction was very important. For accurate estimation of gas generation, an accurate determination of thermal conductivity of hydrate-bearing formations is necessary.
3. A larger ratio of sensible heat to heat of decomposition (obtained at lower porosities) leads to faster rates of hydrate recovery.
4. The heat conducted from within the reservoir, as well as that conducted from the cap- and base-rock both had an important effect on the rate of hydrate decomposition.
5. Most of the decomposed hydrate was from the hydrate adjacent to the cap-rock and the free-gas zone, where rate of heat conduction is the most. The

hydrates in between were predominantly insulated by the hydrates at top and bottom. The main source of energy for decomposition of the hydrates in between is the sensible heat of the rock and fluids surrounding the hydrate particles there. Once, the hydrates at top and bottom fully decomposed, further decomposition occurred progressively inwards.

## ACKNOWLEDGEMENT

The authors are thankful to Drs. P. Raj Bishnoi and Tadahiro Okazawa for numerous discussions and to Dr. Scott Dallimore for his continuous support and encouragement. The financial support from Imperial Oil Resources, Alberta Energy Research Institute (AERI), Geological Survey of Canada (GSC) and the Natural Sciences and Engineering Research Council of Canada (NSERC) is gratefully acknowledged.

## NOMENCLATURE

$A_{HS}$	Specific area of hydrate particles, $m^{-1}$
$c_p$	Specific heat of the formation, i.e. rock, hydrate and fluids
$E$	Activation energy of decomposition, J/mol
$h_l$	Specific enthalpy of phase $l$ , J/kg
$\Delta H$	Heat of hydrate decomposition, J/kg hydrate
$k$	Absolute permeability, $m^2$
$k_c$	Thermal conductivity, W/m.K
$k_d^o$	Kinetic rate constant, $kmolCH_4/m^2kPa \cdot s$
$k_{rl}$	Relative permeability to phase $l$
$p_c$	Capillary pressure, kPa
$p_e$	Three-phase equilibrium pressure, kPa
$p_g$	Gas-phase pressure inside the reservoir, kPa
$p_i$	Initial pressure, kPa
$p_o$	Wellbore pressure, kPa
$\dot{q}_{ml}$	Mass production rate of phase $l$ per unit volume, $kg/m^3s$
$\dot{Q}_H$	Heat of hydrate decomposition, J/s
$\dot{Q}_{in}$	Direct heat input, J/s
$R$	Gas constant ( $= 8.314 \text{ J/mol.K}$ )
$Ste$	Stefan number, $Ste = \rho c_p (T_i - T_{oe}) / \rho_H \phi \Delta H$
$S_l$	Saturation of phase $l$
$S_{gi}$	Initial gas saturation



$S_{Hi}$	Initial hydrate saturation
$S_{wi}$	Initial water saturation
$t$	Time, s
$T$	Temperature, K
$T_i$	Initial reservoir temperature, K
$T_{oe}$	Equilibrium temperature of pressure $p_o$ , K
$T_s$	Hydrate surface temperature
$\vec{u}_l$	Velocity of phase $l$ , m/s
$U_l$	Specific internal energy of phase $l$ , J/kg
$\phi$	Porosity
$\rho$	Density of the formation, i.e. rock, hydrate and fluids.
$\rho_l$	Density of phase $l$ , kg/m <sup>3</sup>

### Subscript

$g$	Gas phase
$w$	Water phase
$H$	Hydrate
$R$	Rock
$i$	Initial condition
$s$	Hydrate surface
$e$	equilibrium condition

### REFERENCES

1. Holder, G. D., Malone, R. D., and Lawson, W. F.: "Effect of Gas Composition and Geothermal Properties on the Thickness and Depth of Natural-Gas-Hydrate Zone," *Journal of Petroleum Technology (JPT)* (September 1987) 1147–1152.
2. Kvenvolden, K. A. and Lorensen, T. D.: "The Global Occurrence of Natural Gas Hydrates," in *Natural Gas Hydrates—Occurrence, Distribution and Detection*, Geophysical Monograph 124, edited by Paul, C. K., Dillion, W. P. (2001)
3. Collett, T. S., Lewis, R. and Uchida, T.: "Growing Interest in Gas Hydrates," *Oilfield Review*, Summer 2000, 42–57.
4. Collett, T. S.: "Energy Resource Potential of Natural Gas Hydrates," *AAPG Bulletin*, Vol. 86, No. 11 (November 2002), 1971–1992.
5. Dallimore, S. R., Collett, T. S., Uchida, T., Weber, M., Takahashi, H.: "Overview of the 2002 Mallik Gas Hydrate Production Research Well Program," *Proceedings of the Fourth International Conference on Gas Hydrates*, Yokohama, May 19–23, 2002.
6. Hong H., Pooladi-Darvish, M., and Bishnoi, P. R.: "Analytical Modelling of Gas Production from Hydrates in Porous Media," *Journal of Canadian Petroleum Technology (JCPT)* (November 2003) Vol. 42, (11)p. 45–56.
7. Makogon, Y. F.: "Hydrates of Natural Gas," PennWell Publishing Company, Tulsa, Oklahoma (1981).
8. Kamath, V. A.: "A Perspective on Gas Production from Hydrates," paper presented at the JNOC's Methane Hydrate International Symposium, Chiba City, Japan, October 20–22, 1998.

9. Collett, T. S. and Kuskra, V. A.: "Hydrates Contain Vast Store of World Gas Resources," *Oil and Gas Journal* (May 11, 1998) **Vol. 96**, No. 19, 90–95.
10. Holder, G. D., Angert, P. F., John, V. T., and Yen, S.: "A Thermodynamic Evaluation of Thermal Recovery of Gas From Hydrates in the Earth," *Journal of Petroleum Technology (JPT)* (May 1982) 1127–1132.
11. Pooladi-Darvish, M.: "Gas Production from Hydrate Reservoirs and Its Modelling," paper SPE 86827 submitted to *Journal of Petroleum Technology (JPT)* (October 2003).
12. Holder, G. D. and Angert, P. F.: "Simulation of Gas Production from a Reservoir Containing Both Gas Hydrates and Free Natural Gas," SPE 11105 presented at the 1982 Annual Fall Technical Conference and Exhibition, New Orleans, September 26–29, 1982.
13. Makogon, Y. F.: "Hydrates of Hydrocarbons," PennWell Publishing Company, Tulsa, Oklahoma (1997).
14. Ji, C., Ahmadi, G., and Smith, D. H.: "Natural Gas Production from Hydrate Decomposition by Depressurization," *Chemical Engineering Science* (2001), **Vol. 56**, 5801–5814.
15. Verigin, N. N., Khabibullin, I. L., and Khalikov, G. A.: "Linear Problem of the Dissociation of the Hydrates of a Gas in a Porous Medium," *Izvest. Akad. Nauk. SSR, Mekhanika Gaza* (1980) No. 1, 174.
16. Yousif, M. H., Abass, H. H., Sloan, E. D.: "Experimental and theoretical investigation of methane-gas-hydrate dissociation in porous media," *SPE Reservoir Engineering*, (1991) **Vol. 6**, No. 1, 69–76.
17. Goel, N., Wiggins, M. and Shah, S.: "Analytical modeling of gas recovery from in situ hydrates dissociation," *Journal of Petroleum Science and Engineering*, (2001) **Vol. 29**, pp. 115–127.
18. Moridis, G. J.: "Numerical Studies of Gas Production From Methane Hydrates," SPE 75691, presented at the SPE Gas Technology Symposium, Calgary, Alberta, Canada, April 30–May 2, 2002.
19. Masuda, Y., Kurihara, M., Ohuchi, H., and Sato, T.: "A Field-Scale Simulation Study on Gas Productivity of Formations Containing Gas Hydrates," Proceedings of the 4th International Conference on Gas Hydrates, Yokohama, Japan, May 19–23, 2002.
20. Hong, H. and Pooladi-Darvish, M.: "A Numerical Study on Gas Production from Formations Containing Gas Hydrates," paper CIPC 2003–60 presented at the 2003 CIPC Conference, Calgary, AB, June 10–12.
21. Hong, H.: "Modeling of Gas Production from Hydrates," *M.Sc. Thesis*, University of Calgary, 2003.
22. Kim, H. C., Bishnoi, P. R., Heidemann, R. A. and Rizvi, S. S. H., "Kinetics of Methane Hydrate Decomposition," *Chemical Engineering Science* (1987) **Vol. 42**, No. 7, 1645–1653.
23. Vinsome, P. K. W. and Westerveld, J.: "A Simple Method for Predicting Cap and Base Rock Heat Losses in Thermal Reservoir Simulators," *Journal of Canadian Petroleum Technology*, (July/Sept., 1980) 87–90.
24. Butler, R. M.: "Thermal Recovery of Oil and Bitumen," GravDrain Inc., Calgary (1997) p. 492.
25. Wright, J. F., Nixon, F. M., Dallimore, S. R., and Cote, M. M.: "Thermal Conductivity of sediments within the gas-hydrate-bearing interval at Mallik 5L-38 Mackenzie Delta, Canada," in press.
26. Waite, W. F., deMartin, B. J., Kirby, S. H., Pinkston, J., and Ruppel, C. D.: "Thermal Conductivity Measurements in Porous Mixtures of Methane Hydrate and Quartz Sand," *Geophysical Research Letters*, 29 (24), 82 (2002) 1–4.

*This page intentionally left blank*

# 5

## **An Application Used For Correcting Thermal Gradients Below Permafrost Using An Empirical Diffusion Model Anadarko's Hot Ice #1 Gas Hydrates Case Study**

**K. E. Newsham,\* R. Sigal, and J. T. Kwan**

### **1. INTRODUCTION TO HOT ICE**

Anadarko Petroleum, Maurer Technology, and the U.S Department of Energy began a dedicated gas hydrates drilling operation in March of 2003 on the North Slope of Alaska. The cost of this project was partly supported by the DOE as part of their long term program to evaluate the resource potential of North Slope hydrate accumulations. Multiple purposes were served in the drilling of this well. These include the evaluation of the subsurface hydrate occurrence, demonstrate a new and environmentally safe drilling technology, and characterize potential hydrate reservoirs using in-situ measurements and continuous ice core studies provided on-site by use of Anadarko's Mobile Core Laboratory.

The Anadarko Hot Ice #1 is located 20 miles south of the Kuparuk River Oil Field. The surface location is defined as: latitude; 70 degrees, 6 minutes,

---

K. E. NEWSHAM • Anadarko Petroleum, 1201 Lake Robbins Drive, Houston, TX 77380

R. SIGAL • Anadarko Petroleum, 1201 Lake Robbins Drive, Houston, TX 77380

J. T. KWAN • University of Oklahoma, Norman, Oklahoma

\* [kent\\_newsham@anadarko.com](mailto:kent_newsham@anadarko.com)

31.39 seconds, longitude; 150 degrees, 12 minutes, and 43.23 seconds. The nearest offset wells are the Cirque 2, West Sak 20, and the Ruby State 1. The proposed total depth of the well is 2700 feet.

During the first stage of drilling, Hot Ice #1 was drilled to the base of permafrost and then cased. Due to warming temperatures, operations were suspended on April 21, 2003. The current depth of the well is 1403 feet. The base of permafrost was found at -1046 feet, TVDss, and a 7 inch casing was set in shale between the Ugnuand West Sak formations. They are scheduled to start up in the winter of 2004. No hydrate containing sediments were identified in the first drilling stage.

This shallow section of the Hot Ice #1 was logged and continuously cored. The wire-line logging program included measurements of natural gamma ray spectrometry, compensated neutron and density, array induction resistivity, dipole acoustic, and magnetic resonance. The dipole sonic data acquired included a mono-pole compressional slowness, cross-dipole shear slowness, and stoneley waves. The magnetic resonance was acquired from down-hole, wire-line operations and surface measurements of the core. The cores were acquired using a wire-line coring system that recovered continuous cores with a diameter of 3.3 inches. The chilled mud system was used to aid in the preservation and recovery of the cores. The fluid temperature was maintained at 23 °Fahrenheit (F). Cores were evaluated using Anadarko's on-site Mobile Core Laboratory. Both whole core and plug measurements were completed. Whole core measurements included gamma ray, white light photography, infra-red temperature, acoustic velocity, CT scans, and continuous magnetic resonance provided by Schlumberger. In addition, a complete geologic description was completed. Plug measurements included porosity, permeability, grain density, compression and shear velocities, gas spectrometry, thermal conductivity, resistivity, and magnetic resonance.

## 2. STUDY OBJECTIVES

A three well study was undertaken to understand the shallow hazards associated with the permafrost, gas hydrates, and gas hydrate plumes of the Hot Ice area. The three wells studied included the Cirque 2, West Sak 20, and the Ruby State 1. The results of this study were to be used as an aid in the pre-spud well planning of the Anadarko Hot Ice #1. The purpose of this study was to: (1) identify the base of the hydrate stability zone, BHSZ, using the Katz [3] and Collett [1,2] thermal model, so that the complete potential hydrate zone is cored, (2) aid in the design of the proper casing programs for use in the Hot Ice #1 so as to protect fresh water aquifers by defining the lower boundary of the permafrost, (3) understand the influence of formation salinity on the position of the base of permafrost, (4) assess the presence of any methane plumes within or below the hydrate stability

zone. This paper will focus on the use of a thermal diffusion model to correct local geothermal gradients and the model’s impact on better estimation of the base of the hydrate stability zone.

3. GAS HYDRATE STABILITY ZONE

The zone of hydrate stability is determined by subsurface temperature, pore pressure, the pore water salinity, the pore geometry of the sediment in which the hydrate forms, and the gas composition. The calculations used in this study make the same assumptions and follows the same general approach as Collett’s [1] 1988 regional study of the hydrate stability zone on the North Slope. Figure 1 shows a plot of Collett’s pressure-temperature hydrate stability model. The blue line represents Collett’s thermal model. The green line represents the geothermal gradient. The green square is the base of permafrost. The hydrate stability zone is the interior region defined by the intersection of Collett’s thermal model and the geothermal gradient and represented by the diagonal lines. The top of the hydrate stability zone often occurs at shallow depths within the permafrost region. The critical path in the analysis of the base of the hydrate stability zone is determining the position of the base of permafrost and the sub-permafrost geothermal gradient. We’ll examine the factors that influence the position of the base of permafrost and the geothermal gradient.

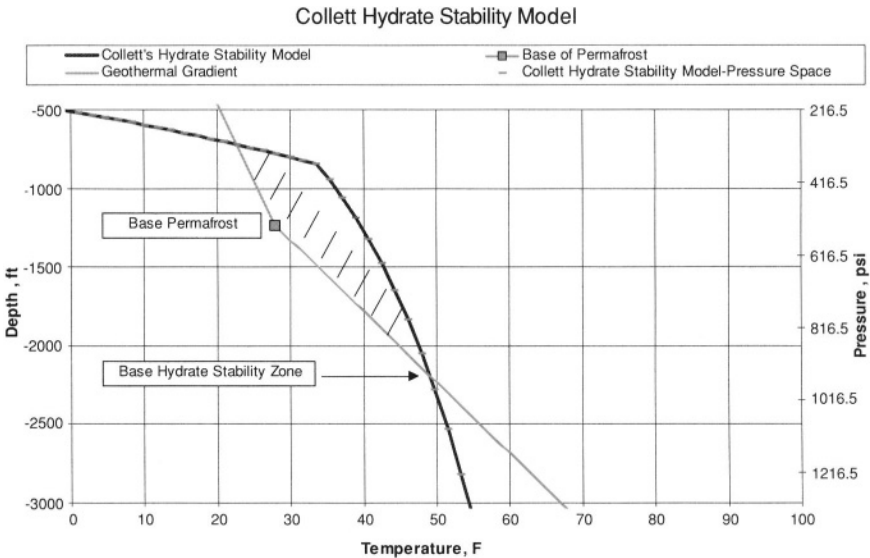


Figure 1. Plot of the Collett thermal model used for defining hydrate stability envelope.

### **3.1. Pore geometry influences on base of permafrost**

Based on the examination of resistivity and sonic logs within the permafrost, it appears that fine grained sediments freeze less readily than coarse grained sediments. Smaller pores tend to suppress the freezing point of water. A similar effect has been documented for hydrates. For the sediments that form good reservoirs this effect should be small. For the purposes of this study, pore geometry has been ignored in calculating the local BHSZ.

### **3.2. Salinity influences on base of permafrost, BOPF**

Salinity variations in the connate waters of the shallow permafrost sediment can alter the freezing point of water which will change the depth of the BOPF. An increase or decrease in the depth position of the BOPF will either expand or contract the hydrate stability zone, respectively. However, direct and indirect evidence shows that the pore water salinity in permafrost is much less than sea water. For example the regional temperatures at the base of ice bearing permafrost reported in Collett's [1], require salinities less than 30 parts per thousand (ppt). Based on the hydrate stability calculator in Slone [4] this salinity will only suppress the stability temperature by about one degree Centigrade.

### **3.3. Pressure influences on base of permafrost**

Pore pressure can be influenced by the salinity of the connate water in the permafrost and by compaction disequilibrium effects. Since the connate waters are considered nearly fresh water and compaction is stalled by the permafrost, there is no evidence for abnormally pressured compartments at the depths at which hydrates are expected to form. The pore pressure is considered to be hydrostatic.

### **3.4. Geothermal gradient influences**

The regional temperature gradient depends on the effective average surface temperature, the regional heat flux and the thermal conductivity of the sediments. The local gradient is also affected by topography and adjacent bodies of water. Because replacing water by ice in a rock raises its thermal conductivity, it is expected that the thermal gradients in the permafrost should be less than that in the sub-permafrost section. Hence, it is customary to use two thermal gradients, one above the BOPF, and one below. Maximum reading or bottom-hole thermometers that are used to determine the sub-permafrost geothermal gradient are influenced by the cooling and/or heating effects of the drilling mud system. Non-chilled drilling fluids will cause a heating in the shallow, near permafrost intervals and a cooling effect at depth. The thermal warming that occurs in the near permafrost area can shift the

interpretation of the hydrate stability zone by as much as 30 °F, creating a false indication that the hydrate stability zone is small to non-existent (see Figure 1). In this study, the local bottom-hole temperature (BHT) data recorded in the three adjacent wells was corrected using the thermal diffusion model documented by Lachenbruch [5], et al. The corrected gradients were used to imply the local subsurface temperature gradient in the Hot Ice #1.

#### **4. STUDY METHODS-DETERMINATION OF GEOTHERMAL GRADIENTS**

The geothermal gradient was determined as a two segment gradient divided at the BOPF. The regional permafrost thermal gradient was determined from the effective average surface temperature and the temperature at the base of ice bearing permafrost using the regional maps in Collett's<sup>2,6</sup>. The permafrost thermal gradient for the three wells in this study was determined by using the average surface temperature and the freezing temperature at the base of permafrost. The freezing temperature at the BOPF was estimated as a function of the shale salinity in the zone between the base of permafrost and the base of the hydrate stability zone (see section on salinity determination).

The sub-permafrost geothermal gradient is determined from a composite of the maximum reading temperatures reported on the log headers for each log run corrected to an undisturbed bottom-hole temperature equivalent. The bottom-hole temperature data was corrected using the diffusion model documented by Lachenbruch [5]. This part of the calculation contains the main deviation from the method employed by Collett [1]. Figure 2 is a graphical representation of Lachenbruch measured temperature diffusion between a temperature profile measured soon after circulation is stopped (red circles) and the undisturbed temperature profile projected to infinite dimensionless time after circulation was terminated. The incremental diffusion correction is represented by the blue diamonds and is mathematically expressed by the line-slope equation.

##### **4.1. Study Methods-Salinity-Based Estimate of Base of Permafrost Temperature**

Salinity was estimated for the three wells within this study using the "Apparent Formation Water Resistivity" method (Rwa) and picked from the shale in the interval between the BOPF and the base of the hydrate stability zone, BHSZ. Figure 3 shows the Rwa minimum value in the shales used to estimate the equivalent salinity. Once the salinity is determined, the freezing point temperature was estimated using algorithms documented by Fofonoff and Millard [7] and available on-line at: <http://gaea.es.flinders.edu.au/~mattom/Utilities/freeze.html>.



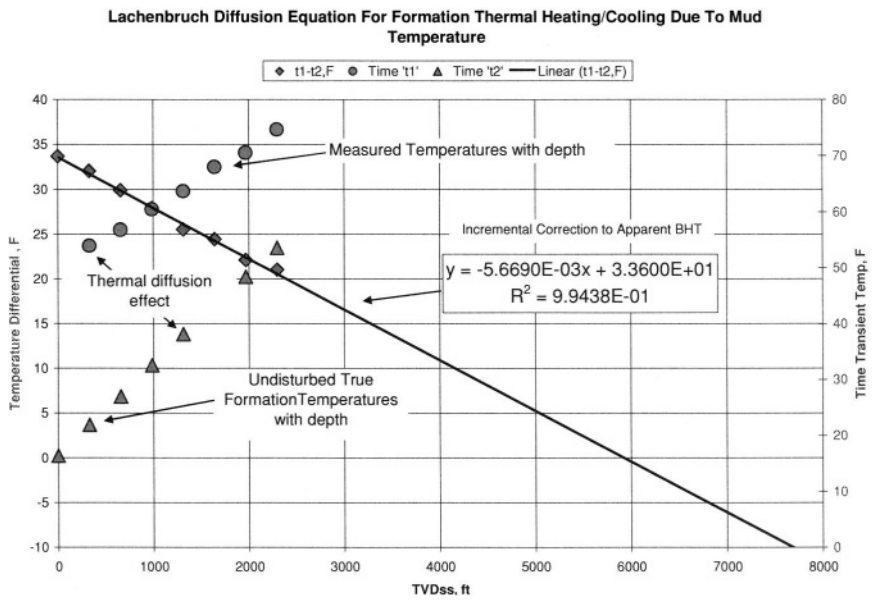


**Figure 2.** Plot of the Lachenbruch thermal diffusion model used for correcting bottom-hole temperature data.

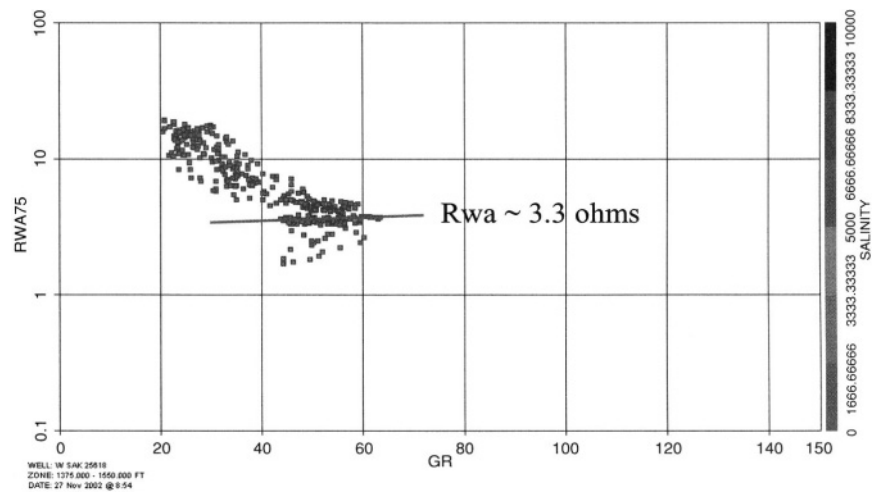


**Figure 3.** Rwa plot of West Sak 20; Base of Permafrost to Base of Hydrate Stability Zone.

**Table 1. Summary of published values for properties of ice and pure gas hydrates (modified from Davidson [9]).**

Property	Ice	Hydrate
Dielectric constant at 273 $\text{\AA K}$	94	=58
NMR rigid lattice 2nd moment of $\text{H}_2\text{O}$ protons ( $\text{G}^2$ )	32	$33\pm 2$
Water molecule reorientation time at 273 $\text{\AA K}$ ( $\mu\text{sec}$ )	21	=10
Diffusional jump time of water molecules at 273 $\text{\AA K}$ ( $\mu\text{sec}$ )	2.7	>200
Isothermal Young's modulus at 268 $\text{\AA K}$ ( $10^9$ Pa)	9.5	=8.4
Speed of longitudinal sound at 273 $\text{\AA K}$ _velocity (km/sec)	3.8	3.3
transit time ( $\mu\text{sec/ft}$ )	80	92
Velocity ratio $V_p/V_s$ at 272 $\text{\AA K}$	1.88	1.95
Poisson's ration	0.33	=0.33
Bulk modulus (272 $\text{\AA K}$ )	8.8	5.6
Shear modulus (272 $\text{\AA K}$ )	3.9	2.4
Bulk density ( $\text{gm/cm}^3$ )	0.916	0.912
Adiabatic bulk compressibility at 272 $\text{\AA K}$ $10^{-11}$ Pa	12	=14
Thermal conductivity at 272 $\text{\AA K}$ (W/m-K)	2.23	$0.49\pm 0.02$

#### 4.2. Study Methods-Base of Permafrost, BOPF

Wire-line well logs were used to examine the response to permafrost (ice and rock mixture). The gamma ray, resistivity, compression sonic, density, and neutron logs are used to pick the base of permafrost based on physical properties compiled by Prensky [8], and Davidson [9]. Table 1, was referenced for determining the appropriate log response to permafrost and gas hydrates. Ice bearing formations have less fluid porosity and tend to be in a more consolidated state than the comparable unfrozen sediments. This causes them to be more resistive and to have a higher sonic velocity. These effects are most pronounced in sandstones and less obvious in shale facies.

#### 4.3. Study Methods-Determining Top / Base Hydrate Stability Zone

The base of the hydrate stability zone, BHSZ, was estimated from the phase envelope described by Katz [3] and Collett [1,2]. A comparison of the gas hydrate model of pressure and temperature phase behavior is made to the local geothermal gradient of each well after correcting for the thermal diffusion effects Lachenbruch [5]. The conditions for hydrate formation are considered favorable when the geothermal gradient is less than the hydrate stability envelope. The depth (equivalent pressure) position of the top and base of the hydrate stability zone is determined where the geothermal gradient intersects the hydrate stability envelope. The depth of the permafrost and the geothermal gradient are the most important parameters controlling thickness of the hydrate stability zone.

Table 2. Freezing point estimates for salinities determined using the Rwa method.

	depth	tvdss	Pressure, psi	Pressure, Mpa	Freezing Point Calculator		
					Freezing Point of Water, C	Rwa@75F	Salinity, ppm
<b>Ruby State 1</b>	<b>KB=</b>	<b>386</b>					
top perma frost	0	386	14.7	0.101352928			
base perma frost	1480	−1094	473.702	3.26606018	−0.498	2.3	2256.882
base hydrate stability	2386	−2000	866	5.970859562			
run1 td	1868	−1482	641.706	4.424406935			
run2 td	3284	−2898	1254.834	8.651775505			
<b>Cirque 2</b>	<b>KB=</b>	<b>170</b>					
top perma frost	0	170	14.7	0.101352928			
base perma frost	1100	−930	402.39	2.776449696	−0.347	1.9	2759.992
base hydrate stability	1850	−1680	727.44	5.015522032			
run1 td	2254	−2084	902.372	6.221635664			
run2 td	7634	−7464	3231.912	22.28324789			
<b>West Sak 20</b>	<b>KB=</b>	<b>133</b>					
top perma frost	0	133	14.7	0.101352928			
base perma frost	1370	−1237	535.621	3.692976639	−0.565	3.3	1543.813
base hydrate stability	2333	−2200	952.6	6.567945518			
run1 td	2133	−2000	866	5.970859562			
run2 td	7133	−7000	3031	20.89800847			

5. DISCUSSION OF RESULTS

5.1. Salinity-Based Estimate of Base of Permafrost Temperature

Table 2 lists the results of the salinity estimates for the wells in this study. The salinity is found to range from 1543 to 2760 ppm. The salinity effect of lowering the freezing point of water is less than −0.6 °Centigrade (C).

5.2. Base of Permafrost, BOPF

The depth to bottom of permafrost was determined in the pre- drilling analysis from well-logs. The base of the permafrost was determined using the log responses from Table 1 and reported in Table 2. An example of one of the study wells is displayed in Figure 4. In this log display for the Ruby State 1, the base of permafrost is evident from the sharp resistivity and acoustic log response breaks at 1480 feet, measure depth (MD). Based on the correlation from these three wells, the expected

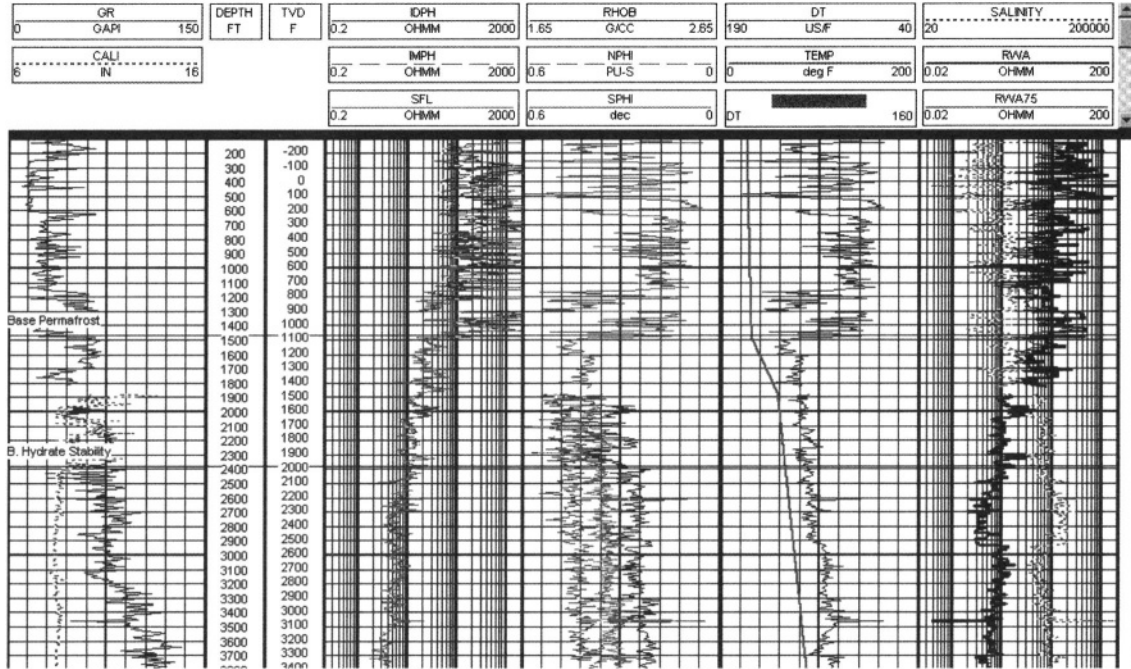


**Figure 4.** In the Ruby State 1, the resistivity (track 3) and the acoustic slowness (track 3) provide the best indication for the position of the base of permafrost found at 1480' MD.

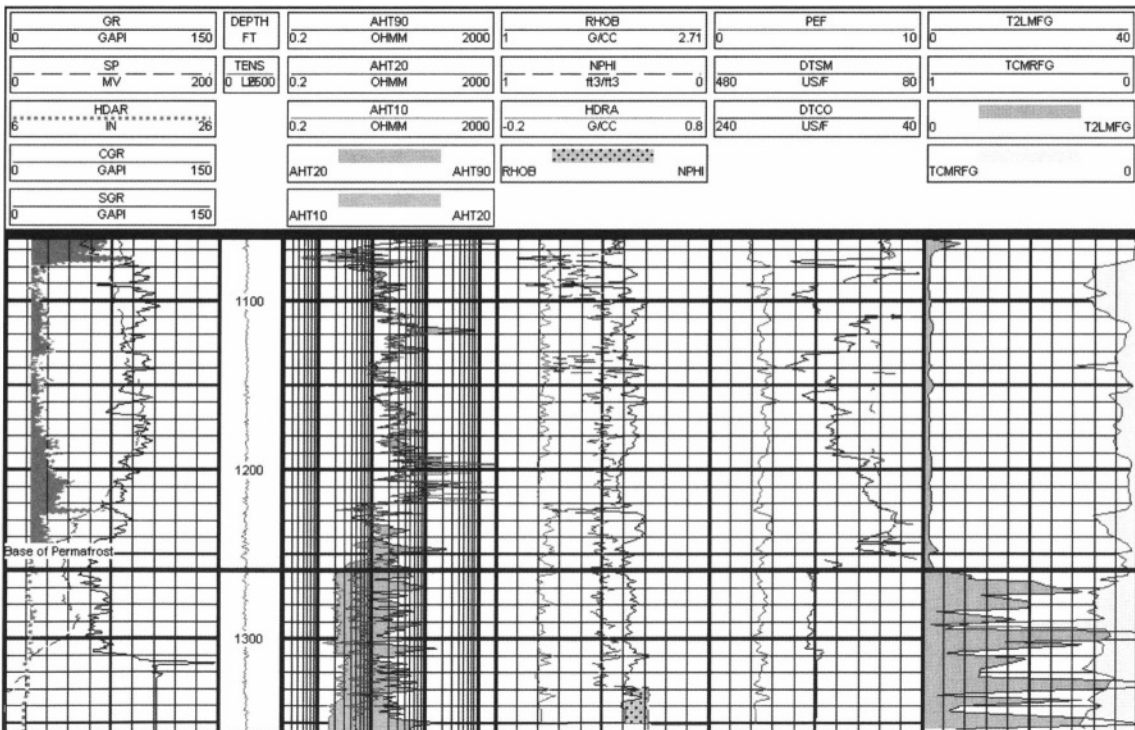


**Figure 5.** In the Hot Ice #1, the resistivity (track 3), the acoustic slowness (track 3) and the magnetic resonance log (track 5) provide the best indication for the position of the base of permafrost.

pre-spud base of permafrost at the Hot Ice #1 location was projected to be at – 1100 feet, TVDss and 1315 feet, MD.

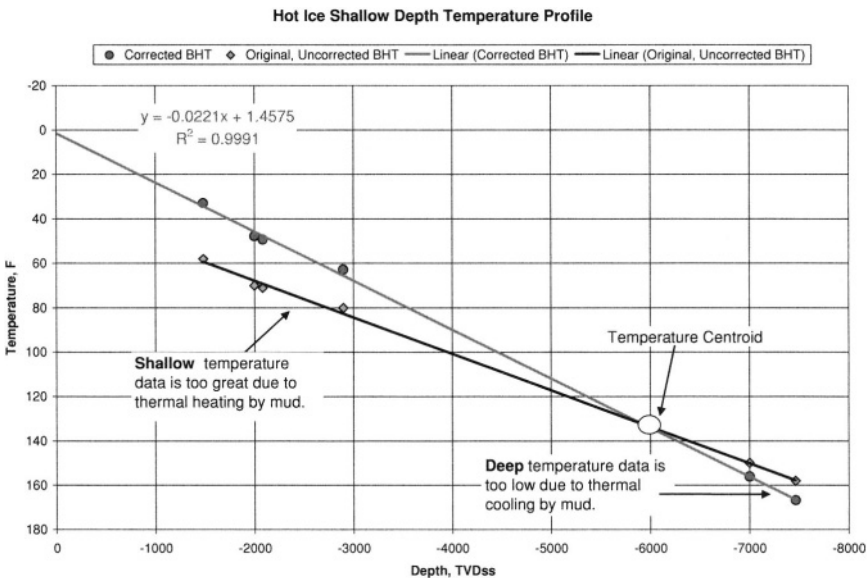
In the Hot Ice #1, both the core and log data show the well entering into unfrozen material at –1046 feet, TVDss. Both observations agree to within a few feet. The base of frozen material occurs in a thick sand interval at this depth and is considered the lowest known permafrost. Figure 5 is a log display for the Hot Ice #1. The resistivity (track 2), acoustic slowness (track 4), and magnetic resonance logs (CMR in track 5) provide the best indication for the BOPF. The CMR measurements were made directly on the cores at the surface.

The core-based estimate of BOPF is slightly subjective since the drilling was done with mud kept at –5 degrees C, and the core passed through decreasing temperature zones as it was brought to the surface so limited refreezing took place. The observation of the transition from “frozen” to “unfrozen” section was made both from visual examination, and from CMR measurements made on the whole core by Robert Kleinberg<sup>10</sup> using a Schlumberger CMR tool located in the well site core analysis lab. The core-based estimate of BOPF was done before the wire-line logs were run. In Hot Ice #1 the transition from frozen to unfrozen sediments occurred in good sand so both the log and core signature was clear.

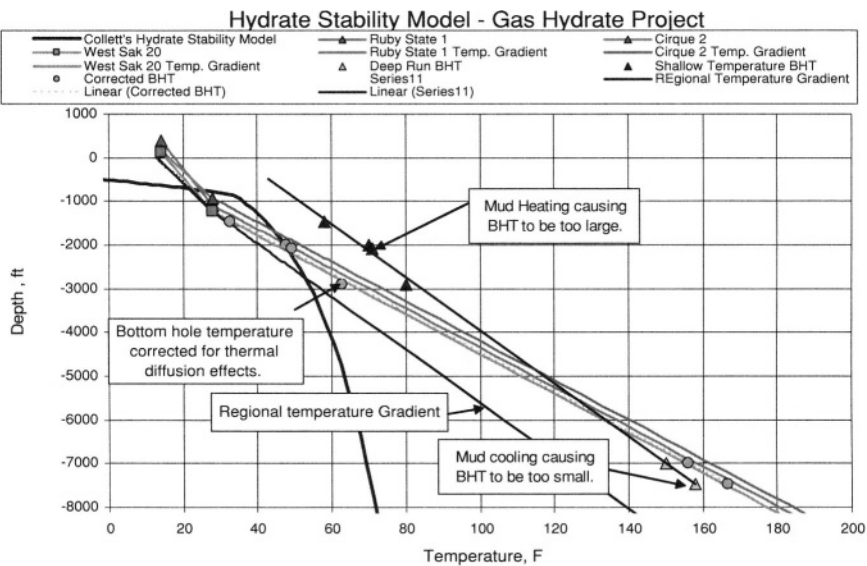
### 5.3. Geothermal Gradients

Figure 6 shows the original and corrected geothermal gradients derived from the composite BHT's of the three wells used in this study. Note that as the permafrost is approached (blue shading); the diffusion corrected temperatures are almost 30 °F lower than the uncorrected BHT's. The drilling fluids cause heating in the shallow intervals versus a cooling effect at depth. The depth at which the diffusion corrected gradient and the uncorrected gradient are equal is defined as the temperature centroid. The temperature centroid occurs at approximately –6000 feet for these data. In the Hot Ice Project, a chilled drilling and coring fluid was used to prevent melting of the permafrost or destabilizing hydrates when encountered. This had the additional benefit of minimizing any thermal warming effects that the mud system would have on the BHT data in this well.

The calculated gradient in the Hot Ice #1 is 1/3 larger than the regional gradient at the Hot Ice #1 location, (see Figure 7). Collett [1] based their thermal gradients primarily on 46 wells in which long term thermal monitoring has been carried out. At the well sites this data is certainly provides the best data on the thermal gradients. This data set though is sparse. To improve coverage Collett [1,2] used well logs in which they could identify the base of ice bearing permafrost, a regional average temperature at this depth, and the effective regional average surface temperature to compute a gradient in the frozen zone. The gradient below the frozen zone was calculated as the permafrost gradient times a regional value for the ratio of the temperature gradient in the unfrozen sediments divided by the gradient in the



**Figure 6.** Plot showing the results of applying the Lachenbruch thermal diffusion model to the BHT's from the three wells in the Hot Ice study.



**Figure 7.** The offset well geothermal gradients are shown after applying the Lachenbruch [5] thermal diffusion model. Note that the local well gradients are greater than the regional gradient estimated by Collett [1].

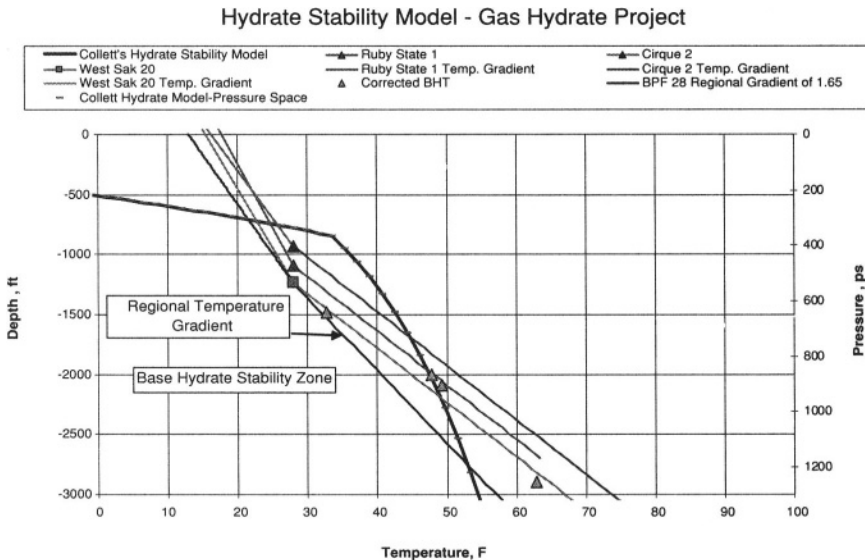


**Figure 8.** The offset well geothermal gradients are shown after applying the Lachenbruch thermal diffusion model. Note that the local well gradients are greater than the regional gradient estimated by Collett (1988).

unfrozen zone. This provides an enhanced grid. The final grid is still sparse and includes data points with more potential for error.

The local uncorrected geothermal gradient estimated from the three wells in the study is found to have the same gradient as Collett's regional gradient but is 30 °F greater at the BOPF position (see Figure 7). Using this uncorrected gradient would result in an interpretation that no gas hydrates would be present in the Hot Ice #1 location, as the temperature gradient is outside the hydrate stability window. However, by correcting the scalar temperature values for the effect of thermal diffusion, a gas hydrates envelope is evident (Figures 7 and 8).

#### 5.4. Determining Base Hydrate Stability Zone, BHSZ

The base of the hydrate stability zone (BHSZ) was estimated from the phase envelope described by Katz [3] and Collett [1,2]. The estimated BHSZ for the three wells used is summarized in Table 2 and ranges from -1680 to -2200 feet, TVDss. By correlation, the pre-spud BHSZ was estimated to be at -2000 feet TVDss, in the Hot Ice #1 location. This is significantly shallower than the BHSZ estimates if the regional geothermal gradient is used which would result in the BHSZ being as deep as -2572 feet, TVDss. The difference in the intersection of the sub-permafrost geothermal gradient and Collett's hydrate stability envelope



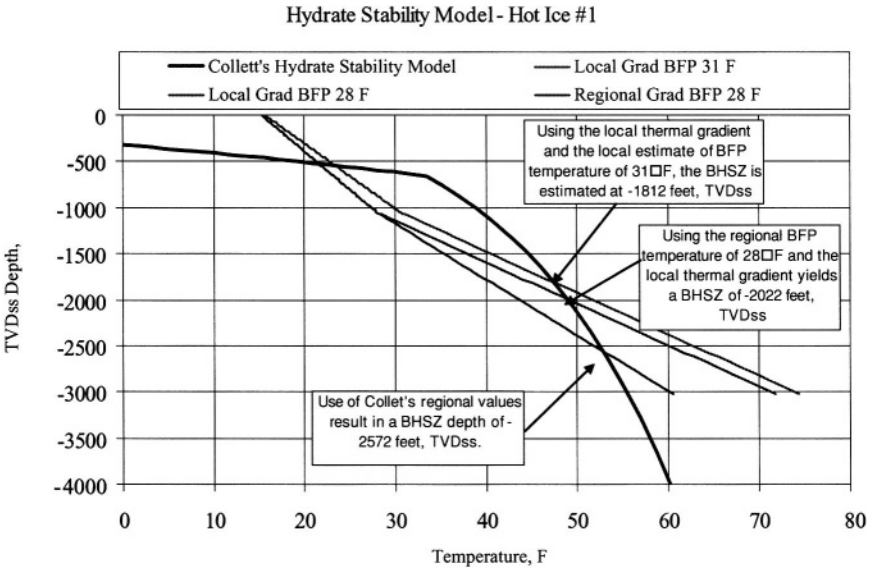


**Figure 9.** This plot shows the estimates of the base of the hydrate stability zone using various combinations of the temperature gradients and base of permafrost temperatures derived from either the regional or local correlations.

is the application of the Lachenbruch<sup>5</sup> thermal diffusion model to the local BHT temperature measurements.

Once the BFP was determined in the Hot Ice #1, the depth of BFP was used to estimate the depth to BHSZ, using the local thermal gradient. This requires the temperature at BFP. Based on salinity calculated in the three study wells this temperature should be 31 °F. The regional temperature map in Collett<sup>1</sup> gives a temperature of 28 °F at BFP. Figure 9 shows the calculations for both temperatures using the local thermal gradient, along with the depth using the regional values. Using the local thermal gradient and the local estimate of BFP temperature of 31 °F, the BHSZ is estimated at -1812 feet, TVDss. Using the regional BFP temperature of 28 °F and the local thermal gradient yields a BHSZ of -2022 feet, TVDss. Use of Collett's<sup>1</sup> regional values result in a BHSZ depth of -2572 feet, TVDss.

## 6. CONCLUSIONS

The BHSZ has been recalculated at the Hot Ice #1 location using data from local wells to estimate pore fluid salinity and thermal gradients in and below the permafrost. The salinity calculated using the Rwa method raises the local temperature

at the base of the frozen zone from that given on the regional maps. The bottom-hole temperature calculated from the measured bottom-hole temperature corrected for thermal diffusion gives a larger local thermal gradient than shown on the regional study. These results combine to estimate BHSZ 760 feet shallower than what would be predicted from the regional studies.

## ACKNOWLEDGMENTS

The authors would like to thank Anadarko Petroleum Corporation and the Department of Energy for providing the opportunity to work and publish this information on the Hot Ice #1. Robert Kleinberg, of Schlumberger, deserves recognition for his efforts in the acquisition and interpretation of the CMR log data on the Hot Ice #1 ice core.

## REFERENCES

1. Collett, T. S., Bird, K. J., Kvenvolden, K. A., and Magoon, L. B., Geologic Interrelations Relative To Gas Hydrates Within the North Slope of Alaska, *USGS Open-file Report* 88-389, 1988, 150 p.
2. Collett, T. S., Natural Gas Hydrates of the Prudhoe Bay and Kuparuk River Area, North Slope, Alaska, *AAPG Bull.*, v. 77, no. 5, 1993, p. 793-812.
3. Katz, D. L., Depths to Which Frozen Gas Fields (Gas Hydrates) May Be Expected, *Journal of Petroleum Technology*, v. 23, 1971, p. 419-423.
4. Slone, E. D. Jr., Clathrate Hydrates of Natural Gases, Marcel Dekker, Inc., New York, 1998, 705 pages.
5. Lachenbruch, A. H., Sass, J. H., Lawver, L. A., Brewer, M. C., Marshall, B. V., Munroe, R. J., Kennelly, J. P., Galanis, S. P., and Moses, T. H., Temperature and Depth Of Permafrost On The Arctic Slope Of Alaska, *USGS Professional Paper* 1399, 1982, pp. 645-657.
6. Collett, T. S., Bird, K. J., and Magoon, L. B., Subsurface Temperatures and Geothermal Gradients on the North Slope of Alaska, *Cold Regions Science and Technology*, 21, Elsevier Science Publishers B. V. Amsterdam, 1993, p. 275-293.
7. Fofonoff, P. and R. C. Millard Jr., Algorithms for computation of fundamental properties of seawater. *Unesco Technical Papers in Marine Science* 44, 1983, 53 pages.
8. Prensky, S. E., A review of gas hydrates and formation evaluation of hydrate-bearing reservoirs (paper GGG), *Presented at 1995 meeting of the Society of Professional Well Log Analysts, Paris, France*, 1995, June 26-29.
9. Davidson, D., Gas Hydrates as Clathrate Ices, in Cox, J., ed., *Natural gas hydrates—properties, occurrence and recovery*: Butterworth, Woburn, MA, 1983, p. 1-16.
10. Kleinberg, R. personal communication, 2003.

*This page intentionally left blank*

# Gas Production from Class 1 Hydrate Accumulations

George J. Moridis\* and Timothy S. Collett

## 1. INTRODUCTION

Gas hydrates are solid crystalline compounds in which gas molecules are encaged inside the lattices of ice crystals. Vast amounts of hydrocarbons are trapped in hydrate deposits [Sloan, 1998]. Such deposits occur in two distinctly different geologic settings where the necessary low temperatures and high pressures exist: in the permafrost and in deep ocean sediments.

Current estimates of the worldwide quantity of hydrocarbon gas hydrates vary widely, and a range between  $10^{15}$  to  $10^{18}$  m<sup>3</sup> has been reported [1]. Note that these estimates are not the result of a systematic attempt at resource evaluation specifically focused on hydrates, but are based on data obtained largely while targeting conventional hydrocarbon resources. Even by the most conservative estimates, the total quantity of gas in hydrates may surpass, by a factor of two, the energy content of the total fuel fossil reserves recoverable by conventional methods [1]. The magnitude of this resource commands attention because it could make hydrate reservoirs a substantial future energy resource. The potential importance of hydrates is further augmented by the environmental attractiveness of gas (as opposed to solid and liquid) fuels. Although the current energy economics cannot support gas production from hydrate accumulations, their potential clearly demands further evaluation.

The three main methods of hydrate dissociation for gas production are: (1) depressurization, in which the pressure is lowered to a level lower than the hydration

---

GEORGE J. MORIDIS • Lawrence Berkeley National Laboratory, Earth Sciences Division, 1 Cyclotron Rd., Berkeley, CA 94720, U.S.A.

TIMOTHY S. COLLETT • U.S. Geological Survey, Denver Federal Center, Box 2504 MS939, Denver, CO 80225, U.S.A.

\* [GJMoridis@lbl.gov](mailto:GJMoridis@lbl.gov)

pressure  $P_H$  at the prevailing temperature, (2) thermal stimulation, in which the temperature is raised above the hydration temperature  $T_H$  at the prevailing pressure, and (3) the use of inhibitors (such as salts and alcohols), which causes a shift in the  $P_H$ - $T_H$  equilibrium through competition with the hydrate for guest and host molecules [1].

The numerical studies of gas production in this paper were conducted using the EOSHYDR2 model [2], a member of the TOUGH2 [3] family of general-purpose simulator for multicomponent, multiphase fluid and heat flow and transport in the subsurface. EOSHYDR2 models the behavior of methane-bearing binary hydrates in porous media. It can describe the nonisothermal hydrate formation and/or dissociation (equilibrium or kinetic), gas release involving any combination of the possible dissociation mechanisms, phase behavior, and fluid and heat flow under conditions typical of natural hydrate deposits.

## 2. CLASSIFICATION OF NATURAL HYDRATE ACCUMULATIONS IN GEOLOGIC MEDIA

In terms of characteristics (which, in turn, have a strong impact on production strategies), hydrate accumulations can be divided into three main classes. Class 1 accumulations comprise two zones: the hydrate interval (often exhibiting a very low effective permeability because of large hydrate saturations in the pore space) and an underlying two-phase fluid zone with free (mobile) gas. In this class, the bottom of the hydrate stability zone (i.e., the location above which the formation of hydrates becomes possible) usually coincides with the bottom of the hydrate interval. In terms of gas production, this is the most desirable class for exploitation because of the thermodynamic proximity to the hydration equilibrium at the highest possible  $T_H$  (necessitating only small changes in pressure and temperature to induce dissociation).

Class 2 deposits feature two zones: a hydrate-bearing interval, overlying a mobile water zone with no free gas (e.g., an aquifer). Class 3 accumulations are composed of a single zone, the hydrate interval, and are characterized by the absence of an underlying zone of mobile fluids. In Classes 2 and 3, the entire hydrate interval may be well within the hydrate stability zone, and can exist under equilibrium or stable conditions. The desirability of Class 2 and 3 accumulations as gas production targets is less well defined than for Class 1 deposits, and can be a complex function of several issues, including thermodynamic proximity to hydration equilibrium, initial conditions, environmental concerns, and economic considerations [4,5].

Production from Class 2 and Class 3 hydrates has been discussed by [4] and [5]. In this paper, we focus on gas production from Class 1 hydrate deposits in permafrost formations for which field data are available. The results generally

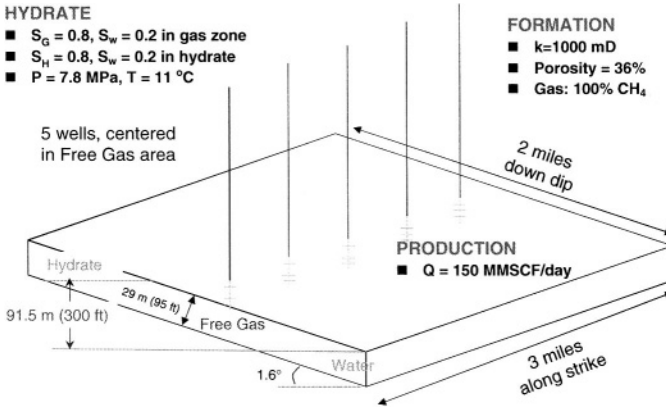


**Figure 1.** Gas production from the Class 1 hydrate accumulation in Case 1, North Slope, Alaska.

apply to ocean deposits, although boundary conditions can play a more important role in such accumulations.

### 3. CASE STUDIES OF GAS PRODUCTION FROM CLASS 1 HYDRATE ACCUMULATIONS

#### 3.1. Case 1: An Accumulation with Significant Potential

The schematic in Figure 1 shows gas production from a Class 1 hydrate accumulation in the North Slope of Alaska [6]. The initial conditions in the hydrate zone and in the underlying free gas zone, as well as all pertinent hydraulic and operational parameters, are listed in Figure 1. Gas is produced from five identical wells producing from the free gas zone at a cumulative rate of  $Q = 4.2475 \times 10^6$  standard  $\text{m}^3/\text{day}$  ( $1.5 \times 10^8 \text{ ft}^3/\text{day}$ ). This production scenario leads to depressurization-induced hydrate dissociation. The specifics of the numerical simulations involved in this study were discussed in detail in [7].

Figure 2 shows the cumulative volumes of hydrate-originating  $\text{CH}_4$  released during the depressurization-induced dissociation (both equilibrium and kinetic) and the cumulative gas volume produced from the system over the four-year duration of the study. A comparison of these curves provides a measure of the level of replacement of gas from the free-gas zone by  $\text{CH}_4$  released during dissociation. Note that the kinetic study had a decidedly conservative bend, assuming large pore spaces and, consequently, low hydrate particle area in the dissociation model of Kim et al. [8] used by EOSHYDR2. Thus, the kinetic solution in Figure 2 represents the worst-case scenario and provides an estimate for the lower

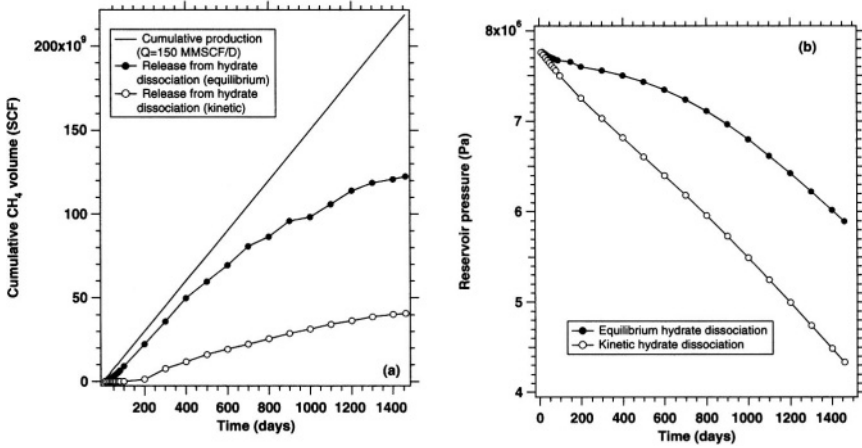


**Figure 2.** Cumulative release of  $\text{CH}_4$  from hydrate dissociation (a) and pressure evolution (b) during gas production from the Class 1 hydrate in Figure 1.

bound of the possible solutions, while the equilibrium solution provides the upper bound.

The results in Figure 2a indicate that, assuming an equilibrium process, dissociation can replace a large portion of the  $\text{CH}_4$  produced from the free-gas zone. This portion can be as high as 90%, and although it declines at later times, is well above the 50% level at the end of the study period. For the reasons explained above, the gas volume released through kinetic dissociation is substantially smaller. The corresponding effects on the pressure evolution in the free-gas zone are shown in Figure 2b. Under equilibrium dissociation, the pressure decline is much milder than that for kinetic dissociation, because the free gas zone is replenished by the large  $\text{CH}_4$  releases from the dissociating hydrate.

The results are elucidated in Figure 3, which shows the evolution over time of the rate of  $\text{CH}_4$  release. For equilibrium dissociation, the rate increases initially because the pressure drop in the free gas zone (caused by the gas production) increases with time, leading to larger pressure differentials and, consequently, to increased depressurization-induced dissociation and larger volumes of released gas. However, the rate begins to decline after a maximum is reached at about  $t = 220$  days. This occurs when the effect of increasing depressurization is overcome by the counteracting progressive cooling of the hydrate (due to the strongly endothermic nature of dissociation), which makes dissociation increasingly difficult. For kinetic dissociation in Figure 3(b), the  $\text{CH}_4$  release rate shows different magnitudes but a similar pattern, characterized by a rapidly increasing initial phase, a maximum, and a declining phase.

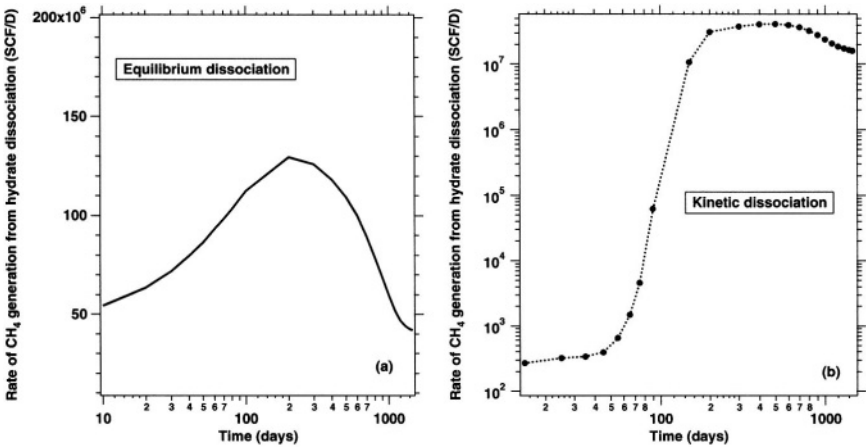


**Figure 3.** Release rate of CH<sub>4</sub> from the (a) equilibrium and (b) kinetic dissociation of the hydrate deposit in Figure 1.

The geologic system in Figure 1 is a particularly appealing specimen of a Class 1 hydrate deposit, characterized by the confluence of all possible conditions favorable to enhanced gas production from hydrate dissociation. This accumulation is endowed by a thick free-gas zone (91.5 m = 300 ft), a thick hydrate zone (about 183 m = 600 ft), a very large interface area of the hydrate with the free gas, and a large intrinsic permeability ( $10^{-12} \text{ m}^2 = 1 \text{ darcy}$ ). The bottom of the hydrate zone is at hydrate equilibrium and marks the lowest point at which hydrate occurrence is possible, i.e., the effect of the geothermal gradient exceeds that of the hydrostatic pressure. Thus, a very small perturbation of pressure or temperature is sufficient for gas dissociation to begin. The large intrinsic permeability  $k$  is indicative of low capillary pressures.

Coupled with the thick free gas-zone, it leads to low water saturations in the free gas zone and rapid drainage of the very large amounts of water released during dissociation. This combination of factors prevents the build-up of water saturation in the vicinity of the dissociating hydrate and alleviates the potential problem of impeded gas flows resulting from adverse relative permeability conditions. The tilted system allows concentration of the draining water near the lowest point of the formation, thus localizing water storage and limiting its adverse effects on flow.

The large  $k$  results in pressure declines that are mild and nearly uniform in the reservoir, resulting in dissociation from practically the entire interface. The mild pressure drops allow cooling to be slower and distributed over the whole interface, thus in turn allowing more effective heat transfer from the surroundings



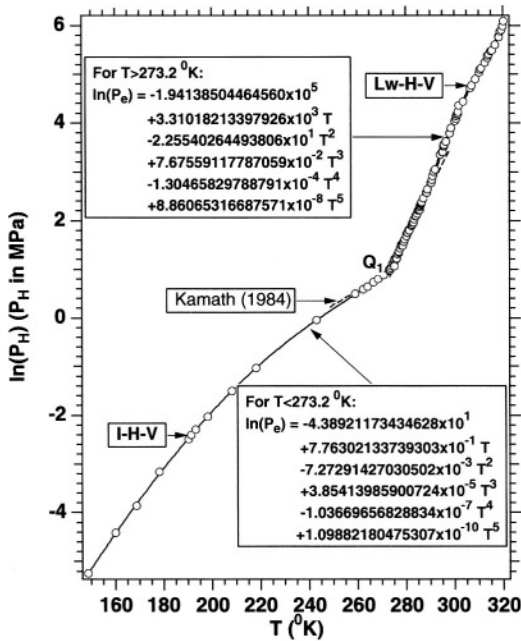
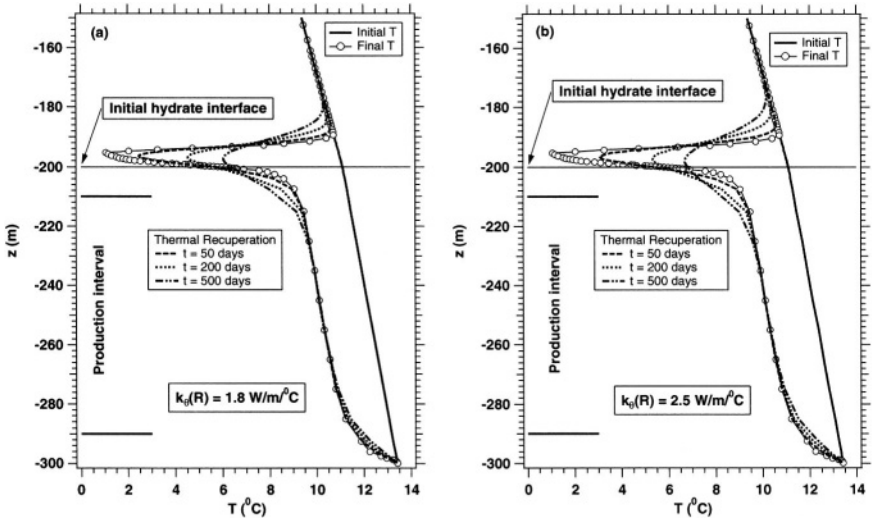


Figure 4. Pressure-temperature equilibrium of the simple methane hydrate [2].

and higher overall temperatures. Such mild processes are far better in allowing the slow process of heat conduction to supply the heat necessary for dissociation than steeper pressure gradients. Steeper pressure drops may lead to an initial burst of gas release, but this is localized and self-limiting because the resulting rapid cooling can overwhelm the slow mechanism of heat conduction (the only energy source under pure depressurization), leading to progressively slower dissociation. An additional advantage of the hydrate deposit in Figure 1 is that  $T_H$  at the interface is at the highest possible level, providing a relatively large heat reservoir to fuel the endothermic dissociation.

Because of its endothermic nature, the depressurization-induced hydrate dissociation leads to a temperature decline, which, in turn, progressively limits further dissociation by shifting the  $T_H$ - $P_H$  equilibrium (see Figure 4). If the pressure fueling dissociation is no higher than the  $P_H$  corresponding to the freezing point of water (as affected by the prevailing salinity), the hydrate saturation  $S_H$  is sufficiently high, and the hydrate temperature is low, then it is possible to experience freezing of the water and a severe reduction in gas production (because of the corresponding reduction in relative permeability). Ultimately, this leads to a complete cessation of dissociation. Thus, an important issue in this case of pure depressurization is



**Figure 5.** Temperature evolution during thermal recuperation along the axis of Well #3 after cessation of production (at  $t = 4$  years, denoted as “final”) in Case 1.

the ability of the hydrate system to thermally recuperate within a reasonable time frame.

The thermal recuperation period  $t_{\Theta R}$  is defined as the time needed for the geothermal gradient (i.e., the heat flux from deeper geologic strata) to restore the hydrate system to its original temperature profile after the cessation of production. The  $t_{\Theta R}$  is affected by the magnitude and rate of pressure decline, the hydrate temperature and saturation, and the thermal properties of the hydrate system. If  $t_{\Theta R}$  is short, then the appeal of pure depressurization is enhanced because the practically inexhaustible deeper geothermal reservoir can provide the necessary heat to sustain dissociation. In such a case, the production strategy would involve alternating cycles of gas production (based on pure depressurization) and thermal recuperation (TR).

Figures 5(a) and 5(b) show the evolution of temperature during the  $t_{\Theta R}$  of the hydrate accumulation of Case 1 (Figure 1) at the end of the four-year period of gas production from the depressurization-induced hydrate dissociation, and correspond to two different rock thermal conductivity values. Note that the EOSHYDR2 model [2] assumes thermal equilibrium and uniform thermal properties in each gridblock of the discretized domain, and employs the parallel model of Bejan et al. [10] to describe the thermal conductivity of the hydrate-bearing porous media. The temperature distribution at the end of gas production is marked by a significant decline in temperature in the vicinity of the dissociation front.

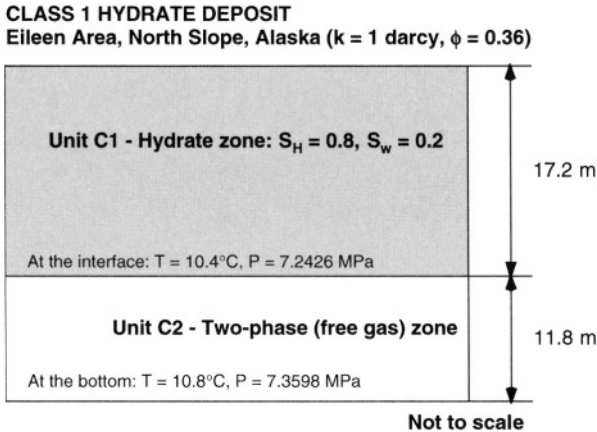


**Figure 6.** A schematic of the Class 1 hydrate accumulation in Case 2, Eileen Area, Alaska.

Figures 5(a) and 5(b) indicate that TR is a rather slow process, with the  $t_{\Theta R} > 500$  days (at which time the temperature distribution continues to exhibit large deviations from the target of the original profile). The significant increase in the rock thermal conductivity from Figures 5(a) to 5(b) does improve the speed of thermal recovery, but the effect appears to be sublinear and does not change the overall recuperation pattern. It is noteworthy that the temperature recuperation is not uniform throughout the profile, but is localized near the region of minimum temperature at the end of the production cycle. Thus, the earliest and largest temperature increases during the TR cycle occur in the area of maximum dissociation, while other parts of the formation (such as the free gas zone) show minimal temperature increases.

The obvious conclusion drawn from Figures 5(a) and 5(b) is that TR is unlikely to be part of a practical production strategy because the  $t_{\Theta R}$  exceeds realistic periods of commercial well shut-down. Consequently, long-term gas production from hydrates based on pure depressurization will have to involve higher operating pressures (i.e., lower depressurization levels and weaker dissociation-driving forces), corresponding to  $T_H$  above the freezing point of water and resulting in lower rates. Alternatively, it may be necessary to employ thermal stimulation in order to provide an alternate source of heat (to counter the adverse effects of dissociation-induced cooling) if large pressure differentials and/or large production rates are involved during depressurization.

### 3.2. Case 2: A Smaller-Scale System

Figure 6 depicts a Class 1 hydrate accumulation in the Eileen area of North Slope, Alaska, and corresponds to the geology and conditions in the Northwest Eileen

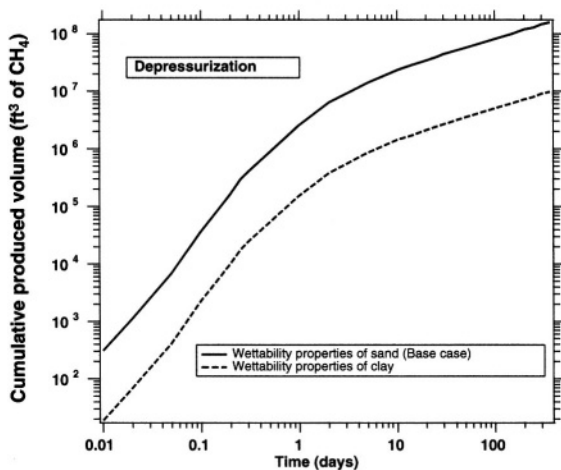


**Figure 7.** Depressurization-induced gas release from dissociating hydrates during production in Case 2.

State-2 well. The initial conditions at the bottoms of the C1 (hydrate zone) and C2 (free gas zone) units are listed on Figure 6. The deposit is confined by impermeable top and bottom boundaries, has no water-saturated zone, and has substantially thinner hydrate and free gas zones than the ones in Case 1. Because of its large areal extent at the site, the hydrate deposit behaves as an infinite system in this one-year study.

Two gas production scenarios are investigated. The first involves simple depressurization from a single well and was simulated using a cylindrical grid involving  $54 \times 47$  nonuniform gridblocks in  $(r, z)$ . The second involves a combination of depressurization and thermal stimulation in a multi-well (5-spot) system, in which the distance between the production and injection wells was 50 m. A cartesian 3-D grid involving  $25 \times 25 \times 47$  gridblocks in  $(x, y, z)$  was used in this case. In either scenario, the wells were completed in the top 1.85 m (5.5 ft) of the C2 unit, and equilibrium dissociation was assumed.

Figure 7 shows the cumulative volume of dissociation-induced gas release under pure depressurization when the single production well is maintained at atmospheric pressure (i.e., at the maximum possible pressure differential). Thus, the results correspond to the upper bound of gas release. Such a production scenario is markedly different from that in Case 1, as it is expected to yield the highest dissociation rates at the early stage of production. This is supported by the evolution of gas production in Figure 8(a), which indicates that significant volumes of gas can be produced from a single well. Additionally, Figure 8(a) demonstrates that gas is by far the dominant component in the production stream, while the production of water constitutes a minuscule portion of the total fluid production.

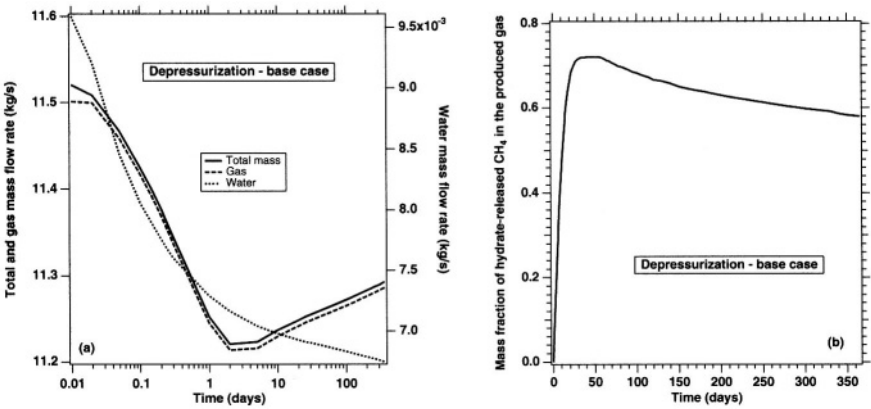


**Figure 8.** Phase mass flow rates (a) and gas mass fraction (b) at the producing well in Case 2.

This is particularly positive because it indicates that the significant amounts of water released during dissociation drain rapidly (aided by the large intrinsic  $k$ ) and do not inhibit gas flow to the well. The very large contribution of hydrates to production is demonstrated by Figure 8(b), which shows the mass fraction of gas from dissociation in the produced gas. Note, however, that the production rate and cumulative volume are significantly lower than those in Case 1, despite the similarity of the initial conditions, and of the hydraulic and thermal properties. This is attributed to the thinner hydrate and free gas zone, resulting in more rapid hydrate cooling over a larger area during dissociation.

Wettability issues (i.e., relative permeability  $k_r$  and capillary pressure  $P_c$ ) are expected to be far more important in deposits with relatively thin hydrate and free gas intervals (such as this one). This is because a lower phase  $k_r$  limits the reach of the dissociation front, while a higher  $P_c$  hinders the drainage of water from dissociation and inhibits gas flow. The wettability effects on gas release from hydrates are demonstrated in Figure 7, which shows that a change in the wettability properties from that of sand to that of clay reduces the released gas volume by over an order a magnitude (although the intrinsic permeability remains the same). Note that the preferred wettability properties in EOSHYDR2 [2] are computed based on the model of Parker et al. [9] that uses common parameters to describe both  $k_r$  and  $P_c$ .

When depressurization is coupled with thermal stimulation, the effect on gas release is multiplicative, as indicated in Figure 9. When a 5-spot well configuration is used (with the production wells kept at atmospheric pressure, while superheated steam at a rate  $Q = 1.85$  kg/s and an enthalpy  $H = 3.2 \times 10^6$  J/Kg is injected into the injection wells), gas release from hydrates increases by a factor of almost

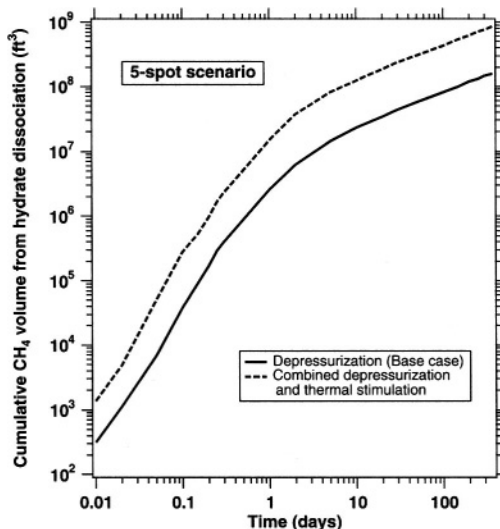


**Figure 9.** Gas release from hydrates in Case 2 using a combination of depressurization and thermal stimulation, and employing a 5-spot injection/production well configuration.

5 in the 1-year duration of the study. This is possible because the buoyancy of the injected steam and the flow field (dictated by the pressure distribution in the C2 unit and in the dissociated part of the C1 unit) enhance steam contact with the dissociating hydrate interface, raising the temperature and readily supplying the heat needed for dissociation.

### 3.3. Case 3: Production from Challenging Class 1 Hydrate Deposits

This case addresses the low end of the spectrum of Class 1 hydrate deposits, which involve thin gas zones underlain by infinite-acting aquifers. A representative specimen is the hydrate accumulation at Mallik, Mackenzie River Delta, Northwest Territories, Canada [11], which is bounded by impermeable top and bottom strata, and involves a 20 m thick hydrate zone, a 1.5 m thick free gas zone and a 20 m thick water-saturated zone [11]. Because gas production from this type of Class 1 accumulation was extensively investigated [4], the subject will not be discussed in detail here—only a short review will be offered instead.

Unlike the Class 1 hydrates discussed in Cases 1 and 2, such deposits do not appear to be appealing candidates for depressurization-based commercial gas production because of serious water upconing problems. These lead to rapid deterioration in the gas-to-water ratio in the production stream (Figure 10a) and/or low production rates (in order to delay its onset). Note the very low production rate

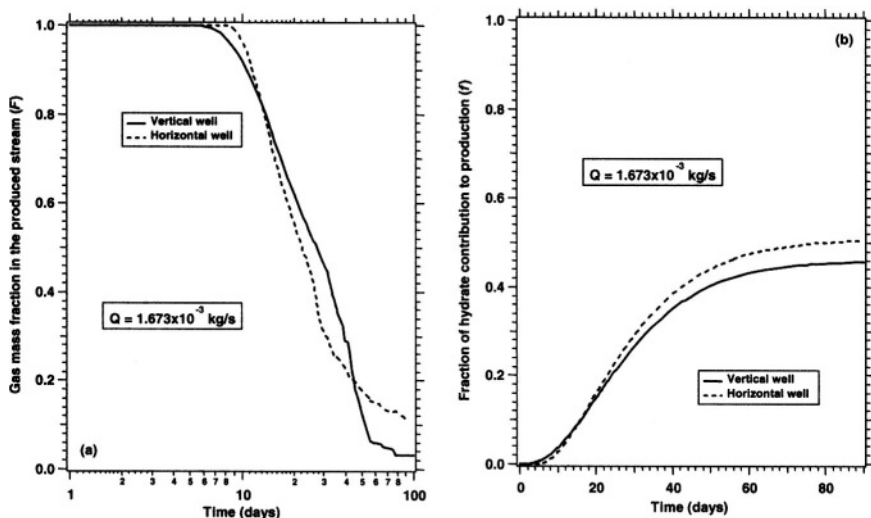


**Figure 10.** Gas mass fraction (a) and contribution of hydrate to gas production (b) at the single producing well (vertical or horizontal) in Case 3 [4].

$Q$  in Figure 10—necessary to sustain gas production for just a few days—and the significant mass fraction of gas from hydrates in the produced gas (Figure 10b). Note that  $Q = 1.673 \times 10^{-3} \text{ kg/s}$  is the mass flow rate of total fluid withdrawal (i.e., gas and water), and corresponds to the rather minuscule volumetric flow rate of 225 standard  $\text{m}^3/\text{day}$  (about 8000 SCF/day) when only gas is produced. The upcoming problem can be reduced by using horizontal wells (Figure 10), and further alleviated if multi-well injection-production systems combining depressurization and steam-based thermal stimulation are employed [4]. Injection of a hot gas can further improve the production potential of such a deposit because it enhances the gas relative permeability while delivering heat (through buoyancy and pressure distribution) to the hydrate interface, i.e., the dissociation target [4]. While this is technically feasible, there are significant technical, safety, and economic challenges that severely limit the potential of such an approach. Moreover, even if these obstacles could be surmounted, the water upconing problem is never eliminated, and stabilization (in the case of steam or hot gas injection) of the gas-to-water ratio may be the best possible outcome [4].

If sufficiently large pressure differentials are applied, or if depressurization continues for a long time, the pressure decline can result in practically complete water saturation over a significant radius from the well, transforming the accumulation from a Class 1 to a Class 2 hydrate deposit. Strategies for gas recovery from different types of this class of hydrates have been discussed in [4] and Moridis [5].

## 4. SUMMARY AND CONCLUSIONS

This paper focuses on the study of gas production from Class 1 hydrate accumulations, i.e., deposits characterized by a hydrate zone underlain by a zone of mobile (free) gas. Three cases that cover the range of Class 1 hydrate deposits are analyzed, and the sensitivity of gas production to several important parameters is investigated.

Simple depressurization appears to be a promising production strategy in a Class 1 deposit located in the North Slope, Alaska. This deposit (Case 1) occurs in a sloping formation, with a thick free-gas zone overlain by a thick hydrate zone and underlain by an aquifer. Under these conditions, depressurization-induced dissociation of the hydrates (when assumed to be an equilibrium process) is capable of re-plenishing over 90% of the very substantial gas withdrawal rate of  $Q = 4.2475 \times 10^6$  standard  $\text{m}^3/\text{day}$  ( $1.5 \times 10^8 \text{ ft}^3/\text{day}$ ) from five wells. Although it is not currently known whether dissociation is an equilibrium or a kinetic process, this study determined the bounds of the possible solutions. The high rates of dissociation and the corresponding large gas volumes originating from the hydrates are made possible by the high intrinsic permeability, the large phase-relative permeabilities, the low capillary pressures and the thick free-gas zone of the hydrate-bearing formation, which allow rapid drainage and unimpeded gas flow to the producing well. This is further enhanced by a high porosity and initial hydrate saturation, as well as by the system geometry, which allows collection of the draining water at the bottom of the sloping formation.

Under pure depressurization, the low operating pressures (needed to maximize production rates) at the production wells result in hydrate cooling, leading to a progressively lower gas-release rate because of the endothermic nature of the dissociation reaction. Sufficiently low pressures and/or high production rates can even lead to water freezing and a drastic decline in gas production. Maintaining the well pressure at a level no lower than the hydration pressure corresponding to the freezing point of water can eliminate such a problem, but may be impractical because this relatively high pressure can greatly limit production. As a potential component of a production strategy, thermal recuperation, defined as the restoration of the deposit temperature to its initial level (i.e., the one prior to production) through geothermal heat fluxes from deeper formations, appears to be impractically slow and ineffective.

Depressurization-induced dissociation in the Class 1 hydrate deposit of Case 2 (also located in the North Slope, Alaska)—with relatively thin hydrate and free gas zones, and having similar properties and initial conditions—appears to produce more modest gas volumes. By coupling depressurization with thermal stimulation in a multi-well injection/production system, the combined effect is multiplicative and leads to substantial increases in gas production because of the constant supply of heat can sustain dissociation. It is noteworthy that, in Case 2,



wettability issues can have a dramatic effect on gas production because of the thinner free gas zone. Additionally, a very large mass fraction of the produced gas originates from hydrate dissociation, while the mass fraction of water in the production stream is encouragingly low.

Gas production from the Class 1 hydrate deposits with very thin gas zones underlain by aquifers (Case 3) does not appear promising with standard dissociation approaches. This is because of the low rates necessitated to limit the water mass fraction in the production stream. Under these conditions, horizontal wells appear to have a slight advantage over single vertical wells. Multi-well injection/production systems employing a combination of depressurization and thermal stimulation appear to be more promising (although still insufficiently productive), and their potential increases when using a non-condensable gas as the heating agent (an issue that may present challenges).

These observations should only be viewed as general principles and observations—because the significant variability and case sensitivity, the lack of field data, and the insufficient body of prior experience and literature on gas production from hydrates [2,5] do not allow the confidence of definitive conclusions. Thus, caution should be exercised in interpreting these results.

## ACKNOWLEDGMENTS

This work was supported by the Assistant Secretary for Fossil Energy, Office of Natural Gas and Petroleum Technology, through the National Energy Technology Laboratory, under the U.S. Department of Energy, Contract No. DE-AC03-76SF00098. Thanks are extended to Scott Digert and Robert Hunter for providing important data for the Class 1 hydrate deposit discussed in Case 1 of the paper. The authors are indebted to Timothy Kneafsey and John Apps of LBNL for their insightful review comments.

## REFERENCES

1. Sloan, E. D., *Clathrate Hydrates of Natural Gases*, Marcel Dekker, Inc.: New York, NY, 1998.
2. Moridis, G. J., Numerical Studies of Gas Production from Methane Hydrates; Society of Petroleum Engineers, SPE 75691, 2002 (in press, *SPE Journal*, 2004).
3. Pruess, K.; Oldenburg, C.; and Moridis, G., *TOUGH2 User's Guide, Version 2.0, Report LBNL-43134*, Lawrence Berkeley National Laboratory: Berkeley, CA, 1999.
4. Moridis, G. J.; Collett, T. S.; Dallimore, S. R.; Satoh, T.; Hancock, S.; and Weatherhill, B., *Numerical Studies of Gas Production Scenarios From Several CH<sub>4</sub>-Hydrate Accumulations at the Mallik Site, Mackenzie Delta, Canada*, Report LBNL-50257, Lawrence Berkeley National Laboratory: Berkeley, CA, 2002 (in press, *J. Petrol. Sci. Eng.*, 2004).

5. Moridis, G. J., Numerical Simulation Studies of Thermally-Induced Gas Production From Hydrate Accumulations With No Free Gas Zones at the Mallik Site, Mackenzie Delta, Canada; Society of Petroleum Engineers, SPE 77861, 2002 (in press, *SPE Res. Eval. Eng.*, 2004).
6. Hunter, R.; and Digert, S. A., Personal communication, 2002.
7. Moridis, G. J.; and Collett, T. S., *Strategies for Gas Production from Hydrate Accumulations Under Various Geological and Reservoir Conditions, Report LBNL-52568*, Lawrence Berkeley National Laboratory: Berkeley, CA, 2002.
8. Kim, H. C.; Bishnoi, P. R.; Heideman, R. A.; and Rizvi, S. S. H, *Chem. Eng. Sci.*, **1987**, 42, 1645–1653.
9. Parker, J. C.; Lenhard, R. J.; and Kuppusamy, T., *Water Resour. Res.*, **1987**, 23(4), 618–624.
10. Bejan, A., *Convection Heat Transport*, John Wiley & Sons: New York, NY, 1984.
11. *Scientific Results from JAPEX/JNOC/GSC Mallik 2L-38 Gas Hydrate Research Well, Mackenzie Delta, Northwest Territories, Canada*; Dallimore, S. R.; Uchida, T.; and T. S. Collett, Eds., Geological Survey of Canada Bulletin 544, 1999.

*This page intentionally left blank*

Section II

Detection of Hydrates

*This page intentionally left blank*

# A Project Update of Methane Hydrate Production from Alaskan Permafrost

**Keith Millheim, Jonathan Kwan,\* Williams Maurer, William MacDonald, Tom Williams, Ali Kadaster, Tommy Thompson, Richard Sigal, David Copeland, Donn McGuire, Steve Runyon, Bill Liddell, Carl Sondergeld, and Chandra Rai**

---

KEITH MILLHEIM • Anadarko Petroleum Corporation 1201 Lake Robbins Dr., The Woodlands, TX 77380

JONATHAN KWAN • Anadarko Petroleum Corporation 1201 Lake Robbins Dr., The Woodlands, TX 77380 • University of Oklahoma 100 E. Boyd St., SEC T-301, Norman, OK 73019

WILLIAMS MAURER • Noble Engineering & Development 13135 S. Dairy Ashford, Suite 800, Sugar Land, TX 77478

WILLIAM MACDONALD • Noble Engineering & Development 13135 S. Dairy Ashford, Suite 800, Sugar Land, TX 77478

TOM WILLIAMS • Noble Engineering & Development 13135 S. Dairy Ashford, Suite 800, Sugar Land, TX 77478

ALI KADASTER • Anadarko Petroleum Corporation 1201 Lake Robbins Dr., The Woodlands, TX 77380

TOMMY THOMPSON • Anadarko Petroleum Corporation 1201 Lake Robbins Dr., The Woodlands, TX 77380

RICHARD SIGAL • Anadarko Petroleum Corporation 1201 Lake Robbins Dr., The Woodlands, TX 77380

DAVID COPELAND • Anadarko Petroleum Corporation 1201 Lake Robbins Dr., The Woodlands, TX 77380

DONN MCGUIRE • Anadarko Petroleum Corporation 1201 Lake Robbins Dr., The Woodlands, TX 77380

STEVE RUNYON • Anadarko Petroleum Corporation 1201 Lake Robbins Dr., The Woodlands, TX 77380

BILL LIDDELL • Anadarko Petroleum Corporation 1201 Lake Robbins Dr., The Woodlands, TX 77380

CARL SONDERGELD • University of Oklahoma 100 E. Boyd St., SEC T-301, Norman, OK 73019

CHANDRA RAI • University of Oklahoma 100 E. Boyd St., SEC T-301, Norman, OK 73019

\* Correspondent [jtkwan@ou.edu](mailto:jtkwan@ou.edu).

## 1. INTRODUCTION

For years natural gas hydrates have portended potential multi-trillion cubic feet of primarily methane reserves both onshore and offshore. Recently, two major events have ignited serious hydrate interest: (1) The perceived ensuing shortage of accessible cost effective energy for North America and other countries like Japan, and (2) The stimulus by the National Energy Technology Laboratory/US Department of Energy (NETL/DOE) hydrate program to fast forward hydrate technology.

Gas hydrates occur naturally in permafrost and deep marine environments around the globe. It is estimated that methane in gas hydrates worldwide is more than  $10^{13}$  tons of methane-carbon<sup>1</sup>. This quantity is equivalent to  $\sim 2 \times 10^{16}$  cubic meters of methane gas, or about twice as much as all other fossil fuels taken together, and about 370 times as much as all of the natural gas ever likely to be produced from conventional sources in North America<sup>2</sup>. Potentially, this resource could be the backbone for the world's energy sector during the 21<sup>st</sup> century.

In respond to a DOE/NETL Request-For-Proposal on Hydrates Research Program in early 2001, Anadarko Petroleum Corporation, Maurer Technology Inc. and Noble Engineering & Development jointly submitted a proposal to drill, core, and produce a hydrate well in Alaska. The three-year project consists of two phases with these major objectives: 1) evaluate existing best technology to drill, complete and produce gas hydrates; 2) plan, drill, and core a gas-hydrate well in Northern Alaska; 3) characterize the resource through geophysics, logging, engineering and core and fluids analysis; 4) test and monitor gas production from the hydrate well; 5) quantify models/simulators with actual field data; 6) learn how to identify favorable stratigraphic intervals that enhance methane production; 7) assess the commercial viability of developing this resource and develop a long-term production plan; 8) provide real hydrate core samples for laboratory testing; 9) develop and test physical and chemical methods to stabilize hydrate wellbores and improve core recovery; 10) step outside of the well-known Prudhow Bay/Kuparuk River area to further delineate hydrate deposits in Alaska; and 11) report the results to the DOE and transfer technology to the Industry.

From the technical aspects, the project has several unique accomplishments.

- Drilling was from an Arctic Platform that erected 12 feet above the Alaska Foothills tundra.
- A fully automated mobile laboratory incorporating state-of-the-art core and hydrate analysis instruments was deployed to test recovered core.
- A real-time drilling monitoring system with satellite linkage provided real time data and video to a web site accessible to all participants.

- A truly corporative research program that gathered the best technical professionals from the government (USGS, LBNL, PNNL, etc.) and the industry (Schlumberger, Noble Engineering, Drill Cool, etc.)

This cost-sharing contract was formally awarded in September 2002 along with two other US hydrate projects. Phase I of the project was immediately carried and the project plan was presented to the DOE officials in December 2002. However, due to the time constrain, Anadarko commissioned the design and construction of the Arctic platform and mobile laboratory in early 2002. The drill site was constrained to be within the 100% Anadarko owned acreage. A drill site was chosen based on proprietary data and the best available public domain geological and geophysical information. Permits were expedited and environmental reports were filed. Drilling/Coring rig and equipments were selected. By late March 2003, the platform was erected on the HOT ICE #1 well site and the mobile laboratory was on location. The hydrate well was spudded on March 31, 2003. Due to unexpected weather condition, the coring operation was suspended on April 20 with the 7" casing cemented at 1400' just below the permafrost. The coring operation will resume in January 2004.

## 2. BACKGROUND

Several major factors have so far prevented the commercialization of gas hydrates to produce clean burning, environmentally friendly fuel. These factors include:

- Remoteness of the hydrate resources from major natural gas markets. Hydrates are either located in deep water or in Arctic areas.
- Insufficient knowledge about the in-situ properties of gas hydrate containing sediments;
- Absence of economical and proven technology for the production of natural gas from gas hydrates;

### 2.1. Remoteness of the resource

Gas hydrates have been observed in at least 90 locations in marine environments globally and in many cases in permafrost conditions onshore, these sites are often situated far from the major natural gas markets. For example, it would take a 5,000 km pipeline to bring gas from Alaska to the continental United States, and even if gas hydrates were to be successfully developed, the cost of transportation may be prohibitive. However, the situation changed when the tightening of the N. America gas market got tight and the active consideration of several plans for gas



pipelines from Alaska and Canada to the United States. The known gas resource on the North Slope, 35 trillion cubic feet (Tcf) is the energy equivalent to six billion barrels of oil, half the oil reserves in Prudhoe Bay. Up to 100 Tcf of gas could eventually be developed on the slope. This does not include the potential hydrate deposit under the permafrost and offshore Beaufort Sea. Due to its shallow depositional environment this resource could be the first to become economic.

To evaluate the costs and benefits of bringing natural gas from gas hydrates to markets, a better understanding of their geographical distribution is needed, and knowledge of hydrate physical properties and the technologies for their production have to be developed and tested. Significant laboratory knowledge in pure gas hydrates is available, but properties of hydrates in sediments and in situ is lacking.

## **2.2. Insufficient knowledge**

While synthetic gas hydrates have been studied, there are few hydrate samples) from natural deposits that have been studied. In 1998, the completion of a 1150 meters hydrate test well Mallik 2L-38 in the MacKenzie Delta, NWT, Canada provided significant improvement in the knowledge base of naturally occurring hydrates<sup>3</sup>. The scientific project focused on geophysical measurements with limited hydrate coring. Approximately 37 meters of hydrate cores were recovered. Subsequently, the second Mallik well was commissioned in 2000 with successful core recovery. The scientific results will be reported in Tokyo December of 2003. Limited knowledge about gas hydrates properties in natural environments is a serious handicap for the development of technologies to produce methane from gas hydrates.

## **2.3. Absence of proven technologies**

The 1998 Mallik well employed several new and innovative coring designs and procedures with reasonable but limited success. There are several proposed technologies to extract natural gas from gas hydrates, mostly based on the use of techniques leading to the decomposition of the hydrates in-situ and the subsequent production of the gas by conventional or adapted gas wells. For example, gas hydrates decompose when the pressure and temperature are beyond certain limits, or when inhibitors are injected, and the gas is released and can be produced by wells.

There is one known case where natural gas has been commercially produced from gas hydrates for a sustained period of time. In permafrost onshore North Siberia in Russia, inhibitors were injected to cause the decomposition of the gas hydrates, and the released gas was produced at the Messoyakha gas field. Production was discontinued when it was judged uneconomic. In recent publications, the claim that the produced gas did actually originate from the gas hydrates, and not from free gas trapped under the gas hydrates in the Messoyakha field, has been disputed. It is inevitable that the hydrate production technology will be

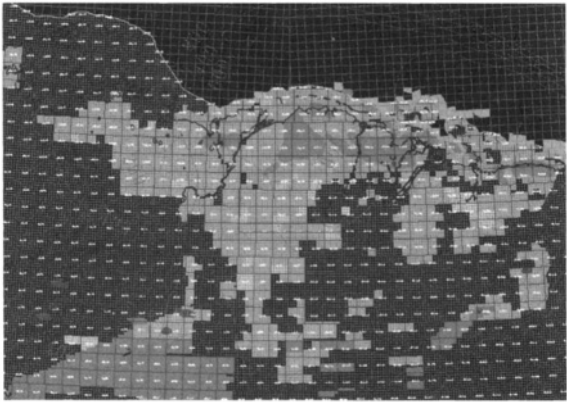


**Figure 1.** Alaska North Slope Area.

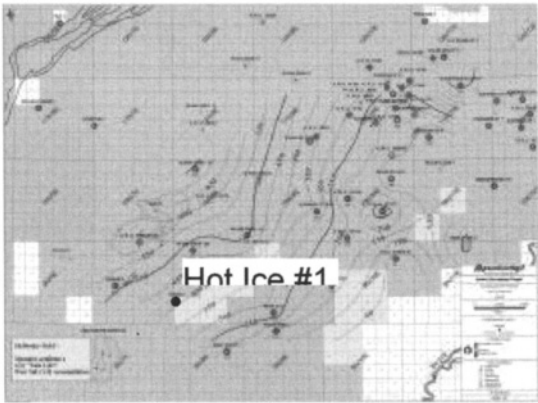


**Figure 2.** Hot Ice #1 Location; Yellow blocks are 100% Anadarko.

derived from the well-developed oil and gas practices. Under the contract terms with NETL/DOE, the Anadarko, Maurer, Noble research program focused on the identification of the hydrate area, coring operation, test hydrate properties and monitor the wellbore. Production is only a secondary objective.

### 3. SITE SELECTION AND PERMITTING

Site selection was based on Anadarko proprietary seismic data and available public information from various well logs integrated with regional geological data. The current selection of Hot Ice #1 (Figures 1 & 2) drill site is a balance between lease



**Figure 3.** Winterized Dynatec Rig.

access, easy access to roads, and safe operation conditions, and locations with the a thick hydrate stability zone, evidence of gas in the system, good thickness of potential reservoir rocks, and near known hydrate occurrences. Due to environmental concerns and regulatory stipulations in the Alaska Coastal and Foothill areas; the permitting processes was very lengthy. Other than the permitting requirements from the Federal and State agencies, local authorities, native and various citizen groups have to be informed of all drilling activities. The drilling season in the Arctic spans only a few months in winter. With all the logistic of mobilizing the equipment, the actual drilling window is very limited. Water and gravel usage to build ice road and site preparation is under rigorous control.

### 3.1. Drilling and Coring

A small-footprint mining/coring rig from Dynatec (Figure 3) of Salt Lake City was used in the drilling and coring operation to minimize the environmental impacts in the tundra. The HOT ICE #1 was drilled and cored through the permafrost into the hydrate stability zone. Fluid chilling (Figure 4) was used through out the coring operational. Based on the work os Steve Kirby and Laura Stern<sup>5</sup>, the mud temperature was kept at a narrow window around  $-5$  degrees C which helps to stabilize the core and improve recovery. Other than the thermodynamic properties, the kinetics reaction during coring of the hydrate is critical. The time-dependent hydrate freeze and thaw cycle in the presence of coring fluid can provide a self-preservation mechanism. Several drilling/coring fluids were tested in the laboratory for its compatibility with the hydrate (laboratory simulated).



**Figure 4.** Mud Cooling Equipment.



**Figure 5.** Drill Smart on-site in Alaska.

The stringent requirement of the coring fluid should maximize hydrate core recovery. The data from laboratory measurement will feed into a computer well-bore simulator to ensure a safe operation. All equipment were tested prior moving on location. Drilling data are collected by the Drill Smart (Trademarked by Noble Engineering & Development) real time monitoring system (Figure 5) and transmitted via satellite to Houston and then patched over to Anadarko's Operation Center in The Woodlands (Figure 6).

#### **4. ARCTIC PLATFORM**

The reusable Arctic Platform is a modular design drilling and supporting structure with low environmental impact. The 100'X100' drilling platform plus a 75'X75'

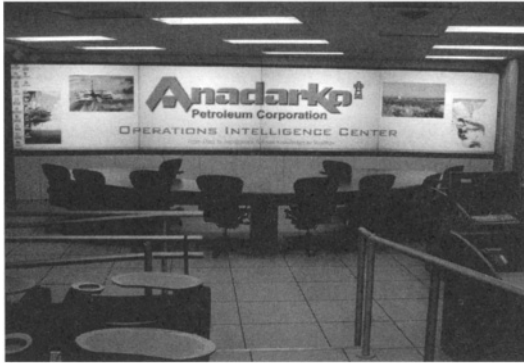


**Figure 6.** Operation Center in Woodlands, TX.

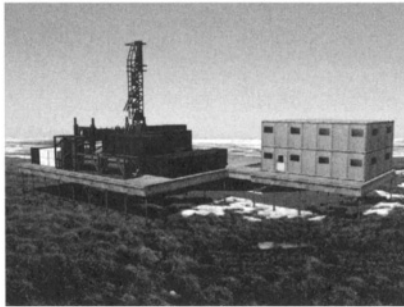


**Figure 7.** The Concept Animation, Stacked, June 2002.

housing platform are 12' above the tundra when installed. These platforms are assembled with interlocking modules which are then supported by piles. The motivation to incorporate Arctic Platform in this project was prompted by the limited operating window in the Arctic tundra environment. The historic data showed tundra travel day has shortened from 200 days in mid 70s to 150 days in 2000. That is a 25% reduction on operation days in 25 years. More alarmingly, in the last 5 years the travel time has decreased in a faster pace. In 1998, the tundra was opened for slightly over 100 days.

The design phase of the platform was started in June 2002 (Figure 7). After static and dynamic (wind loading) numerical structural analysis and design modifications, the module construction and platform assemble were begun in August of 2002. At the same time, piling experiments was initiated in Alaska to finalize the installation process and loading requirement. After the structural integrity was ensure and approved with a trial run in Houston. The modules were then transported to the well site in January 2003 (Figures 8 & 9).

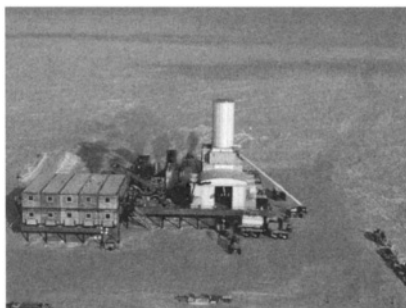


**Figure 8.** Arctic Platform on Location, March 2003.

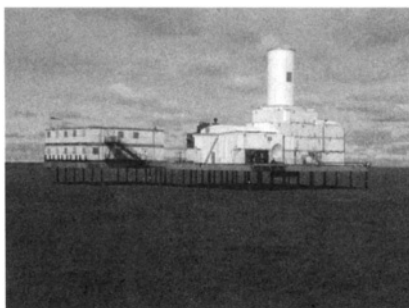


**Figure 9.** Arctic Platform, September 2003.

## 5. CORE PRESERVATION AND LABORATORY TESTING

An onsite lab was chosen to maximize the ability to test recovered hydrates in as close to insitu conditions as possible. Data will also be generated for reservoir quality evaluation, seismic characterization, petrophysical evaluation, and hydrate reservoir mechanical/chemical stability evaluation.

The stability of gas hydrate depends on gas pressure, temperature, pore water salinity, pore geometry, and gas composition. Understanding of the thermodynamics of methane and other gas hydrates is very important from the view-point of preserving cores and exploiting natural gas production from hydrate wells. The hydrate handling experiences from various National Laboratories and the USGS indicated the hydrate has a pseudo stable zone around  $-5$  C. During the coring operation, recovered cores are kept at this temperature to preserve its original properties by means of a controlled low temperature mud system and cooled lab modules. For longer term core storage, the hydrate cores will be kept in pressure core storage containers, or at Liquid nitrogen temperatures.

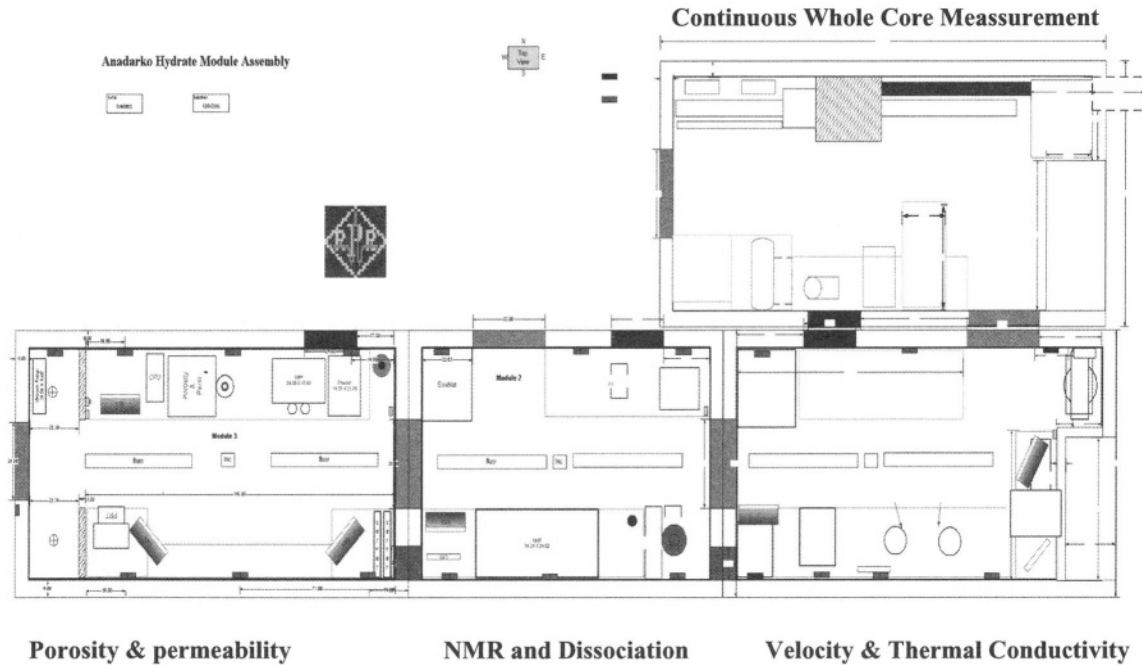


**Figure 10.** Four Interconnected Modules of the Mobile Laboratory.

## 6. MOBILE LABORATORY

The mobile core laboratory was built to house the basic instruments that are needed to analysis the transient properties of hydrate. It was designed to be deployed at remote sites with high levels of automation and the low temperature requirement to preserve and analyze the permafrost and hydrate samples. Four modules were designed and built by Rock Properties Resources in Tulsa (Figure 10). The system was built to analyze core recovered from this project. These cores could consist of various types of materials – from unconsolidated friable sediments, gravels, permafrost, hydrates rich sediments to conventional sediments.

## 7. CONTINUOUS WHOLE CORE MEASUREMENT

The design objectives of the system include minimizing unnecessary operator intervention, automatically capturing instrument output in a database, and the capability of multi-tasking or parallel processing and operation. All samples are tracked with bar code to minimize reporting errors.

The design objectives of the system include minimizing unnecessary operator intervention, automatically capturing instrument output in a database, and the capability of multi-tasking or parallel processing and operation. All samples are tracked with bar code to minimize reporting errors.

### 7.1. Whole Core Measurements

After the core is pulled out of the hole and transferred to the staging area, the core is then retrieved from the core barrel and cleaned before it was brought to the first module of the mobile laboratory. This lab module is kept at  $-5^{\circ}\text{C}$ . In this unit, the whole core will be carried by the conveyor belt (Figure 11) for the measurement of the following properties:

1. Natural Gamma
2. Dimensions
3. Compressional Velocity
4. IR Surface Temperature
5. White Light Photographs
6. CMR surface log (on loan from Schlumberger w/operators)

Cutting and Plugging is also done in this module (Figure 12).



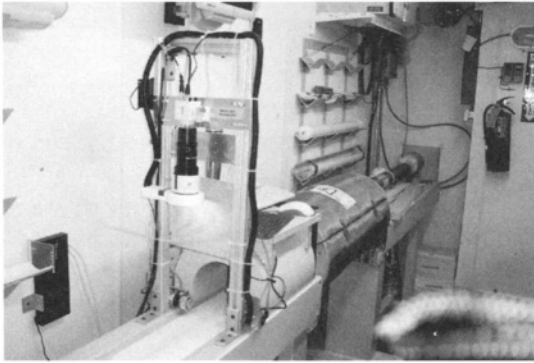


**Figure 11.** Conveyor belt & whole core Measurement w/CMR.

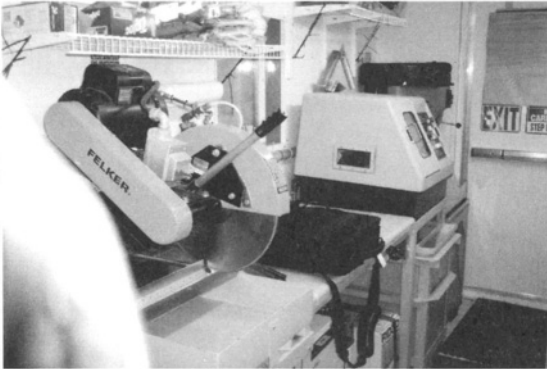


**Figure 12.** Cutting and Plugging Tools.

## 7.2. Core Plug Measurements

The 1–1/2” core plugs are plugged from selected cores and are tested for the following parameters. Data are automatically entered into an integrated relational database.

1. Densities (grain, bulk)
2. Porosity (function of pressure) (Figure 13)
3. Permeability (function of pressure) (Figure 13)
4. Pore Volume Compressibility (function of pressure)
5. Velocities ( $V_s$ ,  $V_p$  as a function of pressure and temperature) (Figure 15)
6. Resistivity (function of pressure and temperature)
7. Thermal Conductivity (function of pressure and temperature)

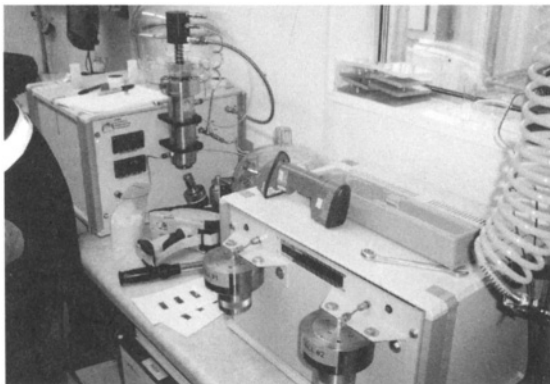


**Figure 13.** Porosity & Permeability.

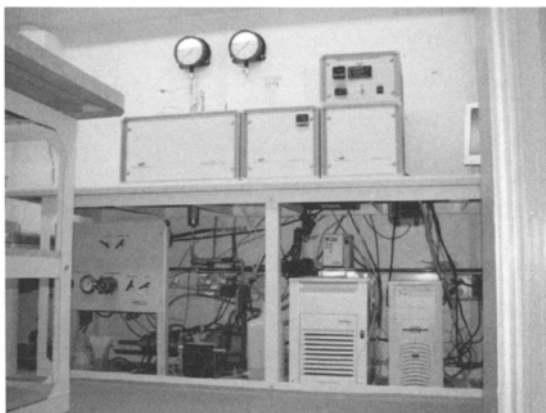


**Figure 14.** Low Temp NMR.

8. NMR (function of pressure and temperature) (Figure 14)
9. Gas Dissociation (function of pressure and temperature) (Figure 16)
10. Cleaning and Drying

## **8. OPEN HOLE LOGGING AND COMPLETION**

The basic sonic, SP and Gamma logs plus Schlumberger's CMR (NMR) log were run after the cores were recovered and the hole was underreamed. The electronic logs will be analyzed in conjunction with the laboratory core testing results, the mud log data and seismic data. After the logs are done, if the well is tested it will be



**Figure 15.** Velocity & Thermal Conductivity.

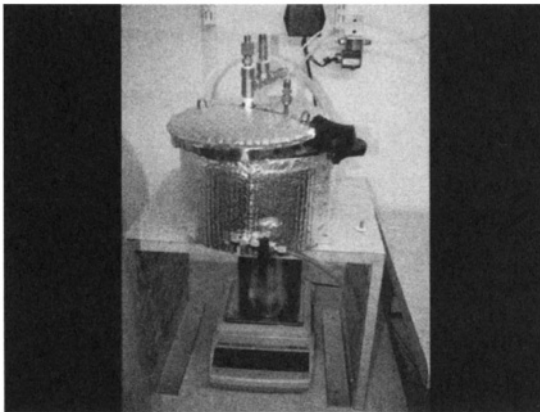


**Figure 16.** Hydrate Dissociation Test.

equipped with temperature strips and downhole pressure gauges for temperature and pressure profile monitoring. Simple techniques such as depressurization will be applied to the wellbore to observe its respond.

## 9. CONCLUSIONS

The objective of this research project is to develop technologies that can be used for the continuation of a long-term product test at one or more hydrate sites in the arctic environment, and upon the confirmation of its viability, the immediate commercialization of the technology. The project is also expected to assess the natural gas reserves of gas hydrates resources in the arctic and the elaboration of



**Figure 17.** Mobile Lab Pick Up from Tulsa, February 2003.



**Figure 18.** Mobile Lab on Location, March 2003.

recommendations to facilitate the commercialization of a vast, environmentally friendly source of fossil energy in Alaska and worldwide. Many of the scientific investigation described in this review have been reported and will be published with detailed results in the near future. Nevertheless, following are the highlights of this project at the current stage.

- The ability to recover frozen core with high recovery and minimal damage was demonstrated from the minimum footprint rig, low temperature mud system, continuous coring equipments, operating procedure and platform
- Concept of low/minimal/virtually zero negative impact on the sensitive environment has been demonstrated by the Arctic Platform.

- The ability to drill/auger the piling holes and to haul heavier loads using a rolligon (tundra travel vehicle) was successfully demonstrated
- Leaving the temporary facility on location, loaded w/equipment, has been demonstrated with minimum/no impact on surrounding wildlife and flora
- The Arctic Platform was successfully operated as a “no discharge facility”
- The ability to characterize the whole core on site using the mobile lab was demonstrated
- The ability to make petrophysical measurements on core plugs at reservoir conditions was demonstrated

## ACKNOWLEDGEMENTS

The authors like to thank the National Energy Technology Laboratory (NETL), Department of Energy for their generous funding with contract # DE-PS26-01NT40869-2 and the management of Anadarko Petroleum Corporation, Maurer Technology Inc., a unit of Noble Drilling Company for their supports. Special thanks to Brad Tomer and Francis Toro of NETL, George Moridis and Barry Friedfeld of LBNL, Tim Collett, Steve Kirby and Bill Winter of USGS, Phil Long of PNNL, Bob Kleinberg and Doug Griffin of Schlumberger, Tadeu De Sousa of University of Oklahoma, Craig Woolard of University of Alaska Anchorage and many others for their scientific contributions to this project.

## REFERENCES

1. Kvenvolden, K. A., Ginsburg, G. D. and Soloviev, V. A. – *Geo-Marine Letters.*, **1993**, 13, pp. 32–40.
2. Kvenvolden, K. A., *Natural Gas Hydrate: Introduction and History of Discovery* Chapter 2 in *Natural Gas Hydrate in Oceanic and Permafrost Environments*, Max, M. D., Ed.; Kluwer Academic Publishers, **2000**; pp. 9–16.
3. Dallimore, S. R., Uchida, T. and Collett, T. S., *GSC Bulletin 544 Scientific Results from JAPEX/JNOC/GSC Mallik 2L-38 Gas Hydrate Research Well, Mackenzie Delta, Northwest Territories, Canada*, **1999**.
4. Ruppel, C., *Thermal State of the Gas Hydrate Reservoir*, in *Natural Gas Hydrate, Chapter 4 in Oceanic and Permafrost Environments*, Max, M. D., Ed.; Kluwer Academic Publishers, **2000**; pp. 29–42
5. Stern, L., Circone, S., Kirby, S., and Durham, W. (2001). Anomalous preservation of pure methane hydrate at 1 atm. *J. Phys. Chem. B*, **105** (9) 1756–1762.

# 8

## Seismic Detection and Quantification of Gas Hydrates using Rock Physics and Inversion

**Haibin Xu,\* Jianchun Dai,\* Fred Snyder, and Nader Dutta**

### 1. INTRODUCTION

Locating gas hydrates using seismic technology is relatively straightforward in many parts of the world where bottom-simulating reflectors (BSR) [1] are readily evident. A BSR is a high-amplitude reflector that approximately parallels the seafloor and is the result of the strong acoustic impedance contrast between the gas hydrate-bearing sediments above the reflector and the underlying sediments containing free gas [2]. Locating gas hydrates in the Gulf of Mexico, however, is much more challenging. Rarely has there been a documented case of a BSR in the Gulf of Mexico. Further, even if BSR does exist, it does not foretell the saturation of gas hydrates in a basin that is as dynamic and young as the Gulf of Mexico. To quantify gas hydrates from seismic data, realistic elastic property inversion techniques and rock physics-based gas hydrate models are needed [3].

---

HAIBIN XU • Schlumberger Reservoir Services / Data & Consulting Services 3600 Briarpark Dr., Houston, Texas, 77042, USA

JIANCHUN DAI • Schlumberger Reservoir Services / Data & Consulting Services 3600 Briarpark Dr., Houston, Texas, 77042, USA

FRED SNYDER • Schlumberger Reservoir Services / Data & Consulting Services 3600 Briarpark Dr., Houston, Texas, 77042, USA

NADER DUTTA • Schlumberger Reservoir Services / Data & Consulting Services 3600 Briarpark Dr., Houston, Texas, 77042, USA

\* These authors contributed equally to this work

### Gas Hydrate Modeling & Analysis: The 5-step process\*

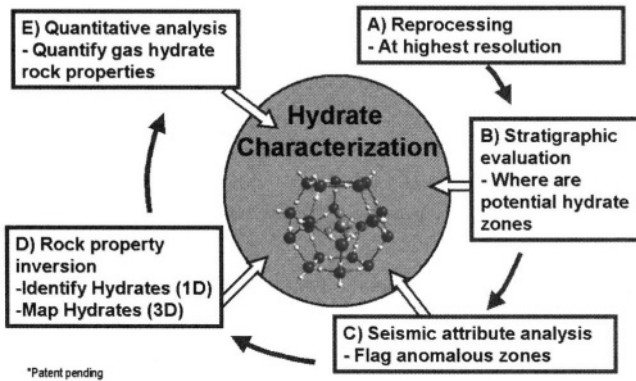


**Figure 1.** A five-step process for gas hydrate detection and estimation using seismic data.

In this article, we discuss the detection and estimation of gas hydrates using seismic data prior to drilling. The absence of well logs and other hard data presented a key challenge in the study. This was overcome by using a five-step integrated multidisciplinary approach (Figure 1) that included: 1). reprocessing conventional 3D seismic data at the higher resolution using an amplitude-preserving flow with prestack time migration, 2) a detailed stratigraphic evaluation and interpretation to identify potential hydrate zones, 3) seismic attribute analysis to further delineate anomalous zones, 4) full waveform prestack inversion to characterize acoustic properties of gas hydrates in 1D [4][5] and map in 3D using hybrid inversion technique [6][7], and 5) quantitative estimation of gas hydrate saturation using rock property models. We illustrate the procedure using 3D seismic data and estimate gas hydrate saturations in two study areas—one with BSR and the other without BSR—in the northern deepwater GOM.

## 2. STRATIGRAPHIC EVALUATION

Two OCS blocks are chosen for this study (Figure 2). One is a Keathley Canyon study area (KCSA) and the other is an Atwater Valley study area (AVSA). We applied detailed stratigraphic evaluation to both study areas.

An example is presented in Figure 3 for the KCSA. A BSR is identifiable that obliquely cuts the stratigraphic reflections approximately 500 ms below the seafloor (Figure 3, left panel). This crosscutting feature can be seen using reflection strength on a vertical seismic section and is definable by terminations of the

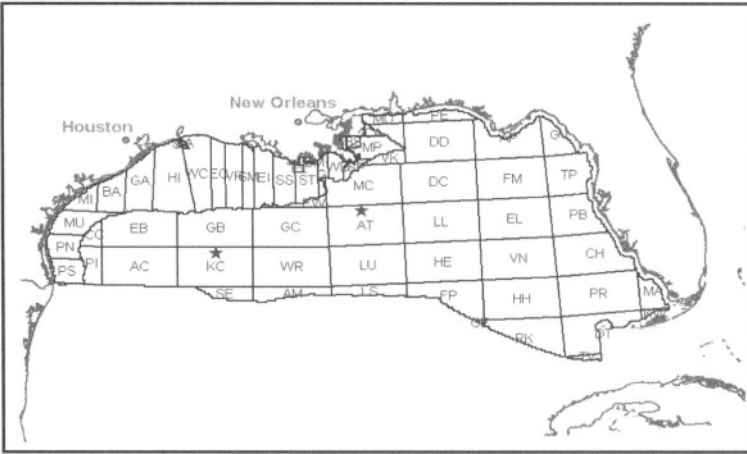


**Figure 2.** Geographical locations of the two study areas are indicated by the red stars.

high-amplitude gas sands underneath (Figure 3, right panel). In addition to the BSR, this area also shows a hydrate mound on the east side of the major fault ridge. Below the mound there is evidence of free gas accumulation and a possible destabilized BSR near the surface. This mound is directly adjacent to one of the major faults, a likely conduit for gas and fluids (Figure 3, left panel).

The AVSA is located within the Mississippi Valley channel complex, and therefore, has a thick clastic blanket above the salt. Sediments deposited during this active period are complex and chaotic with evidence of many channel levee and slope fan systems (Figure 4, right panel). No regional BSR is evident in this area, although numerous seafloor mounds can be seen with amplitude wipeout zones extending about 0.4 s below the mudline (Figure 4). From heat flow and thermal gradient estimates, the hydrate stability zone is estimated to extend approximately to 500 m below the mudline.

### 3. ROCK PHYSICS OF GAS HYDRATES

Gas hydrate drillings worldwide have shown that higher gas hydrate concentrations create an increase in the elastic properties of rocks. There are a number of rock physics models in the literature that attempt to quantify this effect, some of which are shown in Figure 5.

The cemented sand models (Model 1 and 2 in Figure 5) of Dvorkin and Nur (1996) [8] were applied by Ecker et al. (1998) [9]. These models treat the grains as randomly packed spheres where the cement—in this case, the gas hydrates, occur at the contact point (Model 1) or grow around the grains (Model 2). Using these



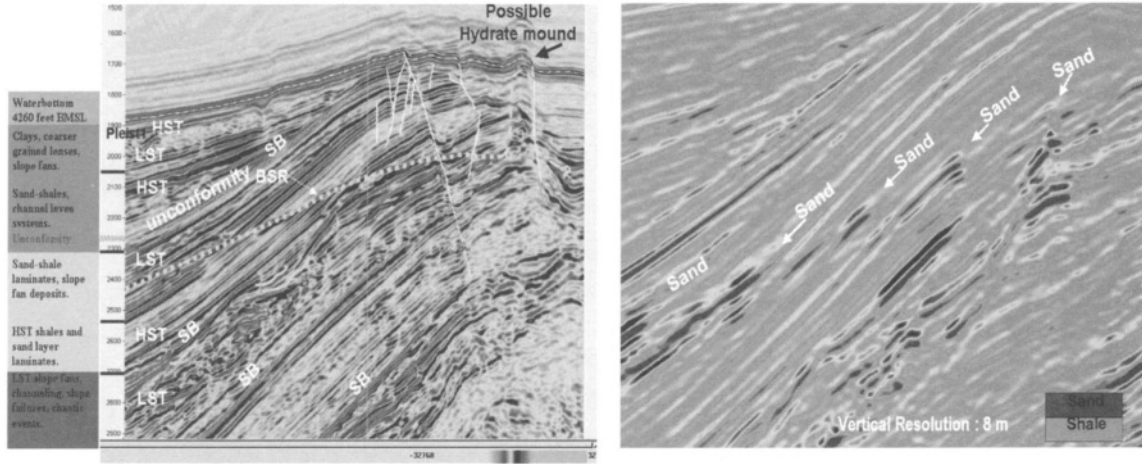


**Figure 3.** Left panel: Seismic section with stratigraphic interpretation at KCSA. The BSR is indicated by the yellow dashed line (LST-low stand, HST-high stand, SB-sequence boundary). Right panel: BSR defined by the termination of bright sands as indicated by the negative amplitude that is caused by the free gas in the pore space.

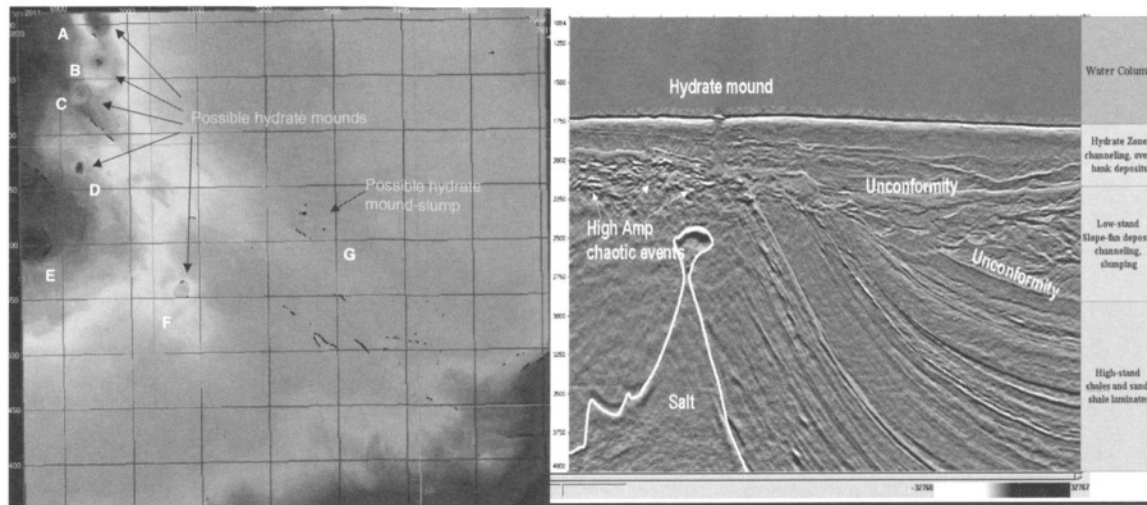


**Figure 4.** Left panel: Seafloor gas hydrate feature in AVSA. Right panel: Typical seismic section from AVSA with stratigraphic interpretation. A seafloor hydrate mound exists at the left side of the section.

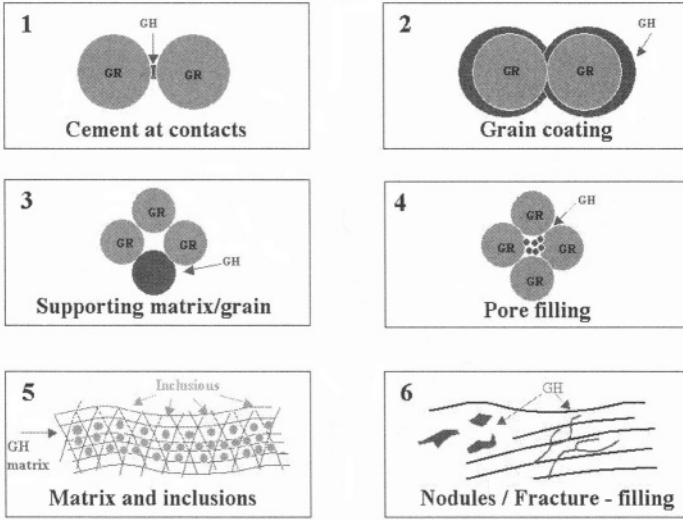


**Figure 5.** Existing microstructural models of gas hydrate-bearing sediments (GR-grain; GH-gas hydrate).

models, P-wave and S-wave velocities are derived in two steps. The models first calculate the effective dry rock moduli,  $K_{eff}$  and  $G_{eff}$ , as follows:

$$K_{eff} = \frac{C(1 - \phi_0)}{6} M_c S_n \quad (1)$$

$$G_{eff} = \frac{3K_{eff}}{5} + \frac{3C(1 - \phi_0)}{20} G_c S_\tau \quad (2)$$

where  $C$  is the grain contact number,  $\phi_0$  is the original porosity, and  $M_c$  and  $G_c$  are the P-wave and S-wave moduli of the cement (gas hydrates), respectively. Parameter  $S_n$  and  $S_\tau$  are proportional to the normal and shear stiffness of the cemented two-grain combination. The values of  $S_n$  and  $S_\tau$  depend on the amount of contact cement and the properties of the cement and the grains. Expressions of the stiffness are listed in the appendix. Knowing the dry rock moduli, the bulk moduli of saturated rock ( $K_{sat}$ ) is calculated through Gassmann's equation:

$$K_{sat} = K_d + \frac{\left(1 - \frac{K_d}{K_m}\right)^2}{\frac{\phi}{K_f} + \frac{1-\phi}{K_m} - \frac{K_d}{K_m^2}} \quad (3)$$

$$G_{sat} = G_d = G_{eff} \quad (4)$$

where  $K_{sat}$ ,  $K_d$ ,  $K_m$ , and  $K_f$  are the bulk moduli for saturated rock, dry rock ( $K_{eff}$ ), mineral grain, and porous fluid, respectively;  $G_{sat}$  and  $G_d$  are the shear

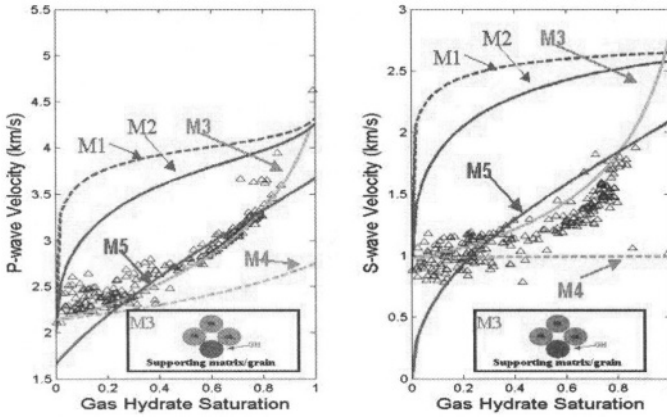


**Figure 6.** P-wave (left) and S-wave (right) velocities versus gas hydrate saturation for the rock physics models shown in Figure 5. Model 3 (M3—inset) is the best model that matches the gas hydrate saturation at the Mallik 2L-38 well.

moduli of saturated rock and dry rock ( $G_{eff}$ ), respectively; and  $\phi$  is the porosity of the rock. Then, P-wave and S-wave velocities are given by:

$$V_p = \left( \frac{K_{sat} + \frac{4}{3}G_{eff}}{\rho} \right)^{\frac{1}{2}} \quad (5)$$

$$V_s = \left( \frac{G_{eff}}{\rho} \right)^{\frac{1}{2}} \quad (6)$$

where  $\rho$  is the bulk density of the rock.

The cementation models predict large increase of moduli and velocities with only a small amount of gas hydrate, but stay relatively flat as the concentration of gas hydrate increases further. This is shown in Figure 6 (curves labeled M1 and M2).

Models 3 and 4 are variations of the cementation models, but consider the gas hydrate as either a component of the load-bearing matrix or filling the pores [8][10][11][12]. The calculation procedure of these two models is documented by Helgerud et al (1999) [11] and Dvorkin et al. (2003) [12]. It starts with the calculation of effective dry rock bulk and shear moduli using the Hertz-Mindlin contact theory (Mindlin, 1949) [13]:

$$K_{hm} = \left[ \frac{C^2(1 - \phi_c)^2 G^2 P}{18\pi^2(1 - \nu)^2} \right]^{\frac{1}{3}} \quad (7)$$

$$G_{hm} = \frac{5 - 4\nu}{5(2 - \nu)} \left[ \frac{3C^2(1 - \phi_c)^2 G^2 P}{2\pi^2(1 - \nu)^2} \right]^{\frac{1}{3}} \quad (8)$$

where  $K_{hm}$  and  $G_{hm}$  are the Hertz-Mindlin bulk and shear effective dry rock bulk and shear moduli respectively,  $G$  and  $\nu$  are the shear moduli and Poisson's ratio of the solid phase,  $\phi_c$  is the critical porosity (35–40%), and  $P$  is the effective pressure. It then calculates rock-frame moduli through modified lower Hashin-Shtrikman (HS) bound [14] for porosity smaller than critical porosity:

$$K_d = \left[ \frac{\frac{\phi}{\phi_c}}{K_{hm} + \frac{4G_{hm}}{3}} + \frac{1 - \frac{\phi}{\phi_c}}{K + \frac{4}{3}G_{hm}} \right]^{-1} - \frac{4G_{hm}}{3} \quad (9)$$

$$G_d = \left[ \frac{\frac{\phi}{\phi_c}}{G_{hm} + Z} + \frac{1 - \frac{\phi}{\phi_c}}{G + Z} \right]^{-1} - Z \quad (10)$$

and a modified upper HS bound for porosities larger than critical porosity:

$$K_d = \left[ \frac{\frac{1-\phi}{1-\phi_c}}{K_{hm} + \frac{4G_{hm}}{3}} + \frac{\frac{\phi-\phi_c}{1-\phi_c}}{\frac{4G_{hm}}{3}} \right]^{-1} - \frac{4G_{hm}}{3} \quad (11)$$

$$G_d = \left[ \frac{\frac{1-\phi}{1-\phi_c}}{G_{hm} + Z} + \frac{\frac{\phi-\phi_c}{1-\phi_c}}{Z} \right]^{-1} - Z \quad (12)$$

Here

$$Z = \frac{G_{hm}}{6} \left[ \frac{9K_{hm} + 8G_{hm}}{K_{hm} + 2G_{hm}} \right]. \quad (13)$$

Once the dry rock moduli are derived, the P-wave and S-wave velocities are calculated using equations (3)–(6). Model 3 predicts a rather gradual increase in the elastic properties with the increase of gas hydrate concentration. However, Model 4 predicts smaller increase in P-wave and virtually no change for S-wave as the gas hydrate concentration increases. This is shown in Figure 6 (curves labeled M3, M4).

Model 5 is an inclusion-type model (based on Kuster and Toksoz (1974) [15]) that treats gas hydrate and grains as the matrix and inclusions respectively, solving for elastic moduli of the system by iteratively solving either the inclusion-type [15] or self-consistent type equations [16].

Models 1 through 5 all consider gas hydrate as homogeneously distributed in the sediments. However, evidence of gas hydrate coring reveals that hydrates often exists as nodules and fracture fillings in the shallow shaly sediments. This geometry is illustrated in Model 6. No quantitative treatment of this geometric model exists in the literature. Not illustrated in Figure 5 are a series of empirical relations to describe the acoustic properties of gas hydrates (e.g., the weighted

*Table 1.* Elastic properties of gas hydrate, compared to those of ice, water, quartz, and clay.

Property		Bulk Modulus (Gpa)	Shear Modulus (GPa)	Bulk Density (g/cc)	P-wave Velocity (km/s)	S-wave Velocity (km/s)
Gas hydrate	sI	5.6*	2.4*	0.90*	3.1~3.7	1.6~1.9
		8.1**	3.3**	0.91**		
	sII	8.3*		0.92*		
Ice		8.8*	3.9*	0.92*		
Water		2.3	0	1.04	1.5	0
Quartz		36	45	2.65	6.05	4.09
Clay***		21	7	2.60	3.41	1.64

All values are from Mayko et al. (1998) [18], except those denoted by asterisks (\* from Sloan (1998) [19], \*\* from Helgerud et al. (2002) [11], \*\*\* from Tosaya (1982) [20], sI—structure I gas hydrate, sII—structure II gas hydrate)

average equation by Lee (1996) [17]). The advantage of an empirical relation is that it is based upon real observations, and very simple to implement. However, empirical relationships are not necessarily valid in geological settings and for rock properties different from where they were formulated.

How good are these model predictions? To make a comparison, the predicted P-wave and S-wave velocities of these models are plotted against gas hydrate saturation that varies from 0 to 100% of the pore space (Figure 6). The modeled velocity responses are calculated using identical input parameters and represent the average background properties of the gas hydrate hosting rocks at the Mallik 2L-38 well. Gas hydrate elastic property values used are listed in Table 1. As shown in Figure 6, the models (colored lines) are compared to the actual well data (blue triangles). It can be observed that large variations exist among the model predictions. The cementation models (Model 1 and 2) predict large increases in both P-wave and S-wave velocities with the first few percent of gas hydrate saturation. Prediction from Model 1 increases even faster than that of Model 2 as it assumes all the gas hydrates occur at the grain contact. But they are far away from the observed data points (Blue triangles). The P-wave prediction from the inclusion model (Model 5, pink color) follows the observed data well at high gas hydrate saturations (>30–40%) but underestimates for lower saturations. S-wave prediction from Model 5 does not follow the observed data at all. The predictions from Model 4 (green dashed line) also underestimate the P-wave velocity response as gas hydrate saturation increases. It almost predicts a constant S-wave velocity response that is obviously not what has been indicated by the observed data. Despite the large variations among these model predictions, Model 3 (the solid green line) that treats gas hydrates as load-bearing matrix, closely matches both the P-wave and S-wave data. As will be shown later, this model also reasonably predicts the

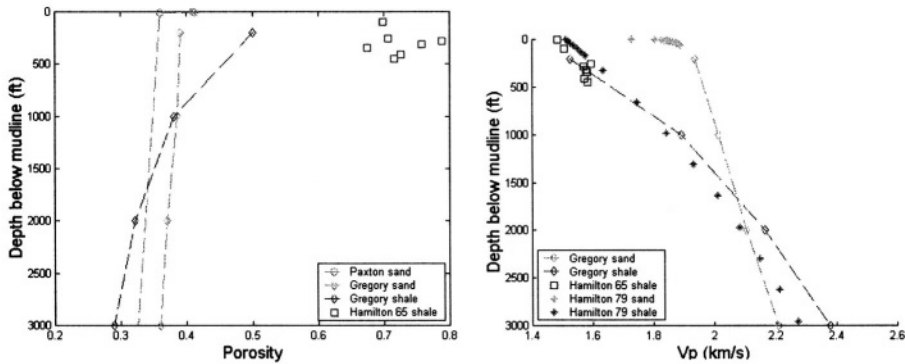


**Figure 7.** Left panel: GOM shales and sands (Gregory, 1977) [21], rigid global sand (Paxton et al., 2002) [22], and Hamilton’s data (1965) [23] showing shale porosity versus depth within the first few thousand ft BML. Right panel: GOM shales and sands (Gregory, 1977) [21], rigid global sand (Paxton et al., 2002) [22], and Hamilton’s data (1965,1979) [23, 24], showing Vp within the first few thousand ft BML.

gas hydrate saturation at the Blake Ridge drill site. Hence, we adopt this model for our modeling work and gas hydrate estimation from the seismic data. It must be noted, however, that this model tends to overestimate S-wave velocity at high gas hydrate saturations. It is also sensitive to the choice of the coordination number, critical porosity, and component elastic properties.

In deep ocean sediments, gas hydrates are only stable at a very shallow interval below the seafloor. This gas hydrate stability zone (GHSZ) is determined by water depth, pore pressure, seafloor temperature, thermal gradient, and gas and fluid composition. Our calculation in the two study areas indicates that majority of predicted GHSZ are within 500 m below the mudline (BML). At shallow depths, rock properties such as porosity, density, P-wave, and S-wave velocities are extremely variable. Porosity of shales can vary from 80% at the seafloor to less than 40% within 500 m of the water bottom. Figure 7 shows the range of porosity and Vp within the first 3000 ft below the mudline. The variations in these values with changing lithology illustrate the importance of understanding the shallow rock properties for gas hydrates delineation and volume estimation.

By understanding the porosity-depth trend at shallow depths due to compaction, and by using an appropriate velocity-porosity model, a background rock physics trend can be constructed. Using the gas hydrate rock physics model (Model 3) discussed earlier, velocities for different gas hydrate saturations can then be predicted. This methodology was applied to the ODP leg 164 hole 995B (Figure 8). The blocky colored lines in the Vp column are the replacement curves for different

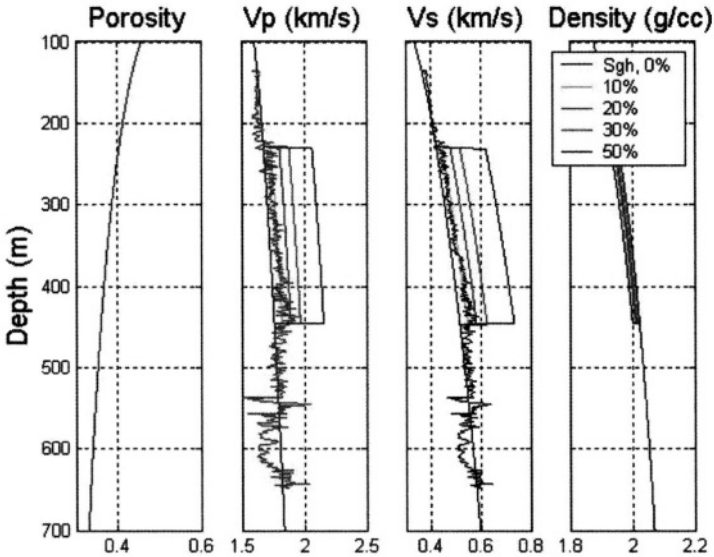


**Figure 8.** Gas hydrate modeling and estimation of gas hydrate saturation from velocity data at ODP Leg 164-995B, Blake Ridge (Sgh—gas hydrate saturation).

gas hydrate saturations (0 to 50%) in steps of 10%. The P-wave measurement falls mostly within the 10% gas hydrate saturation line and between 10 to 20% at the base of gas hydrate zone. This is within the range of gas hydrate concentration estimated by a pressure core sampler (PCS), which ranges from 0 to 9% by volume (Dickens et al., 1997) [25]. It is also in good agreement with estimations made through several other means that were reported in the literature such as by Ecker et al. (2000) [26] that estimated a range of 0–13% of gas hydrate in pore space. Panel 3 shows the S-wave estimation based on the P-wave measurement and  $V_p/V_s$  ratio derived from the P-wave and S-wave background trends predicted by the model. Panel 4 shows the bulk density variation with different gas hydrates saturations. The bulk density decreases as the gas hydrate saturation increases due to the lower density of the hydrate compared to fluid. However, this effect is negligible.

#### 4. ROCK PROPERTY ESTIMATION FROM SEISMIC INVERSION

Besides a practical gas hydrate rock physical model (previous section), gas hydrate quantification also necessitates robust rock elastic property estimation such as P-wave and S-wave velocities and bulk density, from seismic inversion. In this



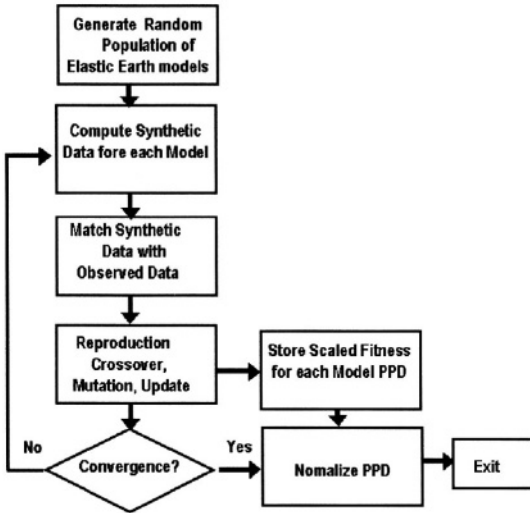


**Figure 9.** Flowchart detailing the steps involved in the FWPI on a CRP gather (edited from Dutta, 2002) [6].

study, to generate a high-resolution property profile of the shallowest one-second interval starting from the seafloor, we applied full waveform pre-stack inversion (FWPI) at selected locations in both study areas. FWPI is developed by Mallick *et al.* [4][5] based on the genetic algorithm. It is a statistical optimization technique that operates much like biological evolution and yields P-wave, S-wave velocity, and density profiles for a given seismic gather. The procedure is outlined in Figure 9. The FWPI process starts with the generation of a random population of elastic earth models ( $V_p$ , Poisson's ratio or  $V_s$  and density) within specified search intervals from the initial model. For each of these random models, synthetic seismograms are crated with a full wave-equation simulator. The modeled synthetics are then compared to the observed data to yield a fitness value for each of the models. Genetic operations of reproduction, crossover, mutation, and update are then performed on the newly generated models. The iterative process continues until the fitness values converge.

The primary advantage of using FWPI is the ability to use full wave equation-based forward modeling on a discrete (thin), layer model. This allows the inversion process to account for tuning effects, the interference of multiples and converted waves, and the reflection and transmission effects due to the velocity gradients. The inversion yields 1D high-definition elastic property profiles. These elastic profiles can then be used as pseudo-well logs to interpret the potential presence of hydrates and for background low-frequency (0–8 Hz) impedance trends for hybrid inversion [6][7][27] to generate 3D elastic volume.

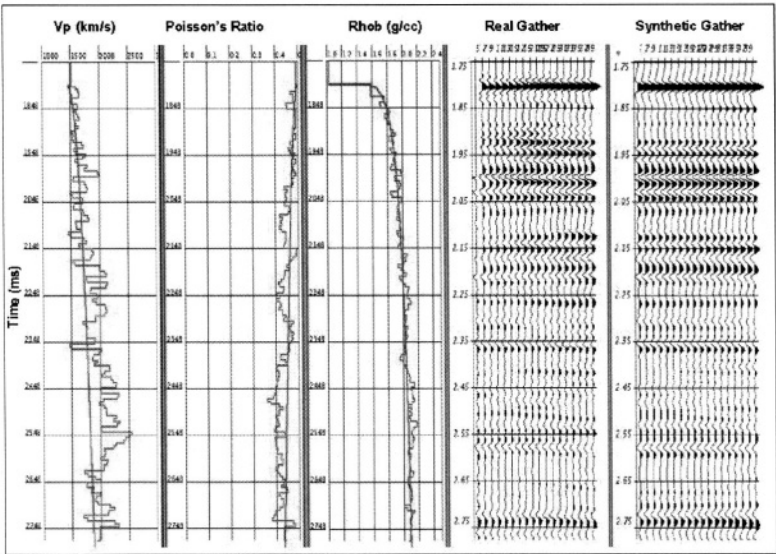
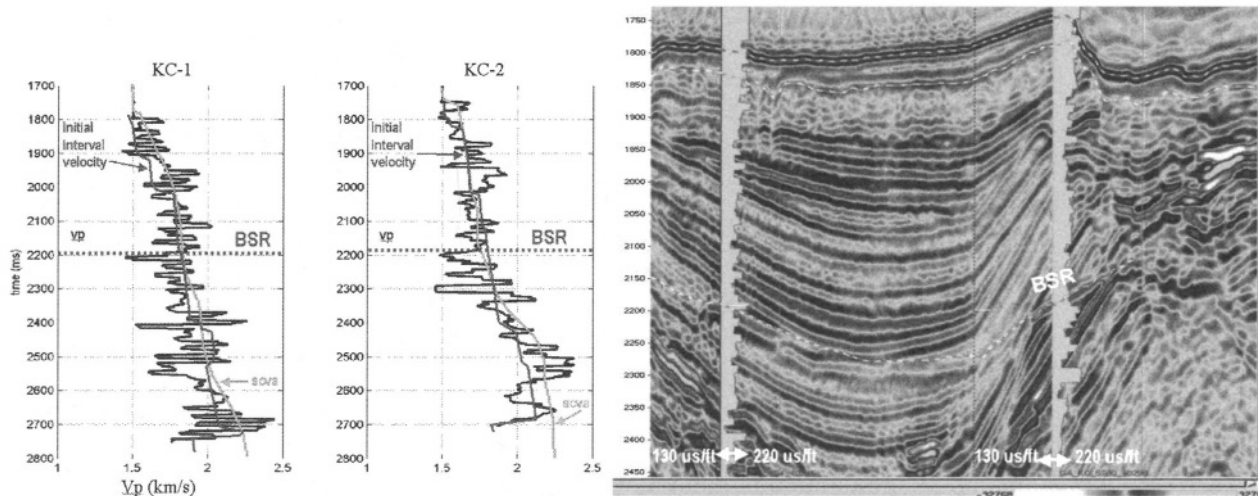


Figure 10. An example result from FWPI in KCSA.

An example of the application of FWPI is given in Figure 10. The pink smooth curves are the input background trend based on the rock physics model. The green curves are the inverted P-wave, Poisson’s ratio, and density profiles. The right two panels display the observed seismic angle gather and the synthetic angle gather, after convergence during the iteration process. Note that the correlation coefficient of the two gathers reaches 0.91.

Two pseudo-well logs generated from FWPI at two locations of KCSA are tied to an arbitrary seismic section as shown in Figure 11. The left panel shows the inversion results. The red curves are the starting interval velocity (derived from stacking velocity) model input to the inversion. Green curves are velocities from spatially continuous velocity analysis (SCVA), which is a high-density velocity analysis procedure to QC the initial velocity model. The blue curves are the P-wave velocity derived from FWPI. The highs and lows in the derived P-wave velocity reflect possible lithology or fluid variations. At the shallow depth, sandy sediments usually possess higher velocity than that of shale because of lower porosity as well as higher grain velocity. Gas hydrate zones have been known to possess high velocities and below the BSR is extremely low velocity. Based on these observations, shallow sand and shale sequences, BSR, and possible gas hydrate anomalies can be interpreted from the pseudo-well logs. The right panel of Figure 11 shows a portion of a stacked seismic section from the KCSA. Superimposed on the figure we show slowness (inverse of  $V_p$  in microseconds per foot) obtained from FWPI at indicated locations. Note the velocity reversal at BSR



**Figure 11.** Left panel: Estimated P-wave velocity versus depth at two Keathley Canyon locations using full waveform prestack inversion (blue curve). Red curves are the starting interval velocity (derived from stacking velocity) model input to the inversion. Green curves are velocities from spatially continuous velocity analysis (SCVA), which is a high-density velocity analysis procedure. Right panel: Matched slowness (inverse of  $V_p$ ) from seismic inversion at the Keathley Canyon area.

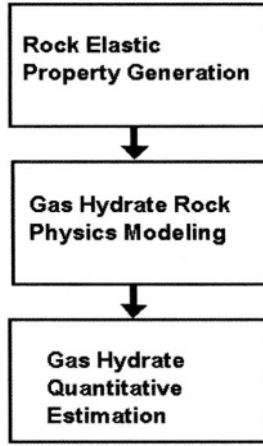


**Figure 12.** A flow chart outlining gas hydrate quantification.

and the match between the seismic data (amplitudes) and the inversion-derived slowness.

## 5. QUANTITATIVE ESTIMATION OF GAS HYDRATE SATURATION

The procedure of gas hydrate quantification includes three steps: rock elastic property derivation, gas hydrate rock physics modeling, and gas hydrate saturation calculation (Figure 12). Rock elastic property generation was discussed in the previous sections. In the following section we describe the modeling and quantification procedure.

We first define a background shale porosity trend, using the exponential compaction trend in the form given by Athy (1930) [28]:

$$\phi = \phi_0 e^{-cz} \quad (14)$$

where  $\phi$  is the porosity, and  $\phi_0$  is the initial porosity (at seafloor),  $z$  is burial depth and  $c$  is a constant. This porosity trend represents the high porosity and low velocity as well as low P-wave impedance bound. Assuming hydrostatic pore pressure, we attribute all variations in the velocity trend to the effect of both lithology and porosity. This is achieved by adding sand grains (quartz) to the shale, thus, reducing porosity and increasing the velocity of the matrix [29]. The sandy shale porosity is calculated by:

$$\phi_{shl} = \phi V_{sh} \quad (15)$$

where  $\phi_{shl}$  is the sandy shale porosity, and  $V_{sh}$  is the volumetric fraction of shale, assuming the solid phase is either quartz or shale. The range of  $V_{sh}$  varies from 1 to 0.8.

The bulk and shear moduli of the solid grain is then derived through Hill's equation [18]:

$$K = \frac{(Kv + Kr)}{2} \quad (16)$$

$$G = \frac{(Gv + Gr)}{2} \quad (17)$$

where Kv, Kr, Gv, and Gr are the Voight and Reuss average [18] bulk and shear moduli:

$$Kv = Ksh * Vsh + Ksd * Vsd \quad (18)$$

$$Kr = \frac{1}{\frac{Vsh}{Ksh} + \frac{Vsd}{Ksd}} \quad (19)$$

$$Gv = Gsh * Vsh + Gsd * Vsd \quad (20)$$

$$Gr = \frac{1}{\frac{Vsh}{Gsh} + \frac{Vsd}{Gsd}} \quad (21)$$

where  $Ksh$ ,  $Ksd$ ,  $Vsd$  are the bulk moduli for shale, sand, and volumetric fraction of sand ( $Vsd = 1 - Vsh$ ).

Then a series of P-wave impedance trends ( $P\_imp\_model$ ) of different  $V_{sh}$  can be calculated based on Model 3 as described previously:

$$P\_imp\_model \Leftarrow M3(\phi_{shl}, K, G, K_f, C, \phi_c, P, S_{gh}) \quad (22)$$

where  $K_f$ ,  $C$ ,  $P$ ,  $S_{gh}$  are fluid bulk moduli, contact number at critical porosity, effective pressure, and gas hydrate saturation, respectively. At this stage, the pores are assumed to be completely filled with brine. Therefore  $K_f$  is the bulk modulus of brine. Also at this stage, we set  $S_{gh}$  to be zero to search for a background impedance trend.

The effective pressure is calculated by:

$$P = S - P_f \quad (23)$$

where  $S$  and  $P_f$  are over-burden pressure and pore fluid pressure respectively. And they are derived through the following equations:

$$P_f = \rho_f g z \quad (24)$$

$$S = g \int_0^z \rho_b dz \quad (25)$$

in which  $\rho_f$ ,  $\rho_b$ ,  $g$ ,  $z$  are fluid density, bulk density, gravitational acceleration, and burial depth.

The difference of the predicted and observed P-wave impedance is calculated using equation (26). The best-fitting trend for the P-wave impedance is then defined by the one that possesses minimum value from equation (26):

$$\Delta = \sum (P\_imp\_model - P\_imp\_obs)^2 \quad (26)$$

where  $P\_imp\_model$ ,  $P\_imp\_obs$  are the P-wave impedance predicted from the sandy shale model, and the seismic inversion result.

Once the best-fitting trend is defined, a series of gas hydrate replacement curves of the porous space on that set of lithology is performed using equation (22) with gas hydrate saturations changing from 0 to 50% of the pore space in steps of 5%. This yields a nomogram that relates gas hydrate saturation to P-impedance. Finally, P-impedance data obtained from seismic inversion is used to derive appropriate gas hydrate saturation values through interpolation based on the nomogram.

Examples of the quantification are shown in Figure 13 where gas hydrate saturation are estimated on two FWPI locations in the KCSA.

The above procedure has been used on 3D P-wave impedance volumes derived through hybrid inversion to generate 3D gas hydrate saturation volumes at KCSA and AVSA. Figures 14 and 15 show the results at two arbitrary seismic lines. Gas hydrate saturation estimated at these two sections range from 0 to a maximum of over 30% of pore space. A word of caution is warranted for the reliability of the inversion results for gas hydrate saturation. There are several sources of uncertainties: noise in the seismic data, ambiguities associated with the inversion results, and inadequacies of the rock model and the parameters that dictate the predictability of hydrate saturation are just a few. In addition, lithology variations are also present that are ignored in the current approach as we assumed an average-mix lithology of sands and shales for background (sediments with no gas hydrate). Thus, relating all observed P-impedance variations above the background as due to gas hydrate saturation only, is expected to yield upper bounds of gas hydrate

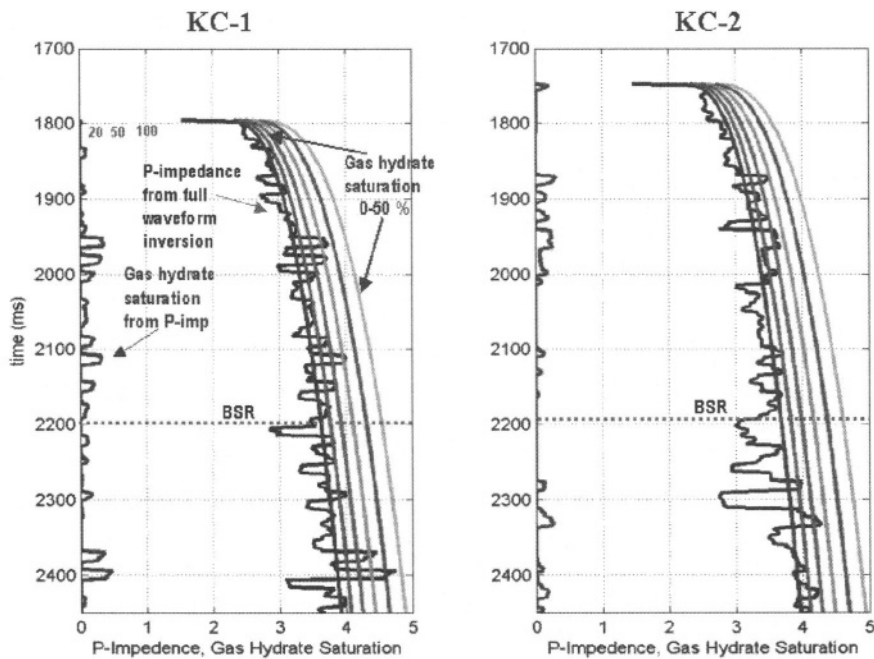


**Figure 13.** Gas hydrate saturation estimation at two locations in KCSA. Black curves are P-impedance values estimated from full waveform prestack inversion. The group of smooth colored curves is gas hydrate saturation estimated from the rock model (Model 3). The blue curves on the left of both panels indicate the estimated gas hydrate saturation.

concentration. Nonetheless, in frontier areas where no well data are available, and lithology heterogeneities are poorly understood, this type of estimation will provide valuable pre-drill information. This sort of information can be useful in selecting potential drill sites to further quantify gas hydrate saturations and properties. For geological environments such as the Blake Ridge area where the host rock does not have distinctive layering structure, this type of estimation may indeed be close to the actual gas hydrate saturation values.

How reliable are our predictions? There are numerous sources of ambiguities as discussed earlier. Gas hydrate saturation cubes such as those shown in Figures 14 and 15 must be calibrated. It should be noted that, despite the large number of drilled hydrate wells worldwide, quality hydrate logging and coring data are scarce, especially in the Gulf of Mexico. Such data are urgently needed. This must also be supplemented by controlled laboratory measurements on the properties of gas hydrates where parameters can be controlled. Until we devote

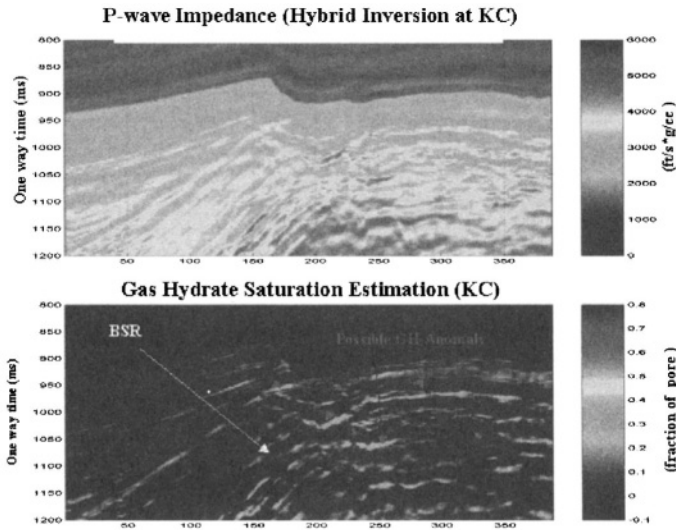


**Figure 14.** Gas hydrate saturation for Keathley Canyon line. The upper panel displays the P-impedance derived from hybrid inversion and the lower panel shows the estimated gas hydrate saturation.

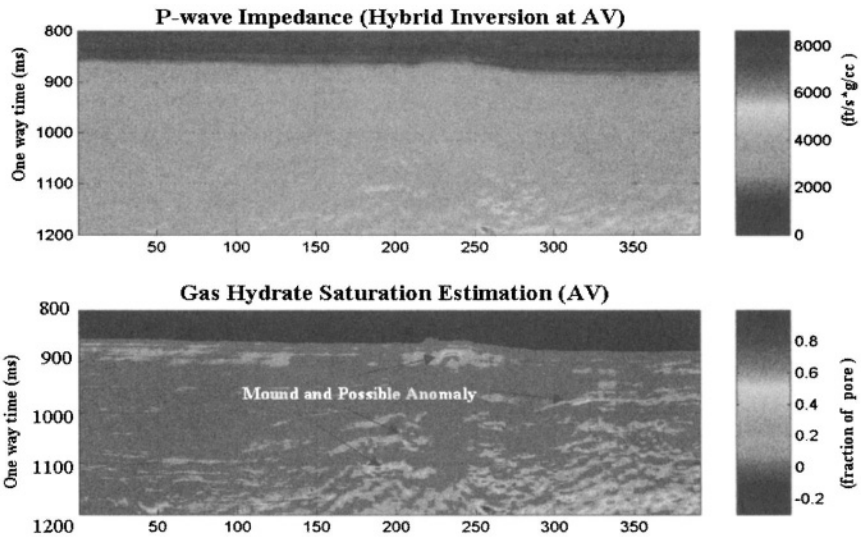


**Figure 15.** Gas hydrate saturation for Atwater Valley line. The upper panel displays the P-impedance derived from hybrid inversion and the lower panel shows the estimated gas hydrate saturation.



resources to undertake such logging, coring, and laboratory measurements, current estimates of possible gas that can be obtained from gas hydrates must be questioned.

## 6. DISCUSSION AND CONCLUSIONS

The proposed workflow for gas hydrate detection and quantification (five-step process) is unique: it is independent of whether BSR is present or absent. It provides a framework for gas hydrate characterization using an integrated geological and geophysical approach. Full waveform prestack inversion and detailed assessment of rock physics models for gas hydrates are centerpieces of the current methodology. It allowed us to produce volume estimation of gas hydrate using 3D data.

Elevated P-wave and S-wave velocities are diagnostic features of shallow gas hydrate-bearing sediments. Seismic detection and quantification of gas hydrates rely on qualitative processing, robust elastic inversion, and practical gas hydrate rock physical model construction. The five-step integrated multidisciplinary approach proves to be an effective tool for gas hydrate characterization. Full waveform prestack inversion and hybrid inversion generate robust elastic property volumes from seismic data. From this, and with our gas hydrate rock physics-based tool, gas hydrate saturation volumes can be generated, thereby providing guidance for the detection of gas hydrates and a potential quantitative resource estimation tool.

We note that the seismic technology—being a remote sensing tool, is appropriate for gas hydrate detection, with or without BSR. However, the data requirements

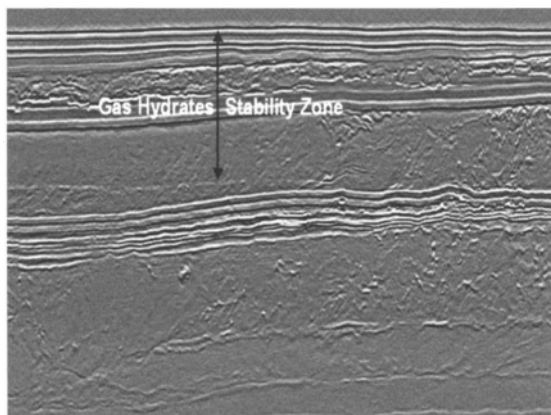


**Figure 16.** BSR shown on high-resolution seismic data (Q data) in the East Breaks region, Gulf of Mexico.

are numerous: high S/N and wider frequency contents are just two of the main prerequisites. Lately, the seismic industry has progressed to meet these requirements. An example is shown in Figure 16 using the single-sensor data (Q data) in the East Breaks area of the Gulf of Mexico. A subtle BSR crosscutting the strata in the shallow sediments is clearly revealed along with several dewatering features (mud volcanoes). These may be related to shallow hazards as well. The high fidelity of the Q data indeed helped in the identification of such features. Use of seismic data will definitely aid in the detection and quantification of gas hydrates in the Gulf of Mexico.

## ACKNOWLEDGEMENTS

We thank Diana Gillespie, Andrew E. Hannan Sr., Tom Dittrich, Adam Koesoemadinata, Lecia Muller, Emil Nassif, Dianna Shelander, Chung-Chi Shih, Randy Utech, and Gary Wool for help with the project. We also thank WesternGeco for permission to publish this paper.

## REFERENCES

1. Hyndman, R. D.; Spence, G. D., *J. of Geophys. Res.*, 1992, 97(5), 6683–6698.
2. Collett, T. S.; Dallimore, S. R., CSEG Convention, 2001, 18–22.
3. Dai, J.; Xu, H.; Snyder, F.; Dutta, N., *The Leading Edge*, January 2004.
4. Mallick, S., *Geophysics*, 1995, 60, 939–954.
5. Mallick, S., *Geophysics*, 1999, 64, 326–336.
6. Dutta, N., *Geophysics*, 2002, 67, 2012–2041.
7. Mallick, S.; Huang, X.; Lauve J.; Ahmad, R., *The Leading Edge*, 2000, 1230–1237.
8. Dvorkin, J.; Nur A., *Geophysics*, 1996, 61, 1363–1370.
9. Ecker, C.; Dvorkin, J.; Nur A., *Geophysics*, 1998, 63, 1659–1669.
10. Dvorkin, J.; Prasad, M.; Sakai, A.; Lavoie, D., *Geophys. Res. Lett.*, 1999, 26, 1781–1784.
11. Helgerud, M. B.; Dvorkin, J.; Nur, A.; Sakai, A.; Collette, T. S., *Geophys. Res. Lett.*, 1999, 26, 2021–2024.
12. Dvorkin, J.; Nur, A.; Uden, R.; Taner, T., *The Leading Edge*, 2003, 842–846.
13. Mindlin, R. D., *J. Appl. Mech.*, 1949, 16, 259–268.
14. Hashin, Z.; Shtrikman, S. A., *J. Mech. Phys. Solids*, 1963, 11, 127–140.
15. Kuster, G. T.; Toksoz, M. N., *Geophysics*, 1974, 39, 587–618.
16. Berryman, J. G., *J. Acoust. Soc. Am.*, 1980, 68, 1809–1831.
17. Lee, M. W.; Hutchinson, D. R.; Collett, T. S.; Dillon, W. P., *J. of Geophys. Res.*, 1996, 101, 20347–20358.
18. Mavko, G.; Mukerji, T.; Dvorkin, J., 1998, Cambridge University Press.
19. Sloan, E. D. 1998, Marcel Dekker, 705 pp.
20. Tosaya, C., 1982, Ph.D. dissertation, Stanford University.
21. Gregory, A. R., *AAPG Memoir* 26, 1977, 15–45.
22. Paxton, S. T.; Szabo, J. O.; Ajdukiewicz, J. M.; Klimentidis, R. E., *AAPG bull.*, 2002, 86(12), 2047–2067.

23. Hamilton, E. L., *Geophysics*, 1965, 30(2), 257–261.
24. Hamilton, E. L., *J. Geophys. Res.*, 1971, 76, 579–601.
25. Dickens, G. R.; Paull, C.; Wallace, P., *Nature*, 1997, 385, 427–29.
26. Ecker, C.; Dvorkin, J.; Nur, A., *Geophysics*, 2000, 65, 565–573.
27. Mallick, S.; Dutta, N. C.; *The leading edge*, 2002, 675–680
28. Athy, L. F., *AAPG Bull.*, 1930, 14(1), 1–24
29. Marion, D.; Nur, A.; Yin, H; Han, D., 1992, *Geophysics*, 57, 554–563.

## APPENDIX: EXPRESSION FOR STIFFNESS OF THE CEMENTATION MODELS

Dvorkin & Nur (1996) [8] presented the expression of stiffness for the cementation models. Parameters  $M_c$ ,  $G_c$ ,  $S_n$ ,  $S_\tau$  in Equations (1) and (2) are:

$$\begin{aligned}
 M_c &= \rho_c V_{p_c}^2 \\
 G_c &= \rho_c V_{s_c}^2 \\
 S_n &= A_n \alpha^2 + B_n \alpha + C_n \\
 A_n &= -0.024153 \Lambda_n^{-1.3646} \\
 B_n &= 0.20405 \Lambda_n^{-0.89008} \\
 C_n &= 0.00024649 \Lambda_n^{-1.9864} \\
 S_\tau &= A_\tau \alpha^2 + B_\tau \alpha + C_\tau \\
 A_\tau &= -10^{-2} (2.26 v^2 + 2.07 v + 2.3) \Lambda_\tau^{0.079 v^2 + 0.1754 v - 1.342} \\
 B_\tau &= (0.0573 v^2 + 0.0937 v + 0.202) \Lambda_\tau^{0.0274 v^2 + 0.0529 v - 0.8765} \\
 C_\tau &= -10^{-4} (9.654 v^2 + 4.945 v + 3.1) \Lambda_\tau^{0.01867 v^2 + 0.4011 v - 1.8186} \\
 \Lambda_n &= \frac{2 G_c (1 - \nu)(1 - \nu_c)}{\pi G (1 - 2 \nu_c)} \\
 \Lambda_\tau &= \frac{G_c}{\pi G} \\
 \alpha &= \frac{a}{R}
 \end{aligned}$$

where  $G$  and  $\nu$  are the shear modulus and Poisson's ratio of the grains;  $G_c$  and  $\nu_c$  are the shear modulus and Poisson's ratio of the cement;  $a$  is the radius of the cement layer and  $R$  is the grain radius. The value of  $\alpha$  can be calculated for the two different schemes. For scheme 1 (cement deposited at grain contact):

$$\alpha = 2 \left[ \frac{S \phi_0}{3 C (1 - \phi_0)} \right]^{0.25}$$

Whereas for scheme 2 (cement grows around the grain)

$$\alpha = \left[ \frac{2S\phi_0}{3C(1 - \phi_0)} \right]^{0.25}$$

Where S is the cement saturation of the pore space:

$$S = \frac{\phi_0 - \phi}{\phi_0}.$$

*This page intentionally left blank*

# Experiment and Modeling of Hydrate Equilibrium Line in Gas, Gas Condensate, Black Oil, and Drilling Completion Fluids

**Keshawa Shukla,\* Aftab Khokhar, and Bayram Kalpakci**

## 1. INTRODUCTION

Gas hydrates occur naturally in Arctic permafrost regions and in shallow ocean sediments and in the subsea regions in the Gulf of Mexico, among others, where temperature and pressure are conducive to the formation of natural gas hydrates (see, for example, [1–5]). Gas hydrates may offer a huge source of energy, a method for deep-ocean sequestration of green house gases, a potentially economic method for transporting natural gas, and novel gas separation processes. On the other hand, they are hazards to the transportation of gas and oils in pipelines, and drilling operations, problems related to the flow assurance. Natural gas hydrates are crystalline, nonstoichiometric, solid clathrate compounds composed of hydrate forming gas molecules entrapped in a cage formed by surrounding hydrogen bonded water molecules. Conditions of formation and dissociation of these gas hydrates depend on gas composition, aqueous phase composition and presence of a liquid hydrocarbon phase along with the suitable low temperature and high pressure conditions.

---

KESHAWA SHUKLA • Technip Offshore, Inc. Value Engineering Department 11700 Old Katy Road, Suite 150 Houston, Texas 77079

AFTAB KHOKHAR • Westport Technology Center International 6700 Portwest Drive Houston, Texas 77024

BAYRAM KALPAKCI • Technip Offshore, Inc. Value Engineering Department 11700 Old Katy Road, Suite 150 Houston, Texas 77079

Reviews on general characteristics and properties of gas hydrates can be found in several recent articles and monographs. (See for review, e.g., [1–13]).

The good quality experimental data play an important role in the development of an accurate model for industrial applications. Numerous data for hydrate dissociation points for gases are available in open literature [1]. However, good quality data for black oils are not available in literature. Unlike gas and gas condensate systems, the hydrate equilibrium points in black oils are largely affected by heating rate, stirring rate, solubility of gases in water and oil, gas/oil ratio (GOR), water/oil ratio (WOR) and solid precipitates. Therefore, measurement of hydrate equilibrium points in black oil systems is a challenging task. Accurate data are needed (within 1–2 °F uncertainty) for developing a reliable model for predicting the hydrate equilibrium lines of gas, gas condensate and black oil so that the model can be applied to, e.g., describe adequately the gas and black oil systems under the subsea and pipeline transport conditions.

The objective of this paper is two-fold: First, we report the good quality data of gas hydrate equilibrium lines for selected gas, gas condensate and black oil systems within 1–2 °F uncertainty. Second, we develop a model for describing the hydrate equilibrium lines of gas, gas condensate, completion fluid and black oil systems more accurately.

Section 2 discusses the measurement of hydrate dissociation points ranging from gas to black oil systems. Section 3 presents a brief account of the model. Section 4 reports results and checks the validity of the model. Section 5 presents conclusion of the paper.

## 2. EXPERIMENTAL PROCEDURE

The measurements of the gas hydrate equilibrium points in both gas and black oil systems were conducted in an efficient and well-controlled experiment. The effect of the rate of heating on equilibrium point has been monitored carefully. Before starting experiments for the black oil systems, calibration tests were performed for methane and Green Canyon gas (0.403% N<sub>2</sub>, 87.243% C<sub>1</sub>, 7.57% C<sub>2</sub>, 3.08% C<sub>3</sub>, 0.51% i-C<sub>4</sub>, 0.792% n-C<sub>4</sub>, 0.202% i-C<sub>5</sub>, and 0.2% n-C<sub>5</sub>, all in mole%) with de-ionized water. The properties of the oils investigated are given in Table 1.

### 2.1. Apparatus and Procedure

A specifically designed hydrate test unit was used to measure hydrate equilibrium line of black oils. The main components of the test setup are shown in Figure 1. It is a high-pressure stirred tank reactor with pressure limit that exceeds 15,000 Psia. The constant mass-constant volume tests were performed. The data acquisition system monitored pressure, temperature of bath and cell, and motor torque.

Table 1. Some selected properties of oils

Oil	GOR (scf/stb)	Bubble Point	Saturates	Aromatics	Polars	Asphaltenes
I	810	(40 °F, 4416 Psia)	62.0	26.2	11.8	<0.2
II	564	(40 °F, 3480 Psia)	40.4	32.1	20.5	7.0
III	267	(40 °F, 1650 Psia)	40.4	32.1	20.5	7.0
IV	146	(40 °F, 1017 Psia)	41.3	32.1	23.7	2.9

Programmable chiller was used to control the heating and cooling cycles. The detailed test procedure is described below.

After cleaning and vacuuming, the cell was charged with brine at the pre-determined amount, WOR = 25, which is based on field data. Using a high-precision piston pump, live oil was injected from a high-P high-T transfer cylinder through a back-pressure regulator set to a pressure that was above the bubble point pressure. A pre-determined quantity of the live oil was injected to achieve WOR = 25. The live oil transfer vessel was always kept at above the bubble point pressure and wax appearance temperature. After injection of the oil, the cell content was stirred several hours keeping the cell temperature at 120 °F. This process mixed brine and oil and solubilized gases in the liquid. The test cell sample was cooled down to a target temperature at a pre-determined rate under continuous stirring of 400 rpm, and then kept at the lowest temperature for several hours, exposing it to the most severe hydrate formation condition. After the hold-time, the autoclave cell was heated back slowly to melt the hydrate. The hydrate dissociation condition was estimated from P-T lines of hydrate formation and dissociation, giving the point where cooling and heating lines met during hydrate dissociation. These steps were

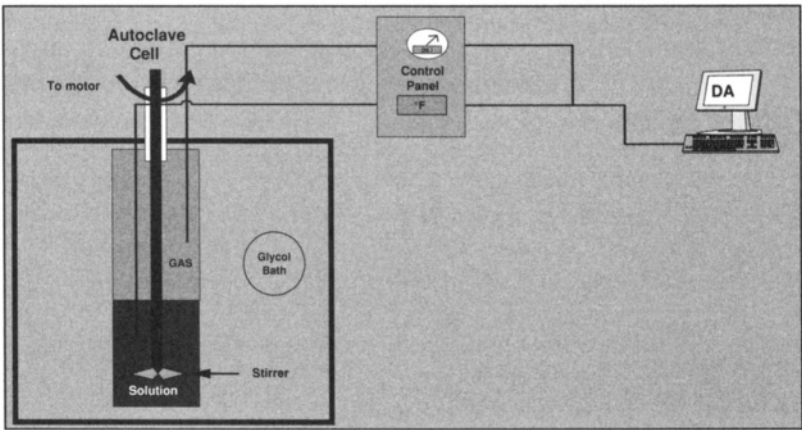


Figure 1. A schematic representation of blind cell setup used for hydrate testing.



repeated 2–3 times to confirm the equilibrium point. The cell content was heated back to 120 °F and kept there for at least overnight to melt hydrates and waxes to confirm that there was no loss of pressure or leakage. After completion of the first cycle, a second injection of brine and live oil through back pressure regulator was done at WOR = 25. However, in this case the starting pressure was greater than the initial pressure. The above steps were repeated for other data points.

## 2.2. Cooling and Heating Rates and Hold Time

Effects of cooling and heating rates were investigated to make sure that the desired equilibrium was reached in each set of the experiment. During the cool-down, a slow optimum cooling rate was selected along with added agitation for the autoclave cell, providing enough time for the fluid agitation so that mutual solubility between phases could occur in a timely manner. A slow cooling rate provided a better cooling line for getting a more representative hydrate dissociation point. A hold time was provided to achieve the optimum sub-cooling to the test solution with adequate agitation and to address the issue of very low mutual solubility of test solutions. The hold time provided a reference point for better interpretation of the hydrate dissociation point. In some cases a shock in terms of fast cooling and a high stirring procedure was used to initiate the hydrate formation especially when the driving force was inadequate.

## 2.3. Effect of Heating Rate on Equilibrium Point

We have tested several heating rates (e.g., 1 °F, 2 °F and 3 °F). The heating rate of 3 °F/hr provided the first point, while others provided the accuracy of the measurement. Slow heating rate was important when the hydrate dissociation point was close to the bubble point. Results for the three heating rates, i.e., 1 °F/hr, 2 °F/hr and 3 °F/hr, are reported in Figure 2. Figure 2 shows that 1–2 °F/hr heating rate is sufficient to obtain the equilibrium point within  $\pm 1$  °F. Therefore, 1 °F/hr heating rate was used to measure the hydrate dissociation point. Because of the solubility of gas in oil and water (brine) the delay in reaching equilibrium between liquid and gas phases could take up to 24 hours. Figure 3 shows sample results for Oil I. The effect of 5wt% NaCl + 5wt% MeOH inhibitor was investigated by heating the sample at the rate of 1 °F/hr. The equilibrium point was located as (43.6 °F, 487 Psia), shown in Figure 4. We repeated the experiment and could hold the temperature well below 5 °F of the previously known equilibrium temperature, started heating in the step of 1.5 °F, and did hold it there for ~1.5 hrs. This heating procedure was continued until the equilibrium point was reached. The new equilibrium point in Figure 5 was found to be identical to the earlier obtained point, suggesting that 1 °F/hr heating rate was sufficient to achieve the equilibrium point within  $\pm 1$  °F uncertainty even in the presence of an inhibitor.

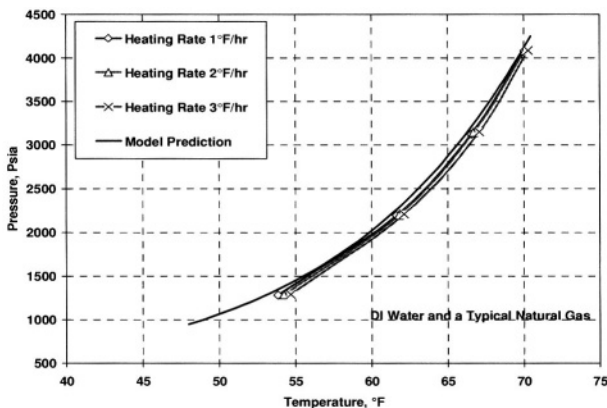


Figure 2. Effect of Heating Rate.

2.4. Effects of Water/Oil Ratio, Gas/Oil Ratio and Fluid Properties

A change in WOR may affect the equilibrium point significantly because of hydrocarbon solubility, especially the hydrate forming components, in DI water. Depending upon the total active volume of the hydrate formation cell, hydrate dissociation pressure and temperature would be dictated by the overall change in the cell fluids. We also measured the hydrate equilibrium line for asphaltene rich Oil II and Oil III, both with the same amount of asphaltene (7wt%) but with two different values of GOR, 564 scf/stb (Oil II) and 267scf/stb (Oil III). The lowering of GOR affects significantly the gas hydrate temperature suppression. The difference was significant at higher pressures where a sub-cooling of 10–13 °F was

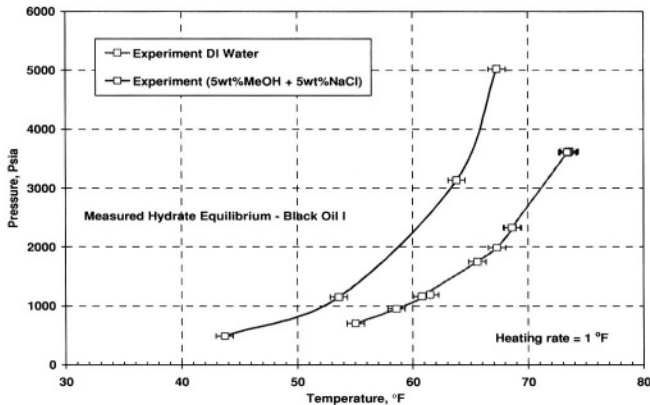


Figure 3. Oil I with 1°F/hr rate.

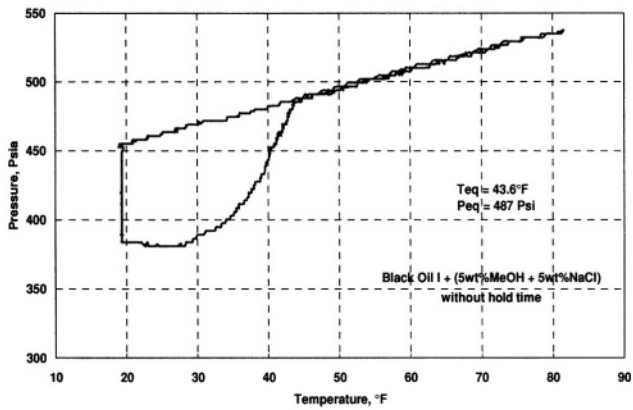


Figure 4. Oil I without hold time.

observed. The maximum difference in sub-cooling between the two oils reduced to less than 4°F at lower pressures. The influence of asphaltenes, polar components and waxes on the suppression or delaying of hydrate formation could also be important. However, their explicit effects were not investigated.

3. MODEL DEVELOPMENT

Following the van der Waals and Platteeuw [14] equation based on statistical thermodynamics along with Kihara spherical core potential function, Parrish and Prausnitz [15] presented a model for predicting hydrate dissociation line which

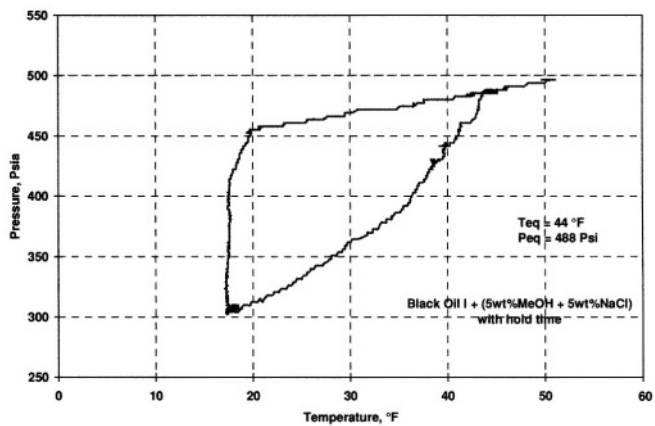


Figure 5. Oil I with hold time.

was found to be very successful for single gas systems. However, when the model was used for multicomponent gas systems, the predictions were not as good [16, 17]. Ng and Robinson [17] modified the equations to make the model applicable to multicomponent gas systems. Since the above developments several hydrate prediction models were suggested which could describe the hydrate dissociation line of gaseous systems reasonably well and within a couple of degree of experimental uncertainty [1]. In all of these models parameters were tuned to reproduce the available experimental data. Several commercial simulators have incorporated gas hydrate prediction models for industrial applications, such as DB Robinson, Infochem, WHyP, PVTsim, etc. WHyP was developed by the first author of this paper couple of years ago in order to meet then the immediate need of the industries for gas systems with mixed multi-component thermodynamic inhibitors. However, reliable models for black oil systems are still being developed as the experimental data for such complex systems were not available to test the accuracy of the models.

WHyP is a special purpose state-of-the-art hydrate prediction model, which could predict the gas hydrate dissociation conditions of drilling fluids and the hydrate temperature suppression in the presence of salts, alcohols and glycols successfully. The model could design the mud line conditions using a selected inhibitor or mixed inhibitors. However, WHyP could not describe well the black oil systems and highly concentrated mixed inhibitor systems. Here, we present the new version of the gas hydrate dissociation model, called WHyP2.

The model is based on statistical thermodynamics [14] and extended to multicomponent systems. In this model, the following equations relate the thermodynamic properties of gas hydrates to the molecular parameters

$$\Delta\mu_w^H = RT \sum_m \nu_m \ln \left( 1 + \sum_j C_{mj} f_j \right) \quad (1)$$

$$\theta_{mj} = C_{mj} f_j / \left( 1 + \sum_j C_{mj} f_j \right) \quad (2)$$

$$C_{mj} = (kT)^{-1} 4\pi \int_0^\infty \exp\{-W(r)/kT\} r^2 dr \quad (3)$$

where  $\Delta\mu_w^H$  is the difference in chemical potential between the filled gas hydrate lattice and the empty hydrate lattice,  $f_j$  is the fugacity of hydrating component  $j$ , and  $\theta_{mj}$  is the fraction of hydrate cavities of radius  $a_m$  occupied by solute  $j$ .  $C_{mj}$  is the fractional occupation of a cavity of type  $j$  and is the Langmuir constant of solute  $j$  in the cavity of radius  $a_m$ .  $W(r)$  is the spherically symmetric cell potential in the cavity with  $r$  measured from the center.  $\nu_m$  is the number of type  $m$  cavities per

molecule of water. For hydrates of structure sI,  $v_1 = 1/23$  and  $v_2 = 3/23$ , while for hydrates of structure sII,  $v_1 = 2/17$  and  $v_2 = 1/17$  [1]. Eq(1) can be used when ice is present with the hydrate. In the presence of liquid water, the chemical potential can be given as

$$\Delta\mu_w^L = RT \sum_m v_m \ln \left( 1 + \sum_j C_{m,j} f_j \right) + RT \ln X_w \quad (4)$$

where  $X_w$  is the mole fraction of water in the liquid phase. To deal with the multicomponent gas mixtures we introduced the short-range interaction parameter in the chemical potential,

$$\begin{aligned} \Delta\mu_w^L = RT & \left[ \prod_j \{ 1 + 3(\alpha_j - 1)y_j^2 - 2(\alpha_j - 1)y_j^3 \} \right] \\ & \times \left[ \sum_m v_m \ln \left( 1 + \sum_j C_{m,j} f_j \right) + \ln X_w \right] \end{aligned} \quad (5)$$

where  $\alpha_j$  is the interaction constant between the least volatile and each of the other more volatile hydrate forming molecule  $j$ , and  $y_j$  is the mole fraction of component  $j$ . In general, the values of interaction parameter adopted for the gas systems are 0.93 for methane, 1.1 for ethane, 1.1 for nitrogen, 1.1 for carbon dioxide and 1 for the remaining components. The nonsphericity of each cavity and contribution of water molecules in other cavities to the potential of each central cavity was accounted via the equation  $C = C^*Q^*$  [12], where  $C^*$  accounts for the change of the potential by water molecules in other cavities, and  $Q^*$  accounts for the nonsphericity of the cavities and molecules. Details on this are given in [12]. Fugacities of components in the fluid phases were calculated from the optimized Soave-Redlich-Kwong equation of state with temperature dependent van der Waals mixing rules. The model can account for the effects of solubility, GOR and interaction parameters responsible for the hydrate dissociation in black oil systems in an effective way. The interaction parameters (gas solubility) and activity coefficient of water were tuned to a set of measured data of the black oil systems as a function of temperature, pressure and GOR. This gave a set of parameters for predicting hydrate dissociation line for all other fluids.

The effect of inhibitors such as salt, alcohol, formate and glycol on gas hydrate temperature suppression ( $\Delta T$ ) was modeled using the following empirical relation

$$\Delta T = AX_{in} + BX_{in}^2 + CX_{in}^3 + D(T, P, X_{in})$$

where  $X_{in}$  is the effective inhibitor composition. A, B, and C are fixed parameters. D is a parameter depending on temperature, pressure and mole fraction of the inhibitors.  $X_{in}$  is related with the molecular weights, weight percentage of the inhibitors and degree of ionization of salts in water [18]. A, B, C and D parameters were determined using the data of hydrate equilibrium lines for multicomponent gases in the presence of inhibitors.

4. RESULTS AND DISCUSSION

In this section we present sample results only for methane, Green Canyon gas and black oil systems, with the major emphasis on black oil systems. The effect of a mixed inhibitor NaCl + MeOH on temperature suppression of black oil hydrate system is also investigated. These results are new and have not been published before. We have checked in detail the accuracy of the model using literature data for numerous gases, gas condensates and completion fluid systems, those results are not presented here due to the lack of space.

4.1. Methane and Green Canyon Gas Hydrates

To validate the experimental study on black oils, gas hydrate dissociation lines of methane and Green Canyon gases with DI water were measured as a calibration test of black oil measurements. Figure 6 compares our model results with our as well as literature data [ 1 ]. The model can describe the experimental data accurately,

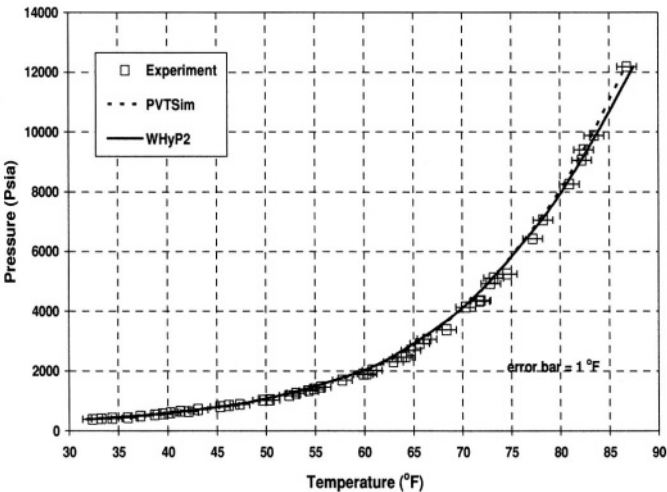


Figure 6. Hydrate equilibrium line of Methane.

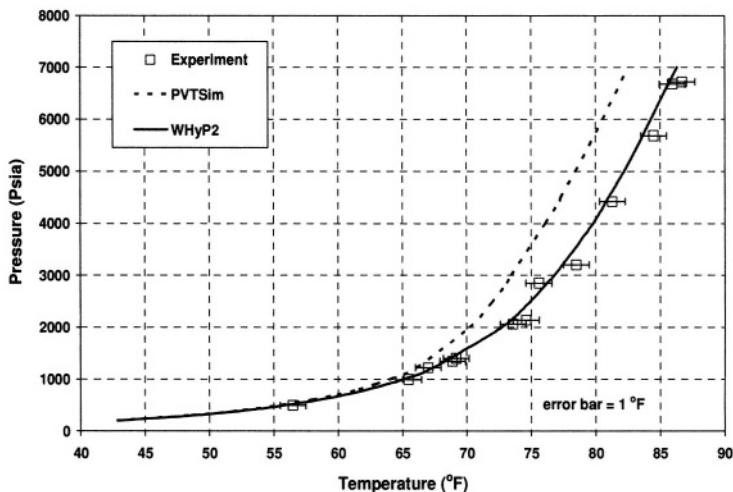


Figure 7. Hydrate equilibrium line of GC Gas.

well within 1 °F. A commercial simulator, PVTsim, can also describe the methane hydrate equilibrium line well. Figure 7 shows similar results for the Green Canyon gas with DI water. Our model results are in very good agreement with measured data. However, PVTsim results are seen to deviate from the data at high pressure (> 2000 Psia) and high temperature (> 70 °F).

#### 4.2. Black Oil Gas Hydrates

Figure 8 compares calculated results with measured data of hydrate equilibrium lines for black Oil I with DI water and also with three sets of inhibitor, 5 wt% NaCl + 5wt% MeOH, 10wt% NaCl + 10wt% MeOH, and 10wt% NaCl + 20wt% MeOH. WHyP2 predictions are seen to agree well with data for all the four cases and over the whole temperature and pressure ranges. For this oil, PVTsim predictions are seen to differ from experimental results, especially at high pressures. Figure 9 shows similar comparisons for Oil II with DI water and with two sets of inhibitor, 10wt% NaCl + 10wt% MeOH, and 10wt% NaCl + 20wt% MeOH. Our model and PVTsim agree with experiment very well. Likewise, Figures 10 and 11 show good comparisons between our model and experiment for Oil III and Oil IV. PVTsim predictions are also in agreement with experimental results. However, at the highest concentration range of inhibitor, 10wt% NaCl + 20wt% MeOH, both PVTsim and WHyP2 predictions are seen to differ from experimental data appreciably. The possible cause of this disagreement may lie in the measurement due to inadequate

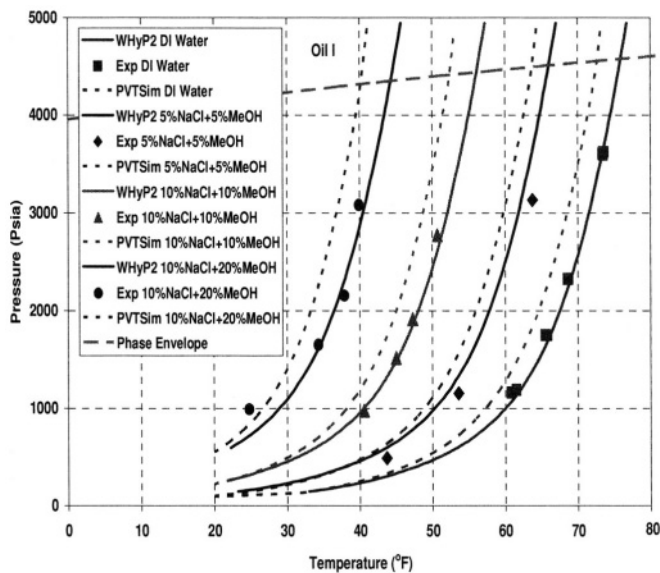


Figure 8. Hydrate equilibrium line of Oil I.

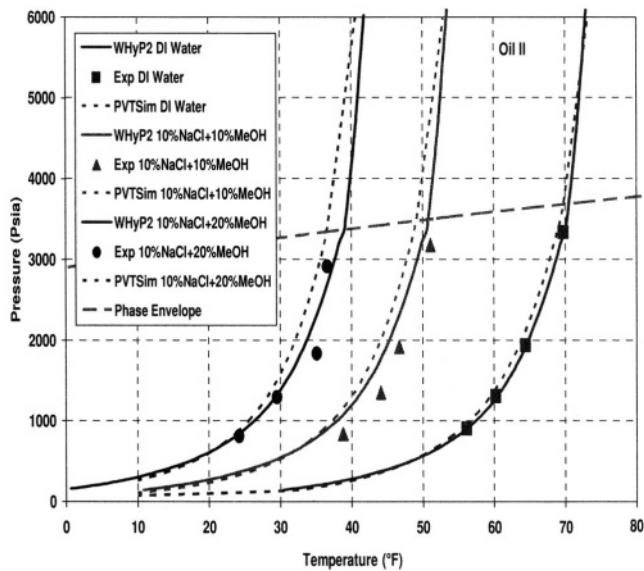


Figure 9. Hydrate equilibrium line of Oil II.



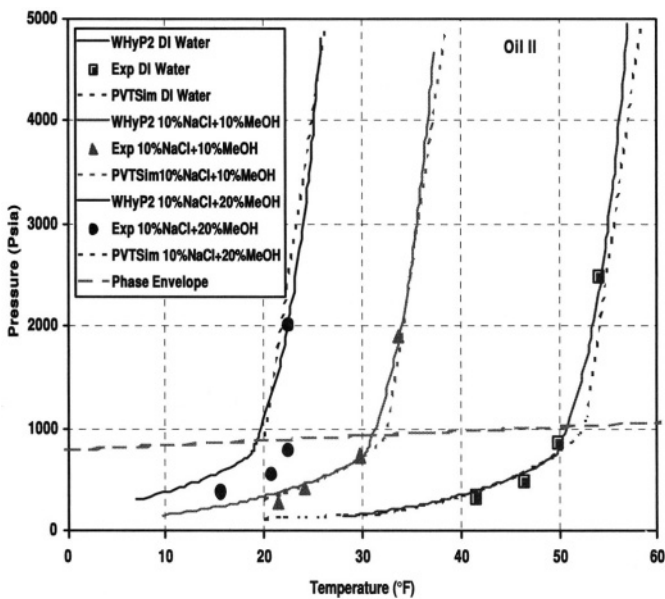


Figure 10. Hydrate equilibrium line of Oil III.

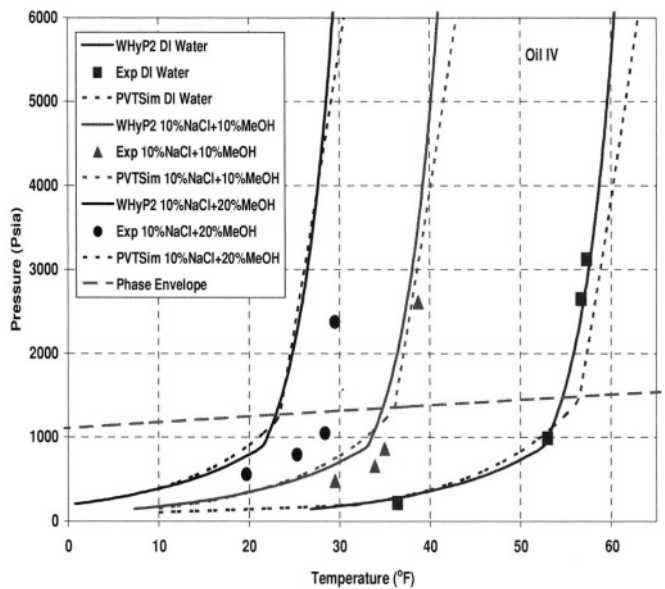


Figure 11. Hydrate equilibrium line of Oil IV.

mixing and competing effects of the limited amount of the hydrate forming gases to form hydrates and dissolve in the liquid solvent with highly concentrated inhibitor.

## 5. CONCLUSIONS

The new sets of results for the hydrate dissociation line of methane and Green Canyon gases are reported. For black oils, the effects of WOR and GOR on hydrate equilibrium lines are found to be significant. For example, the lowering of GOR from 564 scf/stb (Oil II) to 267 scf/stb (Oil III) affects significantly the hydrate temperature suppression. This magnitude depends on pressure and temperature. In black oil systems the heating rate of 1 °F/hr can be adequate to represent the hydrate equilibrium points within  $\pm 1$ –2 °F uncertainty.

An improved version of the gas hydrate dissociation model is developed. The model can predict the dissociation line of gases and gas condensates well within 1–2 °F uncertainty. The model can describe accurately the hydrate dissociation line of high GOR black Oil I and Oil II with and without the inhibitor NaCl + MeOH. For the lower GOR (< 300) Oil III and Oil IV, discrepancy between the model predictions and experimental data increases as the strength of the inhibitor NaCl + MeOH increases, especially at lower pressures (< 1000 Psia). This may be attributed to the solubility problem and competing effects of the limited amount of the hydrate forming gases to form hydrates and dissolve in the liquid solvent in attaining the equilibrium during the experiment. We note that Oil II and Oil III exhibit the same characteristic properties, but differ in their GOR appreciably. The model predictions have also been verified successfully with other numerous sets of hydrate equilibrium data for gas, gas condensate and completion fluids with mixed inhibitors, those results are not reported here. In general, the various comparisons of model predictions with existing experimental data show that our model can be applied to gas, gas condensate, drilling completion fluid and black oil systems reliably.

## ACKNOWLEDGMENT

We would like to thank DeepStar for funding this project through project number CTR 5208. Our special thanks are to David Hopgood of Unocal for serving as the champion of the project. We thank to C. Irani, R. Banda, R. Petruska and K. Hoffman of Westport for their help during the course of this study.

## REFERENCES

1. Sloan, E. D. *Clathrate Hydrates of Natural Gases*, 2<sup>nd</sup> Edn., Marcel Dekker, New York, 1998.
2. Sloan, E. D. *Hydrate Engineering*, SPE Monograph (J. Bloys), V.21, Richardson, TX, 2000.

3. Makogon, Y. F. Hydrates of Natural Gas, Pennwell Publishing, Tulsa, 1997.
4. Carroll, John. Natural Gas Hydrates- A Guide for Engineers, Butterworth-Heinemann, 2003.
5. Paull, C. and Dillon, W. P. Natural Gas Hydrates: Occurrence, Distribution and Detection. Geophysical Monograph Series. 2001, V.124.
6. Kvenvolden, K. A. A Primer on Gas Hydrate, ed. D.G. Howell, The Future of Energy Gases, USGS Professional Paper. 1993, 1570, p. 279, p. 555.
7. Lowrie, A., Max, M. D., Hamiter, R., Lerche, I. and Bagirov, E. Trans. Gulf Coast Ass. Soc. 1997, XLV11, p. 311.
8. Howell, D. G. The Future of Energy Gases, USGS Professional Paper. 1993, 1570, p. 890.
9. Collett, T. S., Lewis, R. and Uchida, T. Growing Interest in Gas Hydrate, Oilfield Review, 2000, Summer, p. 42.
10. Proceedings of the 4<sup>th</sup> International Conference on Gas Hydrates, Yokohama, Japan. 2002, Vols. 1 & 2, May 19–23.
11. Dallimore, S. R., Uchida, T. and Collett, T. S. Scientific Results from JAPEX/JNOC/GSC Mallik 2L-38 Gas Hydrate Research Well, GSC Bulletin. 1999, 544, p. 281.
12. Holder, G. D., Zetts, S. P. and Pradhan, N. Reviews in Chemical Engineering, 1988, 5, 1; Holder, G.D. (ed) Gas Hydrates: Challenges for the Future, Annals NY Acad. Sci. 2000.
13. Max, M. D. Natural Gas Hydrate: in Oceanic and Permafrost Environments. Kluwer Academic Publishers, Dordrecht, The Netherlands, 2000, p. 414.
14. van der Waals, J. H. and Platteeuw, J. C. Adv. Chem. Phys. 1959, 2, p. 1.
15. Parrish, W. P. and Prausnitz, J. M. Ind. Eng. Chem. Process Des. Dev. 1972, 11, p. 26.
16. Wu, B.-J., Robinson, D. B. and Ng, H.-J. J. Chem. Thermodyn. 1976, 8, p. 461.
17. Ng, H.-J. and Robinson, D. B. Annals NY Acad. Sci. 1994, 715, p. 450.
18. Yousif, M. and Young, D. Proceedings of the 73<sup>rd</sup> GPA Annual Convention, 1994, p. 94.

## Section III

# Laboratory Studies of Hydrates

*This page intentionally left blank*

# 10

## Solubility Measurements for CO<sub>2</sub> and Methane Mixture in Water and Aqueous Electrolyte Solutions near Hydrate Conditions

**Ying Irene Zhang, Pallav Jain, Roger Chen,  
Douglas Elliot,\* Kyoo Song, Walter Chapman,  
Riki Kobayashi, and Heng-Joo Ng**

### 1. INTRODUCTION

Gas hydrates are crystalline molecules formed by a physical reaction between water and low molecular weight gases [2]. Hydrate formation involves entrapment of gas molecules in the cavities of the hydrogen-bonded structure of water. The research on ice has shown that as the temperature of water decreases there is increasing

---

YING IRENE ZHANG • IPSI LLC 3000 Post Oak Blvd., Houston, TX 77056, U.S.A.

PALLAV JAIN • IPSI LLC 3000 Post Oak Blvd., Houston, TX 77056, U.S.A.

ROGER CHEN • IPSI LLC 3000 Post Oak Blvd., Houston, TX 77056, U.S.A.

DOUGLAS ELLIOT • IPSI LLC 3000 Post Oak Blvd., Houston, TX 77056, U.S.A.

KYOO SONG • Chemical Engineering Department, Rice University, P.O. Box 1892, Houston, TX 77251, U.S.A.

WALTER CHAPMAN • Chemical Engineering Department, Rice University, P.O. Box 1892, Houston, TX 77251, U.S.A.

RIKIKOBAYASHI • Chemical Engineering Department, Rice University, P.O. Box 1892, Houston, TX 77251, U.S.A.

HENG-JOO NG • Oilphase-DBR, Schlumberger Canada Limited, Edmonton, Alberta, Canada

\* delliot@bechtel.com

tendency for water molecules to associate and to form clusters. Similarly, when the temperature of a water and hydrate forming gas system is decreased, the water molecules start to form hydrogen-bonded clusters, which trap the gas molecules. The gas molecules contribute to hydrate formation by stabilizing these cage-like structures. It has been proposed by several researchers that hydrate formation is preceded by the formation of hydrate nuclei [3–5]. These hydrate nuclei are merely individual cage-like structures, which are randomly formed and broken till the temperature (of the hydrate forming gas—water system) decreases below a critical point. After this critical point is reached, the hydrate nuclei start to agglomerate to form hydrates. The theoretical temperature at which a gas and water in equilibrium will form hydrates is called the catastrophic temperature,  $T_{ct}$ . In laboratory scale experiments, hydrate formation may be observed easily because it is associated with the sudden increase in the gas solubility in the aqueous phase.

The solubilities of methane and natural gas components such as  $\text{CO}_2$  and ethane in water are of considerable interest to petroleum and gas industries. The solubilities of natural gas components in water are essential in determining the formation, growth, and dissociation of gas hydrates. Recent studies on solubilities of gases such as methane, ethane, and  $\text{CO}_2$  in water, near the hydrate formation temperature indicated that the solubility of the gas in water increased significantly at a temperature slightly above the hydrate formation temperature [3–5]. The increase in the solubility may be due to the formation of hydrate precursors near the hydrate formation point. Since the distribution coefficients of gas components in gas phase and water phase are different near hydrate conditions, separation of  $\text{CO}_2$  from the multi-component gas mixture can be achieved by contacting the gas with water, just above the hydrate formation point. Knowledge of gas solubility is required for successful design of gas separation processes. Several papers and patents discussed about the use of hydrates for separation of gases [6–8]. However, since these processes involve formation of hydrates, special equipment is required to handle slurries. A few studies have been carried out on hydrate phase equilibria of  $\text{CO}_2$  and  $\text{CH}_4$  mixture in pure water and electrolyte solutions [9–14]. Most of those studies focused on the hydrate formation region and little published experimental data exist on the solubility of  $\text{CO}_2$  and  $\text{CH}_4$  mixture in water and electrolyte solutions near but above the hydrate formation temperature. High solubility is only a part of the requirement for gas separation. In addition to high solubility, good selectivity is also essential for decreasing the loss of valuable hydrocarbon due to co-absorption. Loss of hydrocarbons due to co-absorption is a major disadvantage of physical absorption processes. Thus, this work aims to investigate the solubility and selectivity of  $\text{CO}_2$  and  $\text{CH}_4$  gas mixture in pure water and electrolyte solutions near (but above) the hydrate formation conditions where incomplete data had existed previously.

## 2. EXPERIMENTAL

Two types of experiments were conducted at Rice University and Oilphase-DBR respectively. Most of the experimental data presented in this work were obtained using the temperature ramping technique described below at Rice University. The experiments at Rice University were equilibrium experiments, *i.e.*, gas and liquid were contacted for a long time to ensure that an equilibrium was established and then the gas composition and solubility measurements were performed. The results obtained from these experiments represent the best separation that can be achieved in a single stage contactor. At Oilphase-DBR, a few experiments were conducted to find out the equilibrium compositions by running the process in a closed loop without regeneration. These experiments were performed to confirm the results from Rice University.

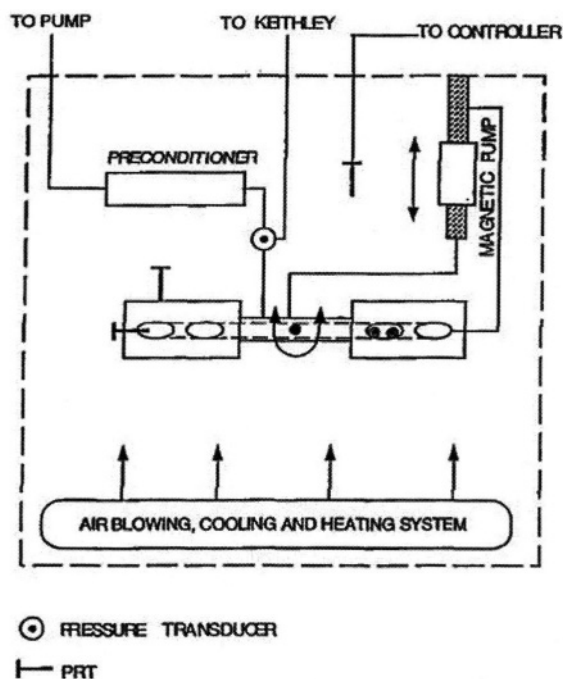
### 2.1. Apparatus

Figure 1(a) shows the experimental apparatus that was used to conduct the experiments at Rice University. The equipment is the same as that described by Song *et al.* [3] The isobaric solubility of the gas mixture in the solvent was observed at various temperatures by temperature ramping. A fully automated Ruska pump shown in Figure 1(b), a Digital Positive Displacement pump, was coupled to the temperature-ramped hydrate apparatus to maintain the system pressure constant. This pump was capable of adding and/or pulling gas to or from the cell at precise rates. The hydrate reactor and the pump were each controlled at a fixed constant pressure whilst being connected with capillary tubes of known dimensions. Thus, it was possible to precisely follow the volume of the gas mixture dissolving in the solvent at any given time or temperature to generate the curves of volume and temperature versus time as shown in Figure 2. The experimental apparatus included the following parts:

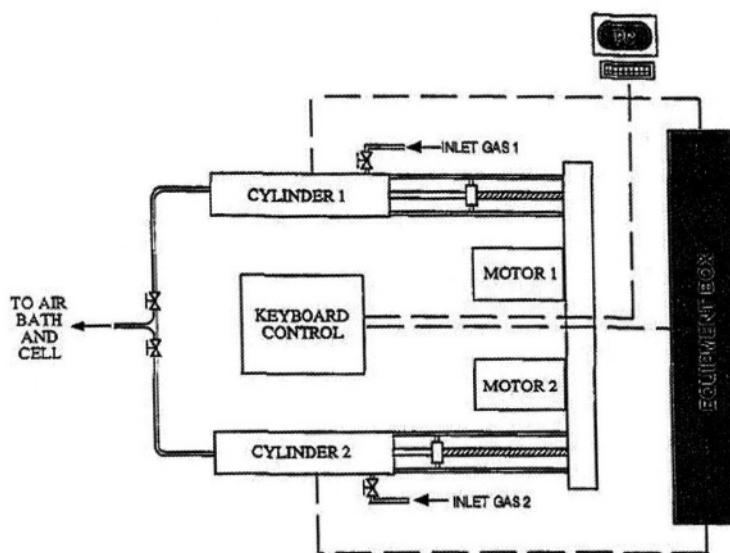
#### 2.1.1. Rocking cell and magnetic pump

A rocking Jergunson type visual cell was used as a hydrate reactor. The cell contained ½ in. type 440 stainless steel balls, which rolled back and forth along a 5/8 in. bore. A magnetic pump was also incorporated in the experimental system to recirculate the gas within the hydrate reactor. Two small Beryllium springs were mounted to the cushion and protect the platinum resistance thermometer (PRT), located at the end of the cell and immersed in water. The visual cell made it possible to visually confirm the hydrate formation in the cell. Three PRTs were strategically installed to measure the liquid temperature and the bath temperature. The three





(a)



(b)

**Figure 1.** (a) The thermostatic hydrate apparatus. (b) The Ruska digital displacement pump.

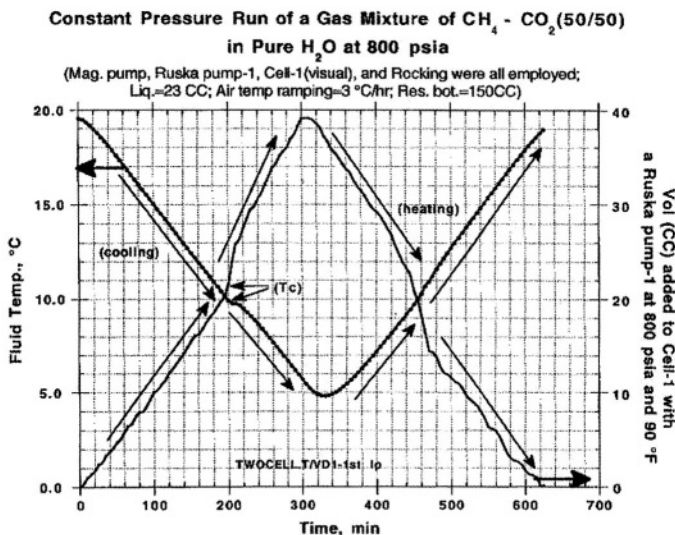


**Figure 2.** Constant pressure run curves of the 50 mole % methane—50 mole %—water system at 800 psia (volume and temperature versus time). (Mag. pump, Ruska pump-1 Cell-1 (visual), and Rocking were all employed; Liq. = 23 CC; Air temp ramping = 3 °C/hr; Res. bot. = 150CC).

thermometers were placed on the cell wall, in the air bath and in the liquid water. A Ruska system pressure transducer measured the pressure in the system. A PC collected the signals from PRTs and the pressure transducer. The cell was also provided with a port to withdraw a small amount of gas, when required, for gas composition analysis by gas chromatography.

### 2.1.2. Air bath

The air bath housed the above-mentioned visible cell, a magnetic pump and a reservoir bottle added in line as a preconditioner. Both heating and refrigeration were used to control the temperature of the bath. It was possible to control the temperature in the air bath with in millidegree range.

### 2.1.3. Ruska digital positive displacement pump

A Ruska positive displacement pump played a very important role in the measurements. The pump had a constant pressure, variable speed option, whereby the pressure in the system (in this case the hydrate reactor) could be maintained at the desired operating point. The pump provided an ability to track the volume of the gas that was injected in the system at any given time.

## 2.2. Materials and Sample Preparation

The 50 mole %  $\text{CH}_4$  + 50 mole %  $\text{CO}_2$  gas mixture was the Gravimetric Standard mixture purchased from MG Industries. The methane and carbon dioxide mixture was used without further purification. Deionized water was used in the experiments. The sodium sulfate ( $\text{Na}_2\text{SO}_4$ ) was Certified ACS grade obtained from Fisher Scientific. The sodium chloride ( $\text{NaCl}$ ) was Certified ACS grade obtained from J. T. Baker Chemical Co.

Appropriate quantities of the electrolyte were weighed on a balance with a readability of 0.002 g and added to a weighed quantity of water. The mixture was stirred at room temperature to dissolve the electrolyte.

## 2.3. Procedure

For the equilibrium experiments at Rice University, the apparatus was purged and evacuated before every measurement. Once the apparatus was evacuated, 23 mL of solvent was injected into the hydrate reactor (visual cell). The system was then charged with gas (using the Ruska pump) and pressurized to the desired system pressure. The temperature in the air bath was controlled so that the system could be equilibrated to an initial temperature of 18 °C (for most of the experiments). The cell was then rocked and the magnetic pump was started to recirculate the gas (for improved contact with the solvent). The system was left to equilibrate for half an hour and subsequently the volume of gas charged to the cell (from the pump) was recorded. Since the cell volume was known, this initial charge provided us with the solubility of the gas in the solvent at 18 °C. Once the initial solubility was recorded, the air bath temperature was changed at a rate of 3 °C/hour. This temperature ramping rate was slow enough to let the system equilibrate at the new temperature. The system temperature was ramped below the hydrate formation point and then the temperature was ramped back to 18 °C. The additional volume (over the initial charge) of gas charged into the cell (during the cooling cycle) and released from the cell (during the heating cycle) was obtained from the Ruska pump reading. The result from one such ramping run was shown in Figure 2. The initial ramping run was used to identify the system hydrate formation point. Using this knowledge, some temperatures between 18 °C and the catastrophic temperature ( $T_{\text{ct}}$ ) were chosen as temperatures of interest. Once these temperatures of interest were established, the gas compositions and solubility at these temperatures of interest were identified in a second run. In this second run, the system temperature was changed abruptly to the various temperatures of interests and the system was allowed to settle down for an hour to equilibrate. Once the system had equilibrated, the volume of gas added to the cell (over the initial charge) was recorded and then a sample of the gas was withdrawn from the cell for gas chromatography to measure the mixture composition. The gas composition in the cell was recorded and the system temperature was changed to the next temperature of interest.

Subsequently, a mass balance method is used to determine the gas solubility in the liquid phase. The volume of gas in the hydrate reactor,  $V_{\text{cell}}$ , was known. As described in the procedure, in the first run, the cell was equilibrated to an initial temperature and pressure, and the initial charge  $V_0$  was recorded. In the second run, once the system was equilibrated to the new temperature, the additional volume of gas charged to the cell,  $V$ , was recorded and a small portion of the gas was withdrawn for analysis. The moles of gases dissolved in the liquid are computed by

$$n = \rho_p(V_0 + V) - \rho(T)V_{\text{cell}}, \quad (1)$$

where  $\rho(T)$  is the gas molar density at the temperature  $T$  and  $\rho_p$  is the molar density of gas at the pump conditions.

Knowing that the mole fraction of solute  $i$  in the gas phase is  $y_i$  at temperature  $T$  and knowing that the initial solute  $i$  mole fraction in the gas phase (in Ruska pump) is  $y_{i,0}$ , the solute  $i$  mass balance gives moles of solute  $i$  dissolved in the liquid phase,

$$n_i = \rho_p(V_0 + V)y_{i,0} - \rho(T)V_{\text{cell}}y_i. \quad (2)$$

Thus, the solubility of solute  $i$  in the liquid phase is given by

$$x_i = \frac{n_i}{n + n_L}, \quad (3)$$

where  $n_L$  is the moles of the liquid.

The carbon dioxide relative selectivity over methane in the aqueous phase,  $\alpha$ , is defined as

$$\alpha = \frac{x_{\text{CO}_2}/y_{\text{CO}_2}}{x_{\text{CH}_4}/y_{\text{CH}_4}}, \quad (4)$$

where the subscripts **CO<sub>2</sub>** and **CH<sub>4</sub>** denote carbon dioxide and methane respectively.

In addition, some experiments were conducted to obtain the gas solubility directly from the Gas/Liquid Ratio (GLR) measurements at Rice University. Figure 3 shows the schematic diagram for the apparatus used for the GLR measurements. The ratio of the gas dissolved in liquid to the liquid was determined gravimetrically as shown in Figure 3 or by expanding the dissolved gas to the ambient pressure.

To determine the amount of gas dissolved in the liquid, a liquid sample was withdrawn from the equilibrium visual cell. A cleaned cell-A with an internal volume of about **10 cm<sup>3</sup>** was evacuated and connected to the equilibrium cell and

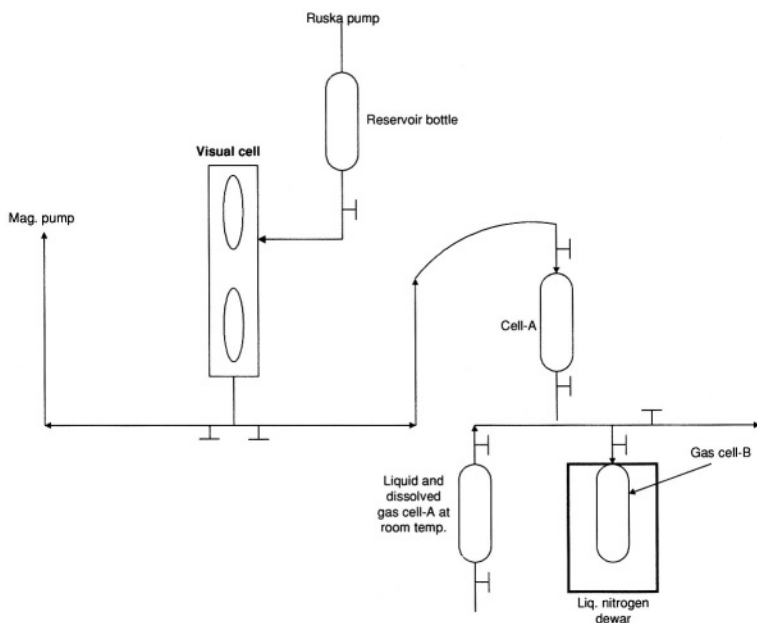


**Figure 3.** Schematic diagram of the Gas/Liquid Ratio (GLR) experiments at Rice University.

kept inside the bath for thermal equilibrium. A valve on the cell-A was opened extremely slowly while the gas source in the constant pressure. The Ruska pump was connected with the equilibrium cell to maintain constant system pressure during the sample withdrawal. When the cell-A was filled with liquid sample, cell-A was disconnected from the equilibrium cell.

An empty steel bottle was connected onto cell-A. The total amount of sample (liquid and gas dissolved in the liquid) was determined from the difference in mass before and after the sample collection in the cell-A. The other end of the empty bottle was further connected to the evacuated cell-B which was placed in a liquid nitrogen dewar. A vacuum gauge with a maximum reading of 760 mmHg was installed between the empty bottle and the cell-B. The valve to cell-A was slowly opened while the pressure was monitored so that the pressure remained below 760 mmHg. We expected that the methane would be trapped in cell-B, which was also indicated by a sudden pressure drop demonstrated by the gauge. Since the vapor pressure of water is small at ambient conditions, we expect little water in cell-B. When the valve to cell-A was fully open and the pressure dropped below 35 mmHg, the valves to cell-A and B were closed. A Seederer-Kohlbusch scale with a capacity of 2.0 Kg and an accuracy of 0.002 g was employed to determine the mass of each cell. The net amounts of liquid in the cell-A and the gas transferred to the cell-B were determined to provide the ratio. The combined amount of liquid

and gas compared well with that previously taken from the equilibrium cell to cell-A. The gas collected in cell-B was injected to gas chromatography for composition analysis.

Another approach was pursued by employing an expansion burette. The cell-A and an empty bottle were vertically connected in series. At ambient temperature, they were connected to a mercury-expansion burette. The expanded volume of the gas to the ambient pressure was converted to mass from the P-V-T relation. The ratio of the gas to liquid was determined from the amounts of dissolved gas and the gravimetrically determined amount of liquid contained in the cell-A. The results from this approach and the previous gravimetric method showed a close agreement within the experimental uncertainty.

### 3. RESULTS

A typical constant pressure run result is presented in Figure 2. The temperature ramping technique shows more details regarding the formation/decomposition of hydrates. The gas intake by the water increases with decreasing the system temperature. Gradually, phase transition occurs and the solid particles become visible. The onset of hydrate formation takes place at point  $T_{ct}$ , which is known as the catastrophic temperature. The amount of solid present in the water increases tremendously and the solidification starts. Heating the system will result in the dissociation of the hydrates. The hydrates melts and the solid phase become invisible.

Using the calculation procedure described above, the results from first and second runs for each system were used to identify the gas solubility in the solvent. Subsequently, some experiments were conducted to obtain the gas solubility directly from Gas/Liquid Ratio (GLR) measurements. These experimental results were compared with the gas solubility results obtained by mass balance in Table 1. For the systems listed in Table 1, the results obtained by the mass balance method

**Table 1.** Comparison of the CO<sub>2</sub> solubility from the cell side mass balance with the CO<sub>2</sub> solubility from GLR measurements (50 mole % CH<sub>4</sub> + 50 mole % CO<sub>2</sub> mixture in various solvents,  $P = 800$  psia)

Solvent	Catastrophic Temperature $T_{ct}$ (°C)	$T$ (°C)	$x_{CO_2}$ from mass balance method (mole-fraction)	$x_{CO_2}$ from GLR method (mole-fraction)	Deviation (%)
Pure Water	10.3	11.0	0.01760	0.01821	-3.35
5 wt.% Na <sub>2</sub> SO <sub>4</sub>	9.0	9.5	0.01100	0.01040	5.77
10 wt.% Na <sub>2</sub> SO <sub>4</sub>	9.0	9.8	0.00894	0.01020	-12.35
4 wt.% NaCl	8.7	9.5	0.00945	0.01140	-17.07
8 wt.% NaCl	6.5	7.5	0.00850	0.00880	-3.41

Table 2. Solubility and selectivity of 50 mole % CH<sub>4</sub> + 50 mole % CO<sub>2</sub> mixture in pure water and various electrolyte solutions at 800 psia

Solvent	<i>T</i> (°C)	CO <sub>2</sub> content in flash gas from liquid (mole %)	<i>x</i> <sub>CO<sub>2</sub></sub> (mole-fraction)	<i>x</i> <sub>CH<sub>4</sub></sub> (mole-fraction)	Selectivity <i>α</i>
Pure Water <sup>a</sup>	10.6	99.3	0.01640	0.000111	192
10 wt.% Na <sub>2</sub> SO <sub>4</sub> <sup>b</sup>	9.8	98.0	0.01020	0.000207	56
4 wt.% NaCl <sup>b</sup>	9.5	96.0	0.01140	0.000462	28

<sup>a</sup>: The data by Oilphase-DBR; <sup>b</sup>: The data by Rice University.

compare relatively closely with the results by the direct GLR measurements. The good agreement of the results by mass balance method with those by GLR method leads to confidence in the validity of the mass balance technique and the quality of the data.

Table 2 shows the composition analysis result of the flash gas (from the liquid sample) from both Rice University and Oilphase-DBR. It was found that in all the cases the flash gas had CO<sub>2</sub> content ranging from 96–99 mole % and had a very small amount of methane. For a CO<sub>2</sub> + CH<sub>4</sub> mixture in water near the hydrate formation temperature, the solubility of CO<sub>2</sub> in water is high while the methane solubility is comparably lower. This confirmed that the co-absorption of hydrocarbons would not be a problem for gas separation using the water near hydrate conditions.

3.1. Pure Water

In this work, Henry’s law is used to model the gas solubility in pure water. The data analysis is based on three assumptions: (1) The liquid phase has nearly constant volume; (2) The gas phase is nearly all CH<sub>4</sub> and CO<sub>2</sub>; (3) There is no interaction between solute species in the aqueous phase, *i.e.*, the solubility of each gas is independent of the other.

Henry’s law provides a good approximation for gas solubility when the solubility is small. At high pressures, Henry’s Law can be expressed as the well-known Krichevsky-Kasarnovsky (KK) equation [1]:

$$\ln \left( \frac{f_i}{x_i} \right) = \ln H_{i,w} + \frac{\bar{v}_i^\infty (P - P_w^S)}{RT}, \tag{5}$$

where *f<sub>i</sub>* is the fugacity of a given solute *i*, *R* is the gas constant, *H<sub>i,w</sub>* is its Henry’s constant, *P* is the pressure, *P<sub>w</sub><sup>S</sup>* is the vapor pressure of the water, and *v<sub>i</sub><sup>∞</sup>* is the partial molar volume of the solute *i* at infinite dilution. The fugacity of the gas was computed by SUPERTRAPP [15], a NIST computer program that calculates

thermodynamic and transport properties based on the Peng-Robinson (PR) equation of state (EOS) [16] and the NIST extended corresponding states model. Henry's constant was given by Harvey [17] for CO<sub>2</sub> in pure water:

$$\ln(H_{\text{CO}_2, \text{w}}) = \ln(P_{\text{w}}^{\text{S}}) - 9.4234/T^* + 4.0087(1 - T^*)^{0.355}/T^* + 10.3199 \exp(1 - T^*)(T^*)^{-0.41}, \quad (6)$$

where the reduced temperature  $T^* = T/T_{\text{c,w}}$  and  $T_{\text{c,w}}$  is the water's critical temperature. The solvent vapor pressure for water is computed with the equation of Saul and Wagner [18]. The partial molar volume of CO<sub>2</sub> at infinite dilution,  $\bar{v}_{\text{CO}_2}^{\infty}$  is calculated with the following correlation [19],

$$\frac{\bar{v}_{\text{CO}_2}^{\infty} P_{\text{c,CO}_2}}{RT_{\text{c,CO}_2}} = 0.095 + 2.4 \left( \frac{P_{\text{c,CO}_2} T}{C_{\text{w}} T_{\text{c,CO}_2}} \right), \quad (7)$$

where  $P_{\text{c,CO}_2}$  is the critical pressure of CO<sub>2</sub>,  $T_{\text{c,CO}_2}$  is the critical temperature of CO<sub>2</sub>,  $C_{\text{w}}$  is the cohesive energy density of water.

Based on the above equations, the CO<sub>2</sub> solubility in pure water was compared against the CO<sub>2</sub> solubility that was predicted by Henry's law in Figure 4. Figure 4 includes the experimental data from both Rice University and Oilphase-DBR for

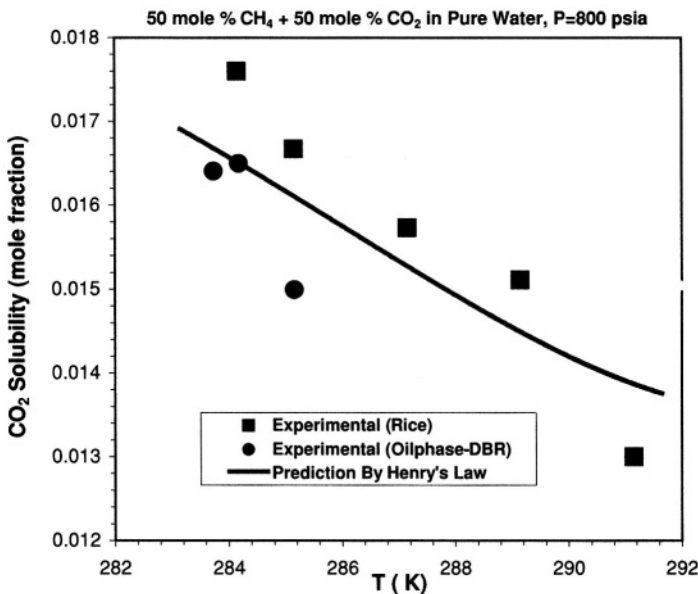


Figure 4. CO<sub>2</sub> solubility for the 50 mole % CH<sub>4</sub> + 50 mole % CO<sub>2</sub> mixture in pure water at 800 psia.



the 50 mole %  $\text{CH}_4$ —50 mole %  $\text{CO}_2$ —water system. The gas solubility data from Rice University compares relatively closely with the results in the flow apparatus from Oilphase-DBR. The agreement between the experimental data and the prediction from Henry's law is good. Within the experimental accuracy, the experimentally measured  $\text{CO}_2$  solubility in the ternary system is close to the solubility predicted by Henry's law in the form of the Krichevsky-Kasarnovsky equation using the parameters of the binary system. The Krichevsky-Kasarnovsky equation was found to be an adequate representation of gas solubility near (but above) hydrate formation point. Our results are consistent with Dhima *et al.*'s conclusion for  $\text{CO}_2$  and  $\text{CH}_4$  mixtures in water under high pressure [20].

### 3.2. Electrolyte Solutions

The  $\text{CO}_2$  solubility in the electrolyte solutions containing  $\text{NaCl}$  and  $\text{Na}_2\text{SO}_4$  of various concentrations is compared with the gas solubility in pure water in Figure 5. These experiments were conducted to see if seawater could be used as a potential solvent for gas separation. These plots demonstrate the salting out effects of the electrolytes. As the electrolyte concentration in the solution increases, the  $\text{CO}_2$  solubility in the solution decreases due to the salting out effect. The catatrophic temperature data in Table 1 also demonstrate the inhibiting effects of the

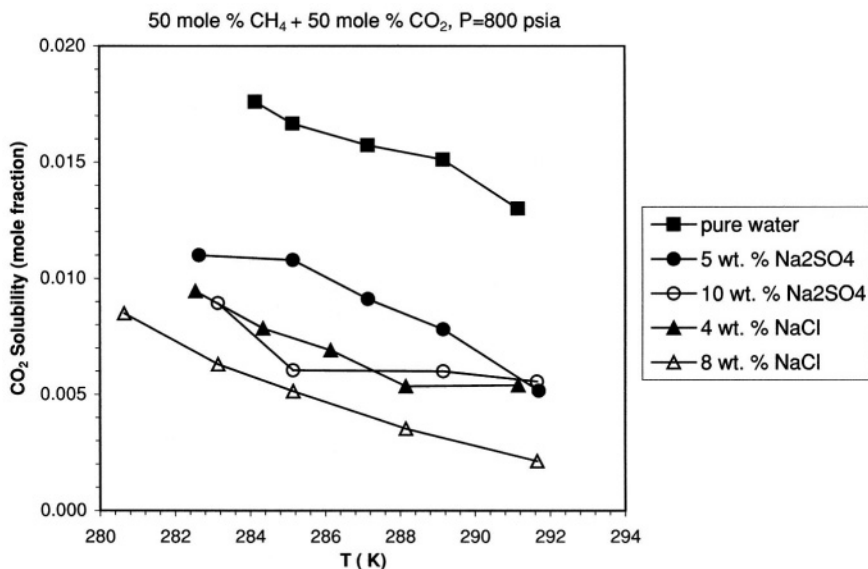


**Figure 5.** Experimental  $\text{CO}_2$  solubility for the 50 mole %  $\text{CH}_4$  + 50 mole %  $\text{CO}_2$  mixture in pure water and various electrolyte solutions at 800 psia.

electrolytes, as indicated by the lower hydrate formation temperature for systems with higher salt concentrations. It is found that the 10 wt.%  $\text{Na}_2\text{SO}_4$  solution shows a less salting out effect than the 8 wt.% NaCl solution. This indicates that NaCl has greater salting out effect than  $\text{Na}_2\text{SO}_4$ .

### 3.3. Selectivity

The selectivity data of  $\text{CO}_2$  over  $\text{CH}_4$  in the aqueous phase are presented in Table 2. The selectivity of  $\text{CO}_2$  over  $\text{CH}_4$  in pure water is about 190 near hydrate formation temperature. Carbon dioxide is selectively dissolved in the aqueous phase. The methane solubility data did not exhibit the salting out effects of the electrolytes. This may be due to the relatively big experimental error in low solubility measurements. No definite conclusion can be drawn on the effects of electrolytes on the relative selectivity of  $\text{CO}_2$  over  $\text{CH}_4$  in the aqueous phase based on the data listed in Table 2.

As the experimental results indicate, high  $\text{CO}_2$  solubility is observed near the hydrate formation conditions. The high selectivity coupled with the high solubility near the hydrate formation conditions would make the gas treating processes operating in this region economical, if the acid gas removed from the feed gas has to be disposed off without venting or incineration. The flow experimental results from Oilphase-DBR indicated that the regeneration of water may be achieved by varying the temperature and pressure conditions of the process.

## 4. CONCLUSIONS

The gas solubility of the  $\text{CH}_4 + \text{CO}_2$  mixture in pure water, and electrolyte solutions containing NaCl and  $\text{Na}_2\text{SO}_4$  was measured in the temperature range of 280–292 K. Within the experimental accuracy, the experimentally measured gas solubility obeys the Henry's law in the form of the Krichevsky-Kasarnovsky equation near (but above) hydrate formation temperature. The ternary solubility data can be predicted by the binary ones. It was found that the  $\text{CO}_2$  solubility in the aqueous phase decreases in the presence of the electrolytes. Very accurate methane solubility data in the ternary system are required to identify the effects of electrolytes on solubility and selectivity.

## ACKNOWLEDGEMENTS

The authors are grateful to Mr. Hans J. Nerenberg for his help with experiments performed at Oilphase-DBR. Also, the authors would like to thank the Ruska Instrument Corporation for providing us with a pump to run the experiments.

## NOMENCLATURE

$C$	cohesive energy density
$f$	fugacity
$H$	Henry's law constant
$n$	number of moles
$P$	pressure
$R$	gas constant
$T$	temperature
$V$	volume
$v$	molar volume
$x$	mole fraction in liquid phase
$y$	mole fraction in gas phase
$\alpha$	selectivity
$\rho$	gas molar density

## Subscripts

0	initial
c	critical
cell	visual cell
CH <sub>4</sub>	methane
CO <sub>2</sub>	carbon dioxide
ct	catastrophic
i	gas component
L	liquid
p	pump conditions
w	water

## Superscripts

S	saturation
$\infty$	infinite dilution
*	reduced

## REFERENCES

1. Krichevsky, I. R.; Kasarnovsky, J. S. *Journal of the American Chemical Society* 1935, 57, 2168–2171.
2. Sloan, E. D., Jr. *Clathrate Hydrates of Natural Gases*; Marcel Dekker, INC.: New York, 1998.
3. Song, K. Y.; Feneyrou, G.; Fleyfel, F.; Martin, R.; Lievois, J.; Kobayashi, R. *Fluid Phase Equilibria* 1997, 128, 249–260.

4. Feneyrou, G. Elucidation of the Formation and Decomposition of Clathrate Hydrates of Natural Gases through Gas Solubility Measurements. M.S. Thesis, Rice University, 1996.
5. Besnard, G. Thermodynamics and Kinetics Studies of Formation and Decomposition of Clathrates Hydrates of Methane, Carbon Dioxide and Their Mixtures Using A Differential Heat Flux Calorimeter. M.S. Thesis, Rice University, 1997.
6. Kang, S.-P.; Lee, H. *Environmental Science & Technology* 2000, 34 (20), 4397–4400.
7. Crowther, J. F.; Vernon, M. Gas Hydration, United States Patent, The M. W. Kellogg Company, 1946.
8. Hutchinson, A. J. L.; Bechtold, I. C. Treatment of Hydrocarbon Gases by Hydration, United States Patent, The Fluor Corporation, LTD., 1945.
9. Seo, Y.-T.; Lee, H.; Yoon, J.-H. *Journal of Chemical and Engineering Data* 2001, 46 (2), 381–384.
10. Dholabhai, P. D.; Bishnoi, P. R. *Journal of Chemical and Engineering Data* 1994, 39 (1), 191–194.
11. Dholabhai, P. D.; Parent, J. S.; Bishnoi, P. R. *Fluid Phase Equilibria* 1997, 141, 235–246.
12. Ohgaki, K.; Takano, K.; Sangawa, H.; Matsubara, T.; Nakano, S. *Journal of Chemical Engineering of Japan* 1996, 29 (3), 478–483.
13. Kang, S.-P.; Chun, M.-K.; Lee, H. *Fluid Phase Equilibria* 1998, 147, 229–238.
14. Lee, H.; Seo, Y.-T. *Journal of Physical Chemistry* 2001, 105 (41), 10084–10090.
15. NIST NIST Thermophysical Properties of Hydrocarbon Mixtures Database (SUPERTRAPP), National Institute of Standards and Technology, 1999.
16. Peng, D.-Y.; Robinson, D. B. *Ind. Eng. Chem. Fundam.* 1976, 15 (1), 59–64.
17. Harvey, A. H. *AIChE Journal* 1996, 42 (5), 1491–1494.
18. Saul, A.; Wagner, W. *Journal of Physical Chemistry Reference Data* 1987, 16 (4), 893–901.
19. Lyckman, E. W.; Eckert, C. A.; Prausnitz, J. M. *Chemical Engineering Science* 1965, 20, 685–691.
20. Dhima, A.; Hemptinne, J.-C.; Jose, J. *Industrial & Engineering Chemistry Research* 1999, 38 (8), 3144–3161.

*This page intentionally left blank*

# Nucleation Mechanisms of Clathrate Hydrates

**A. A. Pomeransky,\* V. R. Belosludov, and  
T. M. Inerbaev**

## 1. INTRODUCTION

From the viewpoint of general crystal physics there exist crystals with so complex (big and non-trivially constructed) unit cell that even the mechanism of formation (nucleation) and growth of such crystals becomes not evident and search of this mechanism is in some cases a non-trivial problem.

Such crystals frequently occur, in particular, among inclusion compounds (of the ‘host-guest’ type). Clathrates are a special class of inclusion compounds having a special cage structure. It includes isomorphous structures of very different materials, such as gas hydrates (water framework with different apolar guest molecules) [1–5], cage zeolites (silica clathrasils) [6, 7], and clathrates of the group-IV semiconductor elements (Si, Ge, Sn, and other) with alkali metals (Na, K, Li, Rb) as guests [8]. All these different materials have in common only tetrahedral geometry of bonding in their host lattices. This makes highly probable existence of a universal mechanism of their formation. At present such mechanism is unknown for any of these materials despite long history of their investigation.

Most of clathrate hydrate crystals have one of three different structures: cubic structures I and II, and the structure H. All these structures contain the same small cages (cavities) differing by size and shape of large cages. A nucleation model

---

A. A. POMERANSKY • Institute of Inorganic Chemistry SB RAS 3, Lavrentiev Ave.,  
Novosibirsk, 630090 Russia

V. R. BELOSLUDOV • Institute of Inorganic Chemistry SB RAS 3, Lavrentiev Ave.,  
Novosibirsk, 630090 Russia

T. M. INERBAEV • Institute of Inorganic Chemistry SB RAS 3, Lavrentiev Ave., Novosibirsk,  
630090 Russia

\* [pom@casper.che.nsk.su](mailto:pom@casper.che.nsk.su)

must explain formation of the definite structure of clathrate for any guest molecule in dependence on its size and other properties (the review of known data and models of nucleation, and references are given, e.g., in the book [1]). For hydrates at present only the model suggested by Sloan [1,9] is developed and presented sufficiently fully. It postulates formation in all cases of small cage precursors, their agglomeration by joining of faces, and subsequent transformation of a part of these small cages into definite large cages of a clathrate structure. Some steps of this process are not defined exactly enough, some are very improbable to realize (as the procedure of joining effaces by two precursor cages or transformation of some part of small cages into large).

In this paper we suggest a simple and universal mechanism of clathrate crystal nucleation applicable equally to all three groups of isomorphous clathrate compounds: hydrates, clathrasils and semiconductor elements. In presentation we consider mainly clathrate hydrates.

The basic points of the suggested model are:

1. Some shell precursors of clathrate cages form in solution around guest molecules. The type of appearing cage precursors is defined by the size of these molecules. As a consequence, for example, for the structure I there are two ways of formation: from small cage precursors, when the guest molecule is small, and from precursors of large cage for larger guest molecules. For other clathrate structures, in solution there are created precursors of corresponding large cages. This defines the first link in the causal chain connecting size of a guest molecule and the structure of the formed clathrate crystal.
2. Cage precursors in solution can form bonds between them, forming dimer and higher configurations of precursors. We consider only the most simple types of bonds, one- and two-shoulder: direct bond between atoms of two precursors and the bond through one intermediate host atom. On the dimer level in the case of structure I one obtains only correct configurations of cages existing in the clathrate crystals and almost only such dimers for the structure II.
3. Subsequent growth of these clusters can be realized, in principle, either by joining of new precursor cages or by ordinary attachment of individual host molecules from solution to cluster. Free connection of precursors to dimer gives many false configurations though for little clusters there is a finite probability to get a correct configuration. So, more real seems the usual mechanism of nuclei growth by successive bonding of single host molecules. Consideration of this process for different dimers shows that in every dimer cluster exist ready parts of several additional cages (three or four ready faces of polyhedral cages) and these parts may be completed to full cages at continual attachment of host molecules from solution. No false configurations are created in this process, i.e. the structural information

contained in configuration even on the level of dimers is sufficient for, probably, unlimited and defectless continuation of clathrate crystal growth. One may suppose that successive formation of neighboring small and large cages ensures really unlimited growth of crystal.

One of advantages of the suggested model is that it does not contain any ambiguous notions or impossible operations, every point may be verified or improved by experimental or computer simulation studies. In particular, much probably can be obtained from simple molecular mechanics models. We will use the term ‘structure-forming units’ (SFU’s) for shell precursors of cages instead of ambiguous terms ‘structure-directing’, ‘structure-controlling’ or ‘secondary building units’ used in zeolite science. While mechanism of ‘directing’ (controlling) is unknown, SFU’s mean simply the cage precursors from which clathrate crystal nuclei are built. The possibility to construct formally clathrate hydrate structures by forming bonds between small cages directly or through additional water molecules, along with sharing common faces, was mentioned in the review [2, p. 63], later this possibility was not discussed. In our model clusters of small cages are very special case of clathrate nuclei.

Our model also gives some new insight in two problems related to multiple filling of cages in clathrate hydrates: unexpected formation of the structure II hydrates by most small guests (Ar, Kr,  $\text{N}_2$ ,  $\text{O}_2$ ,  $\text{H}_2$ ) and by definite mixtures of the structure-I hydrate-formers (see the discussion in the Introduction of our paper [13]). The model shows that in both these cases there initially form nuclei of the structure I hydrates with subsequent transformation to growth of the structure II due to appearance of large cages of this structure around two small guests.

## 2. FORMATION OF CAGE PRECURSORS IN SOLUTION

In this section we give schematic picture of possible formation of precursor clathrate clusters in solution. We start from definition of ‘growth medium’, called below simply ‘solution’. It is water solution of non-polar (hydrophobic) molecules for hydrates; hydrothermal solution of  $\text{SiO}_2$  in presence of an alkali and a ‘structure-directing agent’ in the case of zeolites; or soldered hot mixture of, for example, Si and Na for semiconductor clathrates. In all these cases the general property of this medium is the ability of host and guest molecules (atoms) to move in the medium and form tetrahedral bonds between themselves. We will describe some natural and simple properties of this medium, necessary for formation of clathrate structures.

1. Guest molecules create obstacles for formation of ‘normal’ three-dimensional (3D) disordered system of non-stationary bonds between host molecules, which would exist in absence of guest molecules. In other words, each guest molecule creates a void among neighboring host molecules inside which



there is no bonds between these molecules. It means that action (the effect) of guest is completely non-specific, not depending on its structure or chemical properties and is determined only by its size. Formation of void and destruction of 'natural' network of bonds between surrounding host molecules forces these molecules on the boundary of the void (near-neighbor host molecules for a guest molecule) to form bonds preferably between themselves, i.e. the system of bonds becomes substantially two-dimensional (2D). Besides this, formation of such 'boundary' bonds increases time of staying of definite host molecules on the boundary (they less frequently leave the boundary) and, so, stabilizes the shell around guest molecule. This creates a subunit from a guest molecule and surrounding host molecules.

2. In 2D system of bonds between host molecules in a shell, closed configurations (polygons) of bonds are more stable (have longer lifetime) than simple chains and 'stars' of bonds.

3. Among polygons (4-, 6-, and 8-rings), in the systems forming clathrate crystals, pentagons form most easily, have least internal stresses and exist longer. Formation of non-pentagonal polygons requires action of external forces. Hexagons are created either under stretching, sometimes along with squares (by pairs), or, in other variant, at closing of ring chains of pentagons. Opposite situation is for carbon fullerenes [10] where formation of hexagons is preferable (and in which clathrate crystals do not form).

4. Closed ring configurations of polygons or half-polyhedra (like the coronene molecule in carbon compounds) are more stable than open configurations. The most stable are full polyhedra.

5. For these reasons, the polyhedral shells forming around small guest molecules have only pentagonal faces; these shells are regular 12-hedral pentagon dodecahedra, which have the least volume among polyhedra appearing in clathrate structures.

6. At increasing size of guest molecules, shells formed around them become stretched and two or more hexagonal faces appear along with pentagons, creating successively larger polyhedral shells. (We will denote the polyhedron with 12 pentagonal and  $n$  hexagonal faces as  $P_n$ . So  $P_n = [5^{12}6^n]$  in the standard notations of polyhedra [1, 2]).

Thus, in our model there is the causal chain connecting the size of definite guest molecule, the type  $P_n$  of clathrate cage precursor created around this guest molecule, and the clathrate structure formed from these precursor shells.

Appearance of hexagonal faces in shells satisfies the following rules.

- a) Minimal number of hexagons arises, enough for the guest molecule to fit in the formed shell.
- b) Hexagons cannot have common edges, i.e. cannot be neighbor faces (the rule of isolated hexagons, compare the rule of isolated pentagons in the

fullerene science [9]). This follows from the condition of minimal internal stresses in the shell. From this it also follows that hexagons must be maximally apart on the shell surface.

By the way, clathrate cage polyhedra as well as fullerenes have always 12 pentagonal faces and this number cannot be changed, while number of hexagons can take any value besides 1. This is purely geometric (topological) result following immediately from the Euler theorem applied to 3-connected polyhedra [10, 11]. It is just the action of the 'Isolated Pentagons Rule' that makes fullerenes so large (there must be enough hexagons to 'dissolve' 12 pentagons).

Described properties in common give the qualitative picture of onset of clathrate cage precursors in solution. Analogies with fullerenes show that the problem of formation of clathrate cage precursors is of the same class as formation of fullerenes for which some models had been suggested [12].

### 3. FORMATION OF DIMER NUCLEI

#### 3.1. Cubic structure I (S-I)

This is the structure of hydrates (and corresponding compounds of semiconductor elements) formed with guest molecules of small size. In zeolites the mineral of this structure is melanophlogite (MEP) [6]. The unit cell of this structure contains 46 host atoms (molecules) forming two small  $P_0$  cages (12-hedra) and six large  $P_2$  cages (14-hedra). Centers of small cages form volume-centered cubic lattice with two sublattices. Orientations of cage polyhedra from different sublattices are mutually perpendicular.

In the structure I clathrates with small guest molecules these molecules occupy both small and large cavities, while in clathrates with larger size of guest molecules they are included only in large cavities. It means that larger guest molecules do not fit into small shells and such cages cannot be precursors (SFU). In our model it follows from this that nucleation of the structure S-I clathrates can occur by two different ways, starting from shell precursors of small cages in one case and of large cages in the second, from this Both these different nuclei must give the same structure of crystals. Consider these cases separately.

##### 3.1.1. Small guest molecules

In this case around guest molecules in solution there are formed 12-hedral (pentagon dodecahedral) shells of 20 water molecules  $P_0 = [5^{12}]$  which become structure-forming units (SFU). Connection of two  $P_0$  shells can occur by several ways. The first bond connecting two arbitrary vertices of these shells can be

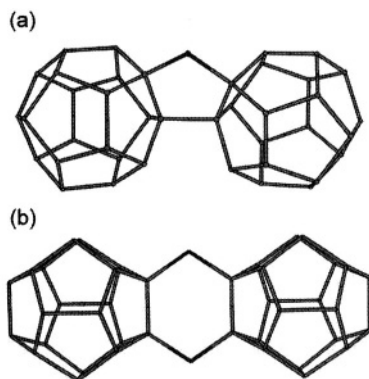


**Figure 1.** Dimer nuclei of the structure S-I formed by small cages  $P_0$  connected by pentagon (a) and hexagon (b).

either direct (one-shoulder) bond ( $d$ -bond) or bond through intermediate molecule (two-shoulder  $i$ -bond).

In the first case of direct-bond connected shells, they can perform mutual rotations around the direction of the bond as axis. In the process of these rotations there can occur configuration of two shells at which the second bond between shells is formed. It can be only two-shoulder  $i$ -bond, because at formation of the second  $d$ -bond there would be square polygon connecting two  $P_0$  shells what is forbidden due to large deviation from the tetrahedral angles. Two bonds,  $d$ - and  $i$ -, together with adjoining edges of polyhedral shells form pentagon connecting two SFU's (Figure 1a). Mutual position of two shells in the formed dimer becomes fixed. It is easily seen that two polyhedral cages in the dimer have the same mutual position and the same connection as any pair of neighbor  $P_0$  cages from different sublattices of the volume-centered cubic lattice of small cages in the clathrate S-I crystals. The connecting pentagon in the S-I structure happens to be one of the faces of a  $P_2$  cavity (it is really common face of two such cavities). One can see also that shells in the dimer are mutually mirror-symmetric with the mirror plane dividing vertically (for the dimer shown in Figure 1a) the connecting pentagon in half.

In the second case, when the two-shoulder  $i$ -bond is formed first between two shells in solution, under mutual rotations of the shells around directions of two shoulders in the bond there can occur two different configurations of shells. In one of them the distance between two vertices from different shells is equal to the length of one-shoulder  $d$ -bond and such bond is formed. This configuration coincides with one formed in the first case and we again get dimer with connecting pentagon (Figure 1a), only the order of formation of  $i$ - and  $d$ -bonds is inverse.

Another configuration can appear, in which the distance between some two vertices from different shells becomes equal to the length of two-shoulder  $i$ -bond. This happens when during rotations opposite edges of two shells become parallel.

Then the second bond forming between shells is just *i*-bond and the dimer configuration shown in Figure 1b with two  $P_0$  shells connected by hexagon. In this dimer shells are parallel (one is obtained by shift of another). Comparing this configuration with the structure S-I clathrate crystal we see that this dimer coincides with any pair of neighbor  $P_0$  cages in the same sublattice of the volume-centered cubic lattice of  $P_0$  cages.

It is not hard to see that these two dimer configurations (Figures 1a, 1b) are the only possible and there are no other connections of  $P_0$  shells by means of direct or intermediated (by one atom) bonds. Therefore, on the level of dimers of  $P_0$  cages, both types of dimers existing in the S-I structure clathrates appear in solution and only such dimers. In other words, on the dimer level spontaneous connection of SFU's produces correct nuclei of the S-I structure and gives no false configurations. The problem of uniqueness of forming configurations and their coincidence with the real elements of clathrate structures may be discussed by means of another, in some sense reversed, argumentation. If we select in a known existing clathrate structure different possible types of SFU pairs with their mutual connections by one- and two-shoulder bonds, then we can consider the chosen connected pairs as precursor clusters formed in solution. The uniqueness of such cluster is provided by unique direction of external bond in every vertex of closed polyhedron formed by atoms with tetrahedral coordination of bonds.

### 3.1.2. Larger guest molecules

There exist clathrate structure I crystals in which only large cavities contain guest molecules, while small cavities remain empty. This occurs when guest molecules are large enough and, presumably, do not fit in to small cages. According to our model, in this case around guest molecules in solution there form large  $P_2$  shells, precursors of big cavities in the structure I clathrate crystals. Then these shells can combine by formation of bonds. There are two types of vertices in 14-hedron  $P_2$ : vertices of hexagons and lying in 'middle line' (common points of pentagonal 'saw teeth'). A direct bond formed can connect the points of middle lines of two shells or such point of one shell with a hexagon vertex on other shell. In the first case, after consequent formation of two-shoulder *i*-bond, also connecting points of middle lines, one gets dimer configuration of two parallel  $P_2$  shells connected by pentagon (Figure 2). Such dimer corresponds to pair of large cages  $P_2$  from

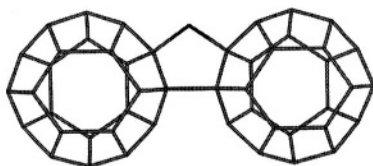


**Figure 2.** Dimer nucleus of the structure S-I formed by large cages  $P_2$  connected by pentagon.

neighbor parallel columns of  $P_2$  cages. In the second case there forms dimer of two orthogonal  $P_2$  shells, also connected by pentagon. Such dimers are also presented in the S-I clathrates: these are pairs of the ‘next-neighbor’ cages  $P_2$  (non-having common faces, in distinction from near neighbor cages) from large cage columns of different directions (mutually orthogonal). Finally, there is possible formation of direct bond between vertices of hexagons from two shells, but in this case formation of second  $i$ -bond seems impossible and we will not consider it further. Therefore, we can conclude that in both variants of the structure I clathrate formation, from small or large cage precursors, the appeared dimers have correct configurations and no false dimers are created.

### 3.2. Cubic structure II (S-II)

Clathrates of this structure form, when size of guest molecules is larger, than in the S-I structure. The unit cell of this structure consists from 8 large cages  $P_4=[5^{12}6^4]$  and 16 small  $P_0$  cages formed by 136 water molecules in host framework. Centers of large cages form a diamond lattice and these cages have common hexagon faces. Four hexagons in each 16-hedron are placed in tetrahedron vertices. From 28 vertices of this polyhedron 24 are equivalent (vertices of hexagons) and 4 vertices (each common to three pentagonal faces) have other symmetry. We will denote these vertices as  $g_i$  and  $e_k$ , respectively, with their Wyckoff symbols. Correspondingly, there are edges of three types: sides of hexagons, edges between two pentagons and those containing one of 4 vertices  $e_k$ .

The direct bond can form between any two vertices from different shells  $P_4$ . Only if both these vertices have the same symmetry, i.e. both are  $g$ -, or  $e$ -vertices, during mutual rotations of shells around this  $d$ -bond there exists possibility of creation of second two-shoulder  $i$ -bond. But in case of direct bond between  $e$ -vertices, even if the second  $i$ -bond is really created (if angles between bonds admit its formation, what requires additional check), orientation of the formed connecting pentagon (upturned relative to shown in Figure 3) seems not corresponding to any polyhedron. In any case, due to small number of  $e$ -vertices, fraction of  $e$ - $e$  bonds is low. Hence, we will consider only  $g$ - $g$  direct bonds. After formation of two-shoulder  $i$ -bond there forms dimer of two large  $P_4$  cages connected by pentagon (Figure 3). In this configuration opposing edges connected by the pentagon of

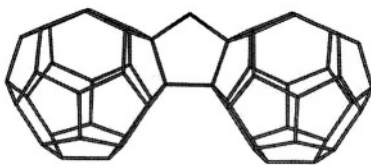


**Figure 3.** Dimer nucleus of the structure S-II formed by two large cages  $P_4$  connected by pentagon.

bonds are of the same type. We see that it is the only possible dimer of precursor large cages appearing in solution for structure II clathrates. It corresponds to any pair of 'next-neighbor' large cages (neighbor cages without common faces) in some hexagonal layer of large cages in full clathrate S-II crystal, i.e., it is the correct configuration. As is known, in the S-II structure there are four tetrahedrally oriented systems of such layers with tetrahedral orientation.

## 4. GROWTH OF NUCLEI

### 4.1. Cubic structure I

Subsequent growth of the structure S-I dimer-level nuclei could be imagined as continuation of described process with formation of trimers, tetramers, and higher clusters of SFU's. The third shell can be connected to an unoccupied edge of any polyhedron in dimer by one of two ways, through pentagon or hexagon (Figure 1a, 1b). Some part of the formed trimers will have correct configuration (existing in the clathrate S-I structure), some will be incorrect. Probability of correct configuration of trimer equals  $5/27 = 1/5.4$ . This probability increases, if one accounts formation of several additional bonds in dimer configuration by attachment of host molecules from solution, due to rise of number of occupied edges. The probability of formation of correct tetramer and pentamer configurations of SFU's from correct trimers will have still more value. So, in principle, there is a finite probability of formation of a correct (existing in the S-I clathrate structure) configuration of any number of SFU's. The process of their connection, when clusters with incorrect configurations, unable to grow unlimitly, are broken and eliminated, may be imagined to continue infinitely. But in reality this mechanism of nuclei growth is hardly realized because large probability of appearance of false configurations, even for big clusters of many SFU's, will lead to formation of many highly defect structures.

But there is another way of dimer nuclei growth, the usual mechanism of crystal growth by attachment of single host molecules from solution with successive formation of bonds in the dimer cluster. This process is the same as during formation of single precursor shells around guest molecules in solution and it satisfies the same rules (see section II above). But now in the dimer nucleus there already exists some number of complete faces of future clathrate cavities and these faces are mutually fixed (their mobility is much lower than in a precursor shell in solution) just at same angles as must be in the complete cavities of the clathrate crystal. So there exist some parts of clathrate cages. After adsorption of a guest molecule inside this part, formation of cage precursor starts in 2D shell consisting from this ready part of cavity and from surface formed by neighboring water molecules. The process of cavity completing is the same, as was already mentioned, as at formation of single precursor shells in solution. But due to indicated causes the

rate of formation of new cavities is much larger than in latter case. It is important to note that the structure of appeared dimer (or correct trimer) defines the places of attachments of new host (water) molecules to it. It means that a bonded water molecule always appears in correct position so that the formed cluster coincides with a part of the clathrate crystal. Such process of growth of nucleus is analogous, as noted above, to ordinary growth of crystals from solution (melt) when attachment of new atoms occurs in angles of growth steps, where the structure of growing crystal is the most near to the structure of full crystal and where is most number of bonds for an ingoing atom. During formation of clathrate structures new water molecules also attach in 'angles' of the formed structure where some edges of a cage face are already formed. Therefore it is possible that even small clusters (dimers or trimers of SFU's) can play role of seeds for growth of clathrate crystals. In other words, the information contained in the form and internal angles in such clusters is sufficient for correct growth of clathrate crystal. So the full process of precursor formation, their joining in dimers and subsequent growth of clathrate nuclei can be described as self-assembling of clathrate structures.

Consider growth of dimer cluster of small cages shown in Figure 1a. One can see that besides the existing connecting pentagon shown in the Figure, two other two-shoulder *i*-bonds can be created which also constitute pentagons with the same direct bond. In total we get three pentagons connecting the shells in this dimer, arranged symmetrically around the direction of *d*-bond with equal dihedral angles  $120^\circ$  between their planes. Each pair of connecting pentagons, together with two adjusting pentagonal faces of shells (situated inside the dihedral angle between these connecting pentagons), form a part of 14-hedral  $P_2$  cavity of the clathrate S-I structure. Three pairs of connecting pentagons create parts of three different mutually orthogonal  $P_2$  cavities. Thus, in the dimer structure of Figure 1a we have now four complete faces (out of 14) for each type of  $P_2$  cavities existing in the structure. These four faces, as one can see, consist two neighboring pairs from 'upper' and 'lower' rows of pentagons in full  $P_2$  cage. After adsorption of a guest molecule to it, any of three parts can be completed to full  $P_2$  cage by bonding of individual host molecules. Then one gets nucleus of the structure I clathrate containing two small and three large cages. It is not hard to see that this cluster again has several parts of cavities and is able to grow further.

In the dimer shown in Figure 1b there are parts of two  $P_2$  cages, consisting each of connecting hexagon and adjusting to it two pentagonal faces of small cages. Thus each part contains three ready faces of  $P_2$  cage. With ingoing guest molecules in these parts they can be finished to complete  $P_2$  cavities by bonding of host molecules in 'angles' of this framework where maximal number of edges already exists. We get cluster of two small and two large cages that can enlarge still more.

In the dimer of two large S-I cages (Figure 2) bonding of one host molecule creates new connecting pentagon symmetric with the first formed relative to direct

bond. These two connecting pentagons together with two adjusting pentagons on shells (from 'lower' row of pentagons in large cage as it is shown in the Figure) consist the part (from four faces) of small  $P_0$  cavity (placed below the plane of image). This part completes to full small cage by bonding of separate host molecules without necessity in this case of a guest molecule ingoing (remind that with larger guest molecules small cages remain empty).

#### 4.2. Cubic structure II

Looking on dimer of large S-II cages (Figure 3) one sees that yet two *i*-bonds can form, symmetrically positioned relative to the shown existing *i*-bond. Then we have in total three pentagons connecting the shells in dimer. Any two of them together with adjusting two faces of shells (lying inside the dihedral angle formed by these connecting pentagons) consist 4-face part of a cavity. For upper two parts (as it drawn in the Figure) these four faces are pentagons and these are parts of small cages. The lower part contains two connecting pentagons and two adjusting hexagons of shells. That is the part of large cage having common hexagons with both shells of the dimer. Small cages can be completed without guest molecules; formation of large cage requires presence of guest molecule in the ready part of this cage. After closing of three new cavities one has cluster of 5 cages containing three large and two small cages. Some consideration shows that this big cluster is able to grow further.

### 5. CONCLUSIONS

A simple universal model of formation of clathrate crystal nuclei in solution is suggested. The model is applicable equally to all clathrate materials: gas hydrates, cage zeolites (clathrasils) and clathrate compounds of semiconductor elements. The basic feature of the model is joining of polyhedral cage precursors, formed around guest molecules, by means of direct, or intermediated by one host molecule, bonds between precursors. The type of precursor cage formed in solution is determined strictly by the size of guest molecules. This defines the first link of the causal chain connecting the size of guest molecule and the clathrate structure formed. We name such cage precursors 'structure-forming units' (SFU). For the structure I clathrates there are two SFU's: small and large cage precursors, depending on the size of guest molecule, and, correspondingly, two routes of crystal growth. For other structures SFU is always the large cage. It is shown that for any clathrate structure there forms in solution correct dimer cluster of cage precursors corresponding to a pair of neighboring (without common faces) cages in the real clathrate crystal and no other (false) configurations forms. Consideration of initial growth stages after formation of the dimer clusters shows that growth in all cases



can continue by usual mechanism of attaching single host molecules from solution with formation of new cages in the cluster. This growth is, in principle, unlimited and does not create defects. This means that structural information contained in cluster, even on the level of dimers, is sufficient for formation of the clathrate crystal by successive attachment of individual host molecules.

## ACKNOWLEDGMENTS

This investigation was supported by Siberian Branch of Russian Academy of Sciences (Grant No. 147).

## REFERENCES

1. Sloan, E. D. *Clathrate Hydrates of Natural Gases*; Marcel Dekker: New York, 1998;
2. Jeffrey, G. A.; McMullan, R. K. *Progr. Inorg. Chem.* 1967, 8, 43;
3. Jeffrey, G. A. In *Inclusion Compounds*; Atwood, J. L.; Davies, J. E. D.; and MacNicol, D. D., Eds.; Academic Press: London, 1984; Vol.1, Ch.5, pp. 135–190;
4. Dyadin, Yu. A.; Bondaryuk, I. V.; and Zhurko, F. V. In *Inclusion Compounds*; Atwood, J. L.; Davies, J. E. D.; and MacNicol, D. D., Eds.; Academic Press: London, 1991; Vol.5, p. 213;
5. Belosludov, V. R.; Dyadin, Yu. A.; and Lavrentiev, M. Yu. *Theoretical Models of Clathrate Formation*; Nauka, Sib. Div.: Novosibirsk, 1991 (in Russian);
6. Gies, H. In *Inclusion Compounds*; Atwood, J. L.; Davies, J. E. D.; and MacNicol, D. D., Eds.; Academic Press: London, 1991; Vol.5, pp. 1–36;
7. Burkett, S. L.; and Davis, M. E. In *Comprehensive Supramolecular Chemistry*; Atwood, J. L.; Davies, J. E. D.; MacNicol, D. D.; and Vögtle, F., Eds.; Pergamon: Oxford, 1996, Vol. 7, Ch. 16, pp.465–484;
8. Bobev, S.; and Sevov, S. C. *J. Sol. State Chem.*, 2000, 153, 92;
9. Christiansen, R. L.; and Sloan, E. D. *Annals N. Y. Ac. Sci.*, 1994, Vol. 715, pp. 283–305;
10. Fowler, P. W.; and Manolopoulos, D. E. *An Atlas of Fullerenes*; Clarendon: Oxford, 1995;
11. Wells, A. F. *Three-dimensional Nets and Polyhedra*; Wiley: New York, 1977;
12. Lozovik, Yu. E.; and Popov, A. M. *Rus. Phys.-Uspekhi*; 1997, 40, 717;
13. Pomeransky, A. A.; and Belosludov, V. R. This book, p. 20.

# The MSU Micellar-Solution Gas Hydrate Storage Process for Natural Gas

**Rudy E. Rogers,\* Yu Zhong, John A. Etheridge, and Larry E. Pearson**

## 1. INTRODUCTION

### 1.1. Background

Gas hydrates are clathrates where the guest gas molecules are occluded in a lattice of host water molecules. With all cavities of Type I structure occupied by methane molecules, the volume ratio of gas (at standard temperature and pressure) to water can be as high as 185 [1]. In 1942 Benesh first proposed using this unique hydrate property to store natural gas [2]. To store natural gas in gas hydrates, conceptual investigations have been carried out during the past five decades [2; 3; 4]. Even though these investigations proved the concept of storing natural gas in hydrates technically feasible, applications stayed in the laboratory stage due to complexities of the process, slow hydrate formation rates, and costs.

### 1.2. History of Natural Gas Hydrate Study at Mississippi State University

The investigations into storing natural gas in gas hydrates have been carried out at Mississippi State University (MSU) since 1991 with the goal to develop this

---

RUDY E. ROGERS • Swalm School of Chemical Engineering, Mississippi State University

YU ZHONG • Diagnostic Instrumentation & Analysis Laboratory, Mississippi State University

JOHN A. ETHERIDGE • Diagnostic Instrumentation & Analysis Laboratory, Mississippi State University

LARRY E. PEARSON • Diagnostic Instrumentation & Analysis Laboratory, Mississippi State University

\*rogers@che.msstate.edu

technology on a practical and economical basis. In the patent of Rogers and Yevi [5], natural gas is proposed to be stored on-board vehicles in gas-hydrate form as an alternative fuel for gasoline or diesel. Their work also stressed the key issues to be solved for gas hydrate storage to be practical.

In 1997, the Department of Energy (DOE) awarded a grant to the hydrate research laboratory at MSU to determine the feasibility of storing natural gas in gas hydrates for electric power plant use at peak loads. The successful laboratory feasibility study then led to a second DOE-sponsored project to demonstrate and test the process at a proof-of-concept (POC) scale of 142 scm (5,000 scf) natural gas storage.

### **1.3. Applications of Natural Gas Hydrates (NGH) to Store and Transport Associated Gas**

In addition to the project at MSU, storage and transportation of natural gas in hydrate form recently have been investigated, primarily in Japan, Norway, and England. Japan looks toward early commercialization of a natural gas hydrate process to compete with liquefied natural gas (LNG) in transportation [6]. Pilot plants capable of generating 600 kg to 1,000 kg of gas hydrates per day are under construction and testing in these countries [7; 8; 6]. Process diagrams of the different processes are presented in Figure 1 and Figure 2, from which the approaches of the Japanese, British, and Norwegian can be compared.

The Japanese process and Norwegian dry process have the following common characteristics: (1) A hydrate slurry is formed in a high-pressure, continuous stirred tank reactor (CSTR). (2) A series of treatments pack the low-energy-density slurry into high-energy-density dry hydrate. (3) NGH is stored and transported at atmospheric pressure and temperature of  $-10^{\circ}\text{C}$  or lower [6; 9].

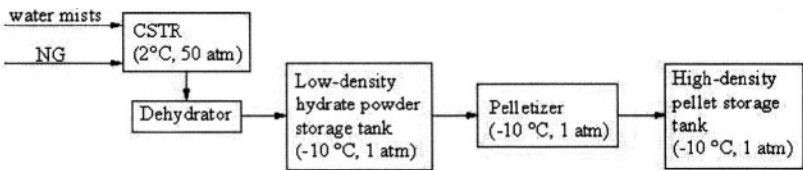
British Gas Group (BG) keeps the gas hydrates in slurry state throughout the formation, storage, and transportation process [7]. Because of the hydrate slurry's lower energy density than LNG, multiple tankers would be necessary to compete with a single LNG tanker.

The Japanese, British, and Norwegian processes are designed primarily to transport natural gas in competition with LNG.

## **2. EXPERIMENTAL**

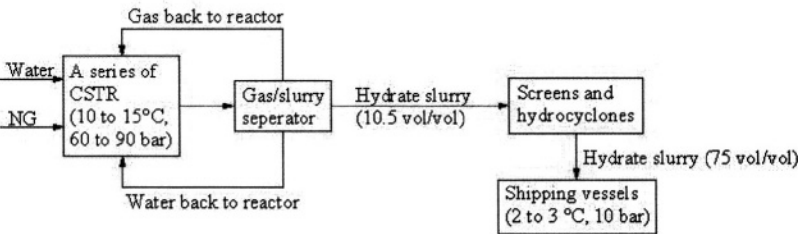
### **2.1. Equipment, Laboratory Feasibility Study**

The laboratory equipment was designed to study the feasibility of a non-stirred system to occlude natural gas in gas hydrates with a minimum of labor. A simple hydrate formation/storage/decomposition tank without any moving parts was



- \* 1 ton/day pilot plant is to complete within 2002.
- \* 1 ton of NGH is equivalent to 5,580 scf NG, assuming NGH has 150 vol/vol storage capacity and 0.95 kg/liter density

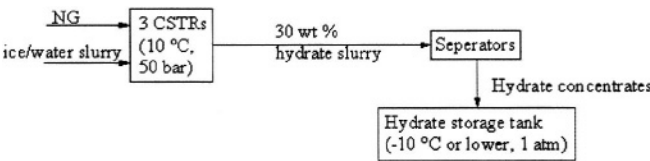
a. Japanese Hydrate Production Process (MES, 2002)



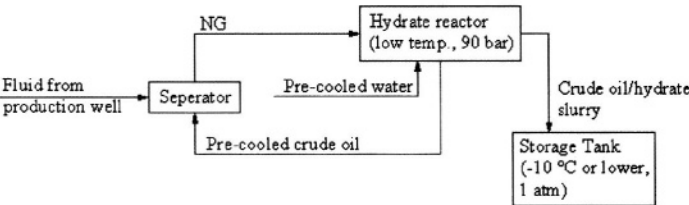
- \* 1 Mg/day pilot plant is under development.
- \* 1 Mg of NGH is equivalent to 2,790 scf NG, assuming NGH slurry has 75 vol/vol storage capacity and 0.95 kg/liter density

b. BG Slurry Hydrate Production Process (Fitzgerald, 2001)

Figure 1. Comparison of Japanese and BG hydrate processes.



c. Norwegian Dry Hydrate Process (Gudmundsson and Hveding, 1995)



d. Norwegian Crude/hydrate Slurry Process (Gudmundsson and Mork, 2001)

Figure 2. Norwegian hydrate formation processes.

preferred in order to reduce maintenance, labor, and capital costs. Ordinarily with distilled water, it could take days to initiate the nucleation of hydrates and achieve appreciable growth in a non-stirred system [10]. Even after hydrate nucleation is initiated in a quiescent system, a thin solid film forms across the gas/liquid interface, thus slowing hydrate formation significantly. Also, when gas hydrate crystals mature, as much as 80% to 90% of interstitial waters of the crystals may remain unreacted.

A sketch of the laboratory test cell is given in Figure 3. The 3800 ml cell walls are 304-stainless steel; the cell is 10 cm (4.0 in.) diameter. A removable top blind flange is bolted to the test cell and sealed with a Teflon gasket. The laboratory hydrate test cell had the following basic capabilities: (1) warm or cool pressurized

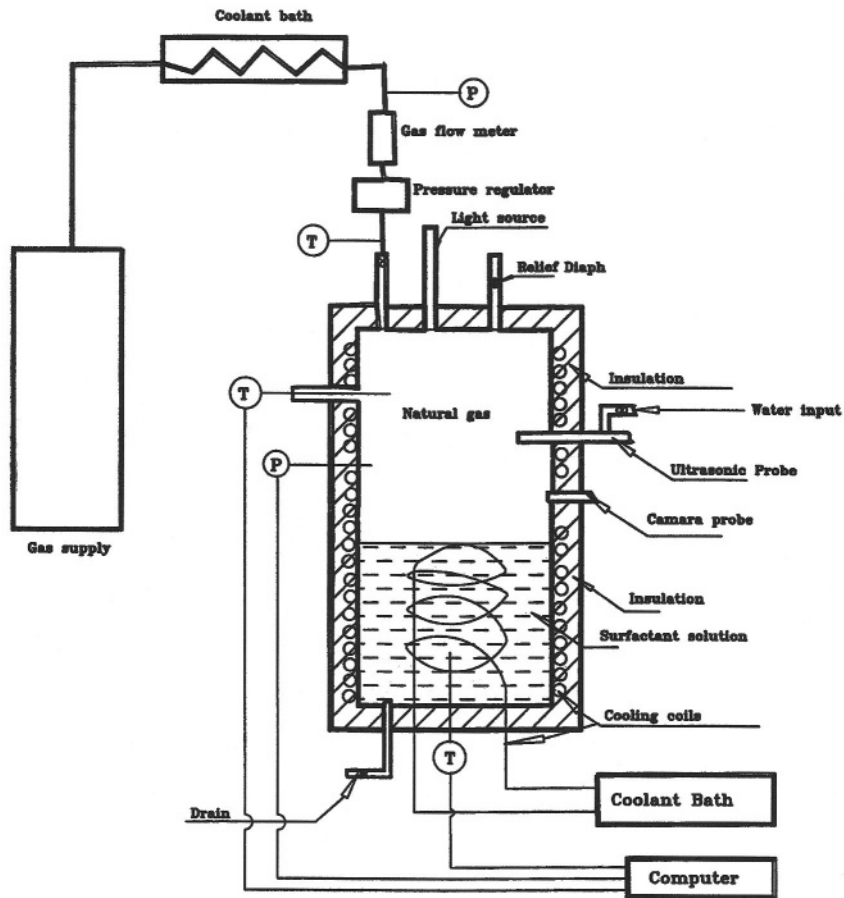


Figure 3. Sketch of laboratory test cell.

cell contents upon demand, (2) monitor pressure and temperatures in cell, (3) view contents, and video record when desired, as process proceeded, (4) collect data continuously and store on computer, and (5) maintain constant pressure while measuring inlet gas flow. A description of the basic capabilities follows.

Stainless-steel cooling coils of 0.953 cm (3/8 in.) diameter surrounds the test cell. A separate set of coils protrudes into the bottom half of the test cell. Water-glycol solution circulates through the coils from two independent, constant-temperature baths that can be alternately cooled or heated. The refrigerated baths maintain  $\pm 0.01$  K of the set point to as low as 253 K. Insulation encloses the test cell and exterior cooling coils. A transducer and RTD probes monitor pressure and temperatures. A Tescom Corporation model 26-1026 constant-pressure regulator maintains a desired pressure in the test cell as gas occludes into hydrates; the regulator can maintain a pressure within  $\pm 6.9$  kPa. Flow rate of gas into the test cell during hydrate formation is monitored with an Omega Engineering Model FMA-8508 mass gas flow meter that has a capability of 0–5000 sccm, at an accuracy within 1 % of full scale and a repeatability of within 0.25% of flow rate.

An Omega Engineering data acquisition system records on computer the outputs from mass flow meter, RTDs and pressure transducers.

A Model AG 204 Mettler analytical balance is used to weigh surfactant. Powdered sodium dodecyl sulfate (SDS) purchased from Strem Chemicals, Inc., was used in the tests; the 98%+ pure SDS (with no alcohols in the residuals) has a molecular weight of 288.4 g/mol. Double-distilled water was used in the surfactant solutions.

A representative natural gas purchased from Matheson contained 90.01% methane, 5.99% ethane and 4.00% propane, as analyzed by a Model 6890 Hewlett-Packard gas chromatograph using a HPPLLOT-Q column and a flame ionization detector. Ethane of 99.6% purity from Matheson Gas Products was used in some preliminary experiments to establish procedure at less stringent test conditions prior to verification with natural gas.

## 2.2. Procedure, Laboratory Feasibility Study

A typical procedure was as follows. Initially, surfactant-water solution was pumped into the empty cell to displace all gases. The hydrocarbon gas was then injected to displace water to a predetermined water level. For example, this level could be selected to be along the line of sight of the camera probe (See Figure 3). Liquid completely covered the internal cooling coils. Under a pressure too low for hydrates to form, the system was cooled to 275–278 K. Pressure was then raised to the operating pressure over a 2–3 min span by flowing pre-cooled gas into the cell; measurement of gas mass admitted was made with the flow meter. Hydrate formation was tracked through monitored temperatures, pressures, and mass flows that were continuously displayed and recorded on the computer. During

the experimental run, cell interior was observed on a TV monitor, and the video was recorded with commentary on videotape.

### 3. RESULTS

Results from the successful laboratory feasibility study were used to design a scale-up process. Three major achievements as a consequence of using micellar solutions led to the scale-up: (1) Gas hydrate formation rates in the non-stirred system were increased orders of magnitude. (2) Hydrate particles were self-packed as they formed in the formation vessel. (3) Interstitial water of the hydrate mass was reacted to near completion.

#### 3.1. Gas-hydrate formation rates

If a gas hydrate storage process is to be practical for industrial applications, then natural gas must be occluded in gas hydrates at a rapid rate. This property coupled with the economic requirement of a non-stirred system, creates a particularly difficult problem because a pressurized and chilled quiescent water/natural-gas system develops a thin hydrate film at the water-gas interface that acts as a barrier to mass transport. For example, Figure 4 illustrates hydrates typically formed in a chilled test cell over a 5–10-day period in which a hydrocarbon gas pressurizes a distilled water phase. A slow, random growth of hydrate crystals is evident.

Rogers and Zhong [11] found that by adding about 284 ppm of SDS, the rate of formation could be increased by a factor greater than about 700.

It is well known that physical properties, such as surface tension, of water-surfactant solutions change abruptly at the critical micellar concentration (CMC) where surfactant molecules organize and orient their hydrophilic heads and hydrophobic tails. However, the concentration of 284 ppm SDS used in the experiments was well below the CMC measured to be about 2700 ppm at ambient conditions. To check the possible change of the solution's CMC at low temperatures and high pressures, a technique was developed to make the difficult measurement of CMC at hydrate-forming conditions. It was found by repeating pressure, temperature, and surface area in the test cell while varying SDS concentration that hydrate induction time decreased rapidly with SDS concentration until the CMC was reached, whereupon abruptly no further decrease occurred with added surfactant. The CMC at hydrate conditions was found to be about 242 ppm.

#### 3.2. Self-packing of gas hydrates

By adding SDS to the water in a concentration above its critical micellar concentration, quite a different time of hydrate formation and pattern of hydrate accumulation

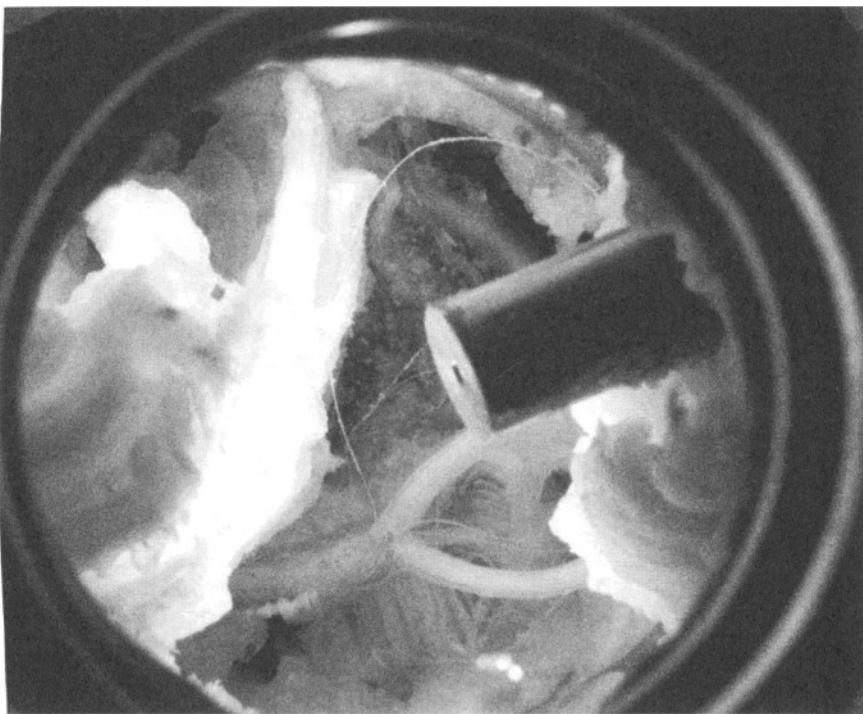


**Figure 4.** Hydrates randomly forming.

resulted as seen in the series of photographs of Figure 5. SDS facilitated the filling of the test cell with hydrates of natural gas in about a two to three-hour period, and the hydrates accumulated symmetrically on the metal cell walls [12].

### **3.3. Reaction of interstitial water**

Ordinarily, unreacted interstitial water adsorbed on hydrate particles can occupy as much as 80–90% of the total volume of the hydrate mass—an important consideration when economics dictates that volume of storage be minimized.

However, when water of the SDS solution goes into the hydrate molecular structure, surfactant is excluded into interstitial water where it promotes hydrate formation of that interstitial water. Hydrates are promoted in the interstitial water because surfactant solution concentrated in the interstices forms micelles that solubilize natural gas, and the surface areas of the surrounding hydrate particles provide large interfacial areas for further reaction.

The reaction of the interstitial water became evident by draining free water from the test cell after hydrates had accumulated and noting the continued fast



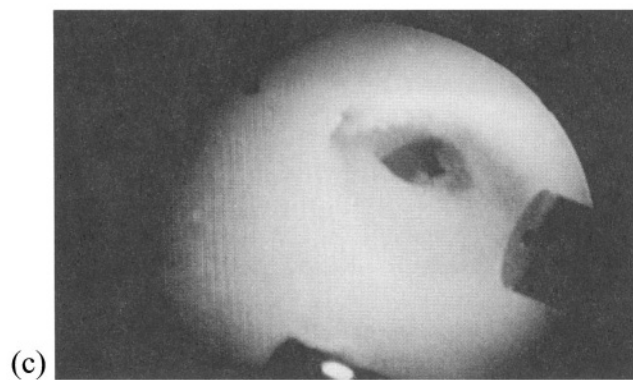
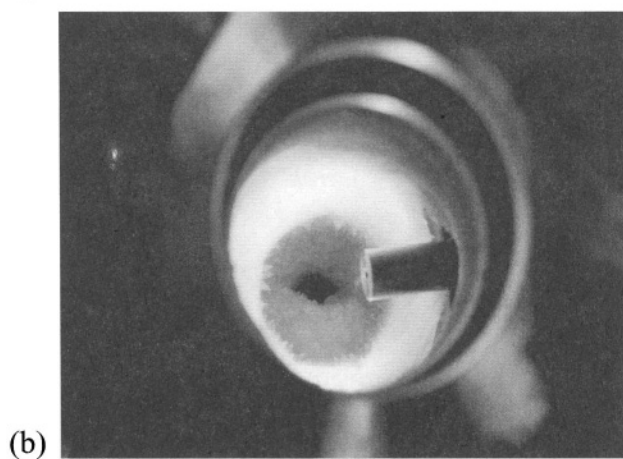
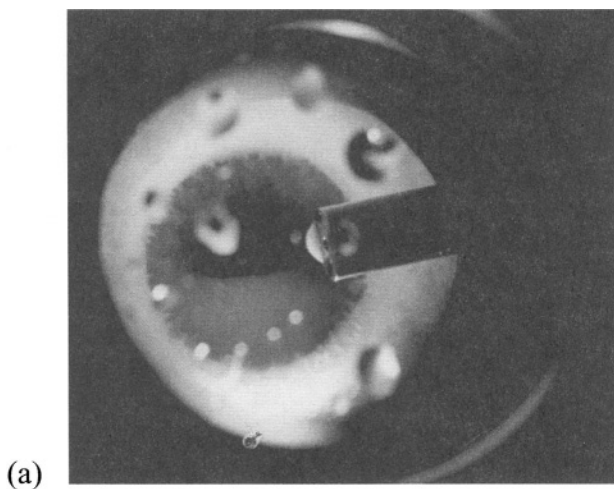


**Figure 5.** Sequence of test cell filling with gas hydrates. (a) Ethane hydrates form initially, (b) Ethane hydrates continue to grow symmetrically, (c) natural gas hydrates till test cell.

formation of gas hydrates. This is because the hydrates formed from micellar solutions accumulate as a porous mass of orderly-packed small particles through which natural gas can permeate and contact unreacted interstitial water.

3.4. Scaled-up process design

The performance of the laboratory process indicated that a scaled-up process could be designed to incorporate notable process attributes enhancing economics of gas hydrate storage of natural gas. These attributes suggest a simple process that minimizes labor [13]. See Figure 6.

Consequently, a proof-of-concept (POC) hydrate gas storage process was designed to form, store, and decompose 142 scm (5000 scf) of natural gas in gas hydrates. In this POC process, hydrates form with no stirring at 274.9 K (35 °F) and 3.79 MPa (550 psi) from a water solution containing surfactant above its critical micellar concentration. As it forms, the hydrate mass accumulates on cold, solid surfaces placed at the liquid-gas interface. These metal surfaces at the liquid-gas interface serve to transfer heat in both formation and decomposition steps, but they also adsorb and collect hydrates during formation. The process was designed so that hydrates attach to the solid interfaces and, as the water level drops, the solid hydrate particles grow radially from those surfaces until the vessel is filled.

Stainless-steel 304 L comprises the pressure vessel, and its shell is 0.876 m (34.5 in.) i.d. and 0.914 m (36.0 in.) o.d. The working length of the pressure vessel is 1.83 m (72 in.). The vessel will be used in the vertical position. The top ellipsoidal dome is Teflon-coated on the inside to prevent hydrate buildup from blocking exit ports.

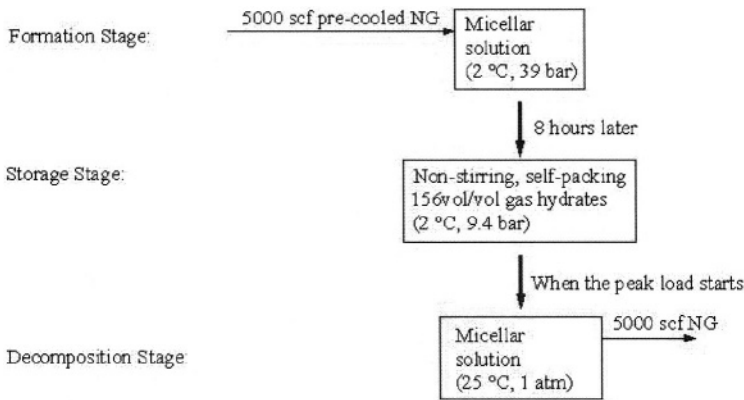


Figure 6. Micellar-solution gas-hydrate storage process.

The jacket surrounding the pressure vessel is made of 0.318 cm (1/8 in.) thick 304 L stainless steel. Baffles direct the flow of circulating water-glycol solution through the jacket. The gap between jacket and pressure vessel is 2.54 cm (1.0 in.).

Thirty finned heat exchanger tubes extend into the pressure vessel: 15 tubes for entering fluid and 15 for exiting fluid. See Figure 7. The 30 tubes are brought into 3 concentric doughnut-shaped ring headers; 12 outlet tubes exit the ring headers and those 12 outlet tubes extend through the top dome of the pressure vessel. The finned tubes are symmetrical. Hydrates also build symmetrically upon those heat-exchanger tubes and fins. At the end of the process, hydrates from adjacent heat-exchanger tubes/fins should touch but leave flow paths to the exit ports at the top of the vessel.

The heat exchanger tubes are designed to withstand a maximum external pressure of 650 psig; the minimum internal pressure is 45 psig for the circulating glycol solution. The design temperature is 20 °F to 110 °F to accommodate heating or cooling in forming or decomposing hydrates.

The fins increase hydrate formation rate in two ways. Rate of formation is directly proportional to the interfacial surface area. Rate of formation is also dependent on heat transfer rate, a parameter dependent on surface area.

The pressure vessel and internal heat exchanger are fabricated to ASME standards as given by the 2001 edition of ASME Boiler and Pressure Vessel Code, section VIII, division 1.

A sketch showing how the finned tubes fit into the shell of the formation tank is given in Figure 8.

Hebeler Corporation (Headquarters Tonawanda, New York) constructed the formation tank at their facility in Vicksburg, Mississippi. The installation of the POC system at MSU is shown in the photograph of Figure 9. In the foreground is the hydrate formation vessel. Seen in the background is the chiller that is capable of circulating glycol-water solution at the required flow rate and temperature. The chiller of 12-tons refrigeration was purchased from Drake, Inc. Glycol-water solution will be circulated from the chiller through the heat exchanger/adsorber inside the formation tank; the solution will flow in parallel through the formation tank's exterior jacket.

To the right of the formation vessel is the surge tank for decomposition gases. Not shown in the photograph are deionized water supply and boiler to burn off-gases.

## 4. CONCLUSIONS

Formidable problems (forming hydrates rapidly, collecting and packing hydrates, reacting interstitial water) to make natural gas storage in gas hydrates an economically viable process are overcome by forming the hydrates from a micellar

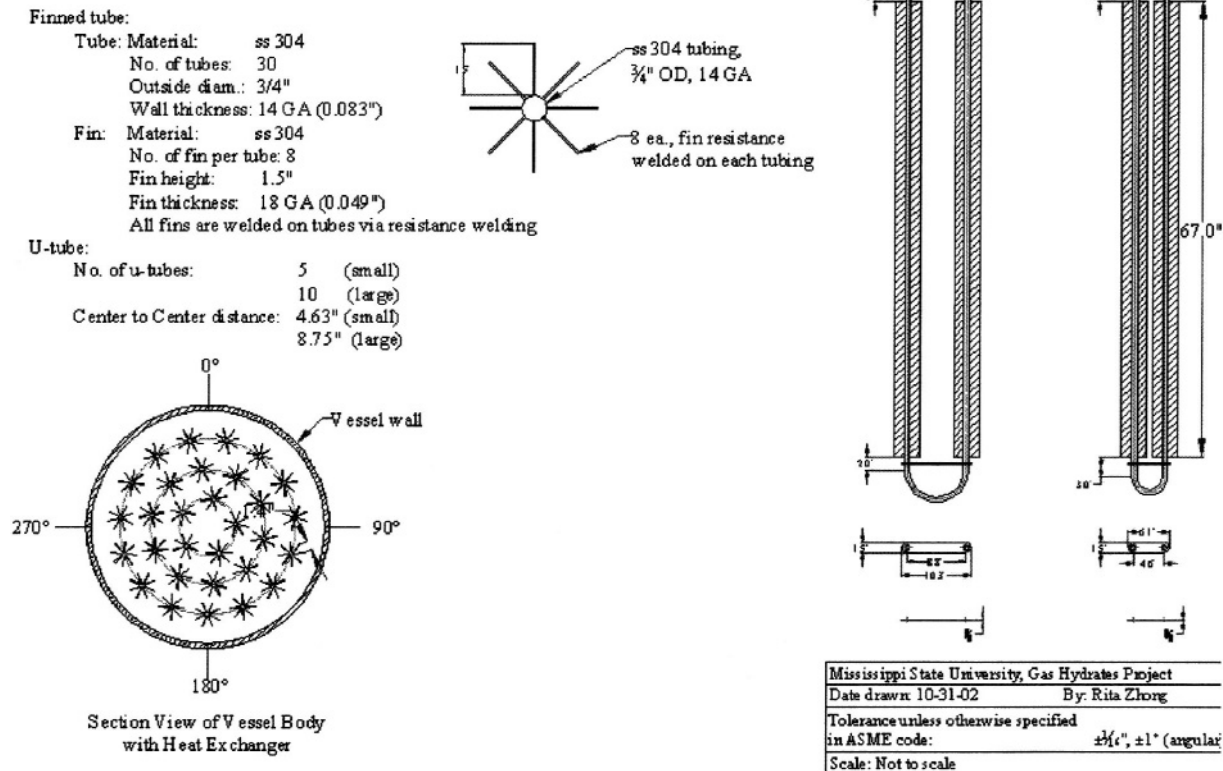
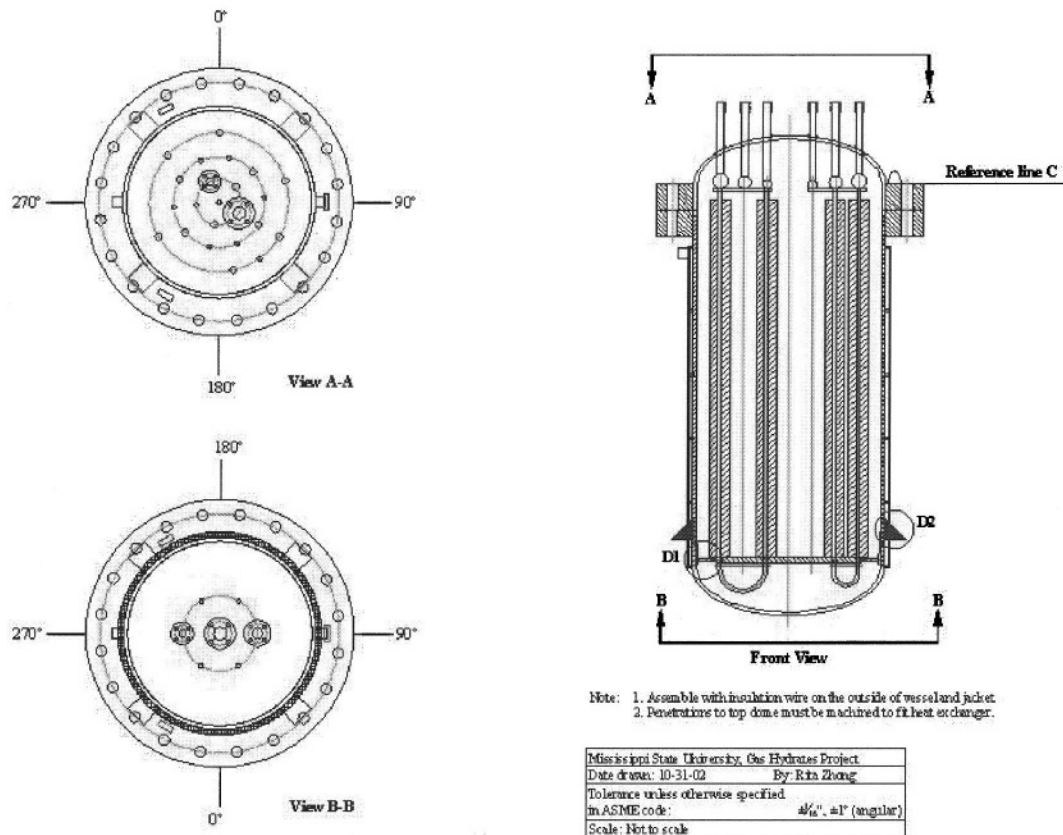
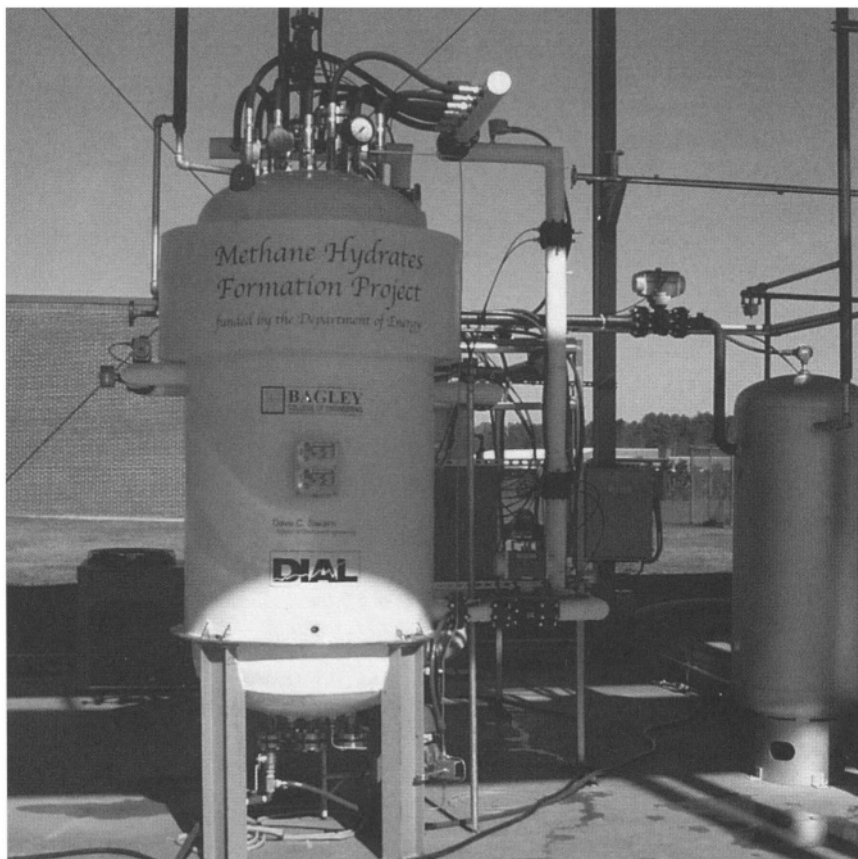


Figure 7. Heat exchanger and hydrate collection finned tubes.



**Figure 8.** Finned tubes arrangement in hydrate formation vessel.



**Figure 9.** POC gas-hydrate installation.

solution. In the feasibility study, a non-stirred laboratory test cell could be filled with hydrates in less than three hours with a capacity of 156 vol/vol. The important attributes of the laboratory process are incorporated in the design for a proof-of-concept scale-up. Simplicity and minimum labor requirements are stressed in the design. The process is designed to store 142 scm (5000 scf) of natural gas in gas hydrates to be formed from micellar solutions at 3.79 MPa (550 psig) and 274.9 K (35 °F). A finned-tube heat exchanger accommodates latent-heat transfer during hydrate formation and decomposition, but the exchanger also serves to collect and to symmetrically pack hydrate particles as they form.

The proof-of-concept facility is based on experimental results of the laboratory feasibility study; the facility has been constructed and installed. Full-scale tests are proceeding.

## ACKNOWLEDGMENTS

The authors would like to acknowledge the support of the Department of Energy through the grants DE-AC26-97FT33203 and DE-FC26-01NT41297. The expertise of DIAL personnel is gratefully recognized: R. Arunkumar, K. Umfress, J. McCown, C. Waggoner.

## REFERENCES

1. Makogon, Y. F. *Hydrates of Hydrocarbons*, PennWell Books: Tulsa, 1997; p. 301.
2. Benesh, M. E. U.S. Patent No. 2270016, 1942.
3. Nierman, J. A. U.S. Patent No. 3975167, 1976.
4. Ehram, C. U.S. Patent No. 4920752, 1990.
5. Ye, G. Y.; and Rogers, R. E. *J. Energy Resour. Technol.* 1996, 118 (3), 209-213.
6. MES, Mitsui Engineering & Shipbuilding Co., Ltd, online news, <http://www.mes.co.jp/english/news/20020806.html>, August 6, 2002.
7. Fitzgerald, A.; and British Gas Group. 2001 SPE Europe Conference, Aberdeen, 4-7 Sept., 2001.
8. Gudmundsson, J. S.; and Mork, M. 2001 International Gas Research Conference, Amsterdam, November 5-8, 2001.
9. Gudmundsson, J. S.; and Hveding, F. *Proceedings of 5<sup>th</sup> International Offshore and Polar Engineering Conference*, The Hague, June 11-16, 1995.
10. Sloan, E. D. *Annals N. Y. Acad. Sci.*, 1994, 715, 17.
11. Zhong, Y.; and Rogers, R. E. *Chem. Eng. Sci.*, 2000, 55 (19), 4175.
12. Rogers, R. E. and Zhong, Y., "Feasibility of Storing Natural Gas in Hydrates Commercially", *Annals N. Y. Acad. Sci.*, 2000, 912, 843-850.
13. Rogers, R. E. and Zhong, Y., "Surfactant Process for Promoting Gas Hydrate Formation and Application of the Same", U.S. Patent No. 6,389,820 (2002).

# Enhancement in the Storage of Methane in Hydrates

**Charles E. Taylor,\* Dirk D. Link, Heather A. Elsen,  
and Edward P. Ladner**

## 1. INTRODUCTION

Estimates by the U.S. Geological Survey project that world methane hydrate deposits contain approximately  $2 \times 10^4$  trillion cubic meters of methane. Estimates of methane hydrate deposits off the coast of the United States is approximately  $9 \times 10^3$  trillion cubic meters of methane with an additional 17 trillion cubic meters of methane in the permafrost on the north slope of Alaska [1]. Access to even a small percentage of this vast fuel resource would provide hundreds of years' worth of additional natural gas resources. If 1% U.S. estimated hydrate resource could be recovered, 2,000 Tcf (a 80-year supply) of new natural gas resource would be available. Much research continues to be performed on accessing the fuel in these deposits, with focuses ranging from mining techniques to use and conversion methods.

In addition to representing a vast amount of fuel resources that remain to be accessed, the physical characteristics of methane hydrates offer other interesting and potentially valuable alternatives to current methods for storage and access

---

CHARLES E. TAYLOR • U.S. Department of Energy, National Energy Technology Laboratory  
P.O. Box 10940, Pittsburgh, PA 15236-0940

DIRK D. LINK • U.S. Department of Energy, National Energy Technology Laboratory P.O. Box  
10940, Pittsburgh, PA 15236-0940

HEATHER A. ELSER • U.S. Department of Energy, National Energy Technology Laboratory  
P.O. Box 10940, Pittsburgh, PA 15236-0940

EDWARD P. LADNER • U.S. Department of Energy, National Energy Technology Laboratory  
P.O. Box 10940, Pittsburgh, PA 15236-0940

\* Email: charles.taylor@netl.doe.gov, tel: 412-386-6058



to methane fuel. Methane hydrates represent the maximum amount of methane gas that can be contained in water. In fact, previous studies have shown that the solubility of methane in water is a limiting factor for some chemical processing methods for conversion of methane [2, 3]. The theoretical maximum uptake of methane as a hydrate is 180 volumes of methane at standard temperature and pressure (STP) [4]. In practice, laboratory experiments on natural systems have struggled to achieve even 30% of this theoretical maximum. One promising method for maximizing the uptake of methane by hydrate formation is the addition of surfactants to the system [5–7].

Some conventional methods of storing natural gas for future use include liquified natural gas (LNG), or pumping the gas into salt caverns or depleted gas reservoirs. The natural gas can then be accessed when needed by pumping it back out of the well. The main drawback to liquification of the gas is the expense, costing as much as 25% of the gas volume used in liquification and transport. A problem with storage of the gas in depleted wells is that the location of the wells is often not adjacent to where the gas is needed. The storage of natural gas in a hydrate structure may be a promising technology for those remote locations that do not have a used gas well in close proximity. In order for this option to be competitive, it must be shown that the hydrate is able to store large volumes of methane, and that the formation stability is appropriate for addressing safety concerns. It also must be a cost-effective technique in order to be a viable storage option. It has been stated that the ability to perform multiple cycles of hydrate formation and subsequent release of the gas may allow gas storage as methane hydrate to compete with the conventional methods of gas storage, with figures of 4, 14, and 54 cycles per year being required to compete with LNG, salt caverns, and depleted reservoir, respectively [6].

Another proposed use of gas hydrates is in the maritime transportation of associated gases from offshore oil production sites, or to remote locations where pipeline transport is not practical [8, 9]. Typically, these associated gases are flared, which is becoming an increasing concern from both an environmental and an economic standpoint. In fact, the ability to utilize these gases may dictate whether oil developments proceed because of the need to find economically feasible methods for disposal or use of the associated gas. Collection and transportation as a gas hydrate may be an effective method of using these gases.

It has been determined that hydrate formation in pure water-natural gas systems suffers from inadequate storage capacity and rate of formation to be competitive as a storage option, but the addition of a surfactant to the system provides many benefits [5–7]. Using surfactants leads to a 700-fold increase in the rate of formation, and the amount of methane absorbed approaches the theoretical limit (86% with sodium dodecylsulfate (SDS)). These studies used SDS as the surfactant at concentrations ranging from 240 to 284 ppm.

While the addition of SDS has enhanced the formation characteristics of gas hydrate systems, it may be helpful to investigate the ability of other surfactants, or other experimental parameters for additional beneficial properties of hydrate formation and dissociation. This research will evaluate the storage capability of methane hydrates formed with a variety of surfactants, and will investigate formation and dissociation characteristics as well. It will also attempt to establish important parameters for maximizing the amount of methane that can be taken up as a hydrate, and elucidate other important parameters that affect the stability, formation, and dissociation of the methane hydrate to further evaluate its use as a viable storage methodology for natural gas usage.

## 2. EXPERIMENTAL

All experiments were conducted in a high-pressure view cell, shown in Figure 1. The cell is constructed of 316 stainless steel with 6.35 cm (2.5 inches) OD and is 27.4 cm (11 inches) in length. The internal volume of the cell is approximately 40 mL. The cell is fitted with two machined endcaps, one of which contains a sapphire window to allow for observation of the contents of the cell using a CCD camera. The cell is fitted with ports to accommodate the fill gas inlet and reaction product outlet, a pressure transducer to monitor the internal pressure of the gas inside the cell, and a thermocouple that terminates inside the cavity of the cell to monitor the temperature of the liquid/hydrate mixture. While the working pressure of the cell is rated at 220 MPa (32,000 psia), all experiments were conducted at 13.8 MPa (2000 psig) or less. The temperature of the cell is controlled by the flow of a glycol/water solution from an external circulating temperature bath through a coil of 0.64 cm ( $\frac{1}{4}$  inch) copper tubing that is wrapped around the outside of the cell. Several layers of insulating material are wrapped around the cell to help maintain constant temperature. A schematic of the entire experimental setup is shown in Figure 2.

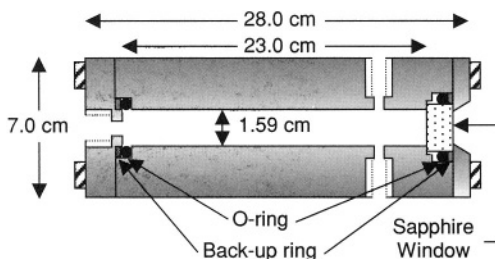


**Figure 1.** Diagram of the high pressure view cell used in the hydrate formation studies.

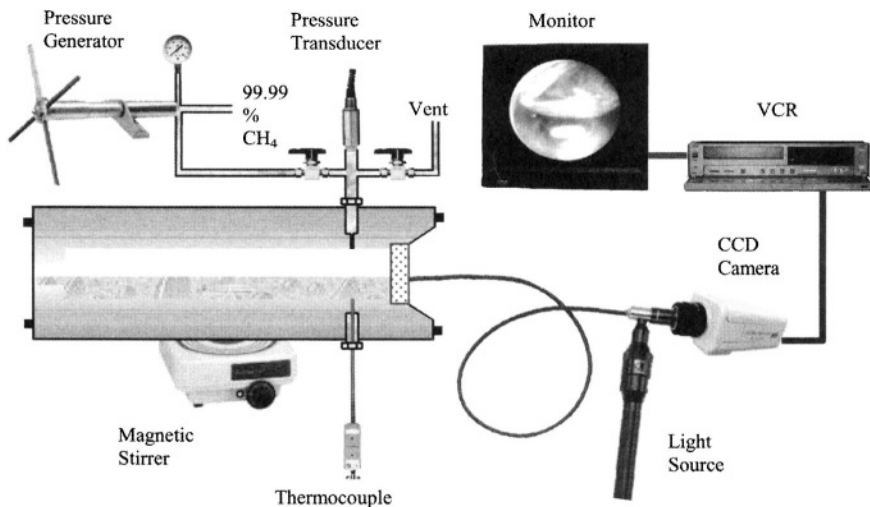


**Figure 2.** Schematic of the entire experimental apparatus as used for formation and dissociation studies.

## 2.1. General Hydrate Formation Procedure

A typical experiment involves filling the cell with approximately 20 mL ( $\pm 0.1$  mL) of double-distilled water. A Teflon<sup>®</sup>-coated stir bar is also placed inside the cell. An external magnetic stirrer is used to obtain a high degree of vortex mixing inside the cell. The cell is connected to the gas manifold and purged several times with methane. Following the purge procedure, the cell is charged with methane at pressures of 8.3–10.3 MPa (1200–1500 psig). Using the external circulating temperature bath, the temperature of the water in the cell is gradually lowered until formation of the methane hydrate is observed. After formation of the hydrate, the temperature of the cell is lowered to approximately  $-10$  °C and held constant as the unabsorbed methane is released from the cell. The cell is then allowed to warm slowly to room temperature, which causes the hydrate to release its absorbed methane gas. The uptake of methane is determined based on the maximum pressure built up by the released methane inside the cell.

## 2.2. Multiple hydrate formations

Multiple hydrate formation experiments were conducted using the following solutions: 30 mL of distilled-deionized water and 30 mL of simulated seawater (made by dissolving 26.8 grams of sodium chloride and 5.3 grams of magnesium chloride in 1 liter of distilled-deionized water). The cell was connected to the reactor manifold and charged with methane as described above. The temperature of the cell was reduced to  $5$  °C and held constant until the methane hydrate formed. After formation of the methane hydrate, the temperature of the cell was increased

to 15 °C. This increase in temperature forced the methane hydrate to dissociate, as observed through the cell's view port and by the return of the cell pressure to the initial pressure prior to hydrate formation. To reform the methane hydrate, the temperature of the cell was reduced to 5 °C. This formation/dissociation procedure was repeated several times using the same methane/solution system.

### 2.3. Maximized methane uptake experiments

The experiments to determine maximum uptake of methane by the hydrate were conducted by adding 10 mL of the distilled-deionized water and surfactant mixture (surfactant concentrations were approximately 225 ppm), adding the Teflon<sup>®</sup> coated stir bar, and sealing the cell, all as described above. The cell was connected to a modified gas manifold containing two single-stage high-pressure regulators in series and was purged several times with methane. Following the last purge, the valves connecting the cell to the manifold remained opened, and the regulators were set to deliver methane at 9.7 MPa (1400 psig). This allowed the experiment to proceed at a constant head pressure of 9.7 MPa (1400 psig) even as methane was taken up during the formation of the hydrate. Again, an external magnetic stirrer was used to obtain a high degree of vortex mixing inside the cell. Temperature of the water in the cell was lowered until formation of the methane hydrate was observed. Following formation of the hydrate, the temperature of the cell was lowered to approximately -10 °C to minimize the dissociation of the hydrate in the subsequent depressurization step. After several hours at -10 °C, the cell was isolated from the manifold and the unabsorbed methane was released, bringing the head pressure to a minimum. After release of the head pressure, the cell was resealed and warmed to room temperature. Methane uptake was determined based on the amount of pressure that built up inside the cell due to outgassing of the hydrate.

### 2.4. Performance Comparison Among Different Surfactants

Using conditions of constant stirring and constant methane headspace pressure, several different surfactants were tested to determine the magnitude of increasing the methane uptake, among them were dodecyltrimethyl ammonium chloride, dodecylamine, dodecylamine HCl, sodium lauric acid, sodium oleate, Superfloc 16<sup>®</sup>, and Superfloc. To maintain consistency for the comparison studies, all surfactants were added at the same concentration range of 200 to 230 ppm. A volume of 10.0 mL of double-distilled water and surfactant was added to the system. Procedures identical to the maximum uptake experiments with SDS were followed. The amount of methane absorbed by each system was determined and the results compared based on percentage of theoretical maximum uptake for methane hydrate formations.

## 2.5. Raman Spectroscopy

The Raman spectra were collected using a Thermo Nicolet Aimega spectrometer. The spectra of the hydrate samples were collected *in situ* by placing the view cell in the spectrometer such that the Raman beam was focused through the cell's sapphire window on to the hydrate. All spectra were collected at the hydrate formation temperatures.

## 3. RESULTS AND DISCUSSION

### 3.1. Hydrate formation and dissociation

Our first experiments were to study the formation and dissociation of methane hydrates in natural (methane-water) systems. Figure 3 shows a typical pressure/temperature profile for this process. During the initial stages of cooling, the pressure inside the cell mirrors that which would be predicted from the ideal gas law. However, as the hydrate begins to form, a sharp decrease in the cell pressure is observed, indicating that methane is being absorbed from the headspace. Formation begins at a temperature of about 5.5 °C for the distilled-deionized water system, which is appropriate for the pressure and temperature conditions of hydrate formation predicted by the hydrate equilibrium stability diagram [4]. Addition of salts to the system, in the form of NaCl and  $\text{MgCl}_2$  at a net salt concentration of 3.2%, lowers the formation temperature by approximately 2 °C. Visually, the initial hydrate formation appears as ice crystals suspended in the water. As formation of the hydrate continues, the hydrate begins to agglomerate, forming a slush. As additional hydrate is formed inside the cell, the slush is transformed into a solid

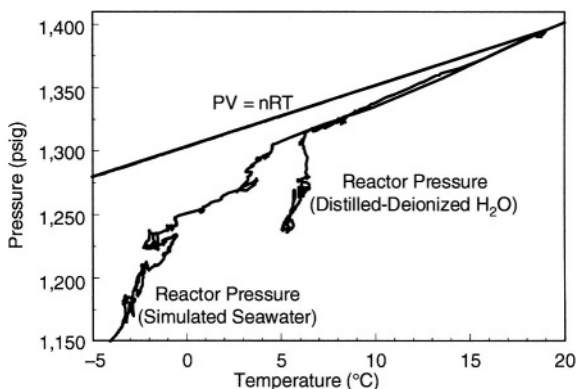


**Figure 3.** Pressure and temperature profile for the formation of a methane hydrate from double distilled water and simulated seawater.

mass. Even after formation of the solid mass, over time the hydrate incorporates more of the free methane into the crystal structure. Upon warming, the hydrate dissociates with evolution of methane.

### 3.2. Multiple Hydrate Formations

The potential existence of a “memory effect” for multiple formations of methane hydrates was investigated. Previous observations in our laboratory determined that after the initial formation and dissociation of a hydrate with a given reactant system, upon lowering the temperature, subsequent hydrate formation occurs more quickly and seemingly at slightly higher temperatures, than the original formation. This is shown in Figure 4. Note that the elapsed time for hydrate formation is notably faster during the second formation (1 hour as opposed to 4 hours). The third and fourth formation of the hydrate occurs at times slightly less than the second formation. This decrease in formation time may be due to microscopic hydrate crystals that are still present in the solution, even at 15 °C. These crystals would act as seeds for future formations [10]. The formation of methane hydrates in simulated seawater followed the same physical changes as that observed for hydrate formed in pure water. In investigating this phenomenon further, we found that when the hydrate is dissociated by warming to slightly higher temperatures (25 °C), this memory effect is not observed (data not shown). The higher temperature may dissociate even the microscopic crystals that could be responsible for the effect.

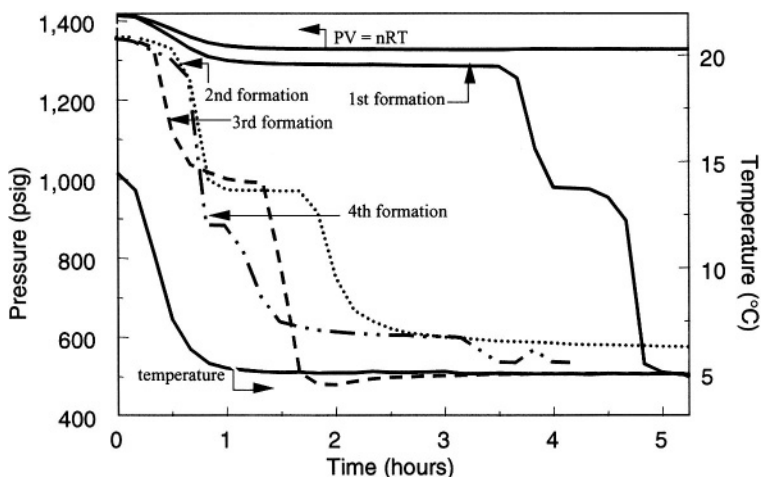


**Figure 4.** Temperature-pressure data as a function of time for repeated formations of methane hydrates using the same reactants.

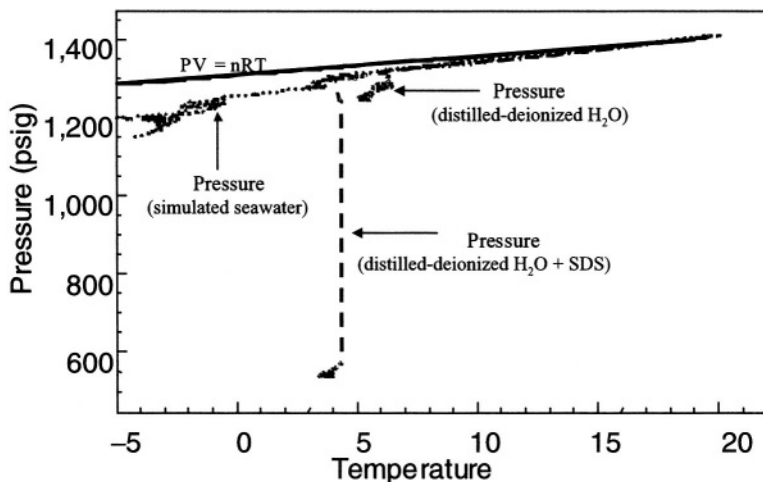


**Figure 5.** Pressure as a function of temperature for the formation of a methane hydrate in double-distilled water, simulated seawater, and water with 224 ppm SDS added.

### 3.3. Maximizing methane uptake

Formation of methane hydrates in double-distilled water, simulated sea water and double-distilled with a surfactant added is shown in Figure 5. The data for the double-distilled water and simulated sea water formations is identical to Figure 3, except that the scale required to accommodate the uptake by the water-surfactant system alters the appearance of the data.

As is shown in the figure, methane uptake by both double-distilled and simulated seawater is  $\sim 1.4$  MPa (200 psig). Also of note is that the onset of hydrate formation in the simulated seawater occurs approximately 3 °C lower than that of the double-distilled water. When surfactant is added to the water, methane uptake by the hydrate increases to  $\sim 5.6$  MPa (800 psig), which is over a four-fold increase compared to hydrates formed without surfactant. The increase observed in the uptake of methane when the surfactant is present can be explained by examining the processes that occur during hydrate formation. Since methane hydrate is less dense than water, hydrates form on the surface of the water.

Even with stirring, enough hydrate will form to essentially cover the water-gas interface with a thin layer of methane hydrate. This severely limits the absorption of additional methane, as it must diffuse through the hydrate layer in order to encounter free water. When the surfactant is present, the hydrate formed is forced to the edges of the surface of the stainless steel cell, allowing significantly more contact between the methane and the surface of the free water. Access to free water allows the concentration of methane in the water to increase, enhancing the amount of hydrate formation.

In order to determine the maximum amount of methane that the water-surfactant system could have taken up during hydrate formation, we formed methane hydrate in the water-surfactant system with a constant supply of methane in the headspace. The results are shown in Figure 6. During this experiment, the hydrate was formed under a constant head pressure of 9.7 MPa (1400 psig), with formation beginning at approximately 3.5 °C. Once uptake of methane appeared to have ended, the temperature of the cell was further decreased to -10 °C, in order to preserve the hydrate during the subsequent depressurization of the unabsorbed methane inside the cell. Following depressurization at a temperature of -10 °C, the cell was warmed to room temperature, accompanied by an increase in cell pressure due to methane outgassing from the melting hydrate. As Figure 6 shows, the cell pressure reached approximately 1350 psig. Our calculations indicate that the hydrate formed by this method contained over 96% of the maximum theoretical amount of methane.

For percent uptake calculations, the maximum theoretical uptake for the methane hydrates was calculated, assuming that the hydrates being formed in our experiments were Type I structures. The theoretical ratio of 5.75 moles water to 1 mole methane per volume of methane hydrate predicts that from a 15 mL volume (0.833 moles) of water, 0.145 moles of methane can be absorbed. Next the experimental amount of methane absorbed was calculated. Using the final pressure that is reached inside the cell after outgassing of the hydrate, the amount of methane that was absorbed was calculated. This value must be corrected for deviation from

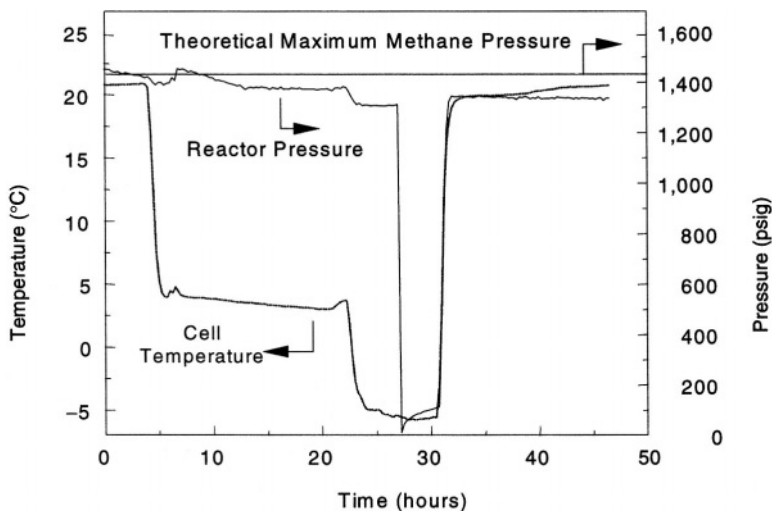


**Figure 6.** Pressure and temperature profile as a function of time for the formation of a methane hydrate with 224 ppm SDS surfactant added, with a constant headspace pressure of 9.7 MPa (1400 psi).



Table 1. Surfactants tested for ability to maximize the uptake of methane in methane hydrate formations.

Surfactant	Pressure following dissociation (psig)	Compressibility factor, $z^*$	Percent Uptake
Dodecyl trimethyl Ammonium Chloride	140	0.9824	13.9%
Sodium Dodecylsulfate (SDS)	1440	0.8206	97.3%
Dodecylamine	100	0.9877	9.9%
Dodecylamine HCl	120	0.9850	11.9%
Sodium Lauric Acid	715	0.9058	77.4%
Sodium Oleate	655	0.9139	70.5%
Superfloc 16 <sup>®</sup>	195	0.9756	19.6%
Superfloc 84 <sup>®</sup>	200	0.9754	20.1%

\* Values for compressibility factor taken from [11].

ideal conditions using the compressibility factor,  $z$ , which ranges from 0.8 to 1, depending on experimental conditions [11]. This compressibility factor is necessary because experimental conditions such as internal pressure make it seem like less gas was released from the hydrate. Without taking this compressibility into account, the calculated results would be biased low, as more methane would have been taken up than the experimental pressures portray.

Based on the results of the uptake studies using SDS, it was determined that maximum uptake was demonstrated under conditions where a constant methane headspace pressure was used, and the reaction mixture was stirred. Therefore, subsequent methane hydrate formation experiments to evaluate the effectiveness of different surfactants were performed using constant headspace pressure and stirring. Under these conditions, the following surfactants were evaluated: dodecyl trimethyl ammonium chloride, dodecylamine, dodecylamine HCl, sodium lauric acid, sodium oleate, Superfloc 16<sup>®</sup>, and Superfloc 84<sup>®</sup>, all added at similar concentrations in the range of 205 to 220 ppm. The results of the uptake evaluations are shown in Table 1. As the data demonstrates, the largest amount of methane absorbed in our study was for the SDS-water system. Uptake for this system surpassed 97% of the theoretical maximum uptake of methane during methane hydrate formation.

Figure 7 shows the *in situ* Raman spectrum obtained on a sample of methane hydrate that was formed in the 200 ppm commercial surfactant-water system. A deconvolution algorithm was used on the spectrum to reveal peaks that can be assigned to the large and small hydrate cages. The unit cell of methane hydrate consists of 46 water molecules, a maximum of 8 methane molecules, and is constructed of two small cages (pentagonal dodecahedron) and six large

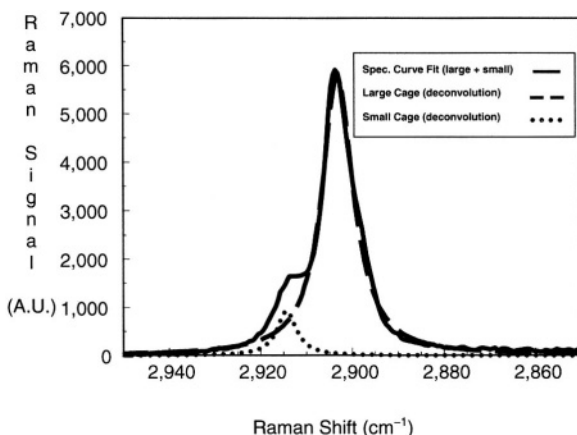


**Figure 7.** Raman Spectrum, with deconvolution, of a formation of a methane hydrate with 224 ppm SDS surfactant added, with a constant headspace pressure of 9.7 MPa (1400 psi).

cages (tetrakaidecahedron) [12]. This results in 5.75 water molecules per methane molecule in a fully occupied hydrate unit cell. The position of the peaks from the large ( $2903.1\text{ cm}^{-1}$ ) and small cages ( $2914.3\text{ cm}^{-1}$ ) along with the intensities obtained on the SDS-water produced methane hydrate are consistent with those of methane hydrate formed from pure water [13].

A commercial surfactant was investigated for its ability to enhance the uptake of methane in methane hydrate. All experiments were conducted following the procedure listed in **Maximized methane uptake** in the experimental section. Based on the results of the uptake studies using SDS, a constant methane headspace pressure was used, and the reaction mixture was stirred. The results of this investigation are listed in Table 2. In the first and sixth formation experiment, uptake of methane surpassed 99% of the theoretical maximum uptake of methane during methane hydrate formation. This value is comparable to that of the SDS-water system. However, the calculated uptake of methane during the other experiments is significantly lower (Table 2). These results were rather puzzling until a detailed observation of the experimental procedure was conducted. The technician performing the experiments where the calculated methane uptake was low was new to the Team. This technician was observed to vent the headspace methane over a much longer time than previous experimentalists (times up to 15 minutes as opposed to 15 seconds). During these longer venting times, the hydrate began to decompose even at temperatures as low as  $-20\text{ }^{\circ}\text{C}$ , producing methane gas which was vented, reducing the amount of methane recovered during the decomposition of the remaining hydrate.

**Table 2.** Commercial Surfactant tested for ability to maximize the uptake of methane in methane hydrate formations

Experiment	Vent Temperature (°C)	Pressure following dissociation (psig)	Compressibility factor, $z^*$	Percent Uptake
1	−17.6	1193.6	0.8576	99.90
2	−16.2	212.5	0.9709	21.37
3	−16.7	261.2	0.9648	26.44
4	−15.0	118.7	0.9827	11.80
5	−17.9	135.6	0.9806	13.50
6	−15.1	1196.3	0.8576	99.90
7	−19.9	153.9	0.9784	15.36
8	−17.3	137.9	0.9806	13.73
9	−19.9	200.7	0.9725	20.15

\* Values for compressibility factor taken from [11].

## 4. CONCLUSIONS

We have produced methane hydrates in our laboratory. The temperature and pressure profiles for hydrate formation for several different starting pressures of methane, as well as different aqueous media, have been determined. The addition of the surfactant SDS increases the uptake of methane during formation of the hydrate. The amount of methane uptake obtained using the surfactant has reached greater than 97% of the theoretical limit. It appears that SDS may be the most appropriate surfactant to use for maximizing methane uptake for storage of methane as methane hydrate.

It is important to note that all surfactants used in this study were compared at the same concentration level. This concentration level corresponds to the critical micellar concentration (CMC) of SDS under temperature and pressure conditions during hydrate formation, as shown in previous work [5, 7]. Future work in our laboratory will involve the determination of the critical concentration of each individual surfactant for methane uptake, as this critical concentration varies significantly from the CMC at ambient conditions. Once these concentrations are determined, the ability of each surfactant to promote methane uptake at their respective critical surfactant concentration will be compared, as this may provide more insight into which surfactant may perform optimally for methane uptake during hydrate formation.

In determining the amount of methane converted to hydrate, care must be taken during the venting of the headspace methane after hydrate formation even at temperatures as low as −20 °C. If vented too slowly, the hydrate will dissociate affecting the experimental results. The experimental procedure has been modified to include rapid venting of the headspace gas.

## DISCLAIMER

Reference in this report to any specific commercial product, process, or service is to facilitate understanding and does not necessarily imply its endorsement or favoring by the United States Department of Energy.

## ACKNOWLEDGMENTS

The authors would like to acknowledge the technical assistance of Jonathan Lekse and Christopher Matranga.

## REFERENCES

1. Collett, T. S. and Kuuskraa, V. A. *Hydrates Contain Vast Store of World Gas Resources*. Oil Gas J., 1998. 96(19): p. 90.
2. Noceti, R. P.; Taylor, C. E.; and D'Este, J. R. *Photocatalytic Conversion of Methane*. Cat. Today, 1997. 33: p. 199–204.
3. Taylor, C. E. and Noceti, R. P. *New Developments in the Photocatalytic Conversion of Methane to Methanol*. Cat. Today, 2000. 55: p. 259–267.
4. Sloan Jr., E. D., *Clathrate Hydrates of Natural Gases*. 2nd ed. 1997, New York: Marcel Dekker, Inc. 705.
5. Rogers, R. E., Report No. DE-AC26-97FT33203, US Department of Energy, 1997.
6. Rogers, R. E., Report No. DE-AC26-97FT33203, US Department of Energy, 1999.
7. Zhong, Y. and Rogers, R. E. *Surfactant Effects on Gas Hydrate Formation*. Chem. Eng. Sci., 2000. 55: p. 4175–4187.
8. Kromah, M.; Thomas, S.; and Dawe, R. A. *Transporting Natural Gas Around The Caribbean*. West Ind. J. Eng., 2002. (in press).
9. Fitzgerald, A. and Taylor, M. *Offshore Gas-to-Solids Technology*. in *Offshore Europe Conference*. 2001. Aberdeen, Scotland: Society of Petroleum Engineers, Inc.
10. Koh, C. personal communication, 2002.
11. Perry, R. H.; Green, D. W.; and Maloney, J. O. *Perry's Chemical Engineering Handbook*. 5th ed. 1984, New York: McGraw-Hill, Inc.
12. Sloan Jr., E. D., *Clathrate Hydrates of Natural Gases*. 2nd ed. 1997, New York: Marcel Dekker, Inc. 41.
13. Sum, A. K.; Burruss, R. C.; Sloan Jr., E. D., *J. Phys. Chem.* 1997, 101, p. 7371–7377.

*This page intentionally left blank*

# Strength and Acoustic Properties of Ottawa Sand Containing Laboratory-Formed Methane Gas Hydrate

**William J. Winters,\* William F. Waite,  
and David H. Mason**

## 1. INTRODUCTION

Although gas hydrate occurs in a wide variety of sediment types and is present and even pervasive at some locations on continental margins, little is known about how it forms naturally. Physical properties of the resultant gas hydrate-sediment mixtures, data needed for input into models that predict location and quantity of in situ hydrate are also lacking. Not only do properties of the host materials influence the type and quantity of hydrate formed and whether a particular deposit may be an economic resource or a geohazard, the properties of the natural sediment are also subsequently changed by the formation of gas hydrate in the pore space. The magnitude of the change is primarily related to the amount and the weighted inter-particle distribution of the hydrate deposits in relation to the actual sediment grains. Our goal is to understand the interaction between natural sediments and gas hydrate formation in order to quantify physical properties that are useful to predictive models.

Because studying gas hydrate in situ is expensive, artificial methods have been used in various laboratories to create pure methane gas hydrate [1] and gas hydrate

---

WILLIAM J. WINTERS • U.S. Geological Survey, 384 Woods Hole Rd., Woods Hole, MA 02543  
WILLIAM F. WAITE • U.S. Geological Survey, 384 Woods Hole Rd., Woods Hole, MA 02543  
DAVID H. MASON • U.S. Geological Survey, 384 Woods Hole Rd., Woods Hole, MA 02543

\* Corresponding author: Tel: 508-457-2358; bwinters@usgs.gov

in sediment [2, 3]. However, the equipment and test procedures used to form gas hydrate in sediment affect the measured results. For example, no laboratory method can approach the time scale required by some natural systems to form gas hydrate, but we have used the Gas Hydrate And Sediment Test Laboratory Instrument (GHASTLI) to create hydrate in sediment over relatively long periods of time (1–3 months) using different methods. In addition, we study natural sediment samples that contain gas hydrate recovered from the field [4]. The purpose of this paper is to: (a) understand the behavior and quantify physical property changes of sediment caused by the formation of natural gas hydrate using laboratory methods, (b) discuss different laboratory techniques used to form gas hydrate in sediment, and (c) present enhanced laboratory methods to better simulate natural hydrate formation.

Methane gas hydrate can be formed by at least four different methods in the laboratory. In this study we have: (1) slowly pushed methane into initially water-saturated specimens (method one), and (2) introduced methane into partly-water-saturated samples in which some of the void space is initially filled with air (method 2). These methods simulate natural gas hydrate formation conditions in regions containing bubble phase gas, for example, Hydrate Ridge [5]. Hydrate can also be formed using finely ground seed ice, however this technique cannot reproduce natural sediment fabric in fine-grained material. The fourth method relies on continually feeding methane-saturated water into a test specimen. This method best reproduces many natural conditions, since [6] demonstrate that gas hydrate may form in the absence of a free gas phase, but this method is more difficult and time consuming to conduct.

Other, more exotic methods also have been used to form hydrates. For example, surfactants were used by [7] to catalyze formation, [8] showed that velocity changes occur when pore-volume saturation exceeds about 35% using sand and R11 ( $\text{CCl}_3\text{F}$ ) refrigerant as the hydrate former, [9] used glass micromodels, and numerous investigators have used tetrahydrofuran (THF).

How measurements on synthesized samples compare with natural gas hydrate is uncertain at this time and will only be answered by continued in-situ testing and by making more measurements on natural specimens recovered from the field. However, acoustic velocities measured during the Mallik 2L-38 gas hydrate program in the Canadian Arctic indicate that gas hydrate does not cement significant numbers of sediment grains in situ [10, 11]. We have arrived at similar conclusions based on rock physics modeling performed on pressurized and frozen drilled samples recovered from the Mallik 2L-38 well in which the natural gas hydrate was preserved [12]. In contrast, visual and tactile observations of methane hydrate formed within various types of sediment and acoustic modeling of some of those specimens [13] have indicated that laboratory-formed methane hydrate does cement sediment grains. Therefore, models attempting to predict behavior of gas hydrate in the natural environment need to account for differences between natural and laboratory-formed hydrate.

We are also interested in the properties of gas hydrates as they relate to permafrost and other regions and as such show test results of frozen sand and pure ice samples. Permafrost exists over approximately 20% of the earth's northern hemisphere [14] and is therefore of interest from a geologic standpoint especially in Russia and Canada where about 50% of their land mass is permafrost [15]. Because gas hydrate can exist within permafrost [16, 17] it may be difficult to differentiate between areas containing one or the other. Hydrate can also be present in sediment beneath permafrost [18], where the temperature is too high due to a combination of subbottom depth and local geothermal gradient.

## 2. EXPERIMENTAL EQUIPMENT AND PROCEDURES

GHASTLI utilizes a number of separate pressure and temperature control subsystems to simulate in situ conditions on a 71 mm diameter by 130–140 mm high right circular sediment specimen (Figure 1). The 25 MPa pressure (equivalent

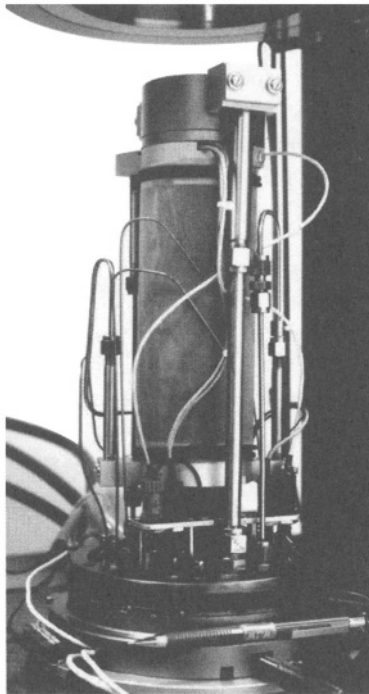


**Figure 1.** Close-up view of a test specimen about to be raised into the main pressure vessel showing the different pressure and coolant lines. The test specimen (Grey cylinder in the central part of photo) is 14 cm high. The sediment sample is vertically raised into the main pressure vessel, located at the very top of the photo, prior to testing.



to the pressure exerted by a 2,500 m column of water) and temperature (about  $-5^{\circ}\text{C}$  minimum) capabilities of the system provide wide latitude in test configurations and procedures within which gas hydrate can be studied in reconstituted sediment or in field samples containing natural gas hydrate. Sensors placed within the different subsystems and in close proximity to the test specimen produce measurements that are logged and displayed by a computer running custom-designed Labview software. During testing, the sample resides within a silicone-oil filled, main pressure vessel. Separate internal sediment pore pressure and external confining pressure systems are used to adjust isotropic consolidation stress to simulate in situ overburden pressure.

Flexible membranes isolate the external silicone oil from the test sample. Top and bottom end caps incorporate acoustic transducers and gas or water flow ports. The bottom end cap rests on an interchangeable internal load cell. The top end cap is contacted by a bath-controlled, variable-temperature heat exchanger that imparts a unidirectional cooling front downward through the specimen. To achieve better sample thermal equilibrium the perimeter of the main pressure vessel is also surrounded by cooling coils.

Four 500 ml capacity syringe pumps are used to maintain the confining pressure surrounding the specimen and the internal specimen pressures that include: pore pressure, back pressure, and methane-gas pressure. Flow rates of 0.001 ml/min to over 80 ml/min are controlled by the syringe pumps. The back-pressure system contains a collector that is capable of separating and measuring water and gas volumes that are pushed out of the specimen at test pressures by the dissociation of gas hydrate. A separate fifth syringe pump controls the movement of the load ram during shear tests and is used to determine the height of the specimen (which may change during a test) to increase the accuracy of acoustic-velocity measurements. Four thermocouples and four thermistors are placed against the outside perimeter of the specimen at different heights to measure temperature variations during cooling or warming stages and during gas-hydrate formation and dissociation events.

Because we can reduce specimen temperatures below freezing, ice formation is possible either alone or within the sediment pores. This is important because some physical properties of gas hydrate and ice are similar [19] and gas hydrate is present in regions where permafrost is present [20, 21].

We used two methods to form methane gas hydrate in sieved Ottawa sand (0.25–0.5 mm diameter). The first method begins with an initially fully water saturated specimen. Confining and pore pressures are raised to 12 MPa and then an additional consolidation stress,  $\sigma'_c$ , typically 250 kPa is applied externally to the test specimen. Methane is slowly percolated up through the sediment until a pre-determined amount of water, measured by the collector, is pushed out of the sample. Flow reversals of methane are sometimes used to achieve better gas distribution within the specimen. Then the temperature of the coolant flowing to the heat exchanger located above the top end cap is lowered until P-T conditions

are within the gas-hydrate-stability zone. Physical properties are measured and recorded during these procedures. To dissociate the gas hydrate the procedure is reversed; that is, the temperature is slowly raised until the phase boundary is crossed. Pressure, rather than temperature can also be used as the trigger to form or dissociate gas hydrate.

The second gas hydrate-forming method uses similar procedures except that the test specimen is initially partly saturated with a combination of water and air in the void space. Internal methane pressure and external confining pressure are raised in tandem to approximately 12 MPa. Then an additional consolidation stress is applied.

P-wave velocity is measured by through transmission using 500 kHz–1 MHz (natural frequency) wafer-shaped crystals that are located on the back side (away from the specimen) of each end cap. A 400-volt pulse is sent to the transmitting transducer and the received signal is amplified, digitized, displayed on a digital oscilloscope, and recorded by a computer. Acoustic p-wave velocity,  $V_p$ , is calculated from the specimen length/measured travel time corrected for system delays.

Four parameters are measured during triaxial strength tests [22]: load, axial deformation, confining pressure, and pore pressure. Loading is produced by a syringe-pump-controlled ram contacting the heat exchanger which then pushes on the sample at a rate related to the syringe-pump-piston travel. Movement of the ram, which can vary from 0.0001 mm/min to 2 mm/min, is measured using a linear displacement transducer connected to the load ram. Interchangeable load cells can be varied according to anticipated strength of the sediment and gas hydrate.

The frozen sediment was created within GHASTLI by simply reducing the temperature of the coolant flowing to a heat exchanger located above a water saturated sediment. Pure ice was formed using the same procedure except that sediment was not present.

### 3. RESULTS AND DISCUSSION

Salinity-corrected water contents were determined for specimens dried at 90 °C for at least 24 hours (Table 1). The water content calculations include all water in the sample, both free water and water that eventually was incorporated into gas hydrate. Porosity values were calculated from initial mass measurements for 100% pore space saturated samples and were based on initial volumetric measurements for samples that were partly water saturated. The amount of methane present was determined from the equation of state relationships presented by [23].

We used method one (initially water saturated) Ottawa sand to create gas hydrate in test GH069. For that and subsequent tests we assume that methane gas hydrate formation is related to p-wave acoustic velocity ( $V_p$ ) (Figure 2).

Table 1. Index and physical properties of Ottawa sand and pure ice specimens.

Test ID (GH)	66	68	69	79	80	83	84	85
<b>General Information</b>								
Sample	Frozen SOS	Pure ice	SOS w/ GH	Water sat SOS	Dry SOS	SOS w/GH	SOS w/GH	SOS w/GH
GH formation procedure			Init saturated			Init partly sat	Init partly sat	Init partly sat
<b>Init Index Physical Properties</b>								
Water content (Mw/Ms) (%)	18.5	—	18.5	18.98	0	12.9	7.8	3.8
Initial water saturation of pore space (%)	100	100	100	100	0	58.5	31.5	16.3
Pore water salinity (ppt)	0	0	30	0	N/A	0	0	0
Grain density (g/cm <sup>3</sup> )	2.65	0.917	2.65	2.65	2.65	2.65	2.65	2.65
Porosity (%)	32.9	100	32.5	33.5	39.5	36.9	39.4	37.9
<b>Gas and GH Quantity</b>								
GH pore saturation (%)	—	—	100? (a)	—	—	70	37	19
<b>Velocities</b>								
Vp baseline (km/sec)	1.86	1.505 (d)	1.9	1.861	—	0.86	1.4	—
Vp max (km/sec)	4.23 (b)	3.83 (e)	3.95 (f)	—	—	4.00 (f)	3.36 (f)	3.08 (f)
<b>Strength Properties</b>								
Consolidation stress, $\sigma'_c$ (MPa)	—	—	0.34	0.252	0.248	0.235	—	0.266
Max shear stress (MPa)	11.17	1.1	10.42	7.73	0.39	10.11	2.61	2.44
Axial strain at failure (%)	11.46	3.48	4.22	10.25	6.96	4.66 (g)	15.02	11.41
<b>Comments</b>								
(a) Gas hydrate visually observed to cement entire specimen								
(b) Frozen								
(d) Water								
(e) Pure water ice								
(f) With gas hydrate								
(g) Membrane failed during shear								

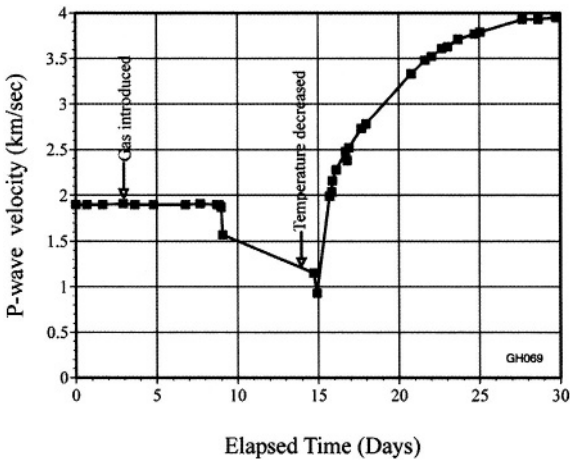


**Figure 2.** P-wave velocity versus elapsed time for Test No GH069. This specimen initially was saturated with water, gas was percolated in to displace some of the water, then the temperature was dropped to initiate gas hydrate formation.

A constant velocity indicates that significant hydrate growth stopped. It is very difficult to achieve uniform gas hydrate distribution in initially water saturated Ottawa sand. We visually observed such behavior in test GH069, but typically significant difficulties are encountered when using that method because of non-uniform methane and water distribution in the sediment pores. For example, test GH082 (Figure 3) shows a completely cemented gas hydrate plug that was removed from the top of that test specimen. Because of signal attenuation in the remaining non-hydrated sample, the hydrate plug caused relatively little increase in measured  $V_p$  in the longitudinal specimen direction.

Although test GH082 did not produce uniformly distributed gas hydrate through out the specimen, it did provide unique insight into the mechanism of hydrate formation by forming a nearly impermeable plug at the top end of the test specimen at the location of methane injection. During gas hydrate formation, a continuous series of inversely tracking pore pressure (measured at the base of the specimen) and small  $V_p$  (measured longitudinally through the sample) trends were observed (Figure 4). Five distinct episodes of continuous reductions in pore pressure were recorded during a 25 day period. Each gradual episode of pore pressure reduction ended abruptly with a relatively quick increase in measured pore pressure.

This interesting behavior is caused by a reduction in the amount of methane present in the pore space at the non-hydrated end of the specimen. The advancement of the hydrate front encapsulating and concentrating methane molecules reduces



**Figure 3.** Sieved Ottawa sand sample test GH082 after removal from GHASTLI. A completely methane gas hydrate cemented plug, removed from the top of the specimen, is resting on top of the remaining non-hydrate bearing sample. The top end cap is in the left center and the bottom end cap is in the right center of the photo. Notice the void adjacent to the top end cap where the hydrate-cemented plug was removed.

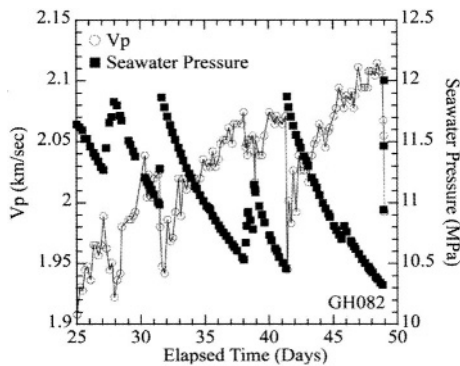


**Figure 4.** P-wave velocity and pore pressure versus elapsed time for Test No. GH082. This specimen initially was saturated with water, gas was percolated in to displace some of the water, then the temperature was dropped to initiate gas hydrate formation. Notice that pore pressure and velocity typically track opposite to each other.

pore pressure. Because the total external stress on the sample remained unchanged, the pore pressure reduction results in an increase in effective stress and  $V_p$ .

Because of the difficulty in forming uniformly distributed gas hydrate within initially fully saturated Ottawa sand samples (method one), we began testing samples using method two. The initial mixtures contained different proportions of water and air for tests GH083, GH084, and GH085. Acoustic velocity versus elapsed time into test (Figure 5) and shear strength (Figure 6) results, are much more consistent using this method.

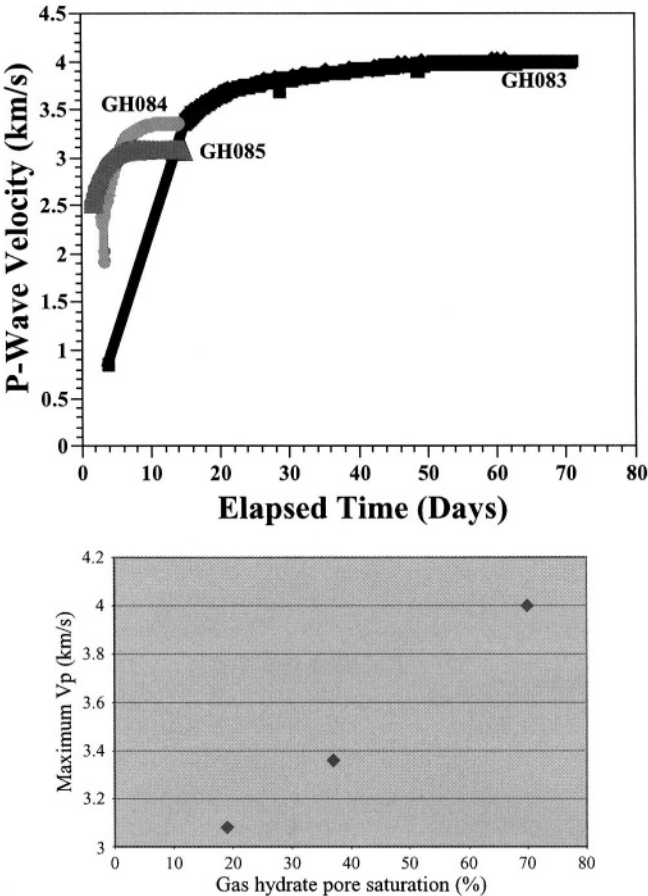


**Figure 5.** P-wave velocity versus elapsed time and  $V_p$  versus gas hydrate pore saturation (insert) for tests GH083, GH084, and GH085. These specimens initially were partially saturated with water. Gas was introduced without allowing drainage, then the temperature was reduced to initiate gas hydrate formation.

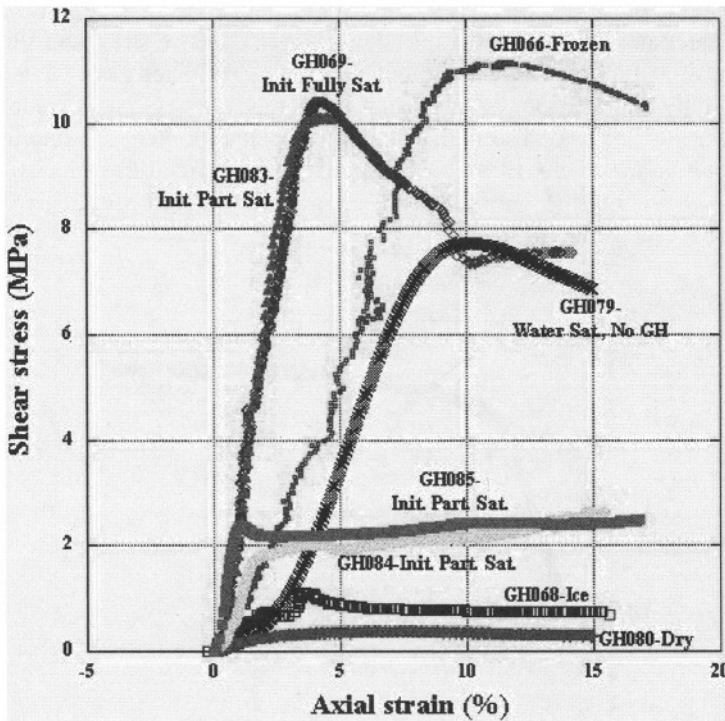


**Figure 6.** Shear stress versus axial strain plots for sieved Ottawa sand specimens containing various materials in the pore space. Results from a pure ice sample are also shown.

The presence of gas hydrate, ice, or air in sediment pores significantly impacts both acoustic and strength characteristics compared to water-saturated specimens (Table 1, Figure 6). Hydrate or ice increases both strength and velocity, whereas air decreases both. Typically, p-wave velocity of water-saturated Ottawa sand was approximately 1.86 to 1.9 km/s. However, the process of freezing pore water, as would occur during permafrost formation, increased  $V_p$  by 2.37 km/s to a final velocity of 4.23 km/s. Interestingly, this is very similar to the velocity increase produced from freezing pure water (2.33 km/s). Evidently, the ice crystal formation process enables acoustic energy to be transmitted similarly whether sediment grains are present or not.

The effect on physical properties of gas hydrate formation in sediment is dependent upon the amount and location of the gas hydrate formed. Hydrate formed at grain boundaries increases  $V_p$  more than hydrate formed in sediment voids [24]. The maximum  $V_p$  increase due to hydrate formation is 2.05 km/s, which is less than the increase caused by freezing pore water, because gas hydrate is present in less quantity than ice in frozen samples or that gas hydrate in sediment is

less efficient at transmitting acoustic energy. Final  $V_p$  for tests GH083, GH084, and GH085 are directly related to hydrate content (Figure 5 insert). Predictably, samples containing higher water contents require additional time to complete the hydrate formation process (Figure 5).

We performed triaxial strength tests on a number of reconstituted sieved Ottawa sand samples with different materials in the pore space to study the relative effect of gas hydrate on sediment properties (Figure 6). Pore fillings consisted of (1) complete or nearly complete gas hydrate formed from initially water saturated sediment, (2) varying amounts of gas hydrate and methane formed from initially partly water saturated sediment, (3) water ice, (4) complete water saturation, and (5) completely dry pore space. We also tested (6) a pure water ice sample without any sediment. This diverse data set enables us to assess the importance of gas hydrate compared to other natural pore fillings and the influence of pore pressure on strength behavior.

An important finding of the test series is the close agreement in behavior between tests GH069 (method one—initially water saturated) and GH083 (method two—initially containing water and gas). In addition to the similarity in final  $p$ -wave velocity of these specimens (Table 1), the stress-strain behavior is nearly identical as well. Hydrate formation method one more closely replicates natural conditions since its initial test conditions are less biased. However, method two produces more consistent results.

As expected, completely dry Ottawa sand possesses the lowest strength followed by pure water ice. Freezing pore water or forming gas hydrate in sediment changes strength properties significantly. The resultant strength is related to the amount of hydrate, ice, water, and methane present in the sample's pores at the time of shear. Fully water saturated Ottawa sand exhibits significant strength because of the development of negative (related to the initial consolidation stress) pore pressure and increase in effective stress. The marked difference in strength between GH080 and GH079 is caused in large part by the development or lack of negative pore pressure. Sediment containing gas hydrate may be stronger or weaker than similar water saturated samples, depending on hydrate content and other test-related factors, such as strain rate, consolidation stress, sediment density, and temperature.

Our tests indicate that pore pressure has a critical effect on behavior of porous media [22, 25], including slope stability. Therefore much more knowledge is needed regarding the generation and dissipation of excess pore pressure as related to the presence of gas hydrate in the natural environment. [26] stress the necessity of knowing in-situ pore pressure, because it affects the calculation of Bottom Simulating Reflector (BSR) depth. Although pore pressure is critical to gas hydrate stability in situ, little is known about it in either gas hydrate or permafrost regions. Pore pressures beneath permafrost may be similar to those beneath gas hydrate because both layers may act as a less permeable boundary to gas



migration and they may also transmit vertical stresses similarly. However, stress history and differences in formation mechanism may limit the comparison.<sup>16</sup> in their review of gas hydrate in regions containing permafrost point out the sparsity of in-situ measurements. Some locations in the Mackenzie Delta, NWT contain elevated excess pore pressure beneath permafrost [27], whereas some regions in Russia have pore pressures lower than hydrostatic (for example, [28]).

Sediment permeability is reduced if significant amounts of gas hydrate occupy intergranular pore space. The changes that are produced are important for slope-stability calculations [29] and in determining if gas hydrate can effectively form a seal that traps bubble-phase gas beneath the gas-hydrate-stability zone (GHSZ). The presence of gas beneath the GHSZ is a major contributor to the formation of a bottom-simulating reflector (BSR) present on seismic-profile records. Certainly, results from test GH082 and other samples prove that gas hydrate creates impermeable or nearly impermeable layers in medium-scale laboratory sediments.

#### 4. CONCLUSIONS

Long-term experiments conducted to determine relative acoustic and shear strength properties of sediment containing laboratory-formed methane gas hydrate exhibit a wide range in behavior. Results are dependent on the amount, distribution, location within pores, and concentration at specific sites of hydrate and other materials (water, gas, and ice) present in the pore space. We have shown that forming hydrate in initially partly water-saturated (method two) sediment produces similar results to tests that begin with fully water saturated (method one) pore space. This is important because initially partly saturated samples produce more consistent test results.

Acoustic p-wave velocities, in sieved Ottawa sand, increase from 1.86 km/s for water-saturated sediment to approximately 4.0 km/s after nearly complete hydrate saturation of pores using the two different formation methods. Similarly, shear strengths of Ottawa sand containing high concentrations of gas hydrate are in close agreement: 10.4 MPa (method one) and 10.1 MPa (method two).

Pore pressure effects and the presence of gas significantly impact sediment behavior and the measurement of physical properties. Formation of gas hydrate can also indirectly increase p-wave velocity by creating impermeable boundaries and reducing localized pore pressure thereby increasing sediment effective stresses.

Acoustic and strength properties of frozen samples or permafrost have similarities to sediment containing gas hydrate. However, permafrost formation will typically increase acoustic velocity more than gas hydrate formation. This difference in acoustic properties may enable modeling in areas that contain a combination of permafrost and gas hydrate to differentiate between the different materials.

Additional laboratory experimentation is needed to produce results that accurately simulate in-situ conditions, such that measured properties can be used to model geologic settings for seafloor and well stability calculations, and for comparison to well logs. Certainly, natural conditions probably form gas hydrate more slowly than many laboratory techniques. In addition, because of the significant effect of gas and pore pressure on sediment behavior, remaining pore space must be filled with water after hydrate formation to produce results that replicate water-dominated conditions present typically in natural settings, rather than gas-dominated laboratory samples.

## REFERENCES

1. Stern, L. A.; Kirby, S. H.; Durham, W. B.; Circone, S.; Waite, W. F., Laboratory synthesis of pure methane hydrate suitable for measurement of physical properties and decomposition behavior. In *Coastal Systems and Continental Margins—Natural Gas Hydrate in Oceanic and Permafrost Environments*, ed.; Max, M. D., 'Ed.' 'Eds.' Kluwer Academic Publishers: Dordrecht, Netherlands, 2000; 'Vol.' 5, p<sup>pp</sup> 323–348.
2. Winters, W. J.; Dillon, W. P.; Pecher, I. A.; Mason, D. H., GHASTLI; determining physical properties of sediment containing natural and laboratory-formed gas hydrate. In *Coastal Systems and Continental Margins—Natural gas Hydrate in Oceanic and Permafrost Environments*, ed.; Max, M. D., 'Ed.' 'Eds.' Kluwer Academic Publishers: Dordrecht, Netherlands, 2000; 'Vol.' 5, p<sup>pp</sup> 311–322.
3. Wright, J. F.; Dallimore, S. R.; Nixon, F. M., Influence of grain size and salinity on pressure-temperature thresholds for methane hydrate stability in JAPEX/JNOC/GSC Mallik 2L-38 gas hydrate research-well sediments. *Bulletin—Geological Survey of Canada, Report: 544* **1999**, 229–240.
4. Winters, W. J.; Pecher, I. A.; Booth, J. S.; Mason, D. H.; Relle, M. K.; Dillon, W. P., Properties of samples containing natural gas hydrate from the JAPEX/JNOC/GSC Mallik 2L-38 gas hydrate research well, determined using Gas Hydrate And Sediment Test Laboratory Instrument (GHASTLI). *Bulletin—Geological Survey of Canada, Report: 544* **1999**, 241–250.
5. Suess, E.; Torres, M. E.; Bohrmann, G.; Collier, R. W.; Rickert, D.; Goldfinger, C.; Linke, P.; Heuser, A.; Sahling, H.; Heeschen, K.; Jung, C.; Nakamura, K.; Greinert, J.; Pfannkuche, O.; Trehu, A.; Klinkhammer, G.; Whiticar, M. J.; Eisenhauer, A.; Teichert, B.; Elvert, M., Sea floor methane hydrates at Hydrate Ridge, Cascadia Margin. *Geophysical Monograph* **2000**, 124, 87–98.
6. Buffett, B. A.; Zatsepin, O. Y., Formation of gas hydrate from dissolved gas in natural porous media. *Marine Geology* **2000**, 164, (1–2), 69–77.
7. Rogers, R. E.; Lee, M. S.; Anonymous, *Biosurfactant from microbial activity in ocean sediments enhances gas hydrate formation*. ed.; Geological Society of America and Geological Society of London, International (III): 2001; 'Vol.' p.
8. Berge, L. I.; Jacobsen, K. A.; Solstad, A., Measured acoustic wave velocities of R11 (CC13F) hydrate samples with and without sand as a function of hydrate concentration. *J. Geophys. Res.* **1999**, 104, 15415–15424.
9. Tohidi, B.; Anderson, R.; Clennell, M. B.; Burgass, R. W.; Biderkab, A. B., Visual observation of gas-hydrate formation and dissociation in synthetic porous media by means of glass micromodels. *Geology (Boulder)* **2001**, 29, (9), 867–870.

10. Lee, M. W.; Collett, T. S., Amount of gas hydrate estimated from compressional- and shear-wave velocities at the JAPEx/JNOC/GSC Mallik 2L-38 gas hydrate research well. *Bulletin—Geological Survey of Canada, Report; 544* **1999**, 313–322.
11. Sakai, A., Velocity analysis of vertical seismic profile (VSP) survey at JAPEx/JNOC/GSC Mallik 2L-38 gas hydrate research well, and related problems for estimating gas hydrate concentration. *Bulletin—Geological Survey of Canada, Report; 544* **1999**, 323–340.
12. Winters, W. J.; Pecher, I. A.; Waite, W. F.; Mason, D. H., Physical properties and rock physics models of sediment containing natural and laboratory-formed methane gas hydrate. *American Mineralogist* **submitted**, Special gas hydrate volume.
13. Waite, W. F.; Winters, W. J.; Mason, D. H., Methane hydrate formation in partially water-saturated Ottawa sand. *American Mineralogist* **submitted**, Special Gas Hydrates volume.
14. Leggett, R. F., Permafrost research. *Arctic* **1955**, 7, (3–4), 153–158.
15. Lunardini, V. J., *Heat Transfer in Cold Climates*. ed.; van Nostrand Reinhold Co.: New York, 1981; ‘Vol.’ p 731.
16. Collett, T. S.; Dallimore, S. R., Permafrost-associated gas hydrate. In *Coastal Systems and Continental Margins—Natural Gas Hydrate in Oceanic and Permafrost Environments*, ed.; Max, M., ‘Ed.’ ‘Eds.’ Kluwer Academic Publishers: Dordrecht, Netherlands, 2000; ‘Vol.’ 5, p`pp 43–60.
17. Skorobogatov, V. A.; Yakushev, V. S.; Chuvilin, E. M. In *Sources of natural gas within permafrost; North- West Siberia*, Permafrost Proceedings Seventh International Conference, Yellowknife, NWT, Canada, June 23–27, 1998, 1998; Lewkowicz, A. G.; Allard, M., ‘Ed.’ ‘Eds.’ Yellowknife, NWT, Canada, 1998; p`pp 1001–1007.
18. Dallimore, S. R.; Collett, T. S.; Uchida, T., Overview of science program, JAPEx/JNOC/GSC Mallik 2L-38 gas hydrate research well. *Bulletin—Geological Survey of Canada, Report; 544* **1999**, 11–17.
19. Kuusstra, V. A.; Hammershaime, E. C. *Handbook of Gas Hydrate Properties and Occurrence*; DOE/MC/19239-1546; Lewin and Associates: December 1983, 1983; p`pp.
20. Dallimore, S. R.; Collett, T. S., Intrapermafrost gas hydrates from a deep core hole in the Mackenzie Delta, Northwest Territories, Canada. *Geology (Boulder)* **1995**, 23, (6), 527–530.
21. Collett, T. S., Natural Gas Hydrates of the Prudhoe Bay and Kuparuk River Area, North Slope, Alaska. *The American Association of Petroleum Geologists Bulletin* **1993**, 77, (5), 793–812.
22. Holtz, R. D.; Kovacs, W. D., *An Introduction to Geotechnical Engineering*. ed.; Prentice-Hall, Inc.: Englewood Cliffs, NJ, 1981; ‘Vol.’ p 733.
23. Duan, Z.; Moeller, N.; Weare, J. H., An equation of state for the CH<sub>4</sub>-CO<sub>2</sub>-H<sub>2</sub>O system. I. Pure systems for 0 to 1000 °C. *Geochim. Cosmochim. Acta* **1992**, 56, 2605–2617.
24. Helgerud, M. B.; Dvorkin, J.; Nur, A.; Sakai, A.; Collett, T. S., Elastic-wave velocity in marine sediments with gas hydrates; effective medium modeling. *Geophysical Research Letters* **1999**, 26, (13), 2021–2024.
25. Lambe, T. W.; Whitman, R. V., *Soil Mechanics*. ed.; John Wiley & Sons: New York, 1969; ‘Vol.’ p 553.
26. Peltzer, E. T.; Brewer, P. G., Practical physical chemistry and empirical predictions of methane hydrate stability. *Coastal Systems and Continental Margins* **2000**, 5, 17–28.
27. Weaver, J. S.; Stewart, J. M. In *In situ hydrates under the Beaufort shelf*, Fourth Canadian Permafrost Conference, 1982; French, M. H., ‘Ed.’ ‘Eds.’ National Research Council of Canada: 1982; p`pp 312–319.
28. Sergiyenko, S. I.; Maydak, V. I., Formation conditions for heavy oil pools and possible hydrate formation in the northeastern part of the Timan-Pechora province. *Geologiya Nefti I Gaza* **1982**, 8, 33–35.
29. Kayen, R. E.; Lee, H., Pleistocene Slope Instability of Gas Hydrate-Laden Sediment on the Beaufort Sea Margin. *Marine Geotechnology* **1991**, 10, 125–141.

# Investigating Methane Hydrate in Sediments using X-Ray Computed Tomography

Barry M. Freifeld\* and Timothy J. Kneafsey

## 1. INTRODUCTION

Thermal and kinetic properties of naturally occurring hydrates are important to evaluate whether a hydrate deposit can be exploited as an economic resource [1]. Investigation of hydrate in sediment samples has been performed using visual and microscopic examination [2], x-ray diffraction [3], Raman spectroscopic methods [4], and x-ray computed tomography (CT) [5][6]. The most common experimental method employed to investigate hydrate kinetics consists of measuring gas production (or uptake) from a dissociating (forming) hydrate sample, while monitoring sample pressure and temperature [7][8][9]. By starting with hydrates of known grain size, researchers have developed kinetic models of hydrate dissociation based upon assumptions of hydrate grain geometry. Unfortunately, batch experiments reveal little about processes as they occur within heterogeneous, natural samples. To understand the influence that the sediment matrix has on entrained hydrate, researchers require a nondestructive technique to visualize hydrate processes within the sample.

Using a medical x-ray CT scanner, Mikami et al. [5] showed dissociation occurring in an unlithified sand sample containing natural hydrate that was retrieved from the Mallik 2L-38 gas hydrate research well. This work was significant

---

BARRY M. FREIFELD • Lawrence Berkeley National Laboratory One Cyclotron Road,  
Berkeley CA 94720, USA

TIMOTHY J. KNEAFSEY • Lawrence Berkeley National Laboratory One Cyclotron Road,  
Berkeley CA 94720, USA

\* [bmfreifeld@lbl.gov](mailto:bmfreifeld@lbl.gov)

because it demonstrated the ability for x-ray CT to spatially and temporally track hydrate dissociation. Gas production was measured using a gas flow meter. Freifeld et al. [6] used a medical scanner to track an advancing dissociation front created by thermal stimulation of a synthetic hydrate/sand mixture. This work compared the amount of gas evolved with the observed spatial progression of the dissociation front through a cylindrical sample. The location of the hydrate dissociation front was compared to a simple moving boundary model that incorporated the latent heat of dissociation. The effective thermal conductivity of the hydrate/sediment mixture was estimated based upon the velocity of the phase change boundary.

The purpose of this paper is to describe a series of experiments performed using a portable x-ray CT system to quantify the dissociation process in a synthetic methane hydrate-sand system. It differs significantly from previous work, demonstrating the use of the CT system to estimate the quantity of hydrate dissociated with high spatial resolution, independent of pressure or gas flow-rate measurements. Gas production is still used to quantify the total amount of hydrate contained within the sample, but this measurement is independent of the CT system's independent determination of the percentage of hydrate dissociated both spatially and temporally throughout the sample. Tracking dissociation with detailed spatial information is important for understanding (at a macroscopic level) the influence hydrate/sediment textural fabric has on the hydrate dissociation process. Such tracking can also answer important questions about whether dissociation is a kinetic or equilibrium process. Portability of the x-ray CT scanner is significant because it allows for hydrate dissociation experiments to be performed at the location of core recovery. This overcomes the difficulty of having to preserve the hydrates at high pressures and low temperatures for transportation to a remote laboratory.

## 2. X-RAY IMAGING SYSTEM

The geometry and layout of the portable x-ray CT system are shown in Figure 1 [10]. The most significant advantage of this system over the more commonly used medical style CT scanners, which typically scan 1 slice at a time, is that a 10 cm volume of core can be imaged simultaneously at high resolution. This is important for imaging transient processes, such as hydrate dissociation, since it allows rapid imaging of a large volume.

To obtain complete volumetric information, we perform a computer reconstruction on 180 radiographic images, acquired using a two degree rotation of the core between each image. The resulting volumetric data set consists of an x-ray attenuation assigned to each 200  $\mu\text{m}$  voxel, or volume element. By calibrating to known standards, we can convert attenuation to density. To accurately discern small changes, we employ the technique of differential imaging, whereby all images acquired are subtracted from a baseline image set.

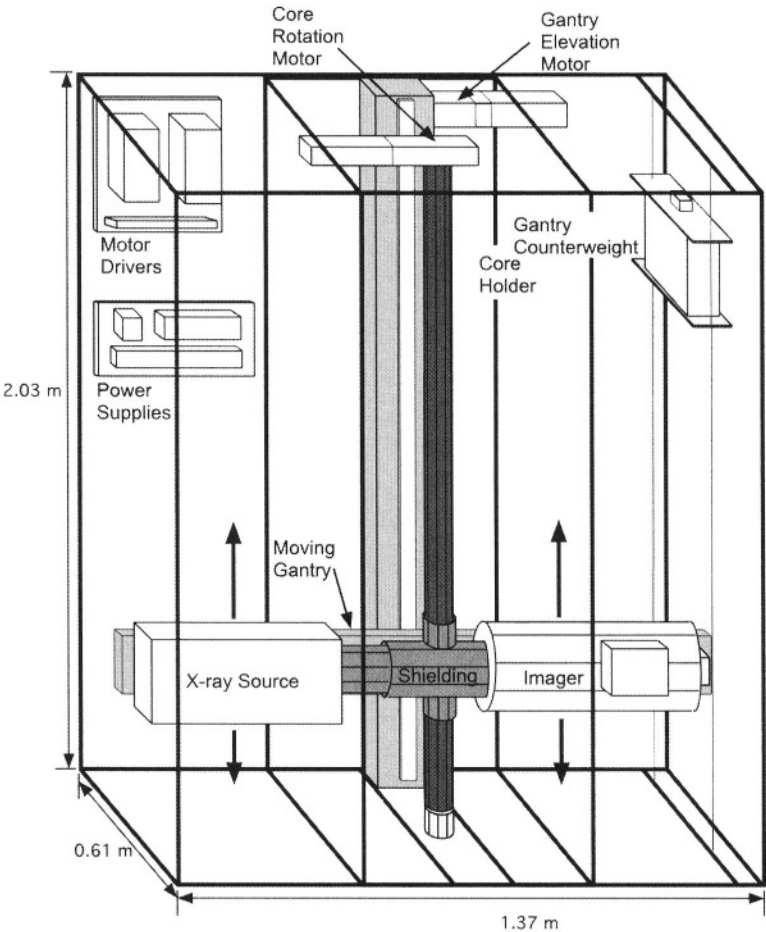


**Figure 1.** A schematic layout of the portable x-ray CT unit.

For the experiments presented here, the beam energy was set at 130 kV and  $200\text{ }\mu\text{A}$ . Because the x-ray beam is polychromatic, it will undergo beam-hardening as it transverses the sample, and soft x-rays will be more attenuated, yielding a beam containing a steadily higher proportion of harder x-rays. Without being corrected, beam-hardening makes the center of the sample appear denser than the outer edges. To reduce beam-hardening aberrations, we placed a 1.6 mm thick copper between the x-ray beam and the sample being imaged. The reconstructed image is post-processed using a polynomial correction to remove beam-hardening artifacts that the copper filter does not eliminate.

### 3. METHANE HYDRATE DISSOCIATION EXPERIMENTS

Methane hydrate dissociation experiments were performed using cylindrical synthetic porous methane hydrate samples. For brevity, two of them will be shown here. The 28.6 mm diameter cylinder of synthetic, 30%-porosity hydrate was fabricated by the USGS in Menlo Park, California by the process detailed in Stern et al. [3]. To preserve the hydrate and prevent dissociation, the hydrate was initially stored in a refrigerator at  $-80^{\circ}\text{C}$  and then transported in a liquid nitrogen (LN) dry shipping dewar to Berkeley Lab.

In each of the experiments, synthetic hydrate was added to a matrix of 12/20 mesh Ottawa sand. To prevent hydrate dissociation while preparing the sample at atmospheric pressure, we cooled the sand and hydrate using LN. Ice made from de-aired water and cooled with LN was used as a reference material. The ice provides a stable reference material because of its low porosity, only influenced by thermal expansion as it warms. The unconsolidated sand is susceptible to thermal-mechanical effects and changes in the density of the gas in the pore space as the sample warms and hydrate dissociates. Early in the experiment, the apparent density of the unconsolidated sand will be influenced by LN evaporation and the release of sorbed nitrogen.

The sand, hydrate, and ice samples were placed in a high-density polyethylene bottle (7.0 cm diameter  $\times$  12.7 cm high) and placed in an aluminum pressure vessel for imaging. Figure 2(a) shows an idealized schematic of the experimental set up, and Figure 2(b) shows a photograph of the pressure vessel used to hold the sample during x-ray CT scanning. The actual geometry of the hydrate and ice contained within the samples are shown in the reconstructed CT images.

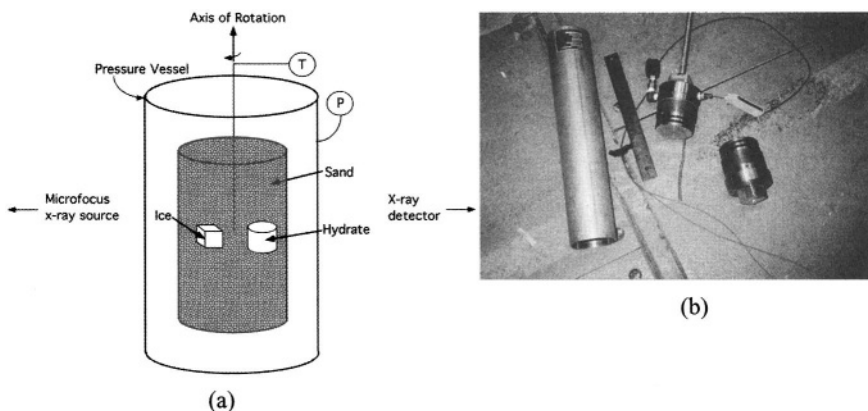


**Figure 2.** (a) Schematic of hydrate experiment and (b) the pressure vessel used to hold the hydrate sample during CT scanning, showing the thermocouple wires and pressure gauge on the top end cap.

*Table 1. Experiment conditions.*

Experiment	Hydrate Geometry	Hydrate Volume (cm <sup>3</sup> )	Moles Methane	Estimated Methane Evolved (moles)
1	Cylindrical segment	20.4	0.12	0.13
2	Nodules	12.2	0.074	0.053

The pressure in the closed vessel was monitored using a pressure gage to track the amount of hydrate dissociated. A thermocouple installed near the center of the sand/hydrate mixture provided a local indication of sample temperature. The exact thermal profile within the pressure vessel was unknown. However, the temperature as reported lagged the average temperature of the sample, which lay close to the temperature indicated by the thermocouple, but somewhere between the indicated temperature and room temperature. This was clearly the case, because the pressure in the vessel increased, indicating hydrate dissociation, prior to the indicated temperature rising above the hydrate stability temperature ( $-76^{\circ}\text{C}$  at 0.1 MPa).

Dissociation was induced by allowing the sample to warm through the stability point using room heat. Temperature and pressure were recorded using a thermocouple with a digital readout and a borden tube pressure gage. Acquiring a set of 180 CT radiographs took 3 minutes, and was performed approximately every 10 minutes. (The experiment conditions are presented in Table 1.) The Feldkamp reconstruction algorithm was applied to the radiographic data to give volume density information. For each reconstructed data set, a file containing  $430 \times 430 \times 400$  voxels was created, each element representing the density of a  $200\text{ }\mu\text{m}$  cubical volume element.

### 3.1. First Experiment

The first dissociation experiment used a 32 mm long section of the 28.6 mm diameter porous hydrate sample. A cube of water ice made from de-aired water was used as a reference material. Figure 3 shows vertical and horizontal cross sections from reconstructed CT images, revealing the layout of the sample. The thermocouple junction is located at the tip of the temperature probe in the sand close to the water ice. Measured pressure and temperature are plotted in Figure 4(a). The time indicated is referenced to the time the baseline set of CT images were acquired. The pressure rise that occurs prior to acquisition of the baseline image set is due to the boiling of residual LN in the sample. When the pressure in the vessel stopped increasing (at about 40 minutes), dissociation was considered



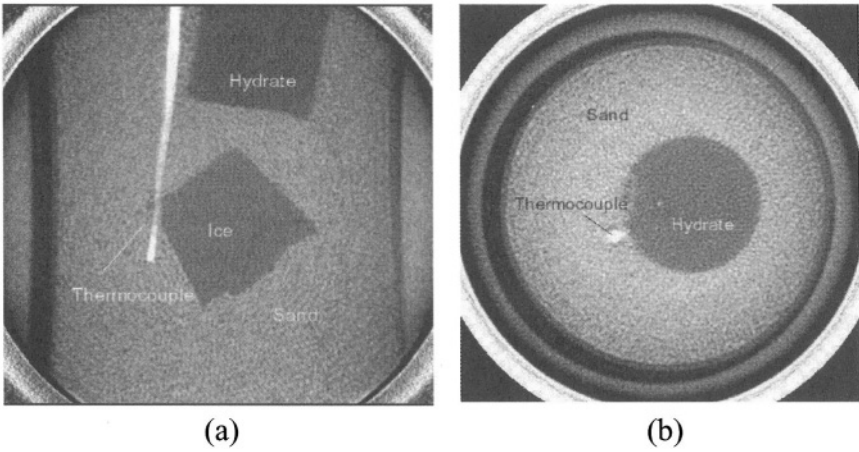


**Figure 3.** (a) Vertical and (b) horizontal cross sections taken during Experiment 1, revealing hydrate and ice in a sand matrix.

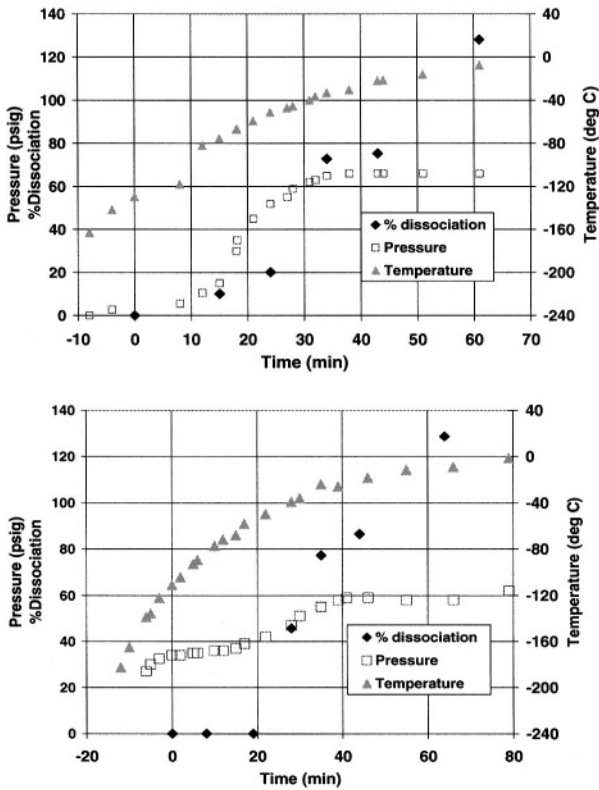


**Figure 4.** Pressure, temperature, and percent hydrate dissociated, as estimated from x-ray CT images, for (a) Experiment 1 and (b) Experiment 2.

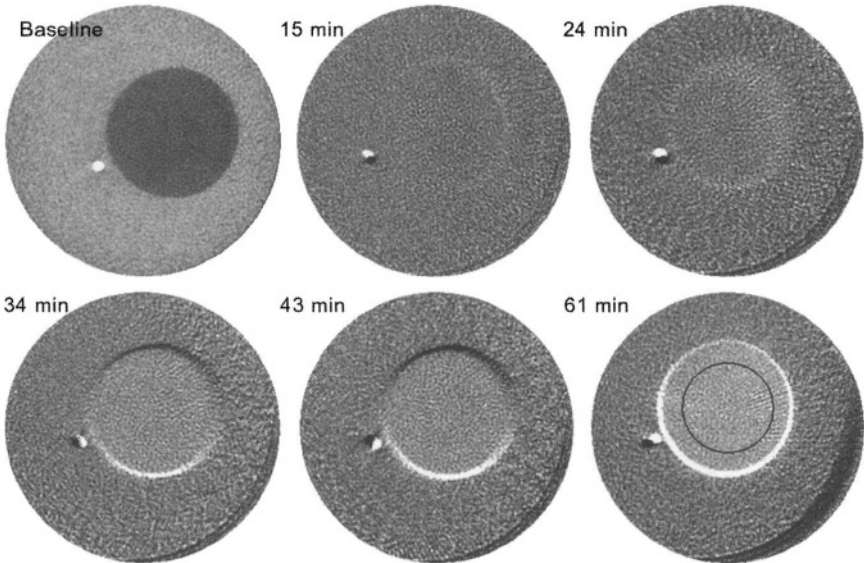


**Figure 5.** A sequence of horizontal images from Experiment 1. The baseline image shows the cylinder of hydrate surrounded by sand. All subsequent images are differences taken from the baseline image. Dissociation starts as a faint halo at the edge of the hydrate, steadily progressing throughout the hydrate. The black circle indicates the region of interest used to calculate the change in hydrate density. The greyscale legend applies only to difference images.

complete. Figure 5 shows a horizontal slice taken through the hydrate cylinder in the sand matrix, along with difference images calculated by subtracting later images from the baseline image. The bright spot near the hydrate is caused by the stainless steel sheath around the thermocouple wires.

### 3.2. Second Experiment

The second dissociation experiment used a 19 mm long section of the 28.6 mm diameter hydrate. Prior to mixing with sand, the hydrate was broken into several pieces of assorted sizes. The smallest clearly discernable hydrate piece was approximately  $2.4 \text{ mm} \times 3.2 \text{ mm} \times 4.8 \text{ mm}$ , having a total volume of about  $0.037 \text{ cm}^3$ . Similar to Experiment 1, a cube of ice was used as a reference standard. Figure 4(b) shows measured pressures and temperatures. Figure 6 shows a horizontal slice taken through the sample, with the baseline image revealing various nodules of hydrate and the one large water ice piece. The difference images were calculated by subtracting subsequent images from the baseline image.

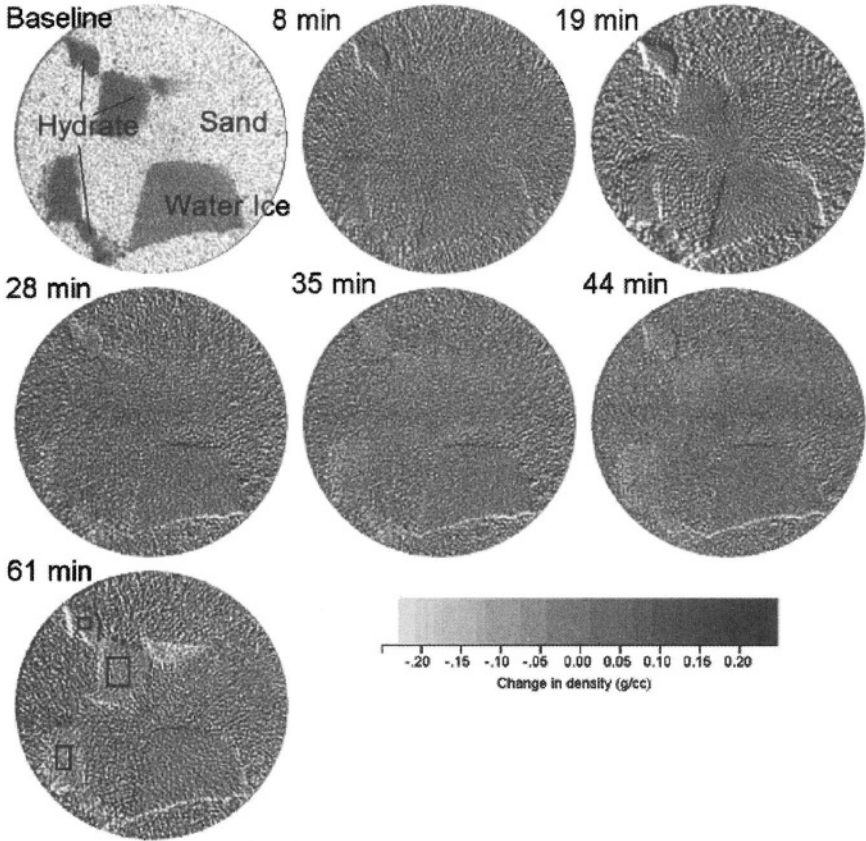


**Figure 6.** A sequence of horizontal slices from Experiment 2, showing both methane hydrate and water ice in a sand matrix. All images after baseline have been differenced with baseline image. The rectangles in the last image (time 61 minutes) show the regions of interest used to calculate the change in hydrate density. The greyscale legend applies only to the difference images.

## 4. DISCUSSION

### 4.1. Pressure and Temperature Data

The pressure and temperature data recorded for each experiment are presented in Figure 4. Table 1 shows the estimated moles of methane gas evolved calculated using the measured increase in gas pressure and the gas-filled volume of the pressure vessel. Both experiments show increases in pressure prior to when the temperature of the sample was above the dissociation temperature for the hydrate. This

early rise is due to the nitrogen boiling off. The subsequent increases in pressure were due to hydrate dissociation. The evolved gas volume, estimated using the ideal gas law, roughly matches the known volume initially contained by hydrate for these two experiments.

## 4.2. CT Data

CT data were collected periodically during the dissociation experiments. Figures 5 and Figure 6 show a baseline image and difference images for Experiment 1 and Experiment 2, respectively. Significant reductions in hydrate density were observed during dissociation, whereas only minor changes in the density of ice and the bulk density of sand were observed. The percent hydrate dissociated for each experiment was estimated using the measured attenuation data from a volume of interest in the interior of the hydrate and plotted along with temperature and pressure on Figure 4. These regions are highlighted on the last difference image shown for each experiment. The volume of interest for Experiment 1 was a central region of the cylindrical hydrate sample. For Experiment 2, which contained many small hydrate nodules, the percent dissociated was based upon an average of three different interior volumes. To convert from x-ray attenuation to density, a calibration used the measured x-ray attenuation from the baseline image for the known materials: sand, hydrate and water ice.

Difference images from Experiment 1 (Figure 5) show the dissociation of a single large cylinder of hydrate. A small halo at the edge of the cylinder first appears in the difference image acquired 15 minutes after baseline. Dissociation progresses inward. The image at 24 minutes shows a continuous ring of dissociated hydrate at the edge of the cylinder with more pronounced dissociation at the warmest area, the edge closest to the pressure vessel wall. At 34 minutes, dissociation has occurred throughout the entire volume of the hydrate, with only a slight change noticeable at 43 minutes. The final image, at 61 minutes, reveals a drastic reduction in density at the edges of the hydrate cylinder and the estimated percent hydrate dissociated has jumped up to 130% of the theoretical value. This large reduction in density results from mechanical expansion of the sample. The bright ring around the final image shows the increase in volume of the original hydrate cylinder, now consisting of water ice.

Difference images from Experiment 2 (Figure 6) show changes similar to those from Experiment 1. Dissociation occurs in the hydrate nodules earliest near the walls of the pressure vessel and progress inward. The image acquired at 28 minutes shows that the hydrate at the edge of the vessel has undergone significant reduction in density, whereas the interior hydrate nodules are unchanged. At 35 minutes, dissociation is visible throughout the hydrate, becoming more pronounced at 44 minutes. The image acquired at 61 minutes shows a large

density reduction (130% of the expected value for hydrate dissociation), again accompanied with apparent displacement of sand and expansion of the hydrate sample.

#### 4.3. Experimental Uncertainty

There are numerous sources of noise, error, and uncertainty in the estimation of density from x-ray CT images. Some of these errors are systematic and arise from the reconstruction process, since the Feldkamp Algorithm that is used for processing the data is an approximate method. These can be corrected during postprocessing. Beam hardening is one of the largest sources of error in making accurate density estimates. To eliminate beam hardening beyond what is removed by passing the x-ray beam through a copper filter, the reconstructed data set is normalized using a polynomial that is a function of the distance from the rotational axis of the core sample. To perform this correction, we normalize the reconstructed image set by the reciprocal of the beam-hardening trend, fitted by a second order polynomial.

Other errors, such as camera noise, are Gaussian, and can be quantified using standard statistical analysis, so that confidence intervals can be determined for the density estimates. There is a significant amount of error in any one **200  $\mu\text{m}$**  cubical voxel. The 95% confidence interval for a density estimate can be expressed as:

$$\rho_{0.95}(x) = \rho(x) \pm t_{0.95,n} \frac{\sigma}{\sqrt{n}} \quad (1)$$

where  $n$  is the number of voxels,  $\sigma$  is the standard deviation of measured voxel densities, and  $t$  is Student's  $t$  distribution. The 95% confidence interval for estimating the density change for the water ice in Experiment 2 is shown in Figure 7(a) as a function of the length of a cubical region of interest. The density estimate as one approaches a region a few millimeters in length decreases to an uncertainty of approximately  $\pm 0.01$  g/cc. For the ice shown, no change in density is expected. Similarly, confidence intervals for a region in the interior of a nodule of hydrate in Experiment 2 are shown in Figure 7(b) for each of the acquired image sets. Changes in hydrate saturation of 10% can easily be discerned for regions of hydrate greater than a few millimeters in diameter.

## 5. CONCLUSIONS

We have used x-ray computed tomography to determine the spatial distribution of hydrates in whole-round cores with high resolution. By repeatedly imaging

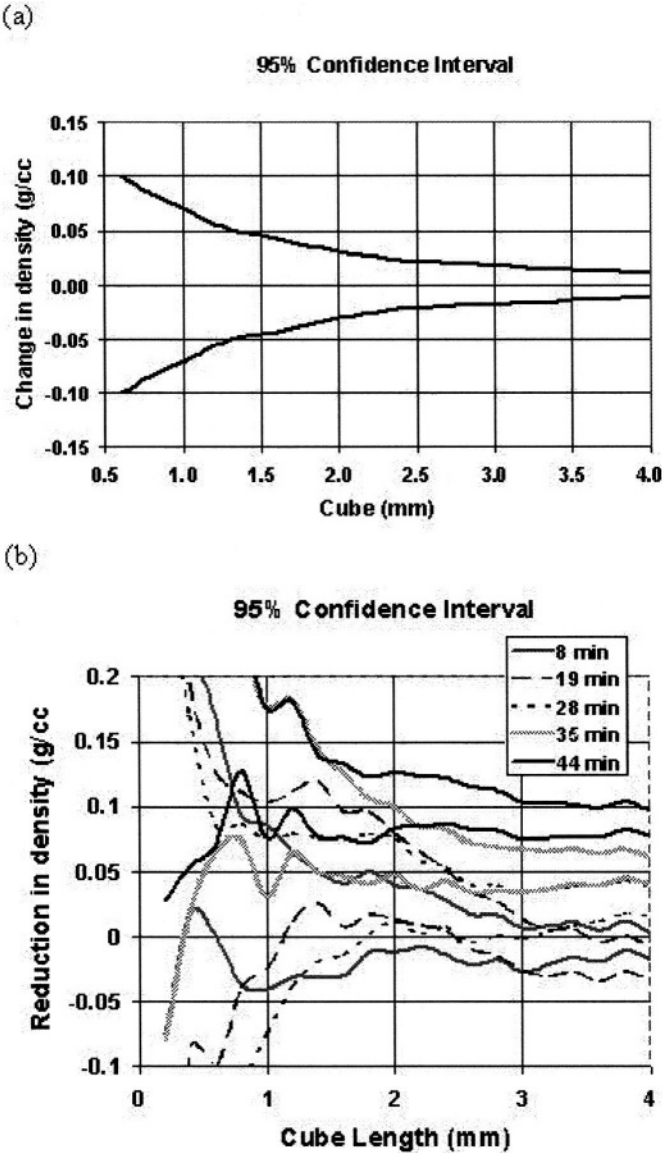


**Figure 7.** (a) The estimated change of density for the water ice in Experiment 2 with upper and lower 95% confidence intervals as a function of region size; (b) The reduction in hydrate density during dissociation. The density changes were estimated using attenuation data contained within a cubical region of hydrate in Experiment 2.

the same section of core as dissociation occurs, hydrate kinetics can be investigated. Because the location of the dissociation front represents a region of known thermodynamic conditions, locating and tracking movement of the front provides information on rates of energy flux and mass transport. Estimation of density confidence intervals indicates that even relatively modest reductions in hydrate saturation can be accurately determined. Future studies will use the x-ray CT to measure hydrate kinetic parameters and determine thermal parameters of hydrate sediment systems.

## ACKNOWLEDGMENTS

This work was supported by the Assistant Secretary of the Office of Fossil Energy, Office of Natural Gas & Petroleum Technology, U.S. Department of Energy under Contract No. DE-AC03-76SF00098. The authors are grateful to Laura Stern from the USGS for supplying the synthetic methane hydrate sample used in this paper. The authors would also like to thank Dan Schneberk for making the CT image-processing code, Imgrex, available to us and Jacob Pruess for assistance in data analysis. In addition, we would like to thank Liviu Tomutsa and an anonymous reviewer for providing careful reviews of this manuscript.

## REFERENCES

1. Moridis, G. J., Presented at SPE Gas Technology Symposium, Alberta, Canada. 2002, SPE 75691.
2. Kobayashi, I.; Ito, Y.; and Mori, Y. H., *Chem. Eng. Sci.* 2001, 56; pp. 4331–4338.
3. Stern, L. A.; Kirby, S. H.; and Durham, W. B.; *Science*, 1996, 273 (5283); pp. 1843–1848.
4. Uchida, T.; Hirano, T.; Ebinuma, T.; Narita, H.; Gohara, K.; Mae, S.; and Matsumoto, R., *AIChE Journal*. 1999, 45 (12), 2641–2645.
5. Mikami, J.; Masuda, Y.; Uchida, T.; Satoh, T.; and Takeda, H., In *Gas Hydrates, Challenges for the Future*, Annals of the New York Academy of Sciences, Volume 912., 2000; pp. 1011–1020.
6. Freifeld, B. M.; Kneafsey, T. J.; Tomutsa, L.; Stern, L. A.; and Kirby S. H.; 2002, In *Proceedings of the Fourth International Conference on Gas Hydrates*, May 19–23, Chiba, Japan, 2002; pp. 750–755.
7. Kim, H. C.; Bishnoi, P. R.; Heidemann, R. A.; and Rizvi, S. S. H.; *Chem Eng. Sci.*, 1987, (42) 1645–1653.
8. Clarke, M. A.; and Bishnoi P. R., *Can J. of Chem. Eng.* 2001, 79 (1), 143–147.
9. Circone, S.; Stern, L. A.; Kirby, S. H.; Pinkston, J. C., and Durham, W. B., In *Gas Hydrates, Challenges for the Future*, Annals of the New York Academy of Sciences, 2000, Volume 912; pp. 544–555.
10. Freifeld, B. M.; Kneafsey, T. J.; Tomutsa, L.; and Pruess, J.; 2003, In *Proceedings of the 2003 International Symposium of the Society of Core Analysts*, September 21–24 Pau, France. 2003; pp. 581–586.

# Methane Hydrate Studies: Delineating Properties of Host Sediments to Establish Reproducible Decomposition Kinetics

**Devinder Mahajan,\* Phillip Servio, Keith W. Jones,  
Huan Feng, and William J. Winters**

## 1. INTRODUCTION

Methane hydrates represent a potentially important alternative energy source. However, recovery is difficult since they are typically found in deep ocean subbottom sediments. Our aim here is to briefly review general information on hydrate research and to summarize cogent information on the geotechnical properties of the oceanic sediments in which they are found. We present results obtained using standard measurement techniques in combination with results of experiments

---

DEVINDER MAHAJAN • Energy Sciences and Technology Department, Brookhaven National Laboratory, Upton, NY 11973-5000 USA and Department of Materials Science and Engineering, Stony Brook University, Stony Brook, NY 11794 USA

PHILLIP SERVIO • Department of Chemical Engineering, McGill University, Montreal, Quebec, H3A 2B2, Canada

KEITH W. JONES • Laboratory for Earth and Environmental Sciences, Environmental Sciences Department, Brookhaven National Laboratory, Upton, New York 11973-5000 USA

HUAN FENG, • Department of Earth and Environmental Studies, Montclair State University, Upper Montclair, New Jersey 07043 USA

WILLIAM J. WINTERS • U.S. Geological Survey, Woods Hole, MA 02543 USA

\* Corresponding author: Tel.:(631) 344-4985; dmahajan@bnl.gov



using high-spatial resolution synchrotron computed microtomography to obtain information at the grain-size scale. We use grain-size measurements to predict the macroscopic geotechnical properties of the sediments. Such a development can be widely used in developing an economical method for commercial recovery of methane from hydrate.

## 2. SUMMARY OF RELEVANT PREVIOUS WORK

Methane hydrate belongs to a general class of inclusion compounds commonly known as clathrate hydrates. Clathrate hydrates owe their existence to the ability of  $\text{H}_2\text{O}$  molecules to assemble via hydrogen bonding and form polyhedral cavities that serve as hosts to gas (guest) molecules. Of over 130 compounds (guest molecules) that form clathrate hydrates, those involving natural gas is of crucial importance due to its potential as an energy resource and geohazard. Natural gas is the cleanest of all known fossil fuels and its importance as a primary energy carrier is well established. Gas hydrates, the most common being methane hydrate ( $\text{CH}_4 \cdot n\text{H}_2\text{O}$  where  $n \geq 5.75$ ) form readily as crystalline solids under certain conditions of relatively high pressure and low temperature [1]. During deep-ocean drilling for natural gas such temperature and pressure conditions are frequently encountered under which facile formation of hydrates result in pipeline plugging that makes natural gas hydrate a nuisance and expensive problem. However, recent estimates [2] indicate that naturally occurring methane hydrates could become the next energy frontier if an economical and environmentally acceptable method to extract methane could be developed.

The development of an economic hydrate dissociation method requires an understanding of its kinetic stability and physical properties. Moreover, sediments that are host to methane hydrate may also influence its stability. Several kinetic studies have been carried out on laboratory prepared synthetic samples [3–6] but the study of host sediments has received less attention. In previously reported studies among others, several workers [7–9] employed the tomographic technique using industrial type scanners with conventional tube-type x-ray sources. Typical voxel sizes for these measurements were  $0.6 \times 0.6 \times 1.0 \text{ mm}^3$  (8) and  $0.2 \times 0.2 \times 1.0 \text{ mm}^3$  (9). In reference 7, the frequency of computed tomography (CT) values were determined by arbitrary assigning unitless value of 0 to pure water. The corresponding CT values were  $\sim +400$ ,  $\sim -100$ , and  $\sim -150$  to  $-275$  for dry ice, ice, and methane hydrate. This scale provides a useful reference to correlate experimentally measured CT data. Since the CT values are density dependent, the value for sediments usually exceed  $+1000$  and the value for common gases such as  $\text{CH}_4$  is extremely small ( $-1000$ ). A subsequent study measured the dissociation of natural gas hydrate samples from the Mallik-2L-38 gas hydrate research well in Mackenzie Delta, Canada that were obtained from the depth of 913.76 m and stored

at 243 K after pressurization with 6.0 MPa  $N_2$  gas (8,9). Assuming estimated 30% porosity of the host sand and cage occupancy of ~80%, the hydrate dissociation front was scanned as a function of time when the temperature was raised from 255 K to 277 K. The well-resolved images showed that the sample dissociated at the exposed surface as well as within the interior (pore spaces) in response to a stepped decrease of 0.1 MPa below the methane hydrate equilibrium pressure: this was attributed to the presence of fluids in the pore spaces. The estimated sample porosity was 25–35% and gas hydrates were observed in intergranular pore space. The same group modeled the CT data by applying the Stefan moving boundary model to track the time-dependent methane hydrate dissociation progression in a laboratory prepared cylindrical synthetic methane hydrate/sand sample. The model using one-dimensional heat flow theory was applied with a simple assumption of constant boundary temperature. The estimated thermal conductivity value for the product water ice/sand mixture, at 2.6 W/mK, was attributed to contribution from heat conduction, methane gas convection and the kinetic effect during dissociation. The model yielded an estimated porosity of 49.5% for the synthetic methane hydrate/sand sample.

It is clear that host sediment affects the formation/decomposition stability of methane hydrate as well as the methane content by controlling pore-space filling. In the above described study [8], it was noted that samples obtained from the Mallik well at the depth of 886–952 m (beneath the permafrost zone), gas hydrates were primarily observed in fine to coarse-grained sands and were rarely, if ever, found in finer-grained silts and clays [10]. Therefore, it is crucial to understand the properties of host sediments.

We recently reported the first CMT study of a sediment sample taken at a depth of 667 meters from the Blake Ridge methane hydrate site that allowed us to resolve the sediment structure at the micrometer level [11]. The reported study complemented other reported CT studies [7–9]. We report here on the continuation of our CMT study in order to delineate host sediment properties along with relevant data from previous geotechnical measurements.

### 3. EXPERIMENTAL

Table 1 lists the origin of three host sediment samples. The selected sediments were taken at 0.2 meters, 49.6 meters, and 666.7 meters below the mud line. Whole-round sub samples obtained during Ocean Drilling Program Leg 164 on the Blake Ridge (49.6 m and 666.7 m) and OC 178 on Georges Bank (0.2 m) were preserved in the original liner, capped, completely covered in wax, and subsequently stored in a refrigerator at a temperature of approximately 4 °C. Water content values were determined according to American Society for Testing and Materials (ASTM) Standard D 2216-92 [12] except that the drying temperature was 90 °C.

*Table 1.* Identification and location of samples used in the present study.

Sample No.	Cruise	Latitude	Longitude	Hole/core	Water Depth m
BLR-0.1	OC178	41° 51.5' N	68° 18.1' W	27-GC2	222
BLR-50	ODP leg 164	31° 48.210' N	75° 31.343' W	995A-7H-1	2278.5
BLR-667	ODP leg 164	31° 48.210' N	75° 31.343' W	995A-80X-1	2278.5

Grain size distributions were measured using a laser light-scattering technique [MicroTrac, Inc., North Largo, FL 33773]. This method was especially useful because of its ability to produce very detailed information on the distributions that are impossible to obtain using traditional sieving methods.

The investigation of the sediment microstructure was carried out using the CMT apparatus at the NSLS beam line X-27A. Synchrotron radiation provides a very high intensity x-ray beam with a continuous energy distribution and its properties are well adapted to study materials such as sediments, sand, limestone, and rock samples. This is illustrated in Figure 1 where values for the brilliance of x-ray beams produced at several synchrotron facilities worldwide are displayed

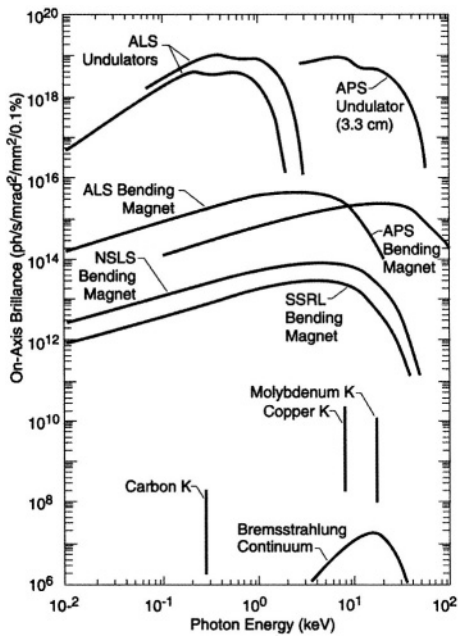


**Figure 1.** X-ray brilliance produced at the NSLS-BNL, APS-ANL, ALS-LBNL and the European Synchrotron Radiation Facility (ESRF). Comparison is also made to conventional x-ray sources. (From Jones *et al.* Ref. 13).

and compared to those found for x-ray tube values. Values for synchrotron are several orders-of-magnitude higher than those for conventional sources. The work reported here is based on use of a bending magnet at the Brookhaven National Synchrotron Light Source (NSLS).

For the present CMT experiment, we used a third-generation approach where the entire sample is exposed to the x-ray beam and the transmitted beam is detected with a scintillator-area detector combination. Exposures are then made as the sample is rotated through 180°. The X-ray beam energy for the measurements were 25 KeV. The data collection procedure is as follows. Typically, an area beam with a size of about 6 mm in the horizontal and about 1 mm in the vertical is used to illuminate the sample and air surrounding it. The x-rays are detected with a YAG scintillator that is viewed by a CCD camera. The complete tomographic data set consists of roughly 2000 exposures taken as the sample is rotated through 180 degrees in 0.09-degree increments. The tomographic volume is then computed using a Fast-Fourier Transformation (FFT) method as developed by Dowd et al. (14). Data acquisition and processing both require about 2 to 3 hours each. Voxel sizes employed in this experiment were 0.068 mm. A schematic diagram of the apparatus is given in Figure 2.

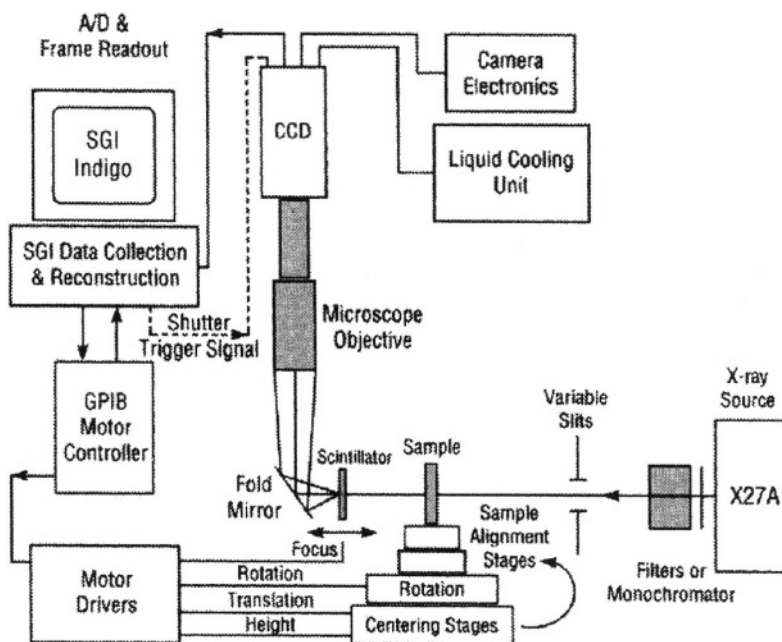


**Figure 2.** Schematic diagram of the major components in the CMT apparatus used at the X27A NSLS bending magnet beam line (From Jones et al. Ref. 13).

4. RESULTS AND DISCUSSION

4.1. Measurement of Bulk-sediment Samples

Winters [15,16] conducted an extensive investigation of the geotechnical properties of sediments from the Blake Ridge and from Georges Bank that helps to define the engineering behavior of the materials. Results include values for water content, porosity, liquid and plastic limits, liquidity and plasticity indices, vane and remolded vane shear strengths, sensitivity and pocket penetrometer shear strength. These results are shown in Table 2.

The porosity of the sediments can be found using conventional methods in which water content is calculated by taking the ratio of the mass of water evaporated during the drying process/mass of solids remaining after drying. After correction for the presence of salt in the pore fluid, porosity is determined from the volume of pore space occupied by the water phase/total specimen volume assuming complete pore space water saturation. Density of the sediment grains was determined using a helium gas pycnometer, Porosity decreases substantially with depth, however, even at 667 m below the sediment surface, the porosity is still 51 % (Table 2). We compare these values to those obtained from CMT below. Values found for the porosity as a function of depth below the surface are shown in Figure 3.

4.2. Measurements on the grain-size scale

The particle distribution in terms of grain size for our three test samples are shown in Figure 4. Although all three specimens contain substantial amounts of fine-grained sediments, they also have grains of relatively large diameters that are greater than 25 micrometers and show the presence of substantial amounts of sand. The finer particles appear to be separable into two distinguishable size components, perhaps reflecting different source locations or transport processes.

4.3. CMT measurements

The CMT technique is suitable for investigation of samples with a size less than 10 mm in the horizontal direction for the experiments. In this experiment,

*Table 2.* Summary of geotechnical evaluations of sediment samples from the Blake Ridge (Data from Ref. 15).

Sample No.	Sub bottom depth m	Water content (Mw/M solids), %	Porosity %	Maximum past stress kPa
BLR-0.1	0.2	141	79.2	4.2
BLR-50	49.57	87.9	70.0	205
BLR-667	666.85	39.3	51.0	2730

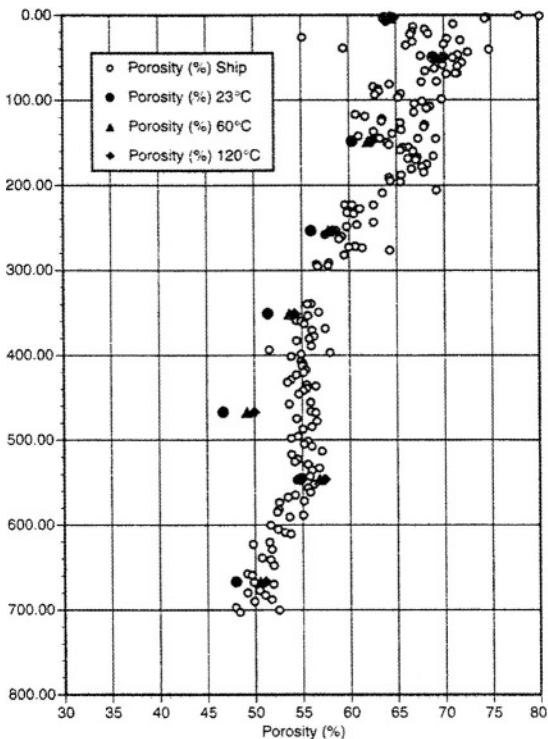


**Figure 3.** Porosity vs. depth derived from air drying of the Blake Ridge sediment sample. (From W. Winters, reference 14).

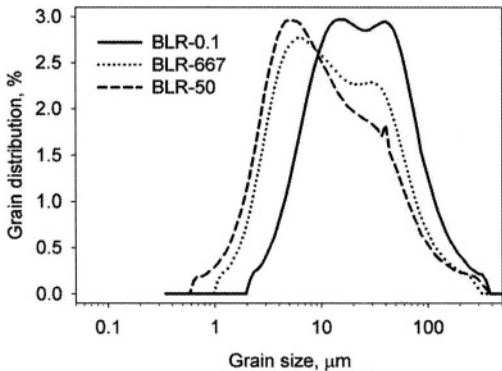


**Figure 4.** Grain-size distributions measured for the three samples.

measurements were made on three samples, BLR-0.1, BLR-50, and BLR-667, obtained at depths of 0.1 m, 49.6 m, and 666.7 m, respectively.

The CMT measurements produce a 3-D matrix representing the X-ray attenuation coefficients found for voxels contained in a volume of the sediment with x,y,z coordinates. We used software developed by Lindquist (17) to segment the voxels into solid and pore space categories. Plots of the histograms found for the attenuation coefficients and values for the porosity as a function of the attenuation coefficient are given in Figure 5. The Lindquist program uses image analysis

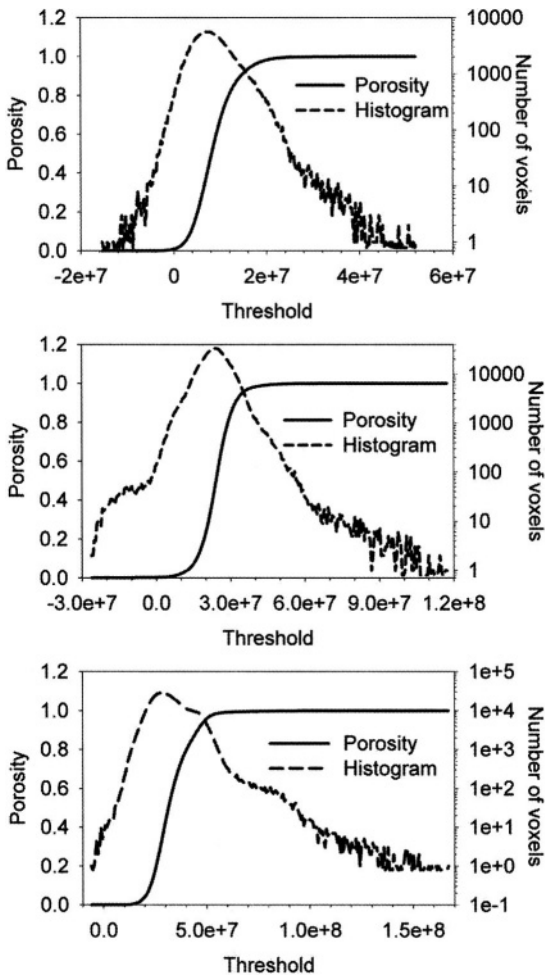


**Figure 5.** Porosities and histograms showing the distribution of attenuation coefficients in the tomographic volumes for the three samples measured. Samples BLR-0.1 (top), BLR-50 (middle) and BLR-667 (bottom).

algorithms in making assignments between the two phases based on values of the coefficients found for neighboring voxels.

Following the segmentation of the data into pore and solid phases, we can display the data either as 2-dimensional sections or as 3-dimensional volumes. Typical results found for the 2-dimensional section are given in Figure 6. Displays for the 3-dimensional volumes are given in Figure 7.

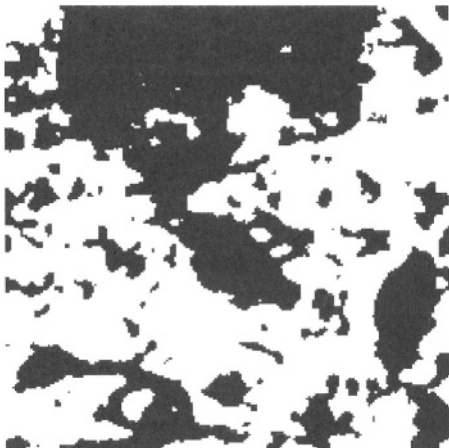


**Figure 6.** Volume CMT image of sediment sample BLR-668. The pixel size is 0.0068 mm. The Green to Purple to Yellow show increased attenuation in the measured attenuation coefficients indicating materials of increasing. The light green color represents pore space.

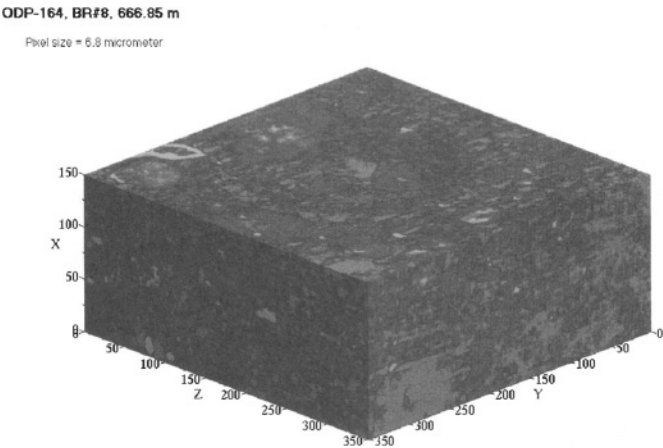


**Figure 7.** A 2-D image of a segmented slice reconstructed from the CMT data of sample BLR-50 from a depth of 49.6 m. The image size is  $200 \times 200$  pixels (1 pixel = 6.8 micrometer). Pore space is shown in white and solids in black.



*Table 3. Comparison of porosity values for the three samples determined by weight and CMT measurements.*

Sample No.	% Porosity Conventional	% Porosity CMT method
BLR-0.2	79.2	80.7
BLR-50	70.0	64.3
BLR-667	51.0	58.1

We stress that the CMT process is non-destructive and that sequential measurements can be made on a given sample as conditions of temperature and volume are changed. For example, porosity can be measured as a function of the stress (pressure) applied to the sample.

The values found for the porosities in the three samples measured are compared with the values determined via the mass measurements by Winters [15] in Table 3. As expected, porosity decreases with depth but the trend is not linear. This agreement between the different methods is evidence for the validity of CMT measurements. The pathways shown in Figure 8 differ greatly from one specimen to another and may depend on the state of the materials. Studies are now underway in which the sediment integrity will be strictly maintained in their transport and handling prior to the CMT measurements. Detailed interpretation of the CMT data will be the subject of a subsequent paper.

## 5. CONCLUSIONS

We have presented a summary of measurements on the physical properties of sediments relevant to methane hydrate recovery. The data includes not only geotechnical determinations, but also the CMT data that gives porosity values and pathways through the sediment material. The results show that CMT techniques can be used to study sediment properties on a micrometer-size scale. Since the technique is non-destructive, changes in the sediment microstructures as a function of pressure and temperature can be measured. It is also feasible to look at formation of methane hydrates in the sediment structure as has already been demonstrated [7–9]. A longer term challenge is to start from the microscale data and calculate the macroscopic quantities shown in Table 2. We also note that the CMT measurements help in identification of different minerals found in the sediments. This feature of CMT was not exploited in this survey.

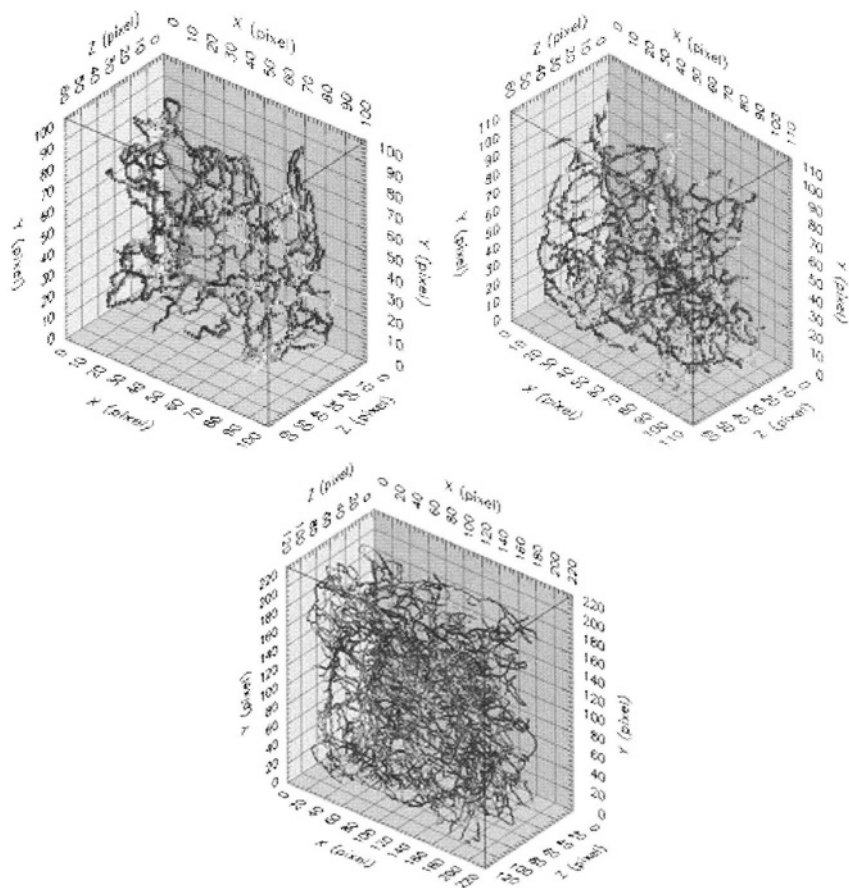


**Figure 8.** Pathways reconstructed from the data such as in Figure 7. Clockwise from left: Samples BLR-0.1, BLR-50, and BLR-668. Colors show different sizes for the pathways. The pixel sizes for the three axes are 0.0068 mm.

## ACKNOWLEDGMENTS

This research was, in part, supported by the US Department of Energy Contract No. DE-AC02-98CH10886 (KWJ, DM, HF). Additional support was provided through the Laboratory Directed Research and Development (LDRD) program at Brookhaven National Laboratory. We thank Professor Brent Lindquist, Stony Brook University for helpful discussions and assistance regarding the 3-D images. The authors wish to thank the captain and crew of the JOIDES Resolution and the R/V Oceanus, as well as the Ocean Drilling Program, for providing the sediment samples upon which this study was based.

## REFERENCES

1. Clathrate Hydrates of Natural Gases, 2<sup>nd</sup> edition; Sloan, Jr., E. D. Ed.; Marcel Dekker, New York, 1998.
2. Dickens, G. R.; Paull, C. K.; Wallace, P. *Nature*. 1997, 385, 426.
3. Makogon, Y. E.; Holditch, S. A. *Oil & Gas J.* 2001, 99 (6), 47.
4. Makogon, Y. E.; Holditch, S. A. *Oil & Gas J.* 2001, 99 (7), 45.
5. Natarajan, V.; Bishnoi, P. R.; Kalogerakis, N. *Chem. Eng. Sci.*, 1994, 49 (13), 2075.
6. Englezos, P.; Kalogerakis, N.; Dholabhai, P. D.; Bishnoi, P. R. *Chem. Eng. Sci.*, 1987, 42 (11), 2647.
7. Mikami, J.; Masuda, Y.; Uchida, T.; Satoh, T.; Takeda, H. In *Gas Hydrates, Challenges for the Future*, Holder, G. D.; Bishnoi, P. R., eds. *Annal. N.Y.A.S.* 2000, 912, 1011.
8. Tomutsa, L.; Freifeld, B.; Kneafsey, T. J.; Stern, L. A. *Soc. Petrol. Engineer. (S PE-75533)*, 2002.
9. Uchida, T.; Dallimore, S.; Mikami, J. In *Gas Hydrates, Challenges for the Future*, Holder, G. D.; Bishnoi, P. R., eds. *Annal. N.Y.A.S.* 2000, 912, 1021.
10. Winters, W. J., Dallimore, S. R., Collett, T. S., Katsube, T. J., Jenner, K. A., Cranston, R. E., Wright, J. F., Nixon, F. M., and Uchida, T., 1999, Physical properties of sediments from the JAPEX/JNOC/GSC Mallik 2L-38 gas hydrate research well: in Dallimore, S. R., Uchida, T., and Collett, T. S., eds., *Scientific Results from JAPEX/JNOC/GSC Mallik 2L-38 Gas Hydrate Research Well*, Mackenzie Delta, Northwest Territories, Canada, Geological Survey of Canada Bulletin 544, p. 95–100.
11. Jones, K. W.; Feng, H.; Winters, W. J.; Servio, P.; Mahajan, D. *Amer. Mineral.* submitted.
12. American Society for Testing and Material, 1997. *Annual Book of ASTM standards*, Vols. 04.08 and 04.09, Soil and Rock, Philadelphia (ASTM).
13. Jones, K. W., Feng, H., Lindquist, W. B., Adler, P. M., Thovert, J. F., Vekemans, B., Vincze, L., Szaloki, I., VanGrieken, R., Adams, F. and Riekell, C. From: Mees, F., Swennen, R. Van Geet, M., and Jacobs, P. (eds.) 2003. *Applications of X-ray Computed Tomography in the Geosciences*. Geological Society, London, Special Publications, 215, 39–49.
14. Dowd, B. A.; Andrews, A. B.; Marr, R. B.; Siddons, D. P.; Jones, K. W.; Peskin, A. M. in *Advances in X-Ray Analysis*, Plenum Publishing Corp., New York, 1999 and references therein.
15. Winters, W. J. *Proceedings of the Ocean Drilling Program, Scientific Results* (Paull, C. K.; Matsumoto, R.; Wallace P. J.; Dillon, W. P., eds.), 2000, 164, 421.
16. Winters, W. J. *Proceedings of the Ocean Drilling Program, Scientific Results* (Paull, C. K., Matsumoto, R., Wallace, P. J., Dillon, W. P., eds.), 2000, 164, 431.
17. Lindquist, W. B., Lee, S. M., Coker, D. A., Jones, K. W. and Spanne, P. J. *Geophys. Res.*, 1996, 101, 8297.

# Author Index

Belosludov, V. R., 19, 173

Chacin, Maria Carolina Gonzalez, 27

Chapman, Walter, 157

Chen, Roger, 157

Civan, Faruk, 27

Collett, Timothy S., 64

Copeland, David, 101

Dai, Jianchun, 117

Dutta, Nader, 117

Elliot, Douglas, 157

Elsen, Heather A., 199

Etheridge, John A., 185

Feng, Huan, 239

Freifeld, Barry M., 227

Gránásy, L., 3

Hong, Huifang, 43

Hughes, Richard G., 27

Inerbaev, T.M., 25

Jain, Pallav, 157

Jones, Keith W., 239

Kadaster, Ali, 101

Kalpakci, Bayram, 141

Khokhar, Aftab, 141

Kneafsey, Timothy J., 227

Kobayashi, Riki, 157

Kuznetsova, T., 3

Kvamme, B., 3

Kwan, Jonathan T., 101

Ladner, Edward P., 199

Liddell, Bill, 101

Link, Dirk D., 199

MacDonald, William, 101

Mahajan, Devinder, 239

Mason, David H., 213

Maurer, Williams, 101

McGuire, Donn, 101

Millheim, Keith, 101

Moridis, George J., 83

Newsham, K. E., 67

Ng, Heng-Joo, 157

Pearson, Larry E., 185

Phillip, Servio, 239

Pomeransky, A. A., 19, 173

Pooladi-Darvish, Mehran, 43

Pusztai, T., 3

Rai, Chandra, 101

Rogers, Rudy E., 185

Runyon, Steve, 101

Sames, Gary P.

Shukla, Keshawa, 141

Sigal, Richard, 101

Snyder, Fred, 117

Sondergeld, Carl, 101

Song, Kyoo, 157

Taylor, Charles E., 199

Tegze, G., 3

Thompson, Tommy, 101

Waite, William F., 213

Williams, Tom, 101

Winters, William J., 239

Xu, Haibin, 117

Zhang, Ying Irene, 157

Zhong, Yu, 185

*This page intentionally left blank*

# Keyword Index

- Acoustic Velocity, 68  
Arctic Platform, 102
- Base of Permafrost, 68, 71  
Black Oil, 141
- Cage Zeolites, 173  
Clathrates, 171, 173  
**CO<sub>2</sub>**, 3, 157  
Computed Microtomography, 240  
Core Characterization  
Core Imaging
- Decomposition Kinetics, 239  
Depressurization, 43, 203  
Dissociation, 45, 113, 141, 158, 201, 216, 227, 240  
Drilling Completion Fluids, 141
- Equilibrium, 5, 21, 46, 84, 141, 158, 204, 216, 228, 241  
Experiments, 9, 108, 142, 158, 189, 200, 224, 227, 239
- Formation, 3, 27, 43, 68, 84, 141, 157, 173, 185, 200, 213, 240
- Gas, 3, 19, 27, 43, 67, 83, 117, 141, 157, 173, 185, 199, 213, 227, 240  
Gas Condensate, 141  
Gas Hydrate, 3, 40, 64, 68, 97, 103, 117, 142, 185, 200, 213, 227, 240  
Gas Hydrates, 19, 41, 43, 67, 83, 117, 141, 157, 173, 185, 200, 215, 238, 240
- Gas Hydrates Stability Zone  
Gas Production, 43, 83, 102, 227  
Gas Storage, 186, 200  
Geothermal Gradient, 43, 69, 87, 215  
Gulf of Mexico, 117, 141
- Heat Flow, 43, 84, 119, 241  
Host Sediments, 239  
Hydrate, 3, 27, 67, 83, 101, 117, 141, 157, 173, 185, 199, 213, 227, 239  
Hydrate Formation, 20, 73, 143, 158, 186, 200, 214  
Hydrate Kinetics, 227  
Hydrates, 3, 19, 27, 43, 67, 83, 117, 141, 157, 173, 185, 199, 214, 227, 239
- Kinetics, 4, 34, 45, 106, 171, 227, 239
- Low Impact Arctic Operation
- Methane, 3, 27, 43, 68, 88, 101, 142, 157, 185, 199, 213, 227, 239  
Methane Hydrate, 35, 64, 88, 116, 150, 214, 228, 240  
Methane Hydrates, 96, 199, 225, 240  
Mobile Laboratory, 102  
Modeling, 4, 27, 65, 126, 141, 214  
Models, 4, 45, 117, 147, 213
- Natural Hydrates, 45  
Natural-Gas Storage  
Nucleation, 3, 28, 173, 188  
Nucleation, Growth
- Phase Field Theory, 3  
Physical Properties, 104, 190, 213, 248

- Production, 43, 83, 101, 200, 227
- Rock physics, 119, 214
- Seismic Inversion, 127
- Shear Strength, 221
- Solubility, 9, 142, 157, 200
- Statistical Thermodynamics, 20, 147
- Surfactants, 200, 214
- Thermal Diffusion, 69
- Thermal Stimulations
- X-Ray Tomography